DOTTORATO DI RICERCA

in FISICA

Ciclo XXI

Settore scientifico disciplinare di afferenza: FIS/04

ISOSPIN DEPENDENCE OF THE AR+NI FUSION-EVAPORATION CROSS SECTION

Presentata da: Dott.ssa Paola Marini

Coordinatore Dottorato: **Relatore:**

Prof. Fabio Ortolani   Prof. Mauro Bruno

Esame finale anno 2009

Ai miei cuccioli, Seymar e Kidar

Contents

Preface

The subject of this thesis is the determination of the isospin dependence of the Ar+Ni fusion-evaporation cross section.

One of the main goals of the current research in nuclear physics in the low and intermediate energy domain is to improve our knowledge about the properties of the occurring reaction mechanisms and their dependence on the characteristics of the entrance channel. By using secondary beams, as the ones produced by the SPIRAL facility, new nuclei are accessible by the fusion reaction channel, both on the side of proton-rich nuclei, in particular close to the $N = Z$ line, and of neutron-rich nuclei, generally not accessible by stable beams due to high neutron evaporation rate at the beginning of the evaporation cascade. The advent of radioactive beams, coupled to judiciously chosen targets, allows for the very first time to explore the properties of a large number of isotopes of compound nuclei of a given Z and, consequently, to test the influence of the mass asymmetry of the entrance channel on the fusion cross section. The fundamental goal of this experiment is to explore the variation of deexcitation properties and thus level density parameters with the N/Z ratio of the compound nucleus when going from the proton drip line to stable nuclei. Nuclear level densities are fundamental quantities which govern the statistical decay of excited nuclei and determine the properties of hot nuclei. Knowledge of the level density is thus highly needed at low and high excitation energies and for the largest possible range of N and Z, from β stability to the drip-lines.

In particular, in this work, fusion cross sections of different Ar isotopes on Ni targets have been analysed.

The measurements had been performed at the GANIL SPIRAL facility, with the high performance 4π detector INDRA, in conjunction with the magnetic spectrometer VAMOS, realizing a very efficient tool for attributing a reaction product to a reaction mechanism.

Three Ar isotope beams, with energies of about 13 AMeV, have been accelerated and impinged onto isotopically enriched Ni targets in order to produce Pd nuclei, with mass number varyiing from 92 to 104.

The first step in the analysis has been the reconstruction of raw data, in order to extract the information on the detectors working status, as well as on their stability and performances during the measurements.

Being the compound nucleus deexcitation process axially symmetric in the laboratory reference system, the computation of fusion-evaporation events can be performed in a restricted $\Delta\phi$ region. This procedure is based on the assumption of a correct beam alignment; beam mis-alignment with respect to the symmetry axis of the apparatus has been estimated and used to correct the data.

A fundamental part of the thesis work has been the discrimination between fusion-evaporation and deep-inelastic events, which present similar features. It has been possible by analysing the $\Delta E - E$ spectra and taking advantage of a dedicated GEMINI simulation, using an "INDRA experimental filter" especially developed for this work and a code evaluating the deep inelastic reaction kinematics. Being performed up to now neither energy and time of flight calibrations, nor Z and A identifications, the performed fusion evaporation events selection is inclusive.

In the present thesis the results for the Ar+Ni cross-sections are shown, as well as the comparison between the obtained cross section values and some theoretical models. Data have been normalized to the elastic cross section and are limited to the angular range covered by the INDRA apparatus. Data acquired by VAMOS have not yet been analysed. Some discrepancies between data and theoretical result have been pointed out, however the observed trend of the different fusion-evaporation cross sections suggests a possible dependence on the reaction entrance channel and, in particular, on the reaction isospin. To obtain a more detailed analysis, energy calibration, particle identification and VAMOS trajectory reconstruction are required.

The thesis is organized as follows: Chapter 1 contains a short review of the physics issues treated in this thesis work, in particular those relevant to inelastic and fusion reactions at low energy.
Chapter 2 contains a detailed description of the experimental apparatuses used for the measurements. A description of electronic and mechanical coupling of the two apparatuses is also presented, with particular focus on the trigger system.

In Chapter 3 the experimental setup is widely described, with special focus on the available trigger configurations and on the on-line checks performed during the measurements.

Chapter 4 is devoted to the preliminary data analysis: the raw data reconstruction is described and a detailed analysis of the available correlations allows to verify the detector stability and performances.

Chapter 5 is dedicated to the INDRA data analysis. In this chapter the beam alignment and the estimation of the mis-alignment with respect to the apparatus symmetry axis is described. Moreover the procedure to discriminate fusion-evaporation events from deep inelastic events is presented. The computation of the fusion-evaporation statistic and its normalization to elastic cross section are described. The obtained results are very preliminary, but the observed trend, compared with the theoretical predicted ones, gives a hint at the possible isospin dependence of the fusion-evaporation cross sections. More quantitative results will require a significant effort to calibrate all the INDRA and VAMOS detectors.

Chapter 1

Physics

1.1 Heavy ion collisions

Heavy ions reactions are one of the most powerful way to study nuclear matter behaviour in extreme conditions of temperature and density.

The heavy ions peculiarity is due to the fact that these reactions are the best way to produce nuclei with high excitation energy and angular momentum. One of the reasons for this property can be found by comparing the mean nucleon-nucleon distance in a nucleus ($d \sim 1.8$ fm) and the reduced wavelength associated with nucleon-nucleon collisions ($\lambda_{DeBroglie}$). If $\lambda_{DeBroglie} \ll d$ the most important effects arise from nucleon-nucleon collisions (2-body effects), which can lead to particle emission from the system (pre-equilibrium emissions). Otherwise, if $\lambda_{DeBroglie} \gtrsim d$, the collective behaviour of nucleons is important, mean field effects (1-body effects) are present and the interaction leads to an energy sharing in the system, which can reach high excitation energies. Some values of $\lambda_{DeBroglie}$ are given in Table 1.1 for different energies per nucleon and are calculated from the following relation [1]:

$$\lambda \cong \sqrt{\frac{40\,\text{MeV} \cdot \text{fm}^2}{(E^{(CM)} - V_{CB})}} \tag{1.1}$$

where $E^{(CM)}$ denotes the incident center-of-mass energy and V_{CB} the Coulomb barrier of two touching nucleons. Both $E^{(CM)}$ and V_{CB} are expressed in MeV. As the bombarding energy increases, the two aforementioned regimes are explored.

A first and schematic classification of heavy ions reactions is based then on the projectile kinetic incident energy (in the laboratory reference system) and in particular on the comparison between the relative initial velocity of the two colliding nuclei and the mean relative velocity of the nucleons inside a nucleus.

Energy (AMeV)	1	10	20	30	40	50
$\lambda_{DeBroglie}$(fm)	6.5	2.1	1.5	1.2	1.1	0.9

Table 1.1 – Reduced wavelength $\lambda_{DeBroglie}$ as a function of incident beam energy per nucleon E/A from eq.1.1

Describing a nucleus in its ground state as a *non-interacting fermionic degenerate gas* at $T = 0$, the energy of the highest energy level occupied by nucleons is the *Fermi energy*. The corresponding momentum, the *Fermi momentum* $p_F = \hbar k_F$, depends only on nuclear density ρ. k_F is given by [2]:

$$k_F = \left(\frac{2\pi^2\rho}{3}\right)^{\frac{1}{3}} \simeq 1.36\,\text{fm}^{-1} \qquad (1.2)$$

where ρ has the experimental value of $\rho \simeq 0.17$ nucleons/fm^3. The Fermi energy is then given by:

$$\epsilon_F = \frac{(\hbar k_F)^2}{2m} \simeq 38\,\text{MeV} \qquad (1.3)$$

where m is the nucleon mass.

We can refer to `low energy` regime if the projectile incident energy is $E_{lab} <$ 10 AMeV, `high energy` if $E_{lab} > 100$ AMeV and `intermediate energy` in the region 10 AMeV$< E_{lab} < 100$ AMeV.

Once the bombarding energy is fixed, a more detailed classification can be based on the centrality of the collision, described by the `impact parameter`. Referring to Fig.1.1(a), with impact parameter b [1] it is generally meant the perpendicular distance from the projectile asymptotic trajectory (during its approach to the target nucleus) to its parallel line passing through the target nucleus center.

The overall features of heavy ion interactions can be described referring to Fig.1.1(b). If b is big enough that there is not overlapping between the two colliding nuclei, the ions do not touch and can interact only through the Coulomb field, resulting in Rutherford scattering (see Fig.1.1(b), trajectory labelled as elastic diffusion) and possibly Coulomb excitation.
When the impact parameter is reduced, the nuclear interaction becomes more and more important and the projectile trajectory is determined by the competition between nuclear attraction and Coulomb repulsion. As a first approximation we can assume that the distance at which the nuclear interaction becomes significant, R_{gr},
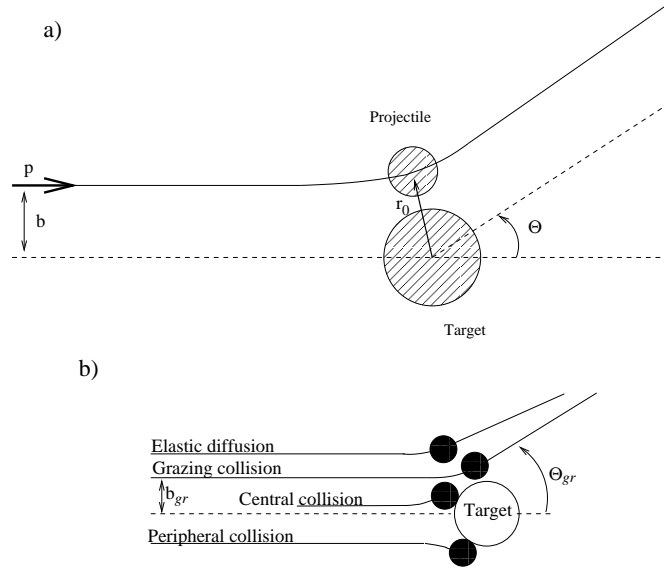
Figure 1.1 – Sketch of two nuclei collision.

is the sum of the radii of the ions. Experimentally [3], due to surface effects, R_{gr} is found to be greater than this latter quantity:

$$R_{gr} = 0.5 \, \text{fm} + r_{0_{gr}} \left(A_1^{\frac{1}{3}} + A_2^{\frac{1}{3}} \right) \tag{1.4}$$

where A_1 and A_2 are the masses of the two colliding ions and $r_{0_{gr}} = 1.36 fm$.
We define *grazing impact parameter* b_{gr} the impact parameter for which the distance of minimum approach r_0 (see Fig.1.1(a)) between the two nuclei is equal to R_{gr}. From the motion equation:

$$b_{gr} = R_{gr} \sqrt{1 - \frac{V_{CB}}{E^{(CM)}}} \tag{1.5}$$

where V_{CB} is the Coulomb barrier between the two colliding nuclei and $E^{(CM)}$ the kinetic energy in the center of mass reference system (CM system). The projectile trajectory of a nucleus colliding on a target with impact parameter b_{gr} is called *grazing trajectory* and the diffusion angle is referred to as *grazing angle* θ_{gr}.
If b is comparable to b_{gr} a grazing collision take place and the ions can be elastically or inelastically scattered or few nucleons can be transferred from one to the other. When the impact parameter is further reduced the ions begin to interact very strongly, providing the incident energy is high enough to overcome the Coulomb potential. This transition is quite sharply because the nuclear densities rise very rapidly in the surface region, causing a suddenly mutation in the interaction characteristics.

Since nuclear reactions properties depend strictly on the impact parameter, typ-

ically the two extreme case are distinguished, referring to collision with $b \simeq 0$ as `central collision` and as `peripheral collision` to collision with $b \simeq b_{gr}$.

The reaction mechanism depends then on the impact parameter, varying significantly moving from central to peripheral collisions. With reaction mechanism it is generally meant the assembly of microscopic processes that lead to transfer part of the initial kinetic energy, stored in the collective translational motion of the two nuclei, to the internal degrees of freedom of the system, ranging from the collective excitation of the projectile and target remnants to fragment or particle emission. The impact parameter is the order parameter of any theoretical description of nuclear collisions, but it is not experimentally accessible. Estimations of b are typically obtained by measurable variables monotonically correlated with b. Experimental evidences [4] suggest that the Total Kinetic Energy Loss (TKEL) during the collision is a good estimation of b: increasing the collision centrality, indeed, the kinetic energy that can be dissipated in internal degrees of freedom of the system increases. From an experimental point of view the TKEL can be obtained from the difference in the CM system between the initial kinetic energy E^{CM} and the kinetic energy of the reaction exit channel, i.e. the total kinetic energy of fragments produced in the reaction, before any decay (TKE Total Kinetic Energy):

$$TKEL = E^{CM} - TKE \tag{1.6}$$

Experimental results have shown that the TKEL is well correlated to the impact parameter, both at low incident energy [4], where pre-equilibrium processes are nearly absent, and at intermediate incident energy [5] .

1.2   Low energy nuclear reactions

At low bombarding energies the wavelength $\lambda_{DeBroglie}$ associated to the relative motion of the interacting nucleons is comparable or greater than the mean distance between nucleons: the excitation energy, dependent on the impact parameter, is then "shared" between all nucleons in the system and the energy transferred to a single nucleon is then not sufficient to bring it in a "free particle state". Moreover, the Pauli Principle reduces the probability of nucleon-nucleon collision (*Pauli blocking*), the most part of the available phase space being occupied. Therefore the energy dissipation can proceed only through the 1-body mechanism, i.e. some nucleons are interchanged between projectile and target and retained by the respective attractive mean fields. This is the energy range dominated by the mean field [6], so that the

main components of the reaction mechanism can be understood in terms of the effective interaction potential between the two heavy ions. Its general form is of the type

$$V_l^{eff}(r) = V_{CB}(r) + V_N(r) + \frac{\hbar^2 l(l+1)}{2\mu r^2} \tag{1.7}$$

where l and μ are the relative angular momentum and the reduced mass in the input channel, respectively. V_l^{eff} has three terms:

the repulsive electrostatic or Coulomb potential $V_{CB}(r)$, equal to $\frac{Z_1 Z_2 e^2}{r}$ outside the ions and rather less inside

the strongly attractive nuclear potential $V_N(r)$, which essentially acts only within the volume occupied by the ions and falls off exponentially outside. This contribution becomes repulsive when the densities of the two nuclei significantly overlap. This is due to the incompressibility of the nuclear matter and to the fact that nuclear shapes cannot evolve rapidly enough during the first stage of the collision.

the repulsive centrifugal potential $\frac{\hbar^2 l(l+1)}{2\mu r^2}$ that accounts for the increasing difficulty for the ions with higher relative angular momentum to approach each other.

This potential describes the forces acting on one ion due to the other, and classically speaking determines their orbits during the interaction. As soon as the ions touch each other additional particle-absorbing processes come into play, and these are usually represented as an absorbing potential. A typical behaviour of V_{eff} is shown in Fig.1.2.

It should be recalled that, because of angular momentum conservation

$$L = p_\infty b = \hbar l,$$

once the energy is fixed, the impact parameter or angular momentum scales are equivalent. We can then classify reaction mechanisms in the energy range between Coulomb barrier region and $\sim 10\,\text{AMeV}$ according to the impact parameter b or to the orbital angular momentum l.

In the most central collisions for $l < l_{crit}$ ($l_{crit} \simeq 100$ in Fig.1.2), and for not too heavy ions, the attractive force is strong enough to form a pocket in the V_{eff} potential. The system is trapped and can fuse to form a *Compound Nucleus* (CN): a single nuclear system kept together by its mean field. A very important aspect of fusion at such moderate incident energies is that the reaction process may be divided into two steps, well separated in time. The first step of the collision itself, which leads to
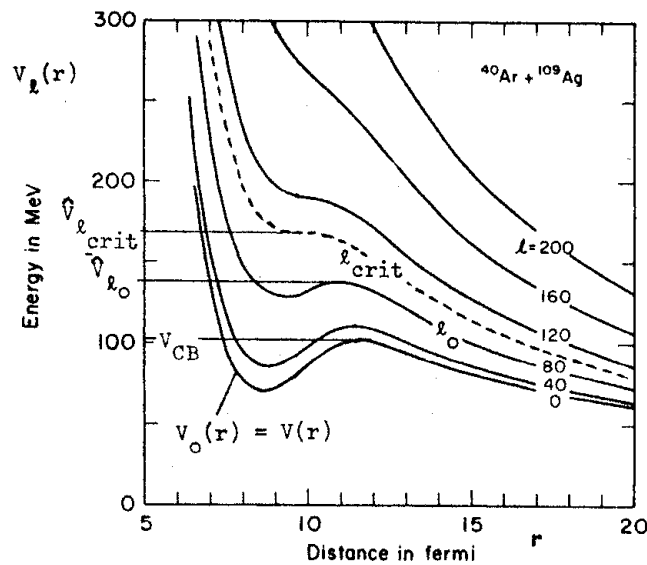
Figure 1.2 – Evolution of interaction potential as a function of the relative distance r for various value of relative angular momentum l, in ^{40}Ar+^{109}Ag reaction. Picture taken from [1].

a fully equilibrated excited nucleus on a timescale shorter than the decay time. Depending on the achievement of the equilibrium during the first step of the reaction and on the result of the competition between fission and nucleons evaporation, a single heavy residue may survive up to the end.

Increasing l, when some critical value l_{crit}, governed by the interaction potential between the interaction nuclei, is reached, the minimum in the potential V_{eff} vanishes, due the effect of centrifugal barrier. The critical angular momentum separates the fusion and the so-called `deep inelastic collision` regions.

As the pocket in the potential disappears, for $l \geq l_{crit}$, the system is never trapped and the two reaction partners experience a more or less prolonged contact, during which they are strongly slowed down by nuclear matter friction and, for a short time, they form a "quasi-molecular" states; at the end they reseparate again. During this step nuclei can exchange nucleons. Depending on the contact time, which is directly linked to the observed rotation angle of the di-nuclear system before its decay, a full equilibrium may be or not be achieved during this first step. As in the case of fusion the produced excited system decay characteristics depend on the achievement of the equilibrium during the first step of the reaction.

These dissipative collisions, where $l_{crit} < l < l_{DIC}$, are the so-called *Deep Inelastic Collisions* (DIC). The exact placing of the border l_{DIC} is ambiguous. The usual terminology of *Projectile Like Fragment* (PLF) and *Target Like Fragment* (TLF) indicates the nuclei that retained the majority of the original projectile and target nucleons,

respectively.

Slightly below l_{gr} ($l_{gr} \sim 190\hbar$ in Fig.1.2 for $E/A \simeq 10\,\text{AMeV}$), but for $l > l_{DIC}$, quasi-elastic and transfer reactions are observed. If both dissipative and fusion reactions are clear signatures of mean-field effects leading to a collective behaviour of the involved nuclei, in quasi elastic and transfer reactions only the nucleons occupying the most external nuclear orbitals are involved and the projectile and the target kinematical properties are only slightly perturbed.

Rutherford elastic scattering is observed for angular momenta $l \geq l_{gr}$, which corresponds to grazing collisions: the two ions do not feel the mutual nuclear interaction and the nuclear reaction cross section is zero.

Reaction cross section   Total reaction cross section σ_R for complex projectiles at energies above the interaction barrier can be described adequately in completely classical terms [1, 7]. This is a consequence of summing over all angles and exit channels, which eliminates quantal interference effects.

In a sharp cut off model, where all trajectories with angular momentum up to l_{gr} lead to absorption, we can write [1]:

$$\frac{d\sigma_R(E^{(CM)})}{dl} = 2\pi\lambda^2 l \tag{1.8}$$

$$\sigma_R = \int_0^{l_{gr}} 2\pi\lambda^2 l\, dl = \pi\lambda^2 l_{gr}^2 \tag{1.9}$$

where l_{gr} is related to the distance R_{gr} where the nuclear interaction becomes significant (eq.1.4).

From a quantistical point of view, since not all real value of l are allowed, l has to be replaced with $(l + 1/2)$ and the integral with a sum over l integer:

$$\sigma_R(E^{(CM)}) = \pi\lambda^2 \sum_{l=0}^{l_{gr}} (2l + 1) \tag{1.10}$$

To take into account a smooth transition of $\sigma_R(E^{(CM)})$ across l_{gr}, transmission coefficients $T_l(E^{(CM)})$ [8], slowly varying with energy, can be introduced, giving:

$$\sigma_R(E^{(CM)}) = \pi\lambda^2 \sum_{l=0}^{l_{gr}} (2l + 1) T_l(E^{(CM)}) \tag{1.11}$$

In a simple geometrical sharp cut-off model the contribution to the nuclear re-
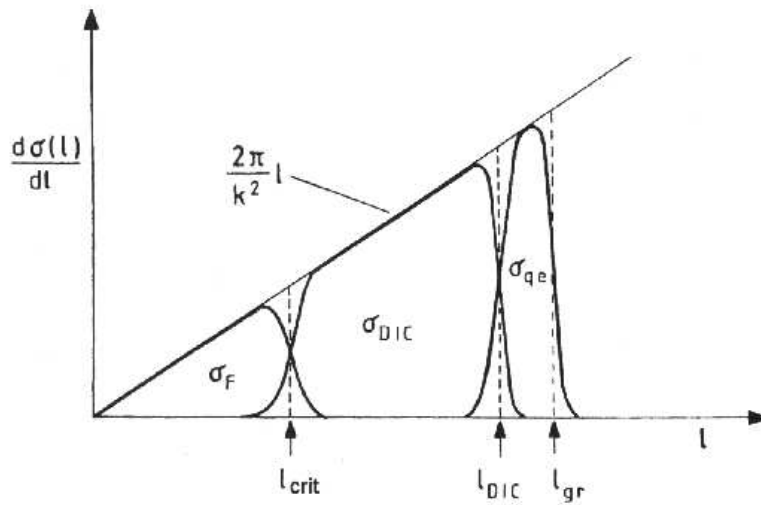
Figure 1.3 – Total reaction cross section dependence on the relative input channel angular
momentum l in the sharp cut-off approximation [9].

action cross section can be depicted like in Fig.1.3. Three components are evident:
the quasi-elastic σ_{qe} ($l_{DIC} < l \leq l_{gr}$), the deep inelastic σ_{DIC}($l_{crit} < l < l_{DIC}$), and the
compound nucleus σ_{CN}($l < l_{crit}$). The importance of the three contributions to the
reaction cross section depends on the relative strength of the nuclear and Coulomb
interaction: in particular, with the increasing of the latter, the fusion component first,
and the deep inelastic after, tend to disappear.

1.2.1   Rutherford collisions

At energy below the Coulomb barrier, and for impact parameter $b > b_{gr}$, the two
colliding ions do not touch and can interact only through the Coulomb field: the
interaction potential in eq.(1.7) keeps only the first term.
Assuming that there is practically no nuclear interaction at distances larger than
R_{gr}, corresponding to angular momentum $l > l_{gr}$, from classical considerations it's
possible to find simple relationships for elastic scattering. If a particle of energy E,
velocity v, and charge Z_1e is scattered by the Coulomb field of the target of charge
Z_2e, then the impact parameter b, the distance of closest approach r_0 and the center-
of-mass scattering angle Θ (see Fig.1.1) are related by [10]:

$$b = a_c \cot \frac{\Theta}{2} \tag{1.12}$$

and

$$r_0 = a_c \left(1 + \frac{1}{\sin \frac{\Theta}{2}} \right) \tag{1.13}$$

where

$$a_c \equiv \frac{Z_1 Z_2 e^2}{2E^{(CM)}}$$

The differential cross section for scattering at an angle Θ is [10]:

$$\frac{d\sigma}{d\Omega} = \frac{b}{\sin \Theta} \frac{db}{d\Theta} \tag{1.14}$$

and, using eq.1.12, this gives the well known Rutherford scattering formula:

$$\left. \frac{d\sigma}{d\Omega} \right|_{Rutherford} = \frac{a_c^2}{4} \frac{1}{\sin^4 \frac{\Theta}{2}} \tag{1.15}$$

The electrostatic potential between two ions is usually assumed to be described [11] with sufficient accuracy, in the physically important surface region, by the potential between a point charge and a uniform spherical charge distribution of radius R, which has the simple form

$$V_{CB}(r) = \begin{cases} \dfrac{1}{4\pi\varepsilon_0} \dfrac{Z_1 Z_2 e^2}{2R_{gr}} \left(3 - \dfrac{r^2}{R_{gr}^2} \right) & r \le R_{gr} \\[3ex] \dfrac{1}{4\pi\varepsilon_0} \dfrac{Z_1 Z_2 e^2}{r} & r > R_{gr} \end{cases} \tag{1.16}$$

Calculating the kinetic energy $E^{(CM)}$ at the distance of closest approach r_0, and imposing the energy conservation, the impact parameter b and the distance of closest approach r_0 are related by:

$$b = r_0 \sqrt{1 - \frac{V(r_0)}{E^{(CM)}}}. \tag{1.17}$$

Eq.1.7 and 1.17 allow to extract the grazing impact parameter b_{gr} and the grazing deflection angle Θ_{gr}:

$$b_{gr} = R_{gr} \sqrt{1 - \frac{V_{CB}(R_{gr})}{E^{(CM)}}}$$

$$\Theta_{gr} = 2 \arctan \frac{V_{CB}(R_{gr})}{2\sqrt{E^{(CM)}(E^{(CM)} - V_{CB}(R_{gr}))}} \tag{1.18}$$

There are two effects which limit the classical description of elastic scattering. These are quantal effects and absorption. In a quantum-mechanical description the

classic approximation is found to be much better as the *Sommerfield parameter*, defined as:

$$\eta = \frac{Z_1 Z_2 e^2}{\hbar v} = \frac{a_0}{\lambda} \tag{1.19}$$

is greater than 1.

The elastic nuclear scattering becomes significant as the energy of incident particles increases and the distance of closest approach decreases to the nuclear radii, and thus the projectile and the target feel the nuclear force.

The nucleus acts as an absorbing disk and diffraction patterns, due to interferences effects from different trajectories, can be observed.

A reaction such as Ar+Ni (at $\sim 13\,\mathrm{AMeV}$ beam energy) is characterized by a large η parameter ($\eta \sim 23$) and is Coulomb dominated. Rutherford scattering is then predominant down to $l \simeq l_{gr}$

1.2.2 Inelastic collision

In HI collision the elastic scattering is limited essentially to impact parameters which do no lead to a considerable overlap of projectile and target. For smaller impact parameters inelastic processes (excitation and transfer of nucleons) occur.

We refer as inelastic collisions to all the collisions where a certain amount of the initial kinetic energy is dissipated in internal degree of freedoms of the system, ranging from those in which a few nucleons are transferred from one ion to the other, with little loss of energy, to the so-called "strongly damped" or "deep inelastic" collisions in which the ions lose a substantial fraction of their kinetic energy.

When two nuclei collide, they interact through their Coulomb field leading eventually to an excitation of one or both the colliding nuclei or to a transfer of nucleons. During the collision a composite system is formed, which preserves a di-nuclear feature: in the contact region a "window" is formed between the two colliding nuclei. Through this window, more or less stretched, the energy dissipations take place by nucleons exchange and angular momentum transfer.

The composite system does not reach complete statistical equilibrium, because there are a few distinguished degrees of freedom ("collective variables") which relax very slowly, over times larger than or comparable with the contact time of the two fragments. These relaxation phenomena are connected with mass transfer, kinetic-energy loss and angular momentum dissipation. Afterward the system splits into two primary fragments, called *Projectile* and *Target Like Fragments* (PLF and TLF), or *Quasi Projectile* (QP) and *Quasi Target* (QT), which preserve memory of the entrance channel. The PLF and the TLF velocities $\vec{v_{PLF}}$ and $\vec{v_{TLF}}$ are quite similar to the projectile and the target nuclei velocities ($\vec{v_p}$ and $\vec{v_t}$), respectively.
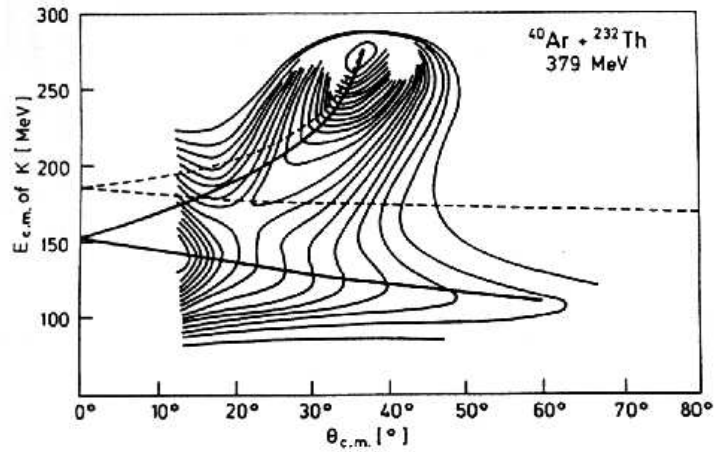
Figure 1.4 – Experimental Wilczyński plot for ^{40}Ar+^{232}Th at $379MeV$ total beam energy. The picture is taken from [9]. In such a plot, the center-of-mass energy of a given product of the reaction (here K nuclei, $A_K \sim A_{Ar}$) is plotted as a function of its center-of-mass emission angle Θ_{CM}. A large bump is observed at $E^{(CM)} \approx 280MeV$ and $\Theta_{CM} \approx 40°$: this correspond to quasi-elastic collisions ($l \sim l_{gr}$). Inelastic collisions, $l_{crit} < l < l_{gr}$, where a large decrease in the energy occurs, are associated with large deflection angle. The broken line (and the similar full line) correspond to model calculations based on trajectory calculations with two different interaction potentials such as the one depicted in Fig.1.2.

Primary fragments deexcite essentially by light particles emission or sequential fission (followed by evaporation), giving rise to 3 or 4 fragments in the exit channel.

Typical usefull correlations between physical variables to study inelastic collisions are:

- the $TKE - \Theta_{CM}^{PLF}$ correlation, known as *Wilczyński Plot*, where Θ_{CM}^{PLF} is the PLF polar deflection angle in the CM system and TKE the Total Kinetic Energy of the fragment

- the $TKE - A$ correlation, known as *Diffusion Plot*, where A is the PLF atomic mass

In the *Wilczyński Plot* (Fig.1.4 and 1.6(a)) the differential cross section $\frac{d^2\sigma}{d\Theta dTKE}$ is shown in the plane $TKE - \Theta_{CM}^{PLF}$. Both the quantities Θ and TKE are referred to the primary fragment, i.e. to the fragment before its evaporative deexcitation.

From a classical point of view, the loss of the kinetic energy is due to friction forces [1] (both radial and tangential) that act during the collision and decelerate the fragments on their classical orbits: the longer the two body stay in contact, the larger is the energy dissipated.
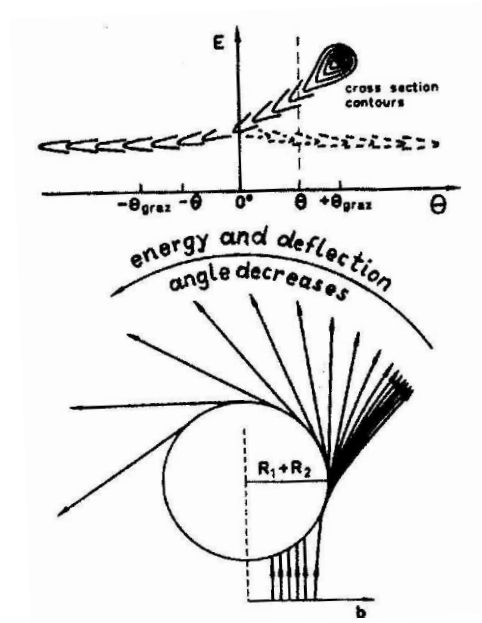
Figure 1.5 – Schematic picture of the trajectories deflection in an inelastic collision. The lower part shows the classical trajectories, while the upper one shows the expected $\frac{d^2\sigma}{dTKEd\Theta_{CM}^{PLF}}$ behaviour. The picture is taken from [1].

Starting from the grazing angle ($\Theta_{CM} \approx 40°$ in Fig.1.4), which corresponds to a TKE value equal to the available kinetic energy in CM system ($E^{(CM)} \approx 280MeV$ in Fig.1.4), and moving towards more dissipative collisions (i.e. the interaction time increases), the PLF polar diffusion angle moves backward towards the beam ($\Theta_{CM} < \Theta_{CM}^{gr}$), due to the nuclear interaction, and then the Θ_{CM} distribution becomes isotropic when $TKE \sim V_{CB}$.

This behaviour is clear if we look at Fig.1.5 and we keep in mind the relation between the TKEL ($TKEL = E^{(CM)} - TKE$) and the impact parameter b. As b decreases, Θ_{CM}^{PLF} decreases, because of Coulombian repulsion and nuclear attraction competition acting between the two nuclei, and reaches negative values. If one considers that the sign of the Θ_{CM} angle cannot be experimentally discriminated, Fig.1.4 is composed by two branches: the branch with the higher kinetic energy corresponds to a process leading to a $\Theta_{CM}^{PLF} > 0$ trajectory, the other one to process leading to a $\Theta_{CM}^{PLF} < 0$ trajectory.

Kinetic energy relaxation is associated with a rotation of the di-nuclear system towards lower values of Θ_{CM}.

In the *Diffusion Plot* (Fig.1.6(b)) the differential cross section $\frac{d^2\sigma}{dAdTKE}$ is shown in the plane $TKE - A$. Both the quantities A and TKE are referred to the primary fragment. The mean mass of the primary fragment is the initial one, but the mass distribution increases its width moving from peripheral collisions (high TKE) to central
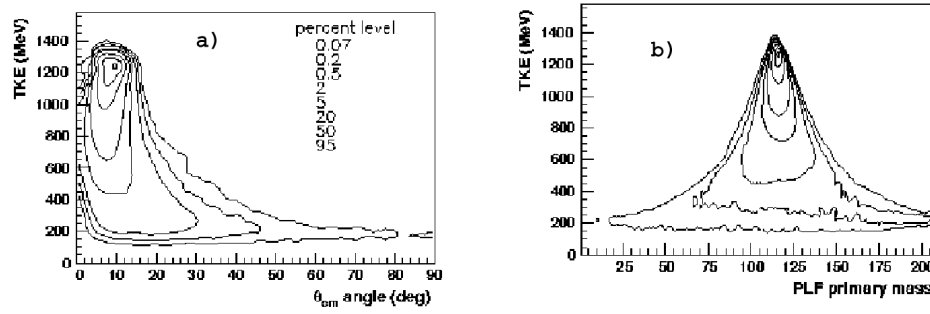
Figure 1.6 – Example of experimental *Wilczyński* and *Diffusion Plots* for ^{93}Nb+^{116}Sn at 25 AMeV beam energy [12].

(and the more dissipative) collisions.

Both in *Wilczyński* and *Diffusion Plot* there is a minimum TKE value permitted (~ 150 MeV in Fig.1.6), for which both the differential cross sections cover all the available Θ_{CM} and A, respectively. The minimum mean kinetic energy of the outgoing ions is very similar to the electrostatic repulsion energy of two just-touching nuclei. This agreement between the mean energy of the deep inelastically scattered ions and the simple electrostatic value confirms the two-body nature of the interaction. It also shows that the transfer of initial kinetic energy to excitation energy is essentially complete, and for this reason the reactions are sometimes referred to as *strongly damped*, *thermalized* or *relaxed* collisions.

Friction forces, which cause the loss of the initial kinetic energy of the two reaction partners, can be decomposed into two components: a radial and a tangent components. Including in the collective potential of eq.1.7 a tangential component the relative angular momentum of the two bodies, *l*, cannot remain constant and decreases from the initial value to a lower one; in the meanwhile the potential shape also changes during rotation. The shape of the potential determines the evolution of the reaction. The final decision in favour of trapping to form a compound object or of reseparating then depends critically on the ratio between tangential and radial friction and this complicates the scenario quite a lot [1]. Here we avoid the discussion of all such details and remark that such friction is the result of 1-body mechanism: there are no nucleon-nucleon collisions but rather a stochastic migration from PLF to TLF and vice versa through the potential window that forms when the two nuclei get in contact. The longer the time such window remains open, the bigger the number of exchanged nucleons and hence the larger dissipated energy. Due to the non deterministic nature of such a transfer of matter from the two nuclei, for a selected incident energy and impact parameter, the TKEL is fixed only on average and fluctuations are expected: the correlation, then, has an intrinsic

width. Moreover there are also perturbations originated during the deexcitation phase. These two contributions give rise to a correlation with a certain width. The qualitative picture in Fig.1.4 is rendered quantitative in microscopic models like the Nucleon Exchange Model [13–18]. The advantage over a classical trajectory calculations including friction forces is clear, as this approach allows the calculation of the intrinsic contribution to the second momentum of the distribution.

An order of magnitude estimate is now discussed for typical relaxation time of inelastic collision in the low energy domain.
For the mean field the period of a typical Giant resonance oscillation in monopole mode can be considered $\tau_{monopole} \approx 70\,\text{fm/c}$ [9]. For the single particle interaction with the mean field an estimation is given by [7,9]

$$\tau_{1-body} \approx \frac{R}{v_F} \approx 20 \div 30 \text{fm/c} \tag{1.20}$$

where R is of the order of the sum of the radii of the two nuclei and v_F is the Fermi velocity. The transit time of a nucleon with Fermi momentum through the nuclear diameter is a measure of the response time of the intrinsic nucleonic structure to external disturbance and, in this energy domain ($E_{inc} \ll \epsilon_F$), it is a good estimation of the thermalization time (τ_{therm}), i.e. the time required by an incident nucleon to dissipate all its energy, exciting the intrinsic degrees of freedom (related to thermal excitation) of the target nuclei.
These values have to be compared with typical traversal times, defined as

$$\tau_{inter} \approx \frac{R}{v_{AA}} \tag{1.21}$$

that are of the order of $\approx 85\,\text{fm/c}$ for $15AMeV$ beam energy (v_{AA} is the initial relative velocity of the two colliding nuclei).

For collision between complex nuclei, where two fragments are re-emitted without the formation of a single system, two more characteristic times can be defined: a rotational period, which corresponds to the time required for a (hypothetical) complete revolution of the two touching fragments ($\tau_{rot} \approx 900\,\text{fm/c}$ [9]), and a interaction time (or contact time) during which the fragments interact strongly by nuclear forces ($\tau_{interac} \approx 300$ and $50\,\text{fm/c}$ in central and peripheral collisions [9], respectively). For a given initial system, both times will in general depend on bombarding energy, relative angular momentum and Q value. If the interaction time is much shorter than the rotational period, then we expect asymmetric angular distribution peaked in the

vicinity of the grazing angle. Otherwise, if the interaction time is long compared to the rotational time, it will result symmetric with respect to 90°. The latter situation, which implies the existence of an orbiting quasi-molecular system, correspond to the Wilckyǹsky plot region where the angular distribution is isotropic.

1.2.3   Complete and incomplete fusion

Central collisions are the key reactions which really probe matter in its extreme state since they correspond to the largest dissipated energies. In these conditions one has the largest compression because close collisions lead to a considerable overlap of the density distribution of the colliding nuclei. In these processes the interacting composite system may break apart again preserving its di-nuclear feature, as we have seen in dissipative collisions, or form a fused system. This latter phenomenon can be described as the result of a strong friction between the two participating nuclei which leads to a merging of all their nucleons. If the interaction time is long enough with respect to the thermalization time, i.e. when the impact parameter approaches zero, this dissipative process may eventually establish complete thermodynamical equilibrium between the two ions. The reaction proceeds then, according to Bohr's hypothesis [19], through the intermediate stage of a completely equilibrated system, known as `compound nucleus` (CN) which is formed by the absorption of the projectile by the target nucleus.

At low incident energies many nuclear reactions proceed through the capture of the incident particle by the target nucleus to form a CN, but CN reactions between heavy ions are of particular interest because they provide the most efficient way of forming highly excited systems in high-spin states. Since many nucleons are involved, the energy may be high but it is shared by all nucleons. Therefore nucleon velocities are not so high to lead to direct reactions without CN formation.

In addition the high orbital angular momenta make it possible to form compound states of high spin.

The CN is formed in an excited state and it decays, after a time long compared with the transit time, by a statistical process, such as γ rays and/or particles emission (or eventually fission), that may be treated by the methods of nuclear thermodynamics, such as the statistical model, which is essentially based on Bohr's CN picture. Once a nucleon enters a nucleus, it interacts very strongly with the other nucleons, thus significantly reducing its mean free path, and the carried energy is quickly shared and re-shared among the constituent nucleons, until all memory of

the system's mode of formation is lost, except that required by the conservation of energy, angular momentum and parity. The particles emitted ("evaporated") by this heated, equilibrated system will accordingly have a distribution in energy that is typically of the order of the total energy of the system and independent of its mode of formation and an isotropic angular distribution in the CN reference system. The CN mass before any decay is the total initial mass of the system: this process is called `complete fusion` and dominates central collisions between heavy ions for projectile energies $E \lesssim 10AMeV$ [20].

When the incident energy increases ($E \gtrsim 10$ AMeV), the projectile and/or the target may lose, in the early stage of the collision, cluster of nucleons, emitted as light fragments, which remove an appreciable part of the kinetic energy initially carried by the entire projectile. It has been shown that nucleons may escape if the velocity in the center-of-mass framework of the nucleus they belong to is larger than a given threshold ($\sim 0.06c$) [21]. These fragments have either a velocity close to the beam velocity or a small velocity depending on whether they have been emitted by the projectile or the target respectively. On a longer time scale the remnants of the two colliding nuclei fuse. Again a complete statistical equilibrium of the merging nucleons is achieved. In this process, commonly called `incomplete fusion` [20,22,23], as a result, the mass of the "reduced" CN formed is less than the total mass of the system, the velocities of the evaporation residues and of the fission fragments are different from those of the fragments emitted subsequent to complete fusion. Moreover the "reduced" CN obviously does not absorb the full linear momentum of projectile and target. Hence, the measurement of the linear momentum transferred to the CN gives an insight into the reaction mechanism.
Later on we refer as compound nucleus to the compound system produced both in complete and incomplete fusion reactions.

With increasing projectile energy ($E \simeq 20 \div 40$ AMeV), incomplete fusion becomes preponderant with respect to complete fusion; the global fusion cross section diminishes progressively and, for Ar-induced reaction , vanishes around 35 AMeV incident energy [24–27], but persist to much higher energies for very asymmetric collisions, for example C or N impinging on heavy targets [28].

The way in which a CN is formed is a dynamical problem and it is connected with the problem of friction or viscosity, i.e. the transfer of energy from one degree of freedom (the relative motion) to the many degrees of freedom describing the compound nucleus.

We now consider the energy balance in nuclear fusion. The excitation energy of the CN, U, at a given center-of-mass bombarding energy $E^{(CM)}$, can be written as:

$$U = E^{(CM)} + Q_{fu} = E^{(CM)} + (M_1 + M_2 - M_{1+2})c^2 \tag{1.22}$$

where Q_{fu} is the Q-value associated with the formation of the CN in its ground state and M_1, M_2 and M_{1+2} the mass of the projectile, target and CN respectively, at their ground state. This shows that CN formation represents the limit of a completely inelastic process, where all of the relative kinetic energy in the incident channel is absorbed.

Compound nucleus lifetimes can be deduced by statistical model calculations, which relate the lifetime of the CN to its level density and to the effective number of open decay channels. Typical lifetimes are of the order of $300 \div 3000\,\text{fm}/\text{c}$ for excitation energy around $U \sim 100 MeV$ and are long with respect to thermalization times.

Limitation on compound nucleus formation are due to:

- the existence of the Yrast line

- prompt fission

- entrance channel effects

Yrast level and CN formation   The formation of a CN with a given excitation energy (U), angular momentum (J) and parity (π) is limited by the existence of the Yrast line [29] that marks the limit of nuclear stability (available levels) with respect to angular momentum at a given excitation energy.

Referring to Fig.1.7, the Yrast line is indicated by the solid curve. To the left of this line, nuclear levels are available. The second line, indicated as *population line*, is the boundary, in U vs J plane, given by the angular momentum of incoming ions [1]: level must exist in the CN at appropriate U and J^π. Only the area to the left of the Yrast line and above the population line is available in the heavy ion fusion reactions.

Critical angular momentum and instability against fission   The total angular momentum in heavy ion reactions is usually very large. The high angular momentum barrier may lead to instantaneous instability of the compound system against fission. The smallest angular momentum for which this happens is the critical angular momentum l_{crit} and it corresponds to the maximum l value for which it is
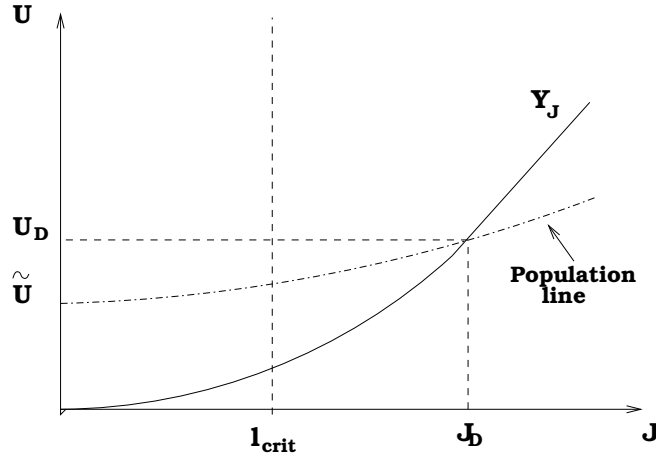
Figure 1.7 – Limitations in compound nucleus formation due to the Yrast line. The crossing point between the Yrast line and the population line is labelled with (U_D, J_D). Being usually $J_D > l_{crit}$, the limitation of compound nucleus formation is due to fission and not to the absence of compound levels according to the Yrast line.

possible to observe a pocket in the nuclear potential (Fig.1.2). When $l = l_{crit}$ the fission barrier B_f between the two colliding nuclei vanishes: the compound system is unstable against prompt fission and CN formation is impossible. The phenomenon can be understood in terms of competition between the Coulomb repulsive interaction and the surface potential in a deformed nucleus, within the liquid drop model. We introduce the fissility parameter x:

$$x = \frac{E_{coul}}{E_{sup}} \tag{1.23}$$

and the rotation parameter y

$$y = \frac{E_{rot}}{E_{sup}} \tag{1.24}$$

where E_{rot} is the rotational energy associated with the angular momentum l. For $x = 1$ and zero angular momentum ($y = 0$) the system becomes unstable against prompt fission, i.e. the fission barrier vanishes. Qualitatively speaking the addition of angular momentum enhances the nucleus ability to undergo fission, since $E_{rot}(l)$ decreases with increasing deformation. For $x < 1$, the fission barrier decreases with increasing angular momentum l and vanishes at a finite value of l. Since in absence of fission barrier the lifetime of the composite system is of the order of the vibrational period (classical nucleonic period), a CN in classical sense should not exist.

The effect of the existence of a critical angular momentum l_{crit} on CN formation in HI reactions can be seen in Fig.1.8(a), which classifies nuclear reactions as functions of the impact parameter b and the center-of-mass energy $E^{(CM)}$. The figure

(a) Light nuclei   (b) Heavy nuclei
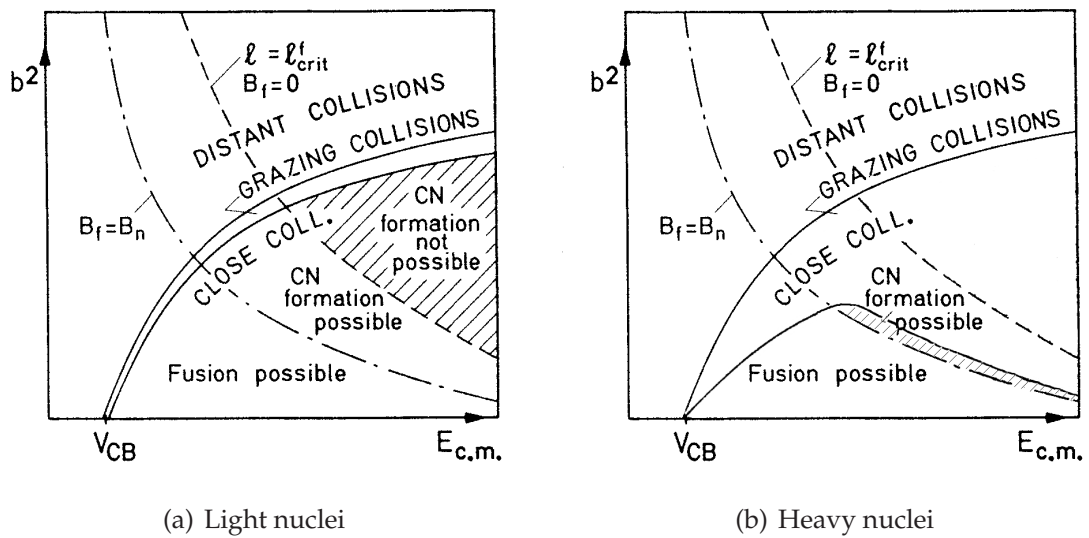
Figure 1.8 – A classification of nuclear collisions in b^2 vs. $E^{(CM)}$ plane, and limitation arising from l_{crit}. The picture is taken from [1].

shows three areas, denoted by *distant collision*, *grazing collision* and *close collisions*, respectively. The critical angular momentum l_{crit}, defined by the condition $B_f = 0$, corresponds to the dashed line. To the right and above the dashed line, CN formation is impossible. The dot-and-dash line correspond to the condition where $B_f = B_n$, the separation energy for the last neutron. To the left and below this line we have $B_f > B_n$, so that the phase space available for neutron emission exceeds the density of state at the fission barrier. In this region we expect the CN, once formed, to decay by emission of light particles and, therefore, to survive (fusion-evaporation). Between the two curves the CN should decay preferentially through fission (fusion-fission).

Entrance channel effects For fusion to occur, the system must penetrate to distance where strong dissipative forces remove energy from the relative motion and hence cause trapping in an attractive region of the effective 2-body potential. Then fusion, in this classical scattering model [3,30–33], is possible only for systems where the effective 2-body potential for zero angular momentum has a maximum ($B_f > 0$), i.e. the potential must have a pocket in which the system can be trapped. As consequence, fusion is forbidden for very heavy systems, like $^{238}U + ^{238}U$ at all energies, the fission barrier being null for the composite system. Therefore the reaction mechanism depends from the entrance channel. The effect of the entrance channel can be depicted as in Fig.1.8(b), where the area where CN formation is possible is strongly reduced by the increasing of the surface collisions area.
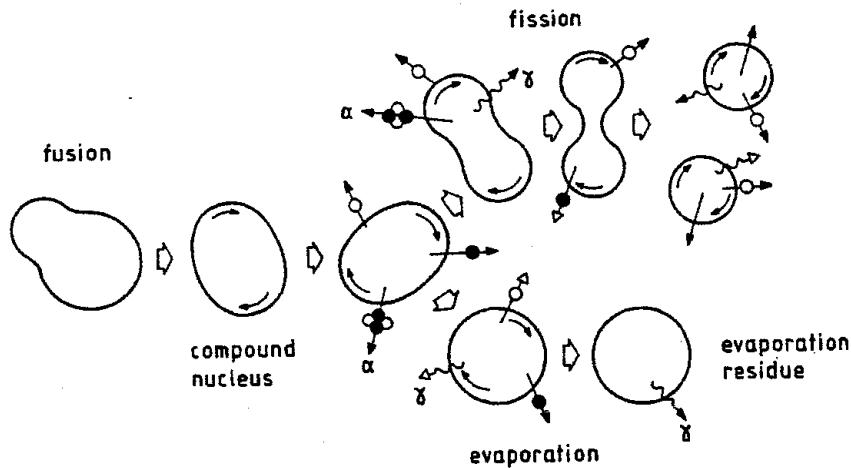
Figure 1.9 – Sketch of the competition between fission and evaporation in the decay of an hot compound nucleus. Taken from [9].

Experimentally speaking, it is mainly in terms of their deexcitation that the properties of excited nuclei may be accessed.

Decay modes   By nature, hot nuclei, once formed, are metastable objects, the major tendency of which are precisely to decay, in one way or another.

A primary decay mode for an equilibrated compound nucleus, in low energy regime, involves light charged particles evaporation, which takes place until the CN excitation energy becomes smaller than the particle separation energy. In the final state evaporated particles and an evaporation CN residue in its ground state are present. Later on we refer as `residue` to the big fragment remaining after the evaporation of the CN.

Light charged particles evaporation is a thermal process which does not imply a general motion of the nucleons inside the nucleus and does not exhaust all the possible decay channels for hot nuclei. Due to the competition between Coulomb forces, repulsive between protons and inducing strong deformations, and surface effects which tend to restore the spherical shape of the nucleus, heavy mass systems can experience fission. The balance between these two latter effects sets limits on the border of the nuclear chart.

Generally the fusion cross section can be written as

$$\sigma_{fus} = \sigma_{ER} + \sigma_{FF} \tag{1.25}$$
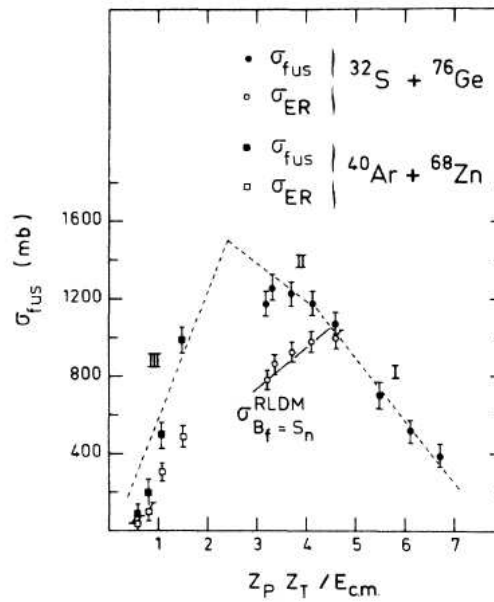
Figure 1.10 – Example of fusion cross section, taken from [36]. The fusion cross section measured for ^{40}Ar+^{68}Zn (squares) and ^{32}S+^{76}Ge (circles) is plotted against $Z_p Z_t / E^{(CM)}$. The open symbols correspond to fusion evaporation cross sections σ_{ER}, and the filled one to fusion cross sections σ_{fus}.

where σ_{ER} is the fusion-evaporation cross section and σ_{FF} is associated to the fusion-fission process. At low temperature as 1 or 2 MeV unexpected large values of σ_{ER} suggest that fission is a slow process, during which cooling, particularly via evaporation, may occur: evaporation and fission compete as dominant decay mode in the deexcitation of hot equilibrated systems. The competition between fission and evaporation is schematically depicted in Fig.1.9.

In inclusive measurement the fusion cross section is obtained by counting evaporation residues, fission products and sometimes by means of the study of light particle decay [34, 35].

It is well established experimentally and theoretically [37–41] that for $A_{CN} \simeq 100$, σ_{fus} is restricted to σ_{ER} at lower bombarding energies and increases according to the energy above the interaction barrier (see Fig.1.10). A change in the slope of σ_{fus} as a function of projectile energy is observed for still increasing projectile energies. Depending on the models, this is interpreted in terms of sufficient level density for the CN to decay statistically [39], or alternatively as being due to the persistence of a pocket in the potential curves resulting from increasing friction [40]. Somewhere along these two regimes, fusion-fission appears when the energetic conditions lead to partial waves such that $l \gtrsim l_{B_f = S_n}$ (B_f and S_n correspond to the fission barrier and

the separation energy of the last neutron, respectively) and σ_{fus} becomes the sum of σ_{ER} and σ_{FF}.

Increasing the projectile energy a second change in the slope of σ_{fus} occur: the residue cross sections are no longer rising rapidly, but decrease slowly with increasing bombarding energy. This behaviour is expected when the partial waves associated with evaporation residues are limited by competition with equilibrium fission or non-equilibrium exit channels such as fast fission or deep inelastic scattering, and described in §1.2.3 .

At projectile energies close to 35 AMeV, the fusion-evaporation cross section vanishes. There are two possible explanation to this phenomenon: since fusion is increasingly more incomplete with projectile energy, one reach a stage where the remnant of projectile becomes very small, or the CN formed cannot retain the excitation energy U brought by the incomplete fusion reaction and can no longer exist.

The fragment emission or fission requires a description based not only on phase space considerations (as in evaporation theory) but also on the fact that such large amplitude motion may be strongly dissipative, as numerous experiments clearly indicate. The reason is that such processes lead to a large deformation of the system during which friction has time to act. Description using diffusion equations, such as Langevin [42] or Fokker-Planck formalisms [43–45], are typically well appropriated.

The study of the decay properties of hot nuclei produced in heavy-ion collisions has to face high excitation energies (up to several hundred MeV) and large angular momenta (up to about $100\hbar$). Clearly under these circumstances one does not deal with individual quantum state (at least not in the primary CN) but with statistical distribution of overlapping levels. For reactions which are associated with compound nucleus excitation energies of less than 300 MeV, data are routinely compared to predictions of statistical model calculations. The successful description of light particle emission remains essentially for evaluation the validity of the model and the parameters choices within it. Studies of evaporated particle energy spectra yield direct information about the main SM ingredients, the nuclear level density and barrier penetration probabilities.

Without entering in the detail of the statistical model, we just give an overview of the main concept, remarking that the decay probability in a certain exit channel depends, according to the statistical model, only on the width of the decaying resonance in a given exit channel [1,7].

Statistical model The statistical model was originally introduced by N. Bohr [19], Bethe [46] and Weisskopf [47]. Wolfenstein [48] and Hauser and Feshbach [49] introduced the conservation of total angular momentum and afterwards the model was extended and generalized by many authors. Actually it has a widespread use in nuclear physics and applied research.

The statistical model is essentially based on Bohr's compound nucleus picture introduced in §1.2.3. The leak of entrance channel memory of the system implies that, once a compound nucleus has been formed with a given excitation energy, angular momentum and parity, its decay is completely determinated by the statistical weights of the various possible final states.

Let us consider an excited nucleus of mass A, excitation energy U, charge Z and angular momentum J. The goal is to evaluate towards which states the system preferentially decays. The transition probability from an initial state i to a final state f is given by the Fermi Golden Rule [9]:

$$\frac{dN_{i \to f}}{dt} \propto |M_{i \to f}|^2 \rho_f \tag{1.26}$$

where $M_{i \to f}$ is the transition matrix and ρ_f is the final density of states. The basic assumption of the statistical model is to consider that all transition matrices are equal, so that the probability of observing a given state is governed only by its density of states.

If the nucleus can be considered as an isolated system, it can be properly described in a microcanonical approach. Considering a nucleus i that emits a particle b, of spin s with a kinetic energy ε and reaches a final status f, the corresponding emission (evaporation) probability per unit of time for the process $i \to b+f$ can be written as:

$$P_b(\varepsilon)d\varepsilon = C_0 \rho_f(E_f^\star)dE_f^\star (2s+1)\frac{4\pi p^2 dp V}{h^3} \tag{1.27}$$

where C_0 is a coefficient and can be obtained from the detailed balance principle [9]. The term $\rho_f(E_f^\star)dE_f^\star$ gives the number of states available for the excited $E_f^\star$ daughter nucleus and it is obtained by the product of the density of states $\rho_f(E_f^\star)$ and the energy interval $dE_f^\star$. The last term, $(2s+1)\frac{4\pi p^2 dp V}{h^3}$, indicates the number of states of the emitted particle with a linear momentum between p and $p+dp$; V is the volume of an imaginary box where the decay takes place. Evaluating eq.1.27 one finally obtains:

$$P_b(\varepsilon)d\varepsilon = \frac{\rho_f(E_f^\star)}{\rho_i^{CN}(U)}(2s+1)\frac{4\pi p^2}{h^3}\sigma_c(\varepsilon)d\varepsilon \tag{1.28}$$

where $\sigma_c(\varepsilon)$ is the capture (fusion) cross-section of the particle b by the final nucleus

f. A deexcitation channel will thus be the most favoured if the number of accessible states ($\propto \rho_f$) is large.

To evaluate the probability of a deexcitation channel it is necessary to evaluate the fusion cross section and the density of states.

Fusion cross section   It is usual in HI reactions to call the cross section for the formation of the CN *fusion cross section*. The fusion cross section depends in a systematic way on the energies and the masses of interacting ions.

Starting from eq.1.11 and denoting by s_1 and s_2 the intrinsic spins of target and projectile (assumed non-identical), the cross section for formation of a CN with total angular momentum J, from an entrance channel ⌐ α > (α specifies all the quantum numbers of the channel), can be written as:

$$\sigma_\alpha^{CN}(J, E^{(CM)}) = \pi \lambdabar^2 \frac{(2J + 1)}{(2s_1 + 1)(2s_2 + 1)} \sum_{lS} T_{lS\,J}(E^{(CM)}) \tag{1.29}$$

where S and l are the channel spin and angular momentum which result from the coupling of the intrinsic spins and of the angular momenta of target and projectile, respectively. Summing over the CN angular momentum J we obtain:

$$\sigma_\alpha^{CN}(E^{(CM)}) = \sum_J \sigma_\alpha^{CN}(J, E^{(CM)}) = \pi \lambdabar^2 \sum_{l=0}^{\infty} (2l + 1)T_l(E^{(CM)}) \tag{1.30}$$

Within the hypothesis that the decay probability of CN in an exit channel ⌐ β > is independent from the entrance channel (statistical hypothesis), the cross section for a transition from the entrance channel ⌐ α > (projectile and target in their ground state) via the corresponding CN to a specific exit channel ⌐ β > is:

$$\sigma_{\alpha,\beta}(E^{(CM)}) = \sigma_\alpha^{CN}(E^{(CM)})P_\beta(E^{(CM)}), \tag{1.31}$$

where $P_\beta(E^{(CM)})$ is the decay probability of the process ⌐ $CN\rangle \rightarrow$ ⌐ $\beta\rangle$.

$P_\beta(E^{(CM)})$ can be calculated by the detailed balance principle

$$P_\beta(E^{(CM)}) = \frac{T_J(\beta, E^{(CM)})}{\sum_\lambda T_J(\lambda, E^{(CM)})} \tag{1.32}$$

The index λ runs over all possible two-body exit channels (defined by discrete quantum states of fragments), and $T_J(\lambda)$ denotes a generalized transmission coefficient

related to the transmission coefficient $T_{lSJ}(\lambda)$ introduced in eq.1.29

$$T_J(\lambda, E^{(CM)}) = \sum_{lS} T_{lSJ}(\lambda, E^{(CM)})$$

Evaluating eq.1.31 one obtains:

$$\sigma_{\alpha\beta}(E^{(CM)}) = \sum_J \sigma_J(\alpha)\frac{\Gamma_J(\beta)}{\Gamma_J} = \frac{\pi\lambda_\alpha^2}{(2s_1+1)(2s_2+1)}\sum_J (2J+1)\frac{T_J(\alpha)T_J(\beta)}{\sum_\lambda T_J(\lambda)} \qquad (1.33)$$

The transmission coefficient $T_J(\lambda, E^{(CM)})$ is related to the partial width for decay, into channel λ, of CN with excitation energy U and angular momentum J by

$$\Gamma_J(\lambda) = \frac{T_J(\lambda)}{2\pi\rho(U, J)} \qquad (1.34)$$

where $\rho(E, J)$ is the spin-dependent level density of the CN. We can write then:

$$\sigma_{\alpha\beta}(E^{(CM)}) = \sum_J \sigma_\alpha(J, E^{(CM)})\frac{\Gamma_J(\beta)}{\Gamma_J} \qquad (1.35)$$

$\Gamma_J(\beta)$ is the decay width of CN into channel $\mid \beta >$ and Γ_J its total decay width (at angular momentum J). We remark that this equation derives from the assumption of equilibrated CN, which implies independence of CN formation and decay from the entrance channel.

The theoretical derivation of the function $\rho(U, J)$ is described extensively in literature [50] and will not be described here. Many efforts have been done to determine the level density dependence from statistical model parameters such as the CN excitation energy and the isospin.

Nuclear level density and its N/Z dependence In the low energy region, the N/Z dependence of fusion and deep inelastic reaction mechanisms, of the transition between these two processes and of the possible pre-equilibrium emissions can be analysed.

In particular fusion reactions, where the composite system deexcites mainly by evaporation, allow to experimentally access the nuclear level density $\rho(E)$ and the limiting temperature[1] T_{lim} in order to study their N/Z dependence.

The nuclear level density is an important quantity for the study of both thermal and decay properties of excited nuclei, for the determination of cross sections used in nuclear astrophysics calculations, like in neutron and proton capture processes, and in supernova dynamics [62, 63]. Moreover ρ is an essential ingredient in calculating the statistical decay of a compound nucleus (CN) by particle evaporation, gamma-ray emission, or fission in statistical models. The knowledge of the level density is thus highly needed in all regimes of excitation energies, compound nucleus spins, and for the full range of Z and N from the β line of stability to the drip lines. It is also important to know its dependence on the excitation energy, p-n asymmetry, and deformation over most regions of the chart of nuclides.

The most extensive informations come from slow neutron resonance data, at energies just above the neutron binding energy [64, 65]. Experimental data far from the valley of stability are very scarce, so that the level density parameter for the nuclei of interest is usually estimated based on information near the bottom of the valley of stability.

In statistical model calculations level density formulas are usually based on the work of Bethe [66], with the assumption that an energy independent density of single particle states g is present. Fermi-gas model approximation provides a useful reference to start with, even if other effects have to be included to get more realistic expression of the level density.

In the independent particle model [66] the nucleus ground state is given by filling the lowest single particle states, according to the Pauli principle, up to the Fermi energy ϵ_F. Therefore, for a compound nucleus with excitation energy U ($U = E - E_{gs}$), angular momentum J and parity π, the nuclear level density $\rho(U, J^\pi)$ depends only upon the density of single particle states g near the Fermi energy ϵ_F, and, for moderate excitation energies ($T \leq 4 \div 5\,\text{MeV}$), can be related to the excitation energy U

---

[1]The limiting temperature is defined as the highest compound system temperature at which the thermodynamically equilibrated system decays by light particle evaporation. Beyond this temperature multifragmentation takes place. The existence of T_{lim} has been predicted by models [51–60] and experimentally verified [61].

by [66]:

$$\rho(U) = \frac{\sqrt{\pi}}{12} \frac{e^{2\sqrt{aU}}}{a^{1/4}U^{5/4}} \tag{1.36}$$

where

$$a = \frac{\pi^2}{6} g(\epsilon_F)$$

is the so-called `level density parameter` and is proportional to the nucleon number A [66].

The zero-temperature single particle level density $g(\epsilon)$, that counts the number of single particle levels per unit energy, is

$$g(\epsilon) = \sum_k \delta(\epsilon - \epsilon_k) \tag{1.37}$$

At the same level of approximation (i.e. Fermi gas approximation), the excitation energy is linked to the temperature (T) by

$$U \simeq aT^2 \tag{1.38}$$

Starting from the Bethe work [66] various refinements to the model have been added since its introduction: angular momentum, pairing and shell effects [67–69], as well as collective effects (many body and effective mass) have been included to get more realistic expressions [70]. Calculations of the nuclear shape and size dependence of the level density parameter are also available [71].

Theoretical and experimental studies suggest the level-density parameter to depend on the excitation energy: at low excitation energy, a has a value of approximately $A/8$ MeV^{-1} [72], in contrast, the Fermi-gas model gives $a \sim A/15$ MeV^{-1}. The level density parameter excitation energy dependence has not already been determined, even if experimental studies has been devoted to it.

Recent experimental studies indicate also a possible isospin dependence of the level density parameter.

In statistical calculations the parameter g is expected to be proportional to A, leading to the result that a is also proportional to the number of the nucleons. Only an A dependence of the level density parameter is generally assumed in calculations, however, some dependence on N and Z should be expected. For instance, in a two-

component Fermi-gas model, the level-density parameter is given by:

$$a = \frac{\pi^2}{6}(g_n(\epsilon_F) + g_p(\epsilon_F)) \tag{1.39}$$

where $g_n(\epsilon_F)$ and $g_p(\epsilon_F)$ are the neutron and proton single-particle level densities at their respective Fermi energies. In Thomas-Fermi calculations of N fermions of mass m in a box of volume V, the zero temperature single particle level density is

$$g \propto V^{2/3} N^{1/3} m \tag{1.40}$$

and thus for a nucleus of N neutrons and Z protons one gets

$$a \propto A^{2/3}(N^{1/3} m_n + Z^{1/3} m_p) \tag{1.41}$$

Assuming $m_n = m_p$ and expanding about $N - Z = 0$, one obtains

$$a \propto A \left[1 - \frac{1}{9}\left(\frac{N-Z}{A}\right)^2\right] \tag{1.42}$$

which suggests a dependence of a on isospin projection $t_3 = \frac{Z-N}{2}$.

At sufficiently large excitation energies, independently on the assumed Z and A of the primary fragments, evaporation models predict that the process of light-particle evaporation moves the position of an excited fragment in the chart of nuclides towards a particular line called `evaporation attractor line (EAL)` [73,74].
The location of this line is mainly determined by competition between proton and neutron evaporation. For compound nuclei on the neutron-rich or on the neutron poor side of the line, neutron or proton emission is the most important evaporation mode, respectively, and this drives the system towards the line. This line thus acts as if it is attracting the decaying systems and it justifies its name.
For light systems, the attractor line is coincident with the line of β stability, while for heavier systems, the larger Coulomb barrier for proton emission pushes this line to the neutron-deficient side of the valley of stability.
A general definition of the attractor can be obtained from the condition [73]:

$$\frac{dN}{dZ} = \langle\frac{\Gamma_N}{\Gamma_Z}\rangle, \tag{1.43}$$

where Γ_N and Γ_Z are partial decay widths for neutron and proton removal including both the contribution from nucleon and cluster evaporation.

At the attractor, the neutron and proton driving forces are about equal. The path by which a decaying fragment approaches the EAL depends on its initial proton-neutron asymmetry and the excitation energy, but the average position of secondary fragments can only approach the attractor, and not cross it [73].

At present, the level density has only been studied in nuclei close to the valley of stability and mainly on the neutron-deficient side. In all these studies isospin effects have been usually neglected, as they are expected to be relatively small for nuclei close to the stability valley, as those produced by stable beams.
The predicted isospin dependence of level density parameter in Fermi gas model indeed (eq.1.42) is small, and, when implemented in statistical-model simulations, the effect could not be observed within the statistical uncertainties of the Monte Carlo simulations [75].
A significantly larger dependence would have important implications.
Recent experiments [75–77] suggest the need for an isospin dependence already at excitation energies below $8\,\mathrm{MeV}$ and for masses $20 \leq A \leq 70$. In this temperature regime $\rho(E)$ cannot be predicted by microscopic theories, and a complete realistic $\rho(E)$ parametrisation is not jet available [78, 79].
In studies on 26 MeV$\leq E/A \leq 50$ MeV Xe+Be, C, and Al reactions [73, 77] it was pointed out that the mean locations of the evaporation residues and the compound systems lie on opposite sides of the evaporation attractor line. An explanation could be given by a level density parameter n-p asymmetry dependence that allows the decaying system to cross the attractor line if the initial excitation energy is high enough.
Moreover, the inclusion of isospin dependence in the level density expression could account for the failure of the statistical model in reproducing experimental evaporative particle multiplicity in some reactions [80].
An asymmetry dependence can also have important consequences on the $n-p$ asymmetry of the evaporation residues [75].
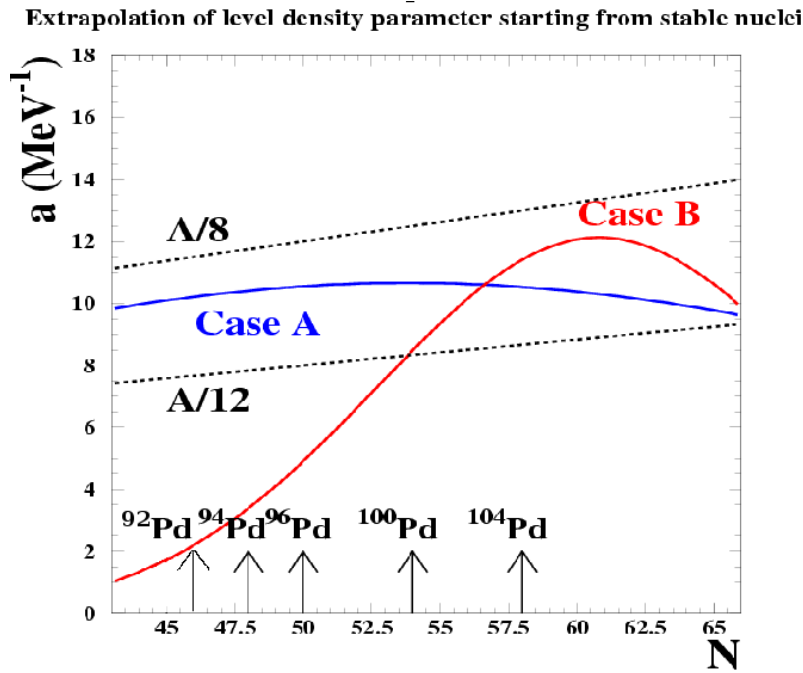
The typically used level density parameter parametrisation, which grows out of the independent particle model,

$$a = \alpha A \tag{1.44}$$

can be replaced by an empirical parametrisations of the form:

$$a = \frac{\alpha A}{e^{\beta(N-Z)^2}} \tag{1.45}$$

extrapolated starting from stable nuclei.

Figure 1.11 – Evolution of the level density parameter according to two different parametrisations (eq.1.45: case A, eq.1.46: case B) for different Pd isotopes (see Ref. [76]). Experimental values $A/8$ and $A/12$ obtained for low and high excitation energies respectively [72] are also reported. The picture is taken from [86]

The analysis described in Refs. [81–85] suggests a different N and Z dependence, which takes into account the distance from the drip lines:

$$a = \frac{\alpha A}{e^{\gamma(Z-Z_0)^2}} \tag{1.46}$$

where Z_0 is the charge of the β-stable isotope of mass A.

Within the N/Z range produced by stable beams, contradictory results have been found.

The analysis performed by Al-Quraishi [76] suggests $(Z - Z_0)$ as the appropriate parameter, rather than $(N - Z)$, to reproduce experimental data. Its analysis is based on nuclear levels listed in the ENSDF data file [87] for nuclei with $20 \le A \le 70$ and on ^{100}Mo, ^{100}Ru, ^{100}Pd, ^{140}Ba and ^{140}Ce (133 nuclei at all) nuclear levels. The nuclear levels of 133 nuclei have been fitted with the two possible n-p dependence (eq.1.45 and 1.46)

More recently Gelli *et al.* [88] have measured and compared with theoretical calculations evaporative proton and α particle energy spectra and angular distributions emitted in the decay on the compound nucleus ^{139}Eu produced at an excitation energy of 90 MeV in ^{32}S+^{107}Ag reaction. It had been pointed out that the prediction by

the $(Z - Z_0)$ prescription (eq.1.46) fails to reproduce data, while the isospin independent eq.1.44 and $(N - Z)$ (eq.1.45) dependences well reproduce the data. The latter one does not produce a significant difference with respect to the first one, leading to the conclusion that in the analysed system the isospin effect is not present or is negligible.

In Charity *et al.* [75] work, no evidence for n-p asymmetry dependence of the level density parameter was found in the measured data (^{60}Ni+^{92,100}Mo at $E/A = 5 \div 9$ AMeV).

It is therefore of primary importance to test the effect of the isospin in level density in the evaporative charged particle emission on systems involving more exotic nuclei as those produced by radioactive beams available today and in future facilities. The advent of radioactive beams, coupled to suited targets, indeed allows to explore the properties of a large number of isotopes of compound nuclei of a given Z from the β stability to the p drip line, and, in correlation, to test the influence of the mass asymmetry of the entrance channel on the fusion cross section.

Experimental measure of a Statistical model has been used for many decades to analyse a variety of observables related to compound nucleus decay, but the successful description of light particle emission[2] is essential for evaluating the validity of the model and the choice of the parameters. Studies of evaporated particle energy spectra yield direct information about the main statistical model ingredients, the nuclear level density and barrier penetration probabilities. From an experimental point of view, while a cannot be directly measured at high energy, the temperature T and $\frac{1}{T} = \frac{dln\rho}{dE^*}$ can be extracted from the exponential slope of kinetic energy spectra of evaporated particles.

Comparisons with calculations [89] constrain the dependence of a with E^* and T and a further comparison between experimental data and `GEMINI` simulation (see §5.2.2) permits, by iteration, to find level densities and level density parameters consistent with data.

Experiments performed up to now on this subject consisted in inclusive measurements, while the data obtained in this experiment are highly exclusive data. The use of a 4π detector like INDRA, coupled to VAMOS, allows to detect, event by event, the residue and the associated charged particles, measuring their characteristic: iso-

---

[2]Charged particles in coincidence with evaporation residues are well suited for a detailed analysis in the context of the statistical model because the spectra are kinematically associated with a single source, in contrasts with the situation for fission coincidence data, for example, which usually require deconvolution of components from several sources.

topic composition, multiplicity and kinetic energies of all the reaction products. All decay chains can be measured, obtaining the percentage with which different chains lead to the same residue. The correct weighting of the different exit channels, which was never measured up to now, allows to put constraints on the values of *a* for nuclei along the deexcitation chain. Moreover INDRA, able to measure variation on the slope of the kinetic energy spectra for all reaction products, provides information on temperature for all decay chains.

The high angular coverage, which maximises the detection efficiency, allows the use of low intensity beams, such as SPIRAL radioactive beams, allowing to explore a wide range of N/Z.

The fundamental goal is to explore the variation of deexcitation properties and thus level density parameters with the N/Z of the compound nucleus when going from stable nuclei to the proton drip line. The fusion cross section as a function of the entrance channel isospin can be investigated by detecting the evaporation residues around the beam direction, studying complete deexcitation properties of several isotopes formed in the same conditions.

Chapter 2

The INDRA+VAMOS experimental setup

The main goal of the experiment is the study of the dependence on $\frac{N}{Z}$ of the level density parameter a by the analysis of the deexcitation properties of hot nuclei, produced in fusion reactions bombarding ^{58}Ni, ^{60}Ni and ^{64}Ni target by ^{34}Ar to ^{40}Ar beams at energy ~ 13 AMeV. As result of complete fusion, the mass number of fused Pd nuclei varies from 92 to 104, including ^{96}Pd, which has a 50 neutrons closed shell (see chap.3).

As previously mentioned, a compound nucleus can deexcite by the emission of a large number of particles. The evaporated particles are emitted isotropically in the compound nucleus system of reference, with a wide kinetic energy range, while the fusion-evaporation residue, with a low kinetic energy of ~ 1.8 ÷ 2 AMeV (see Tab.3.3), is emitted around the beam direction (in the laboratory system of reference) in the same angular region where a high flux of elastically scattered particles is produced. To measure, disentangle and weight all decay channels of an excited CN it is necessary to detect and identify all the reaction products. Thus the use of VAMOS spectrometer, coupled with the multidetector INDRA, is very well suited for such measurements.

The coupling of these two detectors (INDRA+VAMOS apparatuses) allows to have an event by event complete information on the evaporation residue, on light charged particles (LCP), and at last, but not the least for importance, on the neutron multiplicity by means of mass conservation. Moreover, since INDRA covers ~ 4π of the total solid angle and has a high granularity, low energy thresholds, large dynamic ranges in energies and identification capabilities on an event by event basis, it allows a complete reconstruction of the kinematics for each event.
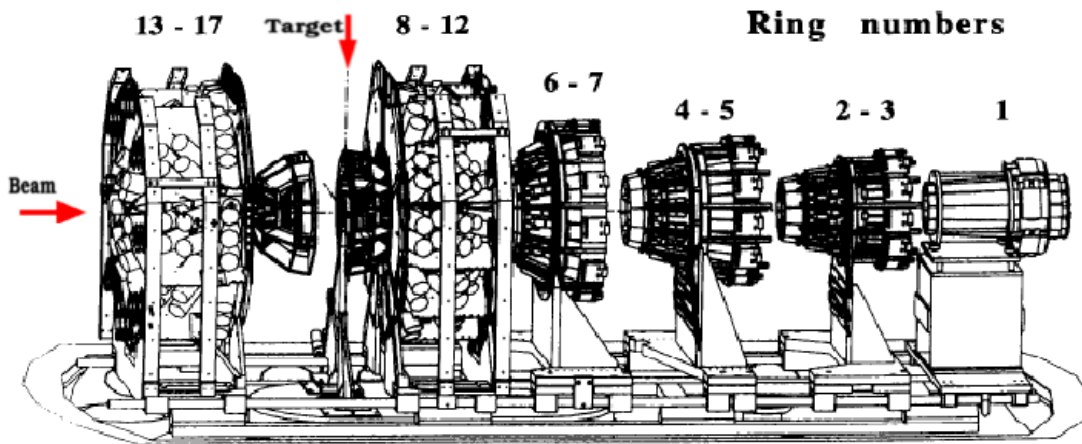
Figure 2.1 – Split view of INDRA. The six carriages which support detectors are separated. The two ionization chamber arrays (ring 8 to 12 and rings 13 to 17) are presented out of their support. The first two carriages (ring 1 and ring 2 – 3) have been removed, in the present experiment, to allow the INDRA-VAMOS coupling.

2.1 INDRA

The multidetector INDRA is 200 cm long with a maximum outside diameter of 80 cm. It is housed in a dedicated vacuum chamber, with a removable cover, that allows an easy access to all detector elements and connections. The different parts of the detector are supported by six carriages which can slide independently on two rails (Fig.2.1).

The target holder (Fig.2.2(a)) is inserted between the two last carriages and it is housed in an apposite vacuum vessel (shown in Fig.2.2(b)), in order to allow the access to the target without breaking the vacuum in the main vacuum chamber.

The INDRA (*Identification de Noyaux et Détection avec Résolution Accrues*) multidetector has been designed to study the deexcitation properties of hot nuclei produced during a heavy ions collision. To this aim the detector is able to detect both light charged, and energetic, particles and heavier fragments ($Z > 2$). INDRA has been built following the main criterion of keeping the multi-hit probability below 5% [90] for both fragments and light charged particles; therefore the first detection layer, the purpose of which is to detect and identify slow fragments, has been divided into 96 cells, while the number of elementary cells, which allow the detection of light charged particles, is 336. Moreover, the detector granularity, as well as the solid angle subtended by each detector cell, varies with the angle (see Fig.2.3), to take into account the effect of the center of mass velocity, which tends to focus the particles in the forward direction. A good granularity is important in both kinematic multipar-
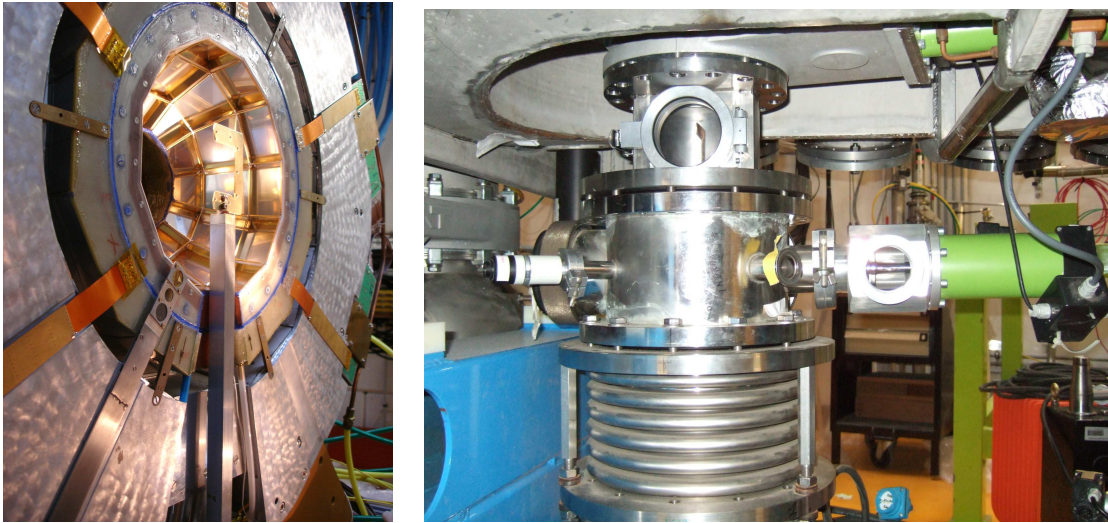
Figure 2.2 – Target holder (a) in its final position and target dedicated vacuum chamber (b).

ticle event reconstruction and elastic diffusion angular distributions accuracy.

The loss of solid angle is 0.2% for the beam entrance and exit holes (which have a diameter of $\varnothing 1.5$ cm and cover $0° < \theta < 2°$ and $176° < \theta < 180°$), 3.5% for the target holder region ($88° < \theta < 92°$) and 6.3% for the ionization chamber walls. Moreover, in order to allow detection of the evaporation residues in VAMOS, rings 1 to 3 of INDRA, covering the angular range from $2°$ to $7°$ have been removed (see §2.4.1). This represents a loss of solid angle of $\sim 0.3\%$ and INDRA still cover $\sim 90\%$ of the 4π solid angle.

INDRA has a structure in rings centered on the beam axis. The total number of rings is 17, and each ring is divided into 8, 12, 16 or 24 cells. The distance of each
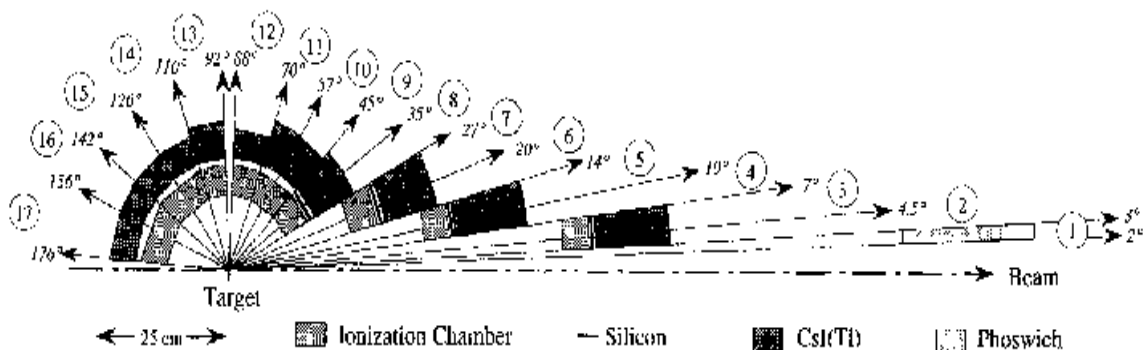

Figure 2.3 – Geometrical outline of the INDRA detector [90], cut along the beam axis. 17 coaxial rings are present, each covering a solid angle dependent on the ring polar angle (see Tab.2.1 for details). Beam entrance and exit holes, such as the target holder region are shown in the picture.
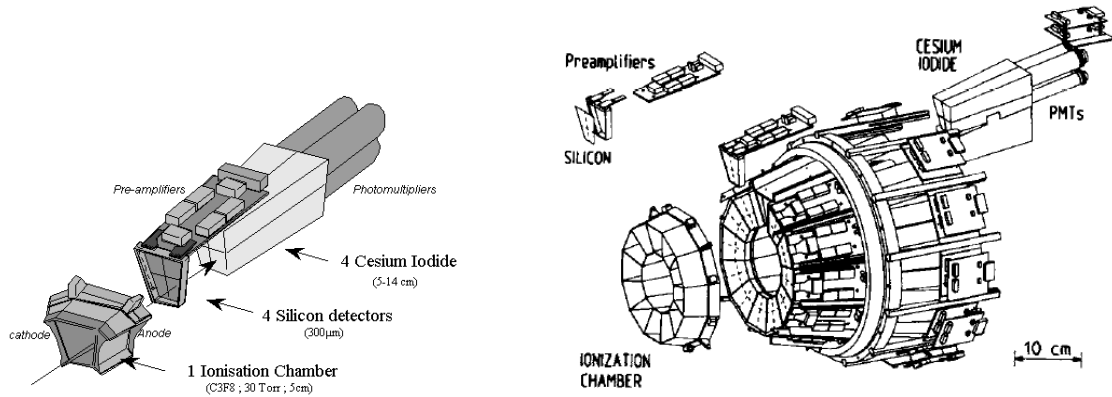
Ring	CsI(Tl)						Si	Ionization chamber					
	θ_{min}	θ_{max}	N	$\Delta\phi$	dx	$\Delta\Omega$	dx	$\Delta\phi$	N	n	d	$\Delta\Omega$
	$[deg]$	$[deg]$		$[deg]$	$[mm]$	$[msr]$	$[\mu m]$	$[deg]$		CsI(Tl)	$[cm]$	$[msr]$
4	7	10	24	15	138	1.70	300	30	12	4	38.4	10.3
5	10	14	24	15	138	3.21	300					
6	14	20	24	15	97	7.01	300	30	12	4	25	37.7
7	20	27	24	15	97	11.2	300					
8	27	35	24	15	90	15.8	300	30	12	4	12	86.0
9	35	45	24	15	90	26.4	300					
10	45	57	24	15	76	39.6		30	12	4	12	183
11	57	70	24	15	76	50.3						
12	70	88	24	15	48	81.0		30	12	2	12	155
13	92	110	24	15	60	82.3		45	8	3	12	240
14	110	126	16	22.5	50	93.5		45	8	4	12	338
15	126	142	16	22.5	50	73.1						
16	142	157	8	45	50	91.2		45	8	2	12	144
17	157	176	8	45	50	50.9						

Table 2.1 – Geometrical arrangement of the INDRA detectors. N: number of detectors per ring, dx: thickness of the detector, $\Delta\Omega$: solid angle of detector, n: number of CsI(Tl) behind each ionization chamber, d: distance of the ionization chamber entrance window from target, θ: polar angle, ϕ: azimuthal angle of the detector.

ring from the target depends on its polar angle (see Tab.2.1).

Different detectors are required to detect and identify all the reaction products, due to their wide energy dynamic range ($\sim$ 1 MeV$\div$4 GeV). The charge identification of the fragments is usually obtained by the $\Delta E - E$ method, therefore the INDRA detectors are telescopes. The first detection layer, composed of gaseous detectors (`Ionization Chamber`), gives the required low energy thresholds, necessary to detect low energetic heavy fragments, which easily stop in materials. The last detection layer, composed of a scintillator detectors (`Cesium Iodide scintillator CsI(Tl)`), gives the required thickness necessary to stop the most energetic light particles, which deposit low energy in materials. High energy resolution detectors (`silicon detector`) give the necessary energy resolution, where it is required. The two or three layer telescopes used in INDRA have thus the intrinsic possibility of satisfying nucleus identification and energy resolution requirements. The telescopes composition depends on the angular position with respect to the target.

Rings 3 to 9 ($7° \leq \theta \leq 45°$) In this region the energy range of the incident fragments is wide, thus the telescopes are composed of three successive detection layers: ionization chambers, filled with low pressure C_3F_8, 300 μm thick silicon detectors and CsI(Tl) scintillators, with variable length with respect to the angular position (see Tab.2.1).

(a) INDRA detection telescope in $7° < \theta < 45°$ region.

(b) Detector assembly for rings 4 ($7° < \theta < 10°$) and 5 ($10° < \theta < 14°$) [90].

Figure 2.4 – The ionization chamber is a 12 cell array. Each ionization chamber is followed by 4 silicon detectors and 4 CsI(Tl) scintillator. The silicon detectors have a geometry identical to the one of the scintillators: 4 pads are designed on the same wafer. The preamplifiers are located on the external wall of the CsI(Tl) support.

The ionization chamber is a 12 cells array. Each ionization chamber cell is followed by a silicon wafer, where 4 independent pads are designed, and by a group of 4 CsI(T1) crystals, each matching in size the corresponding silicon detector (see Fig.2.4). This configuration minimizes dead areas between detectors [90].

For each cell, the preamplifiers (1 for the ionization chamber and 4 for the silicon detectors) are mounted on a single multilayer printed circuit board located on the external wall of the CsI(Tl) scintillator support.

Rings 10 to 17 ($45° \leq \theta \leq 176°$**)** In this region the fragments number and energy range are expected to be reduced, thus the telescopes are composed of two detection layers: ionization chamber and CsI(Tl) scintillator, which surround the target at a fixed distance of 12 cm. Each ionization chamber cell is followed by 2, 3 or 4 CsI(Tl) scintillators, depending on the ring number: their arrangement is presented in Tab.2.1.

Each ring is equipped with a calibration telescope composed of a $80\,\mu m$ thick silicon detector and a $2\,mm$ thick lithium drifted silicon detector, in order to allow an energy calibration of the CsI(Tl).

The 144 photomultiplier bases are placed as close as possible to the photomultipliers, whereas the ionization chamber preamplifiers and the calibration telescope preamplifiers of rings 10 to 12 are located at $\theta = 90°$. Care has been take in order to avoid cross-talk between the photomultiplier bases and the preamplifiers and to remove the excess heat generated by the preamplifiers.
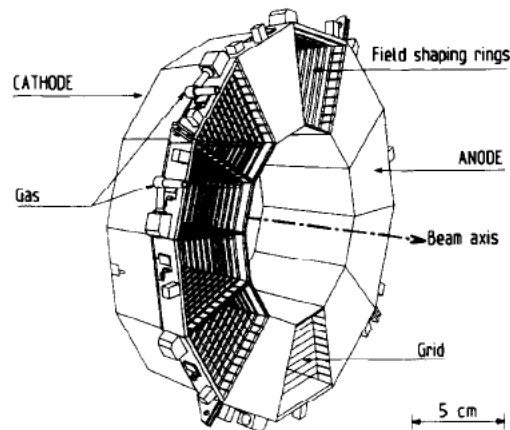
Figure 2.5 – Mechanical structure of the gas ionization chamber for rings 4 and 5. The structure is divided in 12 identical cells with a shape of truncated pyramid. A part of the anode foil is removed to show the grid and the field shaping rings inside the cells. Picture is taken from [90].

2.1.1 The ionization chambers

The first INDRA detection layer ($7° < \theta < 176°$) is composed of 84 gas ionization chambers. These detectors have been designed to be used as transmission detectors (ΔE detectors), so that they operated at $30 \div 50$ mbar of high purity perfluoropropane (C_3F_8), which, thanks to its high molecular weight (~ 188 gr/mol), delivers pulses twice as large as CF_4, with a collection time for the electrons being about twice as long [91], under the same operating conditions. In order to maintain its properties, the gas circulates continuously in all the ionization chambers and it is entirely renewed every 20 minutes.

The entrance foils of each ionization chamber are $2.5 \, \mu m$ thick mylar, for a total length of 5 cm. The entrance window is the cathode of the cell.

11 rings are glued on the 4 side-walls of each cell for field shaping (see Fig.2.5). In order to avoid non-uniform or distorted electric field in the vicinity of the anode and to render the response trajectory-independent (within 1% over the whole cell), it has been introduced a grid. Each grid, made of $50 \, \mu m$ Cu-Be wires, is placed 5 mm far from the anode and it is connected to the last field shaping ring.

Each cell required an anode electrically insulated from its neighbours. The anodes are then connected cell by cell, using conducting glue, to a microconnector in order to easily couple them to the preamplifiers printed circuit board.

Rings	A	n
4 ÷ 5	19.8 cm^2	4
6 ÷ 7	34.5 cm^2	4
8 ÷ 9	26.8 cm^2	4

Table 2.2 – Active areas and numbers of pads (n) designed on each trapezoidal silicon wafer. The external dimension of each wafer corresponds the ionization chamber size.

2.1.2 The silicon detectors

144 silicon detectors, 300 μm thick, are placed on rings 4th to 9th ($7° < \theta < 45°$) (see Tab.2.1) and form the second detection layer in the forward rings, where low energy particles and fragments issued from the target coexist with beam velocity particles and fragments from the projectile. Silicon detectors provide the required resolution and dynamical energy range to identify both low energy fragments, which stop in silicon, together with the ionization chamber signals, and high energy particles, which deposit a very small amount of energy in the gaseous detectors, together with the CsI(Tl) scintillator signals.

The high counting rates expected at the forward angles require a high granularity, therefore 4 pads are designed on the same wafer, in order to allow to minimize the dead zones (up to 0.7 mm [1]) resulting from the mechanical supports. However, in this configuration, cross talk effects and ionization chamber multi-hit events could occur; so that in the analysis it will be necessary to take them into account (see §A.1). Each wafer has a trapezoidal shape and covers a gas ionization cell. The silicon detectors are made by *Intertechnique* using the planar process, that permits to keep a check on the homogeneity and the impurity concentration (B and As) of the detector surface.

The active areas of the detectors are reported in Tab.2.2. In order to avoid crosstalk effects due to the capacitive coupling between the ionization chamber anode and the silicon detectors placed just behind, silicon detectors are reverse-mounted and, consequently, the particles enter the detectors by the low electric-field side. Possible problems in charge collection are then limited to low energy heavy ions which stop in the silicon detector. The detectors are fully depleted and overbiased to 2 or 3 times the depletion voltage, to obtain a rapid and uniform charge collections on the detector volume. The use of high resistivity ($\rho \sim 10k\Omega$ cm) silicon provides low value for the depletion voltage ($V_0 \propto \frac{1}{\rho} \sim 40$ V), moreover a high resistivity gives a smooth variation of the electric field strength across the detector.

---

[1] A border of 0.7 mm has been preserved on the outside of the pads in order to avoid large current flow and breakdown effects when the detectors are biased [90].

Rings	Thickness (mm)
4 ÷ 5	138
6 ÷ 7	97
8 ÷ 9	90
10 ÷ 11	76
12	48
13	60
14 ÷ 17	50

Table 2.3 – CsI(Tl) scintillator thickness. The maximum energy of light particle stopped in the CsI(Tl) detectors varies from 126 MeV (protons in 48 mm) to 948 MeV (α in 138 mm) [90].

The preamplifiers are located as close as possible to the detectors: a few centimetres on rings 3th to 7th and 20 cm on the rings 8th and 9th. The main characteristics of the charge preamplifiers are described in §2.2.1.

All the electronics have a low ballistic deficit in order to obtain energy measurements nearly independent of the large rise-time variations in the detector signals, due to the large energy dynamic range of the incident particles.

2.1.3 The Cesium Iodide detectors

The CsI(Tl) crystal are the last layer of the INDRA telescopes. The advantage of using CsI(Tl) scintillator arises from their high stopping power, that allows, with a careful choice of the crystal thickness (see Tab.2.3), to stop all the incident charged particles, including high energy protons, which have the longest ranges in the matter. The CsI(Tl) thickness have been chosen as a function of the angular energy distribution expected for protons produced in 100 A/MeV nuclear reactions.
The CsI(TI) crystals of the INDRA apparatus have been realized in 30 different shapes and are wrapped to avoid light leakage [90, 92]. The back face of each scintillator is coupled, with optical glue, to the front window of a photomultiplier tube[2] (PMT), which is isolated from the photocathode and grounded to avoid crosstalk with the neighbouring ionization chamber preamplifiers.

The main characteristic of INDRA's crystal are:

- very low phosphorescence after exposition to normal daylight.

---

[2]The use of photomultiplier tubes provides lower energy thresholds for mass identification as compared to those obtained with photodiodes [93].
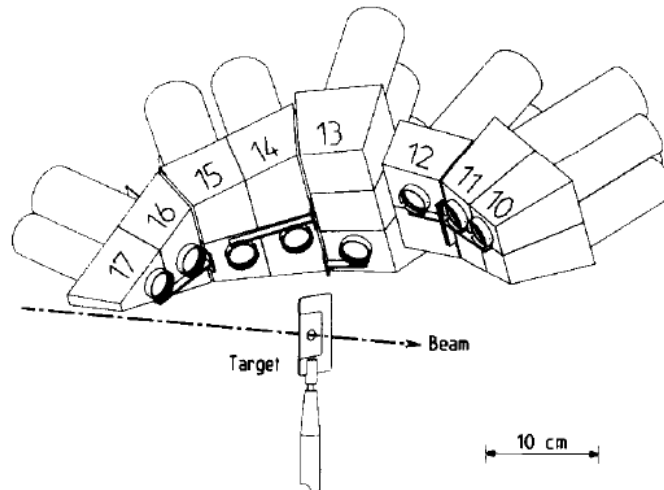
Figure 2.6 – Geometrical arrangement of calibration telescopes. The eight calibration tele-
scopes are distributed in the angular range from 45° to 180°, one module per
ring. The calibration of the first 80μm silicon detector can be obtained with α
particles source, while the calibration of the following Si and CsI(Tl) detectors
can be derived from the measured $\Delta E - E$ maps by adjusting to the prediction
of energy loss and range table.

- scintillation efficiency constant within 5% along the whole length.

- average light outputs within a 15% tolerance for all the crystals of the same
  ring.

The light output consists in two components, with two different time constant ($0.5\,\mu s$
and $7\,\mu s$). We refer to the first one as *"fast component"* and to the second one as *"slow
component"* of the light output. The signal at the output of the photomultiplier is
sent to a dual integrator (there are two integration gates), which provides a *fast* and
a *slow* signal, allowing the mass and charge identification.
One drawback of these detectors is the non-linear dependence of the light output
on the energy of the incident particles [94–97]. In addition, for a given energy, the
light output depends on the nature of the particle: a careful energy calibration is
then necessary to check the crystal stability and to control possible derives, crystal
are regularly enlightened by a laser.

2.1.4 Calibration telescopes

The calibration telescopes are put in rings from 10th to 17th between the ionization
chamber and the scintillator and allow to calibrate CsI(Tl) scintillators (see Fig.2.6).
Due to the azimuthal symmetry of INDRA, one telescope per ring is sufficient to
obtain reference spectra.

Each calibration telescope is constituted by a $80\mu m$ silicon detector and a $2mm$ Si(Li) detector (lithium ion-drift silicon detector), $1in.$ of diameter, which partially covers the associated CsI(Tl). The $80\mu m$ detectors are of the surface barrier type and their active area is $380mm^2$. The Si(Li) detectors thickness, $2\,mm$, do not stop the most energetic protons and α particles which impinge into the CsI(Tl) scintillator.

2.2 INDRA electronics

INDRA electronics have been developed to satisfy the required specifications concerning fragment identifications, dealing with the difficulties associated with the large number of channels (tuning, control and overall management).

- First of all, the signals correspond to a large dynamic range both in energy and in masses. For instance, the signals span $1\,MeV$ to $5\,GeV$ in silicon detectors, with an energy resolution of $100\,keV$ [90], and masses vary from one for protons to the one for heaviest fragments.

- All electronics have been located in the beam cave with full remote control. Due to the high number of detectors (416), a standard, which allows to reduce the number of modules, by regrouping many functions in the same module, had to be used. The `VXIbus` (Vme eXtension for Instrumentation) standard [98] is an extension for analog processing of the VME bus, routinely used for data acquisition at GANIL.

- The noise reduction implies that the front-end electronics (preamplifiers and photomultiplier bases) must be located inside the reaction chamber, as close as possible to the detectors. Special care have been paid to the ground reference in order to avoid cross talk and ground loop effects. The 288 photomultiplier bases associated with the scintillators and the 244 charge preamplifiers coupled to the ionization chambers (84 channels), to the $300\,\mu m$ thick silicon detectors (144 channels) and to the calibration telescopes (16 channels) must work under vacuum.

As far as signal processing and encoding is concerned, INDRA is composed of two kinds of detectors: ionization chamber and silicon detectors, for which energy measurements have to be done on a large dynamic range, and cesium iodide scintillators which need a double signal integration in a "fast gate" and a "slow gate". Fig.2.7
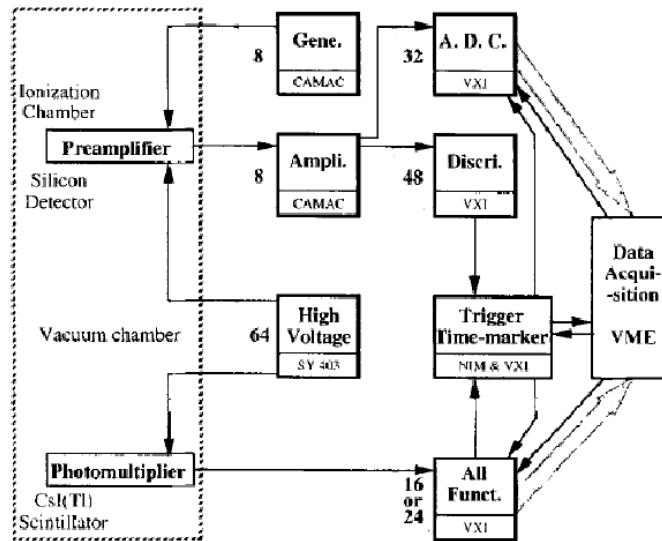
Figure 2.7 – Schematic representation of the main INDRA electronics functions [90]. Signals coming from the detectors are processed by 2 different electronic systems: one dedicated to the ionization chamber and silicon detectors, the other to scintillators.
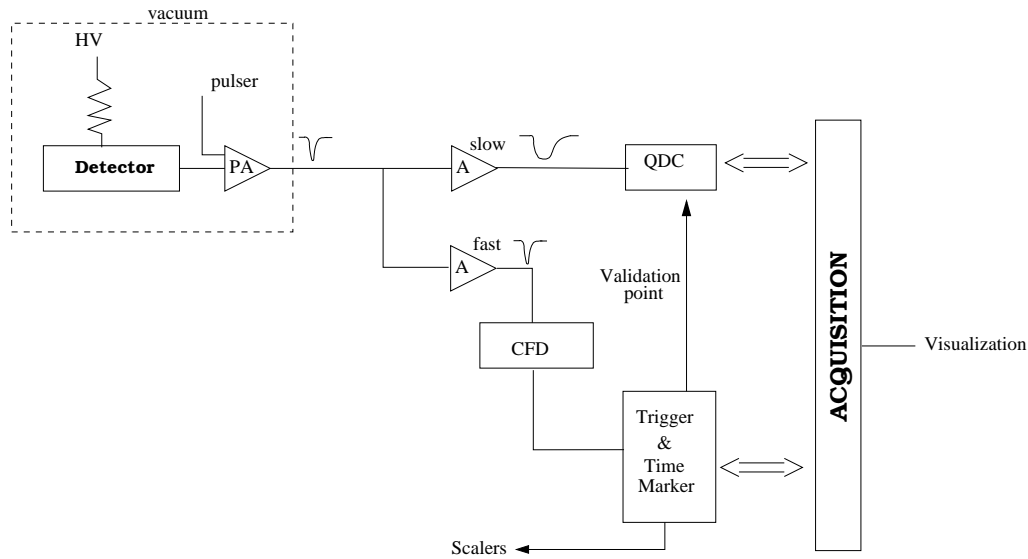
presents a general view of the electronic layout.

2.2.1 Ionization chambers and silicons electronic chain

The detectors signals are treated by charge preamplifiers which present different characteristics depending on the detector types. Due to the low energy deposit and low current conversion in the ionization chamber, the preamplifier must have a low noise and a very high sensitivity, obtained by a low feedback capacitor of about $0.22\,\text{pF}$. Conversely, the required high dynamic range capability of the silicon detec-

	Ionization chamber preamplifier	Silicon detector $(300\mu\,\text{m})$ preamplifier
Energy sensitivity on the 50Ω impedance of the amplifier input	10 mV/MeV (for C_3F_8 gas)	1 mV/MeV
Maximum output amplitude (linear response) on the 50Ω impedance of the amplifier input	±2.5 V	−5 V
Decay time constant	$220\mu\,\text{s}$	$220\mu\,\text{s}$
Rise time	15 ns (without detector)	25 ns (with 200 pF detector)

Table 2.4 – Main characteristics of the charge preamplifiers associated with the ionization chambers and the silicon detectors [99]

Figure 2.8 – General view of the electronics associated with the ionization chambers and silicons detectors. The slow and fast outputs of the amplifier provide the energy and the time marker signals generation, respectively [99].

tor preamplifier leads to a low sensitivity. The main features of the preamplifiers are summarized in Tab.2.4.

The 16 silicon detectors which compose the 8 calibration telescopes are equipped with similar charge preamplifiers which provide positive output signals with maximum amplitudes of $+5\,V$ on $100\,\Omega$.

The preamplifiers are located as close as possible to the detectors and are mounted in groups of 4 to 6 devices on multilayer printed circuit boards.

In Fig.2.8 is shown a sketch of the electronic chain. The preamplifier signal is sent to slow and fast amplifiers.

The slow amplifier, which shapes the signal, consists of $1.5\mu s$ CR-RLC filters followed by a clamp circuit and gives a negative unipolar signal with a $3.5\mu s$ width nearly independent on amplitude. Its output provides the energy measurement: the large dynamic range required for the silicon detectors is reached by double charge encoding in QDCs on two dynamic ranges: the pulse from the amplifier is split into two equal currents which are integrated over capacities of 8700 pF ("low gain") and 540 pF ("high gain"), i.e. gains are in the ratio 1 : 16. The "low gain" data are obtained on the full dynamic range and the "high gain" ones are provided for low energies only (1/16 of the dynamic range).

The fast preamplifier consists of CR-RC filter (50 ns integration and 300 ns differentiation times), has a fixed voltage gain of 8 and a maximum output voltage of
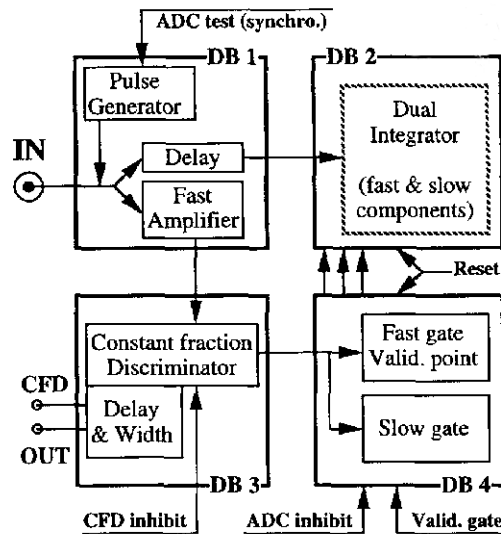
Figure 2.9 – Block diagram of 4 daughter boards which compose the analog circuitry of one channel of CsI VXIbus module [99].

5 V. It has been developed as a specific timing preamplifier, in order to cover a wide dynamic range.

The fast output of the amplifier is sent to a constant fraction discriminator which delivers a signal to the "Trigger and Time-marker" system. The CFD shaping delay is 55 ns.

The "Trigger and Time-marker" system provides the "validation point" of the channel triggering logic.

The ionization chamber and silicon detector chains are equipped with pulse generators, which send signal into the preamplifier, to check the stability of the electronic chain.

The electronic chains used for the calibration detectors are identical to those of the other silicon detectors.

2.2.2 CsI(Tl) scintillator signal processing

The 288 CsI(Tl) detectors form the outer layer of the INDRA detector: the analog circuitry for each channel is implemented on 4 daughter boards, as presented in Fig.2.9.

The CsI(TI) signal processing consists on two integrations, one in a *fast* gate (400 ns) and the other in a delayed *slow* gate ($1.5\,\mu s$ width and $1.6\,\mu s$ delay), and on the generation of a fast time reference which is sent to the trigger.

The photomultiplier signal is split into two parts. On one way the signal is delayed and sent to the two integrators, while on the other one, it is amplified by a factor 3
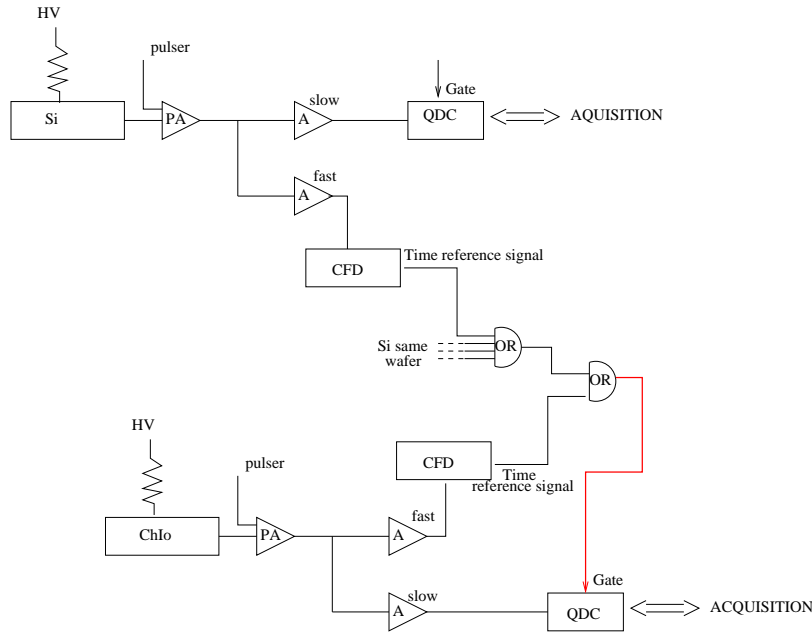
Figure 2.10 – Principle of the ionization chamber's QDC gate generation. Very low energy threshold is assured for particles punching through the ionization chamber.

and sent to the discriminator. The discriminator logic output fires the "gate and delay generators" and the "Trigger and Time-Marker" system which provide the fast and slow gates as well as the validation point of the channel triggering logic.

A test pulse generator, which delivers particle-like signals to the input of the circuit, is used to check the stability of the electronic chain.

2.2.3   Time marker and trigger system

The trigger system relies on a working mode called "asynchronous mode" and performs event selections based on multiplicity functions.

On forward angles ($3° \leq \theta \leq 45°$), the $300\,\mu m$ thick silicon detectors are followed by CsI(T1) scintillators and a low energy loss in the first one generally corresponds to a high energy loss in the second one. The charge integration gate of the silicon QDC starts on a logical OR built between the two time reference signals of the corresponding silicon and CsI(Tl) detectors. This method is also applied to the ionization chamber electronics for which the OR circuit is built between the time reference signals provided by the ionization chamber discriminator and the four discriminators corresponding to the four pads of the associated silicon detector (see Fig.2.10). In such a way a very low energy threshold for the particles which cross the first detection layer is obtained.
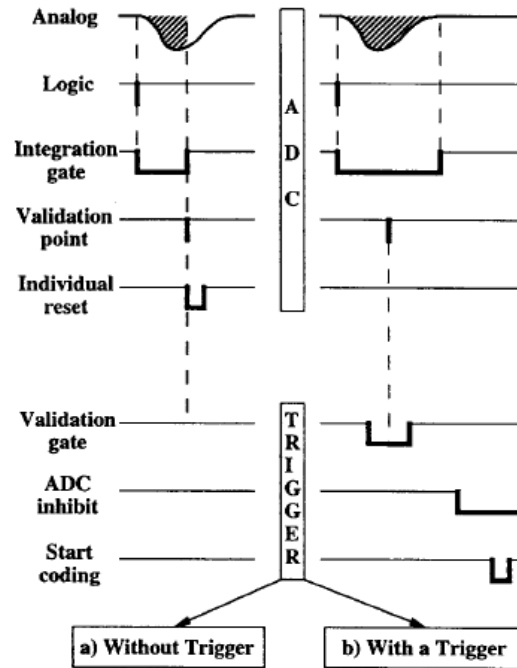
Figure 2.11 – Principles of "asynchronous mode" of triggering [99]. No logic condition coming from trigger is required to open the integration gate. The presence of a "validation point" in each fired channel assures the encoding of only tagged channel in case of accepted trigger configuration.

At backwards angles ($45° \leq \theta \leq 176°$), where there is no silicon detector, the OR circuit is built between the ionization chamber and the corresponding CsI(TI) discriminators, instead of those of the silicon detectors.
The charge integration gates of the CsI's ADC start on the time reference signal of the corresponding CsI(Tl).

The integration gate opens without any logic condition coming from the trigger, when the corresponding discriminator fires, and each tagged channel stores its own analog signal in the integrators: such kind of logic is called *asynchronous mode*. After ~ $1\mu s$ of delay, a "validation point" is generated (Fig.2.11). The introduction of such a delay allows to perform complex triggering functions and to wait for slow detectors. If the event configuration is accepted by the trigger, it sends a "FAST TRIGGER" to all the encoding modules, enabling to convert only those channels which have their "validation point" in coincidence with the trigger gate (Fig.2.11b). A "start coding" (ODC) signal generated by the trigger starts the digital conversion. During this operation, and until a reset is emitted at the end of data acquisition, all the channels are disabled by a general "QDC and ADC inhibit" signal.
Conversely, if a configuration is rejected by the trigger (Fig.2.11a) each channel is

reset.

The trigger system has the role of selecting the events, delivering the logic signals to the QDC and ADC modules and talking with the data acquisition system. It is constituted by four modules:

- the `Regroupeur`, which generates the multiplicity signal and the gates for QDCs

- the `Selector`, which performs the event selection

- the `Correlator`, which provides the conversation between the trigger and the data acquisition system

- the `Time Marker System`, which provides the time marker for each signal in an event

In the forward rings (3 to 9), when a particle hits one or two detectors of the same Silicon-CsI(Tl) telescope, the logic signals produced by the CFDs are sent to an OR circuit allowing the creation of only one individual multiplicity current per telescope. In the backward rings (10 to 17), only the CsI(T1) detectors are considered, except for the cells (one per ring) which include the calibration telescopes for which OR circuits are also needed (see Fig.2.12(a)).

The `Regroupeur` adds all the individual multiplicity currents of one (or two) rings to form 6 independent signals, corresponding to rings 4 and 5, 6 and 7, 8 and 9, 10 and 11, 12 and 13 and finally 14 to 17 (see Fig.2.12(a)), and sent to the `Selector` module.

The event selection is performed in a VXIbus module called `Selector` (see Fig.2.12(b)), in which two modes can be selected: the "physics mode" when the system is triggered by physics events and the "test mode" which ensures the generation of the synchronization signals for the laser system associated with the scintillator detectors and the pulse generators used for stability controls.

Thanks to the axial symmetry of INDRA the physics event selections ("physics mode") is based on ring dependent multiplicity levels, as provided by the `Regroupeur`.

The triggering configuration is selected by software controlled switches on the 6 multiplicity signals coming from the `Regroupeur`. The multiplicity signals are
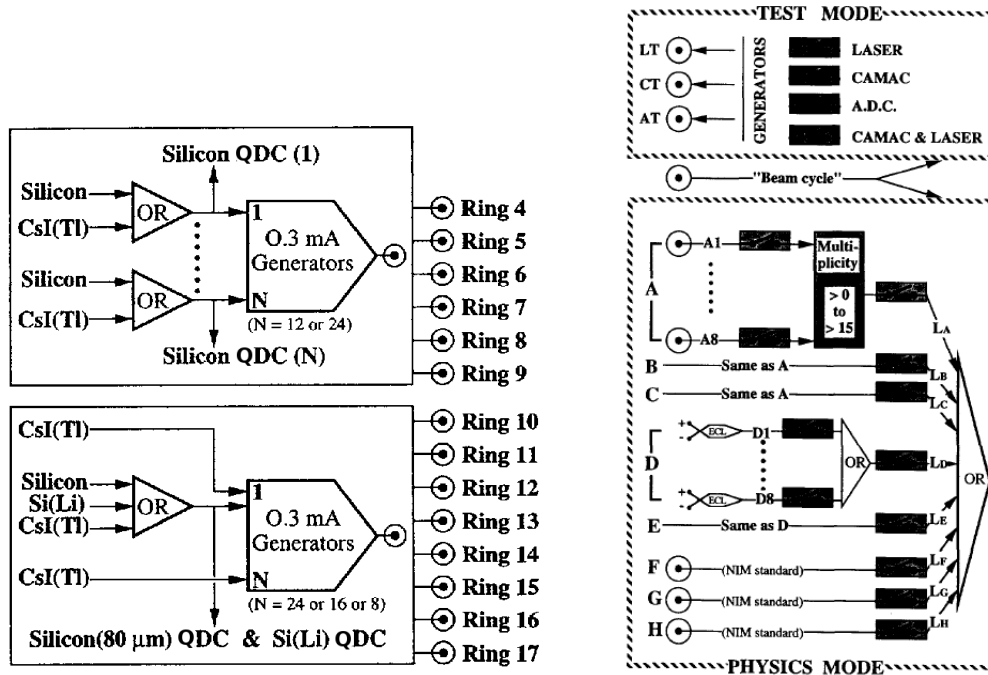
Figure 2.12 – (a) Principles of the multiplicity current generation in the `Regroupeur`. (b) Schematic diagram of the triggering principles in the `Selector` module.

added and sent to a discriminator (Fig.2.13). A coincidence window (*Fenetre de coincidence*) is opened by the `Selector` and the configuration is memorised. The discriminator threshold, with the required final total multiplicity, can be adjusted from 1 to > 15. If the required multiplicity is reached, a logic signal is created (*Trigger rapide* o Fast Trigger) and an `INHIBIT` signal is sent to the QDC and ADC otherwise they reset by themselves.

At this level a slow and external decision can take place: the `Selector` accepts as input an external logic signal (L2). An *Acceptation des voies lentes (AVL)* window is opened; if the logic signal L2 is not within the AVL window, the event is rejected and the system is reset. Otherwise, if the event is accepted the `Selector` sends an *Ordre de codage (ODG)* signal: the QDCs and ADCs encode their signal and, at the end, produce a signal of *End of encoding*.

The `Correlator`, which has the aim of talking with the acquisition, enables the acquisition to acquire the data. Once the acquisition system completes the acquisition, it sends to the `Correlator` an *End of acquisition* signal. The `Correlator` sends a *Reset* signal and disables the *INHIBIT* signal.
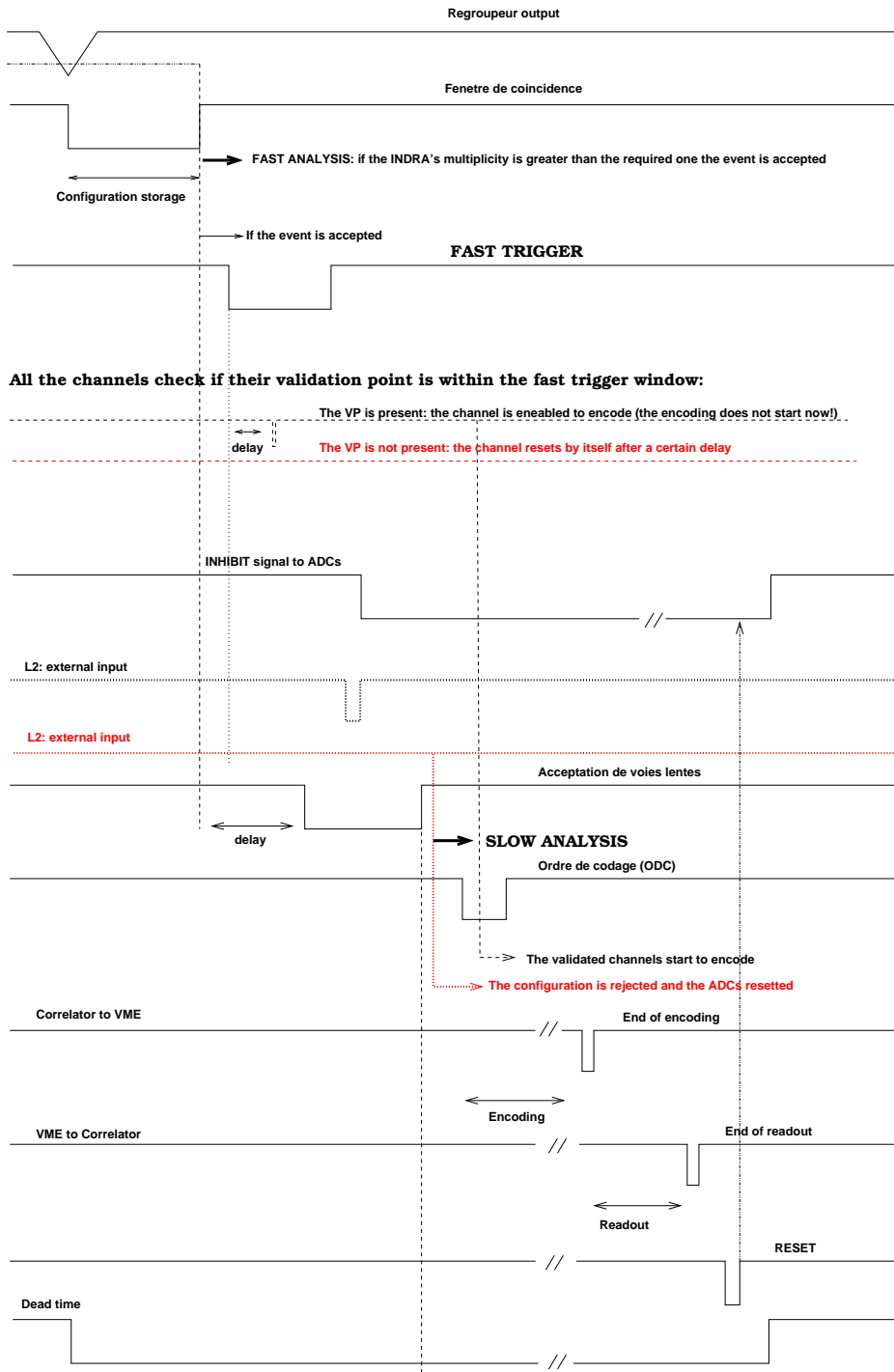
Figure 2.13 – Principles of trigger analysis.

2.3   VAMOS

In heavy ion reactions a huge amount of reaction residues are produced. The study of deexcitation properties of fusion nuclei, which are concentrated around the beam direction, requires a very efficient method, based on the selection and isotope identification (Z, A and E) of the product of interest, in order to assign a reaction product to a nucleus. Moreover radioactive ion beams supplied by the SPIRAL (*Système de Production d'Ions Radioactifs et d'Acceleration en Ligne*) facility have intensities several orders of magnitude below those of stable beams, thus requiring a good background separation. A magnetic spectrometer allows to select, from a large flux of contaminants (beams and elastically scattered particles), heavy reaction-products thanks to its filtering action: the physical separation of one particular kind of particles from other ones provides a background reduction by several orders of magnitude in the particle-detection area (focal plane). Observation of light charged particles or heavier fragments associated to the reaction residue allows, without ambiguity and low statistics, to assign these reaction products to a given system. Moreover, when the projectile mass is lighter than the target one (direct kinematic) the velocity of the composite system is low (see Tab.3.3), and this system exits in a rather large angular cone after the subsequent evaporation process ($\theta_{residue}$ up to $\sim 27°$ in laboratory reference system, see §5.2.2). The low energy of the reaction products implies that very wide angles have to be covered by the detector.

VAMOS *(VAriable MOde Spectrometer)* is a large acceptance mass spectrometer [100–102] operational, since 2002, at GANIL (*Grand Accélérateur National d'Ions Lourds*), where it has been widely used in many experiments for identifying the products in nuclear reactions using both radioactive and stable ions beams from the SPIRAL facility. Coupled with the high efficiency $\sim 4\pi$ detector array INDRA, the spectrometer provides a sensitive and high performance tool for detecting and studying fusion-evaporation reactions products, which can be characterized according to the dispersion parameters (momentum, mass, velocity, etc.) and by the $\Delta E - E$ method of VAMOS.

VAMOS main characteristics are:

1. A very large geometrical angular acceptance, of the order of 85 msr, which is equivalent to an angular acceptance of ±135 mrad in both plans [103].

2. A nominal momentum dispersion [3] of about 2.4*cm*/% at the focal plane, corre-

---

[3]The dispersion can be defined as the transversal distance between a reference trajectory and the trajectory of a particle with $\delta(B\rho) = \frac{\Delta(B\rho)}{B\rho} = 1\%$. In the most general case (real magnet, not focussing,
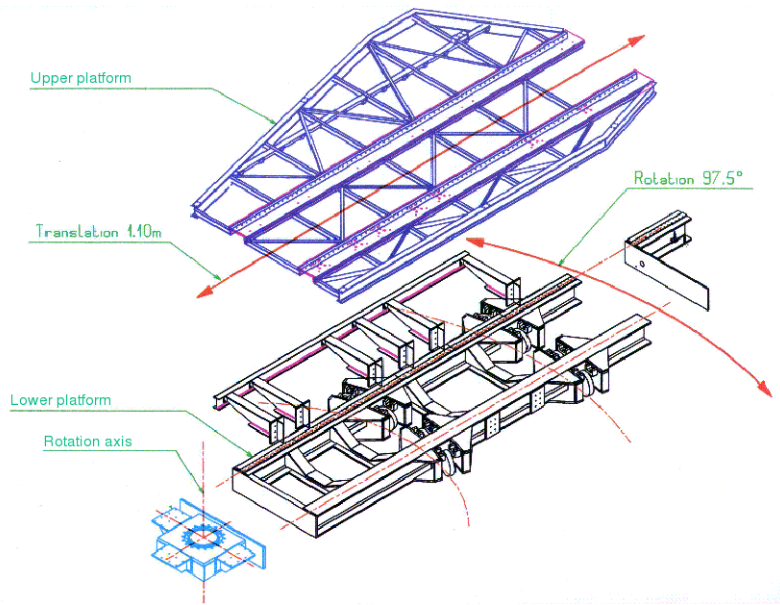
Figure 2.14 – The two sliding and rotating platforms which support VAMOS assure flexibility to the apparatus.

sponding to a nominal momentum acceptance[4] of about 12% [103].

3. A momentum acceptance of the order of ±10%.

4. A velocity filter function which allows the use of the spectrometer as a recoil separator for zero degree operations.

Furthermore, the spectrometer has the flexibility to be horizontally rotated with respect to the beam direction around the target point in the angular range $\sim -5° \div 90°$ [101]. The spectrometer is supported on a platform which can be moved outward to change the distance from the target. The platform rests on another one on rails, allowing rotation around the target point (see Fig.2.14).

The distance between the target and the first quadrupole can be varied from 0.4 m to 1.4 m [104], in order to accept high magnetic rigidities. The minimum distance of 40 cm between the first Q-pole and the target gives the maximum solid angle of the device, about 100msr, and a maximum rigidity of $B\rho_{nom} = 1.6Tm$. At a distance

---

with border effects, etc) the position where an ion lands depends on many factors (i.e. the angle, the path through the magnetic field); it's more correct then to define the dispersion as the partial derivative with respect to the variation of the momentum of the ion:

$$D(\theta, \rho, B...) = \frac{\partial x}{\partial p/p} \tag{2.1}$$

[4]A real ion-optical apparatus in general does not transmit all (for example, it cuts in angle or in momentum) and the volume in phase space which can pass (which is independent of the particle, but it is a property of the apparatus) is called acceptance.
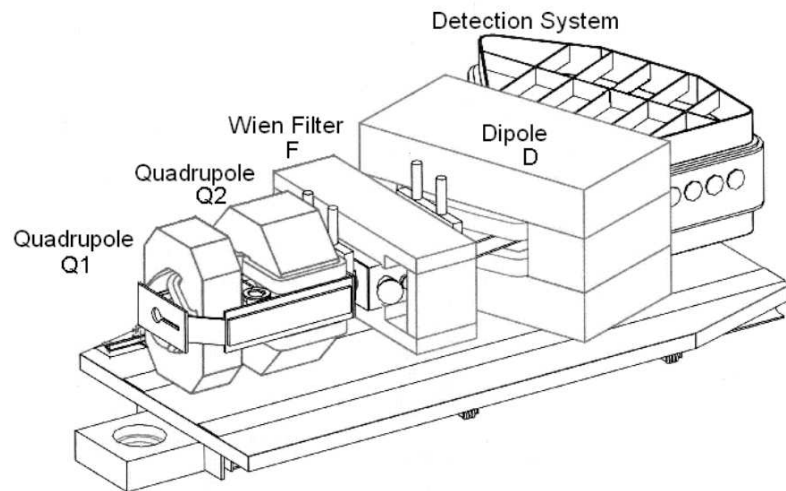
Figure 2.15 – Schematic of VAMOS spectrometer [105]. The quadrupole-quadrupole-wien filter-dipole configuration is outlined. The wien filter was not active during the experiment. The detection system is located on the focal plane of the apparatus.

of 100 cm the solid angle decreases to ~ 40 msr, while the maximum rigidity reaches 2.3 Tm.

The VAMOS solid-angle acceptances of the order of 100 msr is obtained using very large optical elements, whose high optical aberrations, only partially corrected in the hardware, require the reconstruction of the ion trajectories throughout the spectrometer (ray-tracing) to obtain a good resolution.

The ions trajectory in a magnetic field is indeed determined by ion velocity v and A/Q ratio (where Q is the ion charge state). The VAMOS focal plane detectors (an ionization chamber and a silicons wall) allow the identification of the evaporation residues in charge Z and mass A and the measure of their kinetic energy E_{kin}, by measuring their time of flight, their energy loss ΔE in the ionization chamber and their residual energy E. Two position sensitive detectors (SED) allow the reconstruction of the ions trajectories.

2.3.1 ION-OPTICAL COMPONENTS

The ion optical elements of VAMOS consist of a pair of quadrupoles (Q), a velocity filter (F) followed by a magnetic dipole (D) in the configuration Q1-Q2-F-D. Figure 2.15 represents an overview of the spectrometer where the different elements are identified. In this experiment VAMOS is used in dispersive mode, without the Wien filter.

(a) Before correction.   (b) After correction.
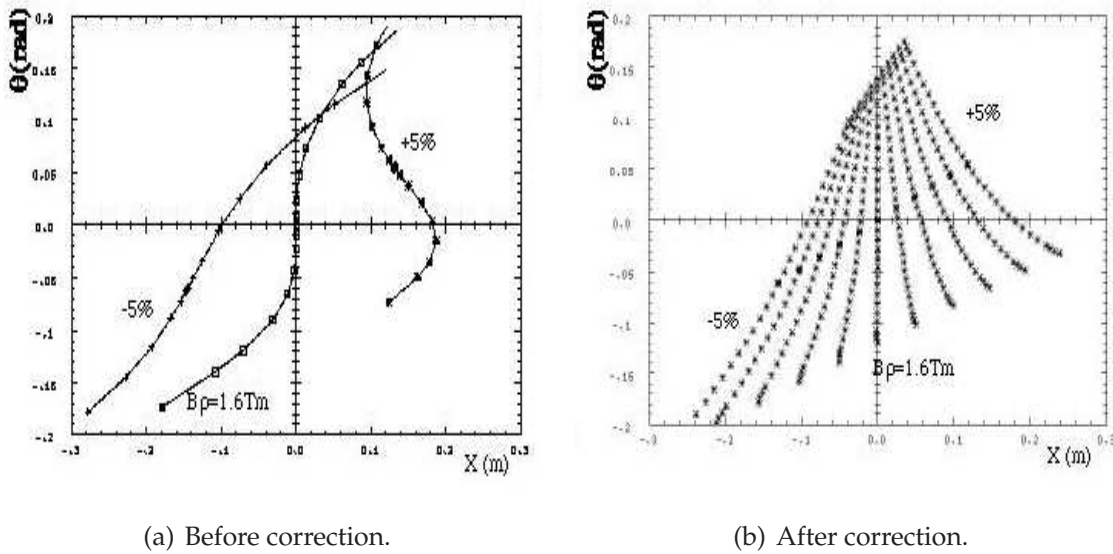
Figure 2.16 – Image aberrations in the focal plane $x - \theta$ for the full momentum acceptance
($\pm 5\%$). Without the pole shape correction, there would be a crossing of particle
trajectories in the focal plane that would not allow the reconstruction.

The focalizing lens are realized with two quadrupoles, rotated of 90° and sepa-
rated by a distance of 0.3 m. The first quadrupole focuses the beam in y-direction, i.e.
perpendicular to the plane of dispersion, whereas the second quadrupole focuses it
in x-direction, i.e. in the dispersion plane.

Both quadrupoles have a large aperture for obtaining the high angular acceptance
of the spectrometer. The diameter of the first quadrupole is 30cm while the aper-
ture of the second is elliptical, with its major axis around 100cm. The very large
acceptance induces large image aberrations[5] of acceptance at the focal plane which
degrade the resolution. For VAMOS aberrations are non negligible and the focal
plane spectra are strongly influenced by them. To minimize this effect, the second
quadrupole has been shaped in the dispersive plane to introduce octupole and do-
decapole components in the field. Fig.2.16 shows, in the focal plane $x - \theta$, the effect
of such correction.

None of the less geometrical 3^{rd}order image aberrations (x/θ^3) are of high impor-
tance and affect the resolution, therefore the reconstruction of trajectories of the reac-
tion products is required in order to calculate their momentum and scattering angle.

The magnetic length of Q1 is 60cm then a rather strong gradient for the magnetic
field is required (6.7T/m). The magnetic length of Q2 is 90cm with a gradient of 2T/m.

---

[5]Aberration is a function of solid angle [106].

| Magnetic lens	Q1	Q2
Magnetic length	0.6*m*	0.9*m*
$\overrightarrow{B}$ gradient	6.7 T/m	2 T/m
Aperture diameter	300 mm	elliptic:
		horizontal ±500 mm
		useful height ±50 mm
Dipole		
Deflection angle θ_{VAMOS}	$0° - 60°$	
Radius of deflection ρ_{nom}	1.5 m	
Maximum field	1.1 T	
Nominal maximum rigidity $B\rho_{max}$	1.6 Tm	
Magnetic length	1.57 m	
System characteristic:		
Flight path length	7.6 m	
Maximum solid angle	100 msr	
Momentum acceptance	±10%	
Magnetic drift	target-Q1=	0.4 ÷ 1.4 m
	Q1-Q2=	0.3 m
	Q2-dipole entrance=	1 m
	dipole exit-first order focus=	1.5 m

Table 2.5 – Main characteristics of VAMOS apparatus [101, 103, 107].

The dipole magnet has a nominal radius of deflection of $\rho_{nom} = 1.5m$, which requires, for the nominal maximum magnetic rigidity of $1.6Tm$, a $B_{max} = 1.1$ T. The field boundaries of the dipole magnet are shaped in order to reduce second order image aberrations.

The dispersion at the focal plane can be varied by changing the bending angle of the dipole with three options of $0°$, $45°$ and $60°$ bending. During the experiment the bending angle was set to $45°$. The gap of the dipole magnet is of 20 cm.

The ion-optical configuration of this arrangement is listed in Table2.5.

The QQFD structure has a great flexibility: depending on the elements which are ON or OFF, three distinct functioning modes (giving the name to VAMOS for VAriable MOde Spectrometer) can be obtained. With only the quadrupole ON the device has a very large non-dispersive acceptance; in the QQD setup VAMOS is a dispersive facility giving an additional mass and charge identification; finally, when the Wien Filter is switched ON, the beam rejection is active if the voltage is applied along the vertical direction. A very selective M/Q selection is obtained applying voltage along the horizontal direction.
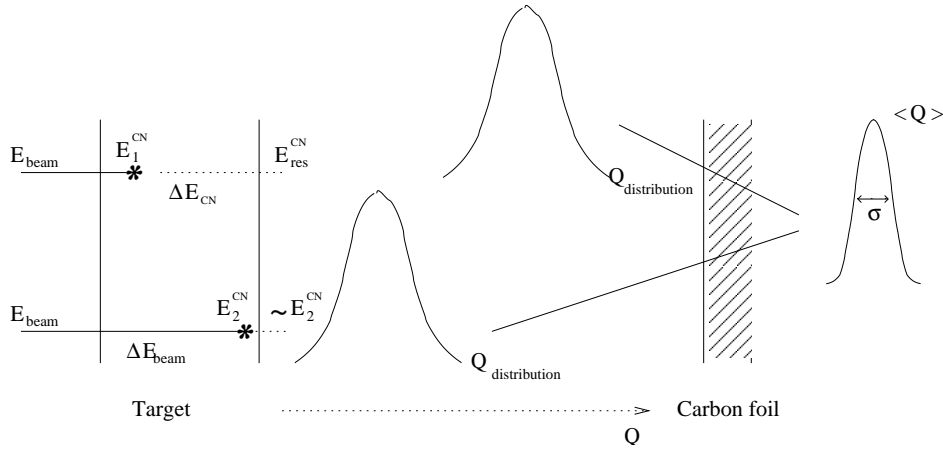
Figure 2.17 – The charge distribution of nuclei exiting a target medium is related to the position where the reaction takes place, therefore the resulting distribution is spread. The suitable thickness of the carbon foil allows to reach an equilibrium between different charge states.

2.3.2   Charge state equilibration

The ion trajectory in an electromagnetic field is determined by its momentum and its charge state (see §3.3). Generally, the change of the ion charge state in a target medium is the consequence of a multiple combination of two fundamental charge exchange processes [108]: the electron capture and the electron loss, whose cross sections, $\sigma(q, q', v, Z, Z_T)$, are related to the initial and final charge state (q and q'), to the ion velocity (v) and to the ion and target atomic number (Z and Z_T, re-

Z	A	E_{res}	θ_{res}	$v_{res}^{10\%}$(cm/ns)	$v_{res}^{90\%}$(cm/ns)	$\Delta v/v$(%)
33	72	126	0°	1.78	1.83	3%
33	72	126	7°	1.78	1.83	3%
33	72	168	0°	2.07	2.12	2%
33	72	168	7°	2.06	2.12	3%
36	78	143	0°	1.82	1.87	3%
36	78	143	7°	1.81	1.87	3%
36	78	176	0°	2.03	2.08	2%
36	78	176	7°	2.02	2.08	3%
40	84	172	0°	1.93	1.98	3%
40	84	172	7°	1.92	1.98	3%

Table 2.6 – Recoil nucleus velocities at the exit of the target for reactions taking place at 10% ($v_{res}^{10\%}$) and 90% ($v_{res}^{90\%}$) of the target thickness. θ_{res} is the residue emission angle in laboratory. The chosen recoil nucleus charge values, Z = 33, 36 and 40 are the mean value and the extremes of the charge distribution, obtained with GEMINI simulation (see §5.2.2), respectively. The masses, A, associated with each Z are the mean values of the mass distribution for each Z. The recoil energies E_{res} are the mean values of the energy distribution (for each Z) fitted with two gaussian (2 kinematic solutions are present).
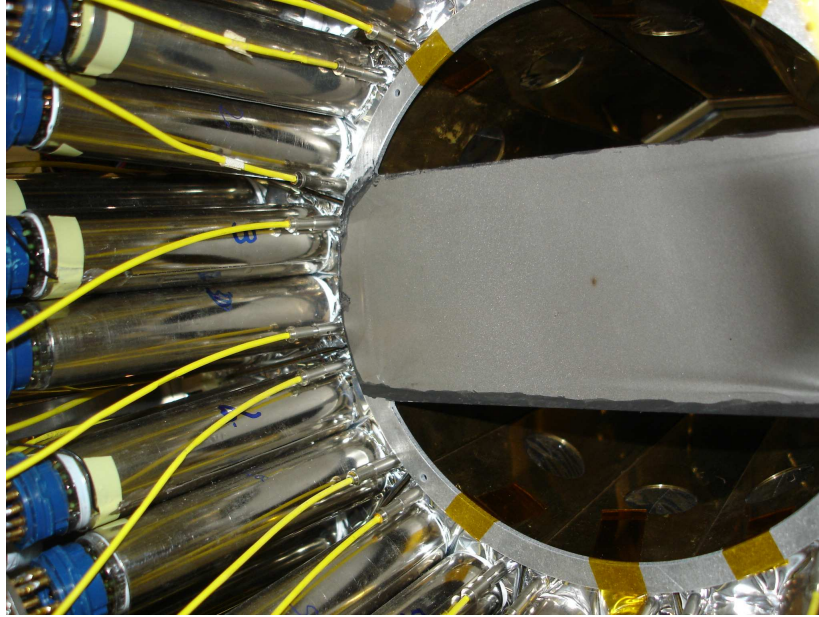
Figure 2.18 – Photo of the carbon foil located in INDRA chamber, in order to equilibrate the ions charge state distribution.

spectively). As the ion pass through a material a certain distribution, related to the ions velocity, of charge state will result. When the beam hits the target, the reaction can take place everywhere inside the target, thus the remaining thickness that the recoil nucleus has to cross, and then its velocity, is related to the reaction position (see Fig.2.17 and Tab.2.6). Therefore the charge state distribution of recoil nuclei at the exit of the target is spread and depends on the crossed material thickness.

To equilibrate the charge state distribution before the ions entering VAMOS, a thin carbon foil ($70\,\mu g/cm_2$) (see Fig.2.18) have been placed in INDRA chamber, on $4^{th}-5^{th}$ rings mechanical support, $50\,cm$ far from the target. As an ion penetrate the carbon foil it undergoes a large series of ion-electron collisions. The charge distribution changes with depth until, at a certain depth, equilibrium between different charge states is reached. This equilibrium distribution [109] is, to a first approximation, a function of the nuclear charge and the velocity of the ions [110]. The ions crossing the carbon foil reach the equilibrium charge state distribution, whose width is smaller than the initial one [111].

2.3.3   Focal plane detection setting

The real focal plane of VAMOS is highly deformed, due to the magnetic aberrations. Its projection orthogonally to the beam, which represents the detectors active zone, is $40\,cm$ wide and $10\,cm$ high.
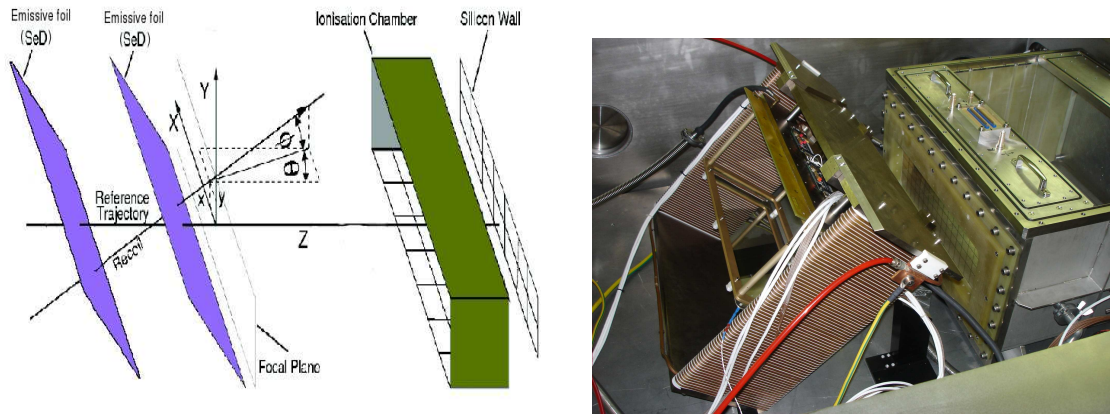
Figure 2.19 – (a) Schematic of VAMOS focal plane detection system showing the focal plane and the coordinate system. Secondary electron detectors are represented by their emissive foils. (b) Photo of the focal plane detection system: the second SeD (SeD2) and the ionization chamber HARPEE are visible. The silicon wall, located behind HARPEE, was not already set.

Direct focal plane measurements alone do not give the required high resolution identification: particle identification is indeed based on the reconstruction of the event. The scattering angle at the target (θ) and $B\rho$ parameters of each particle must be reconstructed by software.

Since the reconstruction of trajectories is required, two-dimensional position measurements are needed at the focal plane of the spectrometer. Moreover, the identification in atomic number (Z) and mass (A) of the reaction products requires total energy and energy loss, as well as time of flight measurements.

The detection system at the focal plane of VAMOS (Fig.2.19) consists of two emissive foils coupled with an ionization chamber and a silicon wall detectors.

The emissive foils, coupled to secondary electrons detectors, are used for x,y-position and time measurements at the focal plane. The time resolution is of the order of 250 ps (FWHM) [103], while the position resolution of about 1 mm (FWHM) [103].

An ionization chamber (HARPEE: *Haute Résolution en A par Perte d'Energie et Energie*), located 380 mm far from the second emissive foil and operating in transmission mode, provides the ΔE measurements, while the E measurement is given by the array of silicon detectors placed 11.225 cm[6] behind the HARPEE's entrance window. An ΔE resolution of 3% [103] have been obtained.

Time measurements are obtained also by silicon detector signals, coupled to the high

---

[6]Value taken from HARPEE design.

Focal plane detectors resolution		
SeD	X_{FWHM}	~ 1 mm [103]
	Y_{FWHM}	~ 2 mm [103]
	t_{FWHM}	~ 250 ps [103]
HARPEE	ΔE	3% [103]
Si wall	E	[8]
	t	2 ns [100]
	A/Q	$2 \cdot 10^{-3}$ [100]
	A	[8]
	Z	[8]

Table 2.7 – Focal plane detectors resolutions.

frequency signal of the cyclotron. Time resolution is limited to about 2 ns [100], due to the width of the beam pulse (~ 2 ÷ 3 ns).

The combination of the $B\rho$ measurement and the time of flight [7] provide the A/Q ratio with a resolution of around $2 \cdot 10^{-3}$ [100]The mass can be obtained by combining the velocity and energy measurements.Reusing the mass value in the $B\rho$ expression, it is possible to evaluate the charge state Q. Determination of the atomic number, Z, is done by $\Delta E - E$ method.
A summary of focal plane detectors resolutions is reported in Tab.2.7.

2.3.3.1 Secondary Electrons Detectors

Position and time of flight of the incident ions are measured by Secondary Electron gas Detectors (SED), used in conjunction with an emissive foil, to detect low energy heavy ions (see Fig.2.20). The main advantage of such detector is that only the thin emissive foil lies on the ion trajectories inducing minimal energy and angular straggling.

The emissive foil is a thin 45° tilted mylar foil (1.5 μm) located on the trajectory of the ions (see Fig.2.21). Its effective size ($40 \times 10 \, cm^2$) covers all the focal plane. Under the impact of the ions, the foil emits secondary electrons (Se$^-$) [113], whose number is proportional to $Z^2/(E/M)$, where Z, E and M are the ion charge state, energy and

---

[7]

$$B\rho = \frac{A}{Q}v = \frac{A}{Q}\frac{d}{tof} \tag{2.2}$$

where d and tof are the flight path and the time of flight of the particle, respectively.

[8]Calibrations are still in progress and no values are available from previous campaigns.
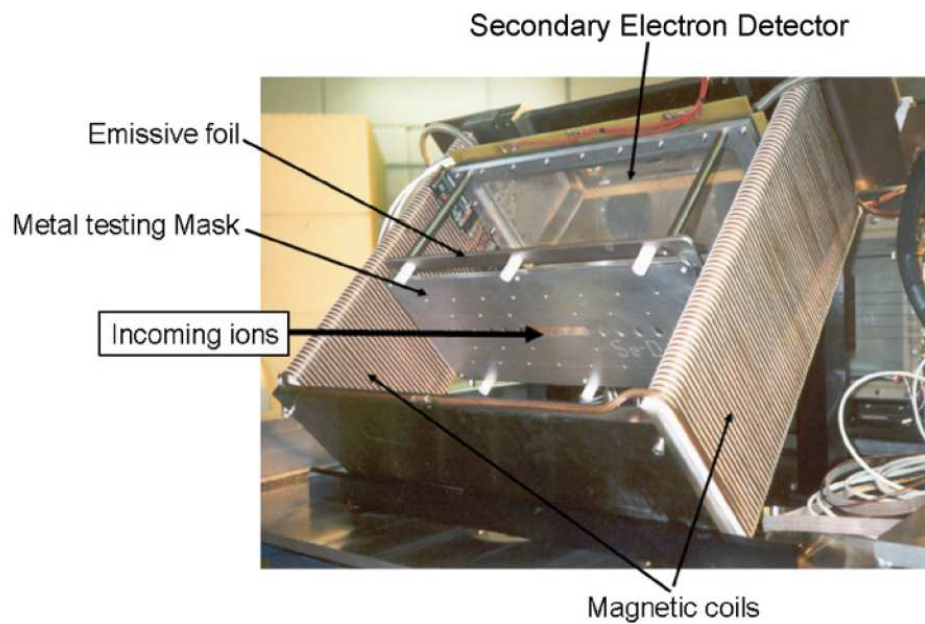
Figure 2.20 – Photo ([112]) of secondary electron detector installed on the VAMOS spectrometer. The different elements are identified. Only the emissive foil lies on the ion trajectories.

mass, respectively.

These electrons are electromagnetically accelerated and guided toward a low-pressure thin gas chamber. Se$^-$ are focused towards the detector by two longitudinal electric and magnetic fields. The first is primarily used to accelerate them, as quickly as possible, in order to minimize their dispersion, and to allow them to cross the entrance foil of the detector, a $0.9\,\mu m$ aluminized Mylar foil[8] (the minimum required energy is 7 keV [112]).

Secondary electrons drift for collection over a ~ 10 cm distance through a 10 kV high voltage, realized by two electrostatic grid of gold-coated tungsten wires (with 1 mm spacing) placed 9 mm apart the foil. The grid is grounded while the emissive foil is at $-10\,$kV (V_0).

In addition to the electric field, a parallel and appropriate field is necessary to focus the Se$^-$ and have good position resolution: from an initial point like source, the Se$^-$ arrive at the detector with a large distribution, shifted from the original position. For a well-chosen value of B (B_0), the trajectories of the electrons are helicoidal with

---

[8]With an incident energy of 10 keV, each Se$^-$ loses, in average, 3.1 keV in the entrance window. After one Se$^-$ crosses the foil, it will lose 290 eV in the isobutane thus creating around 12 electron−ion pairs/electron along the 3.2mm of the active zone between the cathodes (see text and Fig.2.22). This is sufficient for a single Se$^-$ to be detected [112].
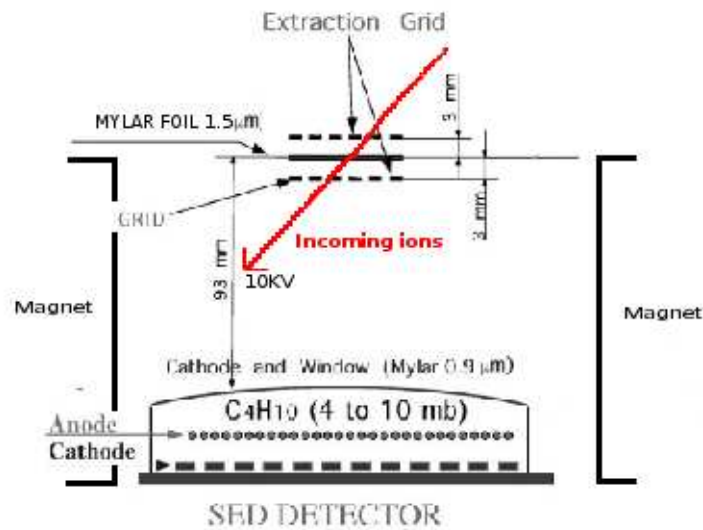
Figure 2.21 – Sketch of SED coupled with an emissive foil. Secondary electrons emitted in the impact of the ions on the foil are guided toward the low pressure gas chamber where they are detected.

an integer number of turns at the cyclotron frequency between the foil and the detector. In this configuration their arrival point is independent of their initial transverse velocity. It has been shown [114] that a "perfect" ("point to point") image of the foil is obtained when the secondary electrons have made an integer even number of turns at their cyclotron frequency between the emissive foil and the SED entrance window.

A nominal field of 110 G has been set, reached for a current of 70 A in the magnets.

Since the magnetic field is not uniform the electrons in the outer parts of the field are deviated (side effect). These deviations ($\sim$ 1 cm) imply that a calibration of the detector is necessary to have precise measurements. For this purpose, a 0.5mm thick aluminium mask with calibrated holes of 5 mm diameter is put in front of the emissive foil. The calibration is valid for a given (V_0, B_0) couple. The calibration procedure will be described in §3.5.1.

The secondary electron detector (SeD) is a low-pressure position sensitive gaseous detector [115], largely based on the CATS, a gaseous tracking detector for heavy ions [116].

This detector, located on the side of the ions trajectories, amplifies the number of electrons, which ionize the isobutane, and provides the position and the time sig-
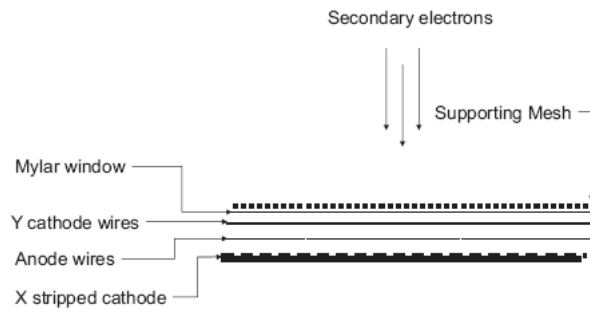
Figure 2.22 – Basic geometry of the low-pressure secondary electron detector. Localization
wires and the stripped cathode allow the ion impact position reconstruction.

nals. The SeD detects the cloud of secondary electrons emitted from the emissive
foil. Therefore, the ions do not traverse the full detector but only a minimal thick-
ness of matter. The secondary electron detector (SeD) gives the time and position of
the Se shower and thus those of the ion traversing the detector.

Fig.2.22 presents its basic geometry. It consists of two elementary cells with a
common anode, a wire plane, equidistant (1.6 mm) from the two grounded cath-
odes. The gas (isobutane CH_4) is enclosed between the entrance foil and the second
cathodes, at the operating pressure (p) of $\sim$ 500 mbar. The entrance foil, a $0.9 \mu m$ My-
lar film, is supported by a metal mesh to limit bulging under the gas pressure.

The amplification of the signal, due to high E/P (electric field over pressure)
occurs in two different regimes: the parallel plate region in the constant field zone
between the cathode and the wire plane, which is predominant at such low pressure,
and a multiwire-like multiplication region in the vicinity of the wires [115].
These properties are advantageous for secondary beam tracking:

- there is an important gain in the detector and a significant signal can be ob-
  tained with a small thickness of gas, without disturbing incident particles tra-
  jectories;

- the fast component of the signal generated by electrons produced in the con-
  stant field region assures a good timing resolution;

- the fast positive ions collection, due to a small anode cathode gap, gives high
  counting rate capabilities.

The first cathode is made of 150 wires of $50 \mu m$ diameter, with a spacing of 1 mm,
and connected 3 by 3 for the charge measurement, so that 48 channels are available

SEDs set up	
V_0	$-10\,\text{kV}$
B_0	$100\,\text{G}$
p	$\sim 7\,\text{mbar}$
V_{SeD}	$475 \div 510\,\text{V}$

Table 2.8 – SEDs set up. V_0: electric potential applied to the extraction grid, B_0: magnetic field intensity, p: gas pressure in the gas chamber, V_{SeD}: anode voltage

for the measurement of the charge distribution and hence the position (at each end, the last 3 wires are grounded). It provides the y-position measurement.

The anode is made of 402 $10\,\mu m$ wires (1 mm spaced), stretched perpendicular to those of the cathode. The wires, grouped in 3 independent parts and raised to a common positive high voltage $V_{SeD} \sim 500\,\text{V}$, are read separately to provide timing signals.

The second cathode is a gold-coated stripped printed circuit. All 128 strips (3 mm wide and 0.125 mm spaced) are independently read for the charge measurement, providing the x-position measurement. The cathodes are grounded.
The anode and the extraction grid voltages, the focusing magnetic field intensity and the gas pressure values set during the experiment are summarized in Tab.2.8.

The anode wires deliver a time signal allowing a time of flight measurement. The cathode strips are individually read out and the position of incoming particles is reconstructed using a charge centroid finding algorithm and allowing the measurement of the incident particles trajectories, event by event.
All the 48 + 128 charge signals are pre-amplified and shaped and sent to ADCs. The fast anodic signals are processed by a fast amplifier and sent to a constant fraction discriminator.

2.3.3.2 The ionization chamber HARPEE

The ionization chamber HARPEE provides the energy loss (ΔE) information of the incident ions, allowing the charge identification by the $\Delta E - E$ method and the mass identification by measuring the time of flight of the particle.
The chamber, filled with isobutane (C_4H_{10}), normally operates at a gas pressure of about $15 \div 25$ mbar in transmission mode, giving the ΔE measurement. The pressure
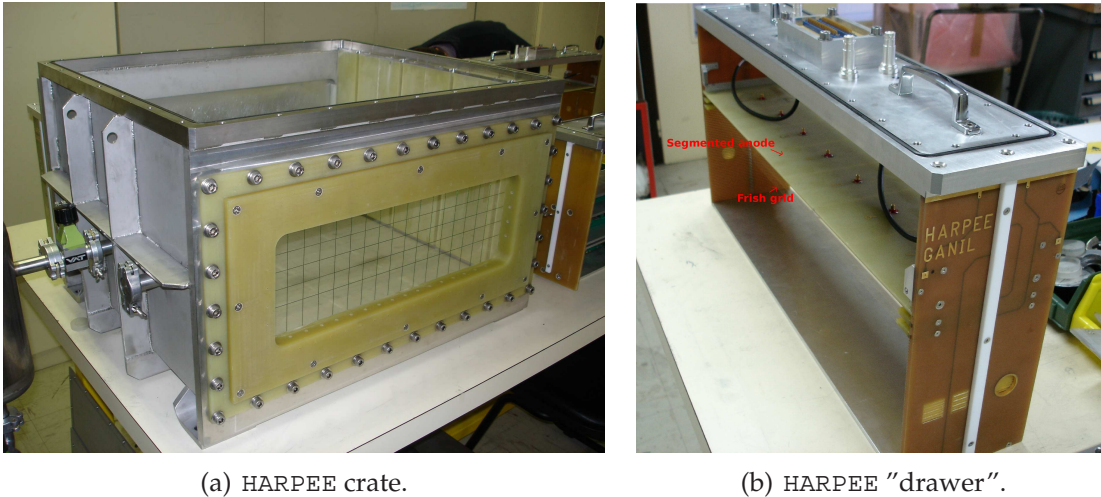
(a) `HARPEE` crate.   (b) `HARPEE` "drawer".

Figure 2.23 – Photos of the ionization chamber `HARPEE`. `HARPEE` is constituted by three "drawers", arranged along the ions flight path. Each "drawer" has a segmented anode and a Frish grid located between the anode and the cathode.

value has been chosen in order to get a good $\Delta E - E$ resolution (see §4.2.1 and Fig.4.8).

A view of `HARPEE` is shown in Fig.2.23(a). The anode is segmented in 7 parts across the focal plane (see Fig.2.23(b)) in order to get a raw position information and to accept a high counting rate. The anode and the cathode are made of copper.

Between the anode and the cathode a Frish grid is present, which is kept at an intermediate potential between the two electrodes. All the ion interactions are confined into the volume between the grid and the cathode of the chamber. The electrons produced in the gas ionization are driven initially from the interaction volume to the grid, without producing any measured signal voltage. However, once the electrons pass through the grid on their way to anode, the grid-anode voltage begins to drop and a signal voltage begins to develop. The use of Frish grid allows to remove the dependence of the pulse amplitude on position of interaction.

The chamber entrance window is made of $0.9\mu m$ of mylar and is supported by a grid (Fig.2.24). The field lines close to the entrance window are kept vertical by the application of graded voltages to the horizontal support wires. To ensure the uniformity of the electric field in the detector, and in particular near to its edge, a series of strip electrodes are placed around the sides of the chamber at 5 mm intervals.

The anode is divided into three sections along the flight path of the recoils, respectively 2 cm, 8 cm and 1.225 cm length. Due to the non uniformity of the field near the entrance windows, the first section of the anode is not connected to the electronic chain. It has been observed that, taking into account the region close to the entrance

Figure 2.24 – Photo of the field shaping wires on HARPEE entrance window. The grid for support of the mylar is also visible.

windows, the energy resolution gets worse. The second section of the anode covers 8 cm of the chamber length: this is the region where the energy lost in the gas (ΔE) by the ions is measured. Neither the last section of the anode is connected to the electronic chain. The energy lost in this region can be reconstructed from the measured ΔE and the silicon signal.

The HARPEE electronic chain is shown in Fig.2.25. Each signal coming from an anode segment is treated by a charge preamplifier, located as close as possible to the detector. The signals are sent to amplifiers, which shape them. Its outputs provide the energy measurement. The ADCs are acquired when the trigger is fired .
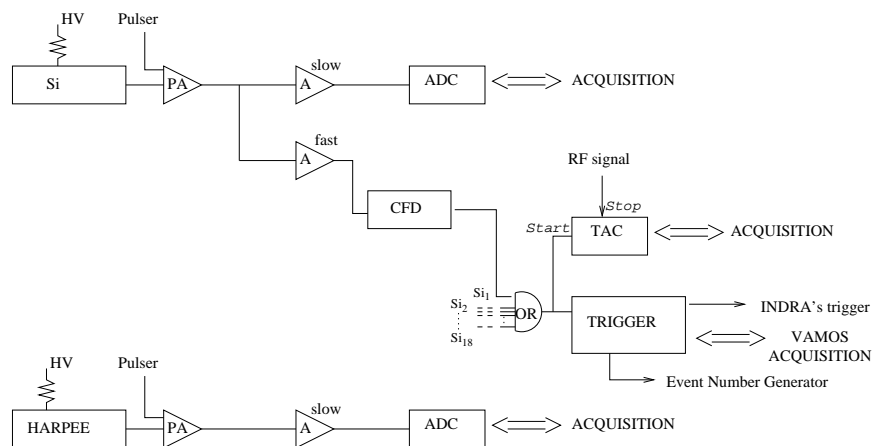
Figure 2.25 – Sketch of electronic associated to HARPEE and to the silicon detectors. HARPEE provides the ion energy loss (ΔE) measurements, while the silicon array provides the residual energy (E) measurements, the *Start* signal for time of flight measurements and the trigger signal generation.

Figure 2.26 – Photo of silicon array. 18 silicon detectors are placed on two rows, covering all the focal plane. The use of a conducting grid for electrical contact reduces the dead thickness, lowering the detection threshold.

2.3.3.3   Silicon detectors array

The silicon detectors have the double task of measuring the energy deposited in the silicon and of providing the trigger signal, as well as giving time signal for time of flight measurements.

The silicon array is constituted by 18 silicon detectors, arranged on two rows and covering all the VAMOS focal plane. The silicon wall is placed 11.225 cm far from the HARPEE entrance window.

To ensure a fast charge collection and to reduce the dead thickness, each silicon is not aluminized, but on its surface is placed a grid (see Fig.2.26). The dead region of each silicon is 2 mm, due to 1 mm of dead edge region and 1 mm of contact.

The silicon presents an high capacitance of ~ 1000 pF.

The silicon wall electronic chain is sketched in Fig.2.25. The detectors signal are treated by charge preamplifiers and sent to slow and fast amplifiers. The output of the slow amplifier, which shapes the signal, provides the energy measurement. The fast amplifier's output is sent to a constant fraction and converted into a logical signal. The trigger is fired by the logic OR built on the logic signal of all 18 silicon detectors. The OR output also gives the "Start" to the TAC, to provide a time of flight measurement ("Stop" is given by the RF signal).
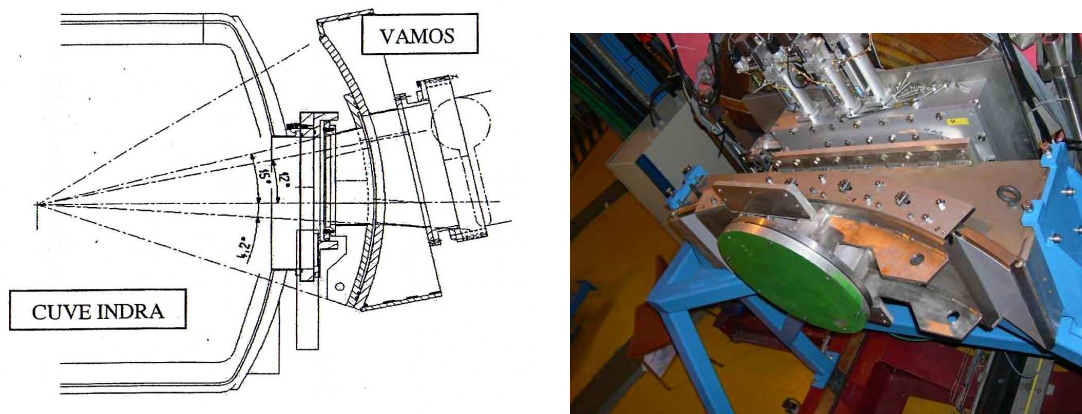
Figure 2.27 – Sketch (a) and photo (b) of the INDRA-VAMOS coupling window. Thanks to it, VAMOS can be rotated with respect to the target without breaking the vacuum in the vacuum chambers.

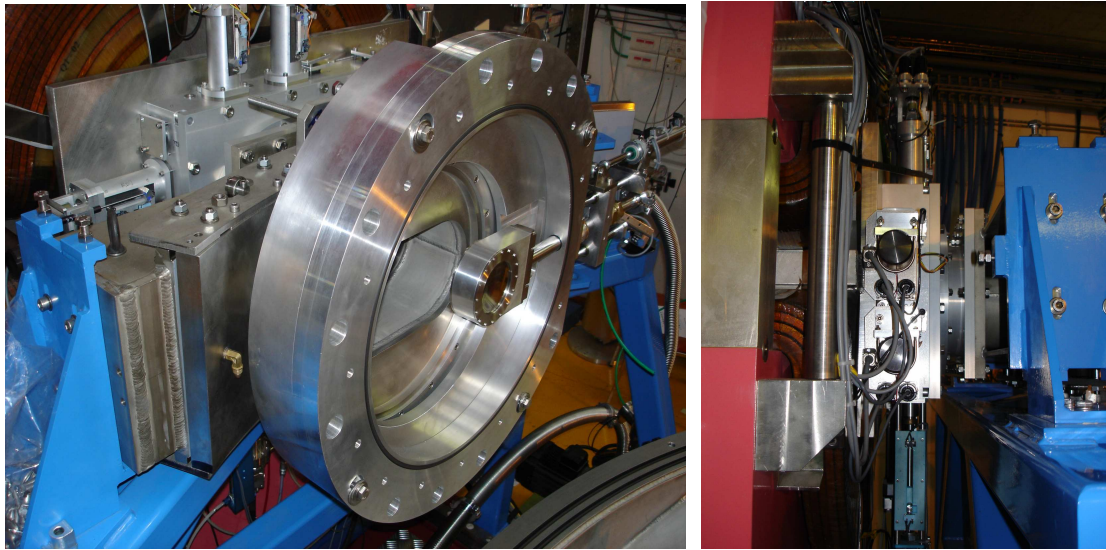## 2.4 INDRA - VAMOS coupling

2.4.1 Mechanical coupling

To allow the INDRA - VAMOS coupling, INDRA has been turned of $180°$ and mechanical problems have required the removal of the first three rings, which cover the angles between $2°$ and $7°$. Moreover, to allow the VAMOS rotation (with respect to the beam axis) up to $8°$, the gas and the entrance window of one ionization chamber cell, located on the horizontal plane of ring 4 and 5, have been removed.

The mechanical coupling has been realized by a sliding window[9], which permits the VAMOS rotation without breaking the vacuum in the INDRA scattering chamber. The sliding window is shown in Figs.2.27 and 2.28. The VAMOS entrance is $200\,mm$ of diameter but the real entrance is limited by two slits, resulting in a $100 \times 100\,mm^2$ entrance window.

2.4.2 Electronic and acquisition coupling

To efficiently coupling INDRA and VAMOS it is necessary to couple their acquisition, i.e. it is necessary:

- an event number distribution to both acquisitions, provided by the CENTRUM module

- a parallel readout of each sub-event by its own data acquisition system

---

[9]The sliding window has been specially designed to couple the two apparatuses, thank to the efforts of J.L. Charvet (supervisor- CEA, Saclay) and Hugnet (mechanical engineer - GANIL, Caen).

Figure 2.28 – Photos of the INDRA-VAMOS coupling system. The VAMOS entrance is visible.

- a global event reconstruction, provided by a `MERGE` module

The `CENTRUM` (*Clock & Event Number Transmitter Receiver Universal Module*) module generates and distributes the current event number to both INDRA and VAMOS acquisition.

The aim of the experiment being the analysis of deexcitation properties of hot fusion nuclei, the trigger configuration must assure the acquisition of an event only if a residue has been detected in VAMOS. In the measurement, therefore, VAMOS act as the master trigger, while INDRA as the slave one. When the VAMOS multiplicity is, at least, 1, it means when the VAMOS trigger is fired, the event is validated. The event validation signal is split and sent to the event number generator and to the INDRA's trigger, and the VAMOS sub-event is readout by its own acquisition (see Fig.2.29). The event number generator supplies the information to both the acquisition systems.

INDRA trigger receives the event validation signal in the *Acceptation des voies lentes* (AVL) input on the `Selector` module.

As we have seen in §2.2.3, if the event validation signal (*L*2 signal in Fig.2.13) is within the AVL window, the `Selector` delivers an `Ordre de codage` and INDRA parameters are acquired by its own acquisition. During INDRA acquisition data, the system is inhibited.

The `Merge` module provides the global event reconstruction, combining the INDRA and VAMOS sub-event with the same event number.
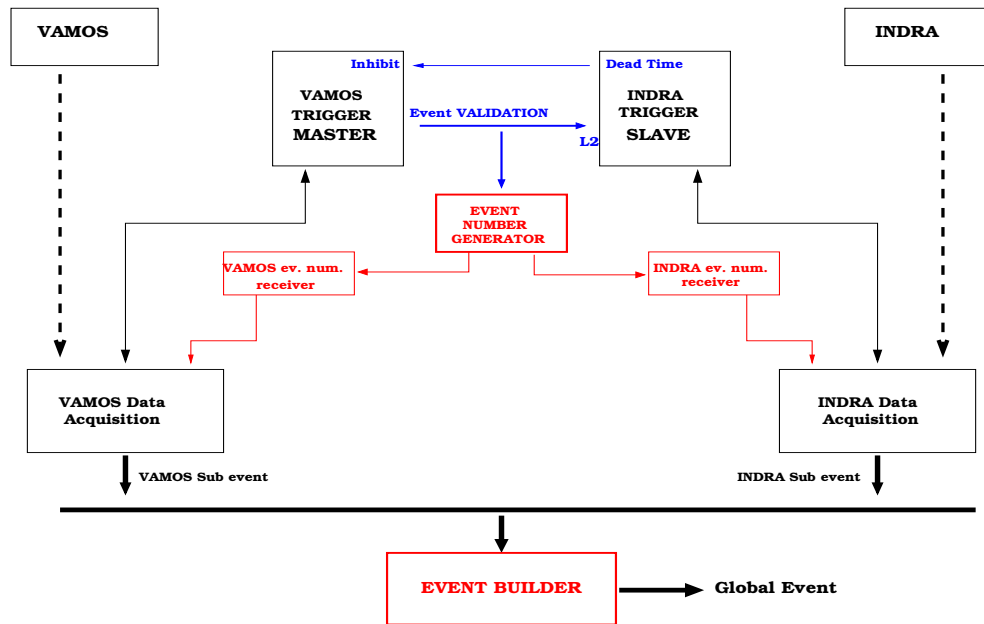
Figure 2.29 – INDRA-VAMOS acquisition coupling system. VAMOS acts as master trigger, validating or not the INDRA subevent. The EVENT BUILDER (MERGE module), basing on the event number, reconstructs the global event.

To get a well working acquisition coupling, it had been necessary to carefully set up the delays on the various signals (well synchronized INDRA and VAMOS acquisitions). The correlation between the two signals have been checked during all the measurement.

Chapter 3

The experiment

The goal of the experiment analyzed in this thesis is the study of the deexcitation properties of Pd nuclei formed in collisions between different Ar isotopes and three different stable Ni isotopes at incident energies around 13 AMeV. Within this framework the aim of the present study is to have quantitative information on the N/Z dependence of the Ar+Ni fusion cross section.

The experiment is part of a wider study on dynamical and thermodynamical properties of the nuclear matter, undertaken by the NUCL-EX group [117–122] and the INDRA collaboration [123–129].

3.1 Reactions

By using radioactive beams, new nuclei are accessible by the fusion reaction channel, both on the side of proton-rich nuclei, in particular close to the $N = Z$ line, and neutron-rich nuclei, generally not accessible by means of stable beams due to high neutron evaporation at the beginning of the evaporation cascade.

The experiment has been performed at GANIL, where the cyclotron CIME (Cyclotron pour Ions de Moyenne Energie), the INDRA vacuum chamber and the VAMOS spectrometer are located.

CIME is a compact, medium energy cyclotron devoted to the acceleration of radioactive ions for the SPIRAL project [131]. The SPIRAL facility, based on the ISOL method, provides for production and separation of radioactive ion beams, with subsequent acceleration by a cyclotron, opening up the study of nuclear reactions around the Coulomb barrier to radioactive nuclei. The cyclotron accelerates ions from 1.7 AMeV to 25 AMeV depending on the mass of the ion. Its main characteristics are listed in Tab.3.1.

Beam characteristics	
Energy spread	±0.5%
Emittance	$15 \div 20\pi$ mm.mrad
Time structure	$\pm 10/360 * T_{RF}$

Table 3.1 – CIME beams characteristics [130]. T_{RF} is the period of the cyclotron radiofrequency, which accelerates the ions.

The CIME beams cover a wide range of N/Z values, allowing to explore a wide range of fused nuclei.

To span the widest range of N/Z values, both radioactive and stable beams have been used. The beam intensity is strongly reduced by the required high charge state, necessary to reach the required beam energy and to reduce the amount of contaminants. Radioactive beam intensity is ~ 2 order of magnitude below that of stable beams.

The ion beam time structure is pulsed. Each ion burst has, as a first approximation, a gaussian distribution with a Full Width Half Maximum (FWHM) of ~ 3 ns.

The beam arriving on the target is synchronized with the ions accelerating electric field radiofrequency (RF). The RF signal can be therefore used as reference for time measurement.

The main beam characteristics are reported in Tab.3.2.

The analyzed reactions and their characteristic are reported in Tab.3.3. ^{34}Ar, ^{36}Ar and ^{40}Ar ion beams with energies ranging from 12.7 to 13.5 AMeV have

---

[1]Beam intensity in "VAMOS master" trigger configuration (§3.2.1).

Beam	I (pps)[1]	E_{beam} AMeV	ν_{RF} (MHz)
^{34}Ar^{+8}	$\leq 10^6$	13.5	10.6076
^{36}Ar^{+8}	$5 \cdot 10^7$	13.3	10.5230
^{40}Ar^{+9}	$5 \cdot 10^7$	12.7	10.2880
^{40}Ar^{+18}	calibration beam	35.0315	8.5500
^{40}Ar^{+9}	reference beam	12.7	10.2880

Table 3.2 – Ar beams intensity (I), energy (E_{beam}) and RF frequency (ν_{RF}). The necessity of an high beam charge state drastically affects the intensity (12% for ^{40}Ar charge state 8^+ against 6% for 9^+ [132]). The last two beams have been used for calibration purpose and to the set up of the apparatus for the ^{34}Ar beam measurements, respectively.

Beam	E_{beam} (AMeV)	Target	dx ($\mu g/cm^2$)	CN	E_{exc} (AMeV)	E_{rec} (AMeV)	v_{rec} (cm/ns)	N/Z
^{34}Ar	13.5	^{58}Ni	2500	^{92}Pd	2.889	1.844	1.888	1.00
^{36}Ar	13.3	^{58}Ni	300 and 2500	^{94}Pd	2.882	1.951	1.942	1.04
^{36}Ar	13.3	^{60}Ni	330	^{96}Pd	2.919	1.870	1.901	1.09
^{40}Ar	12.7	^{60}Ni	330	^{100}Pd	2.900	2.032	1.982	1.17
^{40}Ar	12.7	^{64}Ni	320	^{104}Pd	2.879	1.878	1.905	1.26

Table 3.3 – Analyzed reactions characteristics. E_{beam}: beam energy, dx: target thickness, CN: compound nucleus obtained by complete fusion of projectile and target nuclei, E_{exc}: CN excitation energy, E_{rec}, v_{rec}: CN recoil energy and velocity in laboratory reference system, respectively, N/Z: compound nucleus N/Z ratio.

been accelerated and impinged onto a $300 \div 2500\,\mu g/cm^2$ thick, self-supporting, isotopically enriched Ni targets (^{58}Ni,^{60}Ni and ^{64}Ni) in order to produce fused Pd nuclei, with mass number varying from 92 to 104. The N/Z of the compound systems ranges from 1.00 (^{92}Pd) to 1.26 (^{104}Pd).

The ^{34}Ar radioactive beam allows to get very close to the p-drip line in forming ^{92}Pd. Depending on model, indeed, the drip line is predicted to be between masses 84 and 89 [133]. In this case the deexcitation properties could show special behaviour. The stable ^{36}Ar beam, coupled to the ^{60}Ni target, allows to make the semi-magic nucleus ^{96}Pd, which has a 50 neutron closed shell. Intermediate Pd isotopes, ^{94}Pd and ^{100}Pd, are provided by ^{36}Ar and ^{40}Ar isotopes coupled with ^{58}Ni and ^{60}Ni targets, respectively.

The beam energy ($\sim$ 13 AMeV) is chosen following the criteria of reducing the preequilibrium effects and having sufficient recoil energy for nuclear charge identification of residues [86].

At this incident energy complete and incomplete fusion reaction mechanisms are both present. Recoil energy criteria should allow to determine whether the observed reactions are mostly complete or incomplete fusion ones [134, 135].

The incident energies for each projectile have been precisely chosen to get the same excitation energy per nucleon of compound nuclei ($\sim$ 2.9 AMeV): in this way the experiment allows to study the thermodynamical properties of different isotopes produced in quite the same conditions of formation and detection.

The target thickness of $300\,\mu g/cm^2$, leading to a mean energy loss of about $\sim$ 0.08 AMeV for the considered residue, had been chosen as compromise between a relatively large number of events and a still sufficient residue velocity for identification.

Due to low intensity of the ^{34}Ar radioactive beam, a ^{58}Ni target thickness of $2500\,\mu g/cm^2$

has been used in order to increase the number of events. For comparison, some runs with ^{36}Ar beam on $2500\,\mu g/cm^2$ ^{58}Ni target have been performed.

The expected fusion-evaporation cross sections with ^{58}Ni, ^{60}Ni and ^{64}Ni target are of the order of $\sim 0.8 \div 1.0$ barn, similar to experimental results for ^{40}Ar+Ni [136] and ^{32}S+^{59}Co [137]. Since for a good study of the different deexcitation channels a statistics of $\sim 10^3$ events per isotope is required, checks on the number of detected residues have been performed during the experiment.

According to statistical GEMINI simulations the entrance window opening between INDRA and VAMOS ($\Delta\theta = \pm 4°$) limits the detection to $\sim 1/3 \div 1/4$ of the produced residues. Therefore three angular positions of the VAMOS spectrometer have been explored ($\theta_{VAMOS} = 0°, 4°, 8°$). We remark that the 8° angular position requires the removal of two INDRA's telescopes, located on $\phi = 0$ plane (Ring 4 and 5, Module 17 and 18), in order not to reduce the VAMOS entrance window. This position is mandatory since it allows to normalize the VAMOS data with the INDRA ones.

3.2 Trigger configurations

The trigger setting is an important issue in performing an experiment, since it allows to perform a first selection on the overall events. Two trigger configurations can be selected on the apparatus: the "physics mode" configuration, in which the system is triggered by physics events, and the "test mode" configuration, in which laser and pulser signals used for stability controls are generated.

During the measurement the beam can be masked before its entrance in the experimental cave, in order to allow stability controls. Typically the beam reaches the INDRA cave during $\sim 98\%$ of a time cycle, delivering a *Beam in cave* signal to INDRA `Selector`, which enables the "physics mode" trigger. For the remaining $\sim 2\%$ of a time cycle it is possible to select, on the INDRA trigger, the sequence of test functions to enable, choosing between the laser and the electric pulser.
The selected sequence is 590 s with beam in cave and 10 s without.

	Elastic diffusion			Fusion reaction
	θ_{pr}^{lab}	E_{pr}^{lab}	$B\rho_{pr}$	$B\rho_{res}$
^{34}Ar+^{58}Ni	1°	458.9	1.01	0.25 ÷ 0.86
	4°	457.7	1.28	
^{36}Ar+^{58}Ni	1°	478.7	1.11	0.31 ÷ 0.85
	4°	477.4	1.09	
^{36}Ar+^{60}Ni	1°	478.7	1.07	0.29 ÷ 0.85
	4°	477.4	1.14	
^{40}Ar+^{60}Ni	1°	507.9	1.14	0.26 ÷ 0.92
	4°	506.4	1.28	
^{40}Ar+^{64}Ni	1°	507.9	1.18	0.31 ÷ 0.87
	4°	506.4	1.22	

Table 3.4 – Magnetic rigidity ($B\rho$) values for elastically scattered projectile nuclei and fusion-evaporation residues. Kinematical relations give the projectile kinetic energy (E_{pr}^{lab}) for each diffusion angle (θ_{pr}^{lab}). The charge state has been obtained according to [111]. $B\rho$ values for fusion evaporation residues emitted between 0° and 4° are given by GEMINI simulation (see §5.2.2). The obtained $B\rho$ values differ more than 10% (VAMOS momentum acceptance).

3.2.1 Physics mode

The "physics mode" allows to acquire physical events if they satisfy some requirements. In particular, constraints can be set on the event multiplicity detected in one or in both detection apparatuses.

During the experiment three different physics triggers have been selected:

VAMOS master & INDRA slave This trigger configuration enables the event acquisition only if at least one particle has been detected in VAMOS. The choice is due to the necessity of selecting fusion events, in which "big" residues are emitted close to the beam direction (GEMINI simulations suggest an evaporation residue angular distribution peaked in the forward direction and up to 30° wide, see §5.2.2).

The VAMOS magnetic rigidity has been selected in order to detect, on the focal plane, evaporation residues, while particles or fragments with a different magnetic rigidity do not reach the focal plane.

This configuration therefore performs a first event selection, removing all the events in which none of the forward emitted fragments or particles (within VAMOS coverage) has the selected magnetic rigidity [2]. In such a way the dead time (see §3.4.3) due to the high INDRA counting rate is reduced: the appropriate choice of magnetic rigidity allows to reject the high flux of elastically

---
[2]We remark that the VAMOS momentum acceptance is $\frac{\Delta B\rho}{B\rho} = 10\%$.
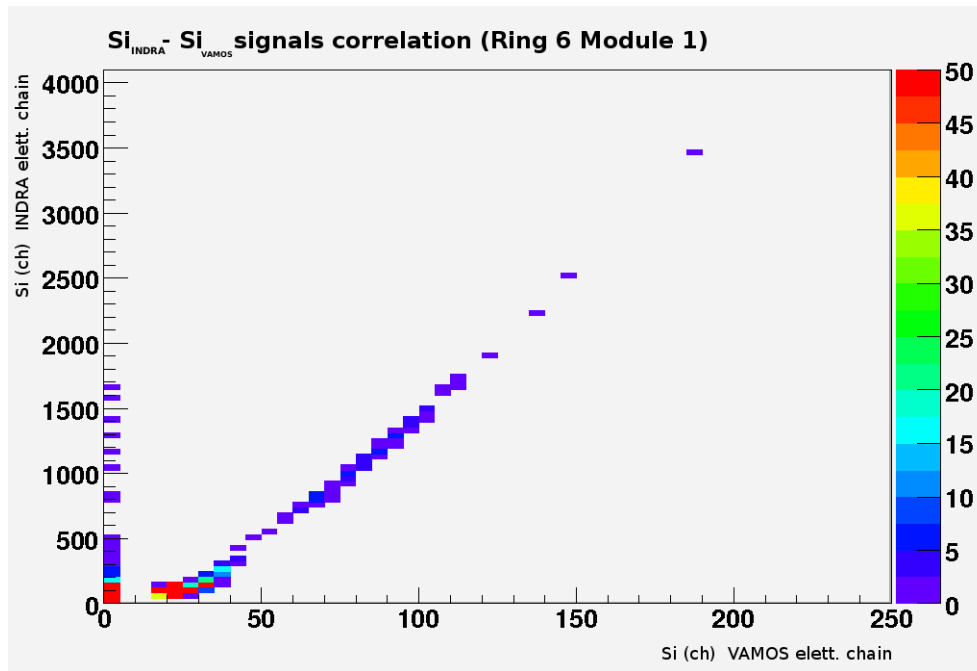
Figure 3.1 – Correlation between an INDRA silicon detector signal treated by VAMOS (on *x* axis) and INDRA (on *y* axis) electronic chains. A linear correlation gives confidence on a good synchronization between the two electronic chains.

scattered projectile nuclei (see Tab.3.4).

From an electronic point of view, when the VAMOS trigger is present, the `event validation` signal (L2 in Fig.2.13) is sent to the *Acceptation des voies lentes* (AVL) input on INDRA Selector (see §2.4.2). If the L2 signal is within the AVL window, INDRA parameters (if present) are also acquired. On the contrary only VAMOS parameters are acquired.

The rate of `event validation` signals and of VAMOS-INDRA coincidences has been monitored during all the experiment.

Special care has been paid to synchronize the AVL window and the L2 signal, by putting appropriate delays on the VAMOS electronic chain. In order to synchronize the two electronic chains, one of the INDRA silicon detector signal is sent and processed by both INDRA and VAMOS electronic chains. The correlation between this two signals assures a good synchronization (see Fig.3.1) of the two electronic chains. This synchronization has been monitored during all the experiment.

INDRA SOLO In this trigger configuration INDRA is master in the acquisition and no conditions are set on the VAMOS signal presence, so that tape recording is

enabled when the selected INDRA multiplicity is reached, independently of VAMOS signals.

Multiplicity $M \geq 1$ This configuration allows to acquire all events where the INDRA multiplicity is, at least, 1. It allows to detect, among others events, elastic events, which will be used in the following analysis to check the beam centering (see §5.1) and to find the *mbarn/counts* conversion factor (see §5.2.3).

Since in the apparatus there is not a Faraday cup, for each reaction INDRA SOLO runs provide a beam intensity estimation, necessary for normalization.

Multiplicity $M \geq 2$ The main difference between this trigger configuration and the previous one is that it forbids the elastic events acquisition, being the target kinetic energy too small to allow the elastically diffused target detection.

Runs realized with this configuration are very useful to determine the detectors Z resolution, being the $\Delta E - E$ spectra cleaner (see §4.2.1) than the one obtained in the $M \geq 1$ configuration.

3.2.2   Test mode

The "test mode" allows to check the stability of the electronics, during the experiment, with a selected number of events and without beam on the target.

During each run laser and electronic pulser generators are regularly enabled by the INDRA trigger, following the required time sequence of the beams delivered by GANIL. Under software command, one can choose different test configurations, which are automatically and successively selected at each beam cycle.

Two test configurations have been used during the experiment: when the beam was masked, the `Selector` enabled, in turns, the laser system and the pulse generators.

We would like to remark that a test event is always accepted and it does not care about the fast and slow INDRA trigger analysis. Physical event acquisition is inhibited.

3.2.2.1   Pulse generators

When the `Selector` enables the pulse generators, a pulse is generated on the 8 output channels of each generator. The pulse amplitude can be adjusted between
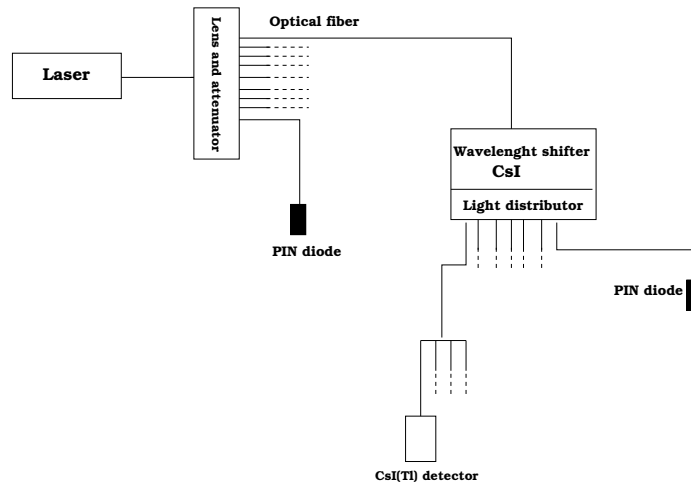
Figure 3.2 – Schematic layout of the laser distribution system. Two PIN diode monitor the laser light amplitude and the CsI wavelength shifter. Their functioning is monitored by pulse generators.

$-10\,V$ and $+10\,V$ with steps of $0.3\,mV$, while the duration is fixed at $6\,\mu s$ [99]. The maximum frequency is $100\,Hz$. There is one generator line for each preamplifier of the ionization chamber, calibration telescope and PIN diodes (see below), while each $300\,\mu m$ silicon wafer shares the same generator signal, thus leading to $120 + 48$ generator channels. VAMOS silicon detector and HARPEE preamplifiers are fired by an INDRA pulser signal during dedicated pulser runs. This control on the electronic stability is performed during all the experiment.

3.2.2.2   Laser system

A simplified description of the light distribution system is presented in Fig.3.2. For a more detailed description refer to [90].

The laser system is equipped with a nitrogen laser, delivering up to 20 pulses per second at a wavelength of $337\,nm$. The UV laser-light is focused and it enters nine UV-quartz fibres. An attenuator (1 to 1/20) allows variations of pulse intensities. One of the nine fibres illuminates a photodiode (PIN diode) which monitors the laser light amplitude. The eight other fibres illuminate a wavelength shifter: a CsI crystal, which shifts the light wavelength to $\sim 550\,nm$. Quartz fibres are mounted on each opposite face of the crystal. One of them illuminates a PIN diode, which monitors the CsI wavelength shifter. The signals of the PIN diode preamplifiers are processed by the same electronics as the one used for silicon detectors, including electronic stability control by pulse generators.

The other optical fibres are coupled perpendicularly to the back face of the scintil-

lators and they illuminate it from a distance of 5 mm, in order to avoid differences due to the surfaces of the crystal. The enlightened surface has a diameter of 2.5 mm. The largest amplitude and the smallest fluctuations of the laser pulse amplitude are obtained at 10 Hz [90].

3.3 VAMOS set up

The low radioactive ion beams intensities, the low CN evaporation residues kinetic energies and the large angular cone in forward direction in which CN evaporation residues are emitted imply the need to physically separate reaction products from beam background.

A magnetic spectrometer, such as VAMOS, thanks to the magnetic field characteristics, deflects, on trajectories depending on particle velocity v and mass/charge ratio (m/Q), charged particles, which have to be detected.

In general, the motion of a charged particle in an electromagnetic field is described by the Lorentz force:

$$\frac{d\vec{p}}{dt} = q(\vec{E} + \vec{v} \wedge \vec{B}) \tag{3.1}$$

where q, $\vec{p}$ and $\vec{v}$ are the charge, the momentum and the velocity of the particle, respectively, $\vec{E}$ and $\vec{B}$ are the electric and the magnetic field, respectively. The electric component gives the acceleration of the particle, while the magnetic component corresponds to the bending. The beam optics is determined by the magnetic field, so that we can assume $\vec{E} = 0$ and consider the bending term only:

$$\frac{d\vec{p}}{dt} = q\vec{v} \wedge \vec{B} \tag{3.2}$$

The "equilibrium trajectory" (or central ray) s_0, with a curvature radius $\rho(s_0)$, described by a particle "p_0" with a momentum $\vec{p_0}$ under the effect of a magnetic field $\vec{B}(s_0)$, is defined by the equal competition between the Lorentz force and the centripetal force, and can be expressed by the relation:

$$B(s_0)\rho(s_0) = \frac{p_0}{q}. \tag{3.3}$$

Every trajectory s travelled by a particle "p" with momentum $\vec{p}$, velocity $\vec{v}$, and position $\vec{r}$ in the laboratory frame, can be described with reference to s_0. Six param-
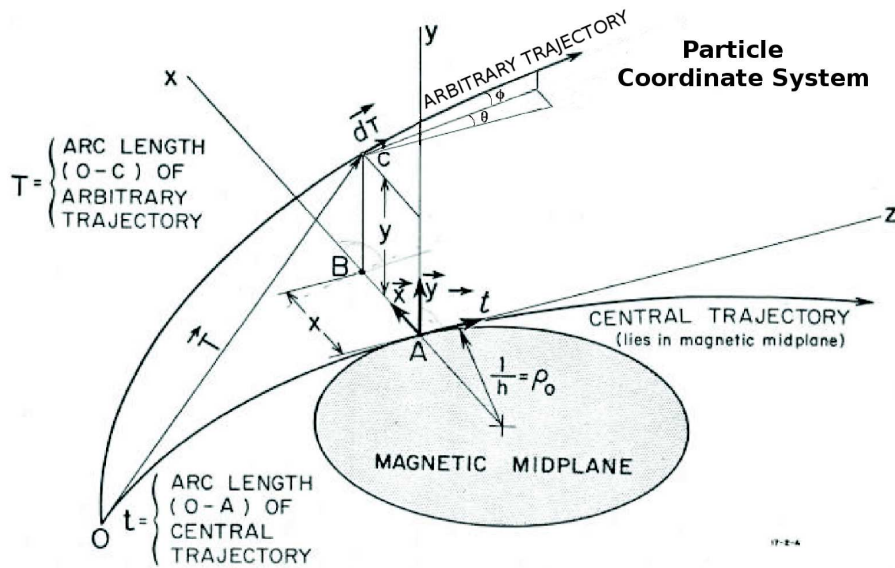
Figure 3.3 – Definition of parameters, relative to the central trajectory (s_0), usefull to describe a generic trajectory s.

eters, all relative to central ray parameters, are used to describe s (see Fig.3.3):

x, y: transverse distances of particle from s_0

θ, ϕ: horizontal and vertical inclination angles

l: path length difference

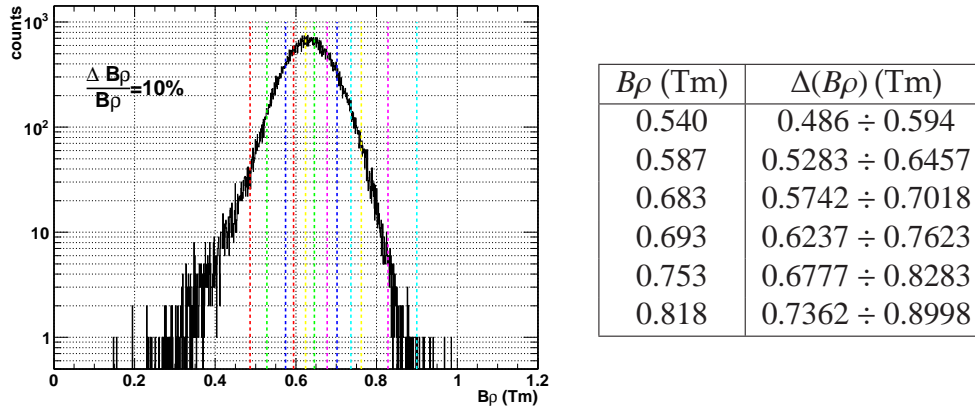δ: *momentum deviation* with respect to the reference particle of momentum $p_0 = qB\rho_0$, defined by the relation

$$\delta = \frac{p - p_0}{p_0} = \frac{B\rho - B\rho_0}{B\rho_0} \tag{3.4}$$

Each reaction product, before its entrance in the spectrometer, can be characterized by its own $B\rho$ value

$$B\rho = \frac{p}{q} = \frac{mv}{q} \propto \frac{A}{q}v \tag{3.5}$$

where A is the particle atomic number. Since the magnetic fields are set so that the particle trajectories split apart according to the different momenta, not only evaporation residues reach the spectrometer focal plane, but all particles whose $B\rho$ value is within the selected $B\rho$ window. For all the particles reaching the focal plane, the position along the focal plane itself, measured by VAMOS, is a measure their A/Q.

At the beginning of the experiment the central trajectory, which intersects the focal plane in the centre, has been identified by selecting a $B\rho$ value corresponding

$B\rho$ (Tm)	$\Delta(B\rho)$ (Tm)
0.540	$0.486 \div 0.594$
0.587	$0.5283 \div 0.6457$
0.683	$0.5742 \div 0.7018$
0.693	$0.6237 \div 0.7623$
0.753	$0.6777 \div 0.8283$
0.818	$0.7362 \div 0.8998$

Figure 3.4 – The evaporation residues $B\rho$ distribution has been obtained by a GEMINI simulation. The six selected $B\rho$ windows ($\Delta(B\rho)$) for the ^{40}Ar+^{60}Ni reaction cover the main part of the expected evaporation residues $B\rho$ distribution, overlapping themselves. The momentum acceptance is $\frac{\Delta(B\rho)}{B\rho} = 10\%$.

to the ^{40}Ar^{18+} beam ($B\rho = 1.1434$ Tm, $E_{beam} = 12.7$ AMeV). The primary beam was directed through the spectrometer with the target off-beam. This optical setting defined the reference trajectory s_0 and the curvature radius ρ_0.

The aim of the experiment was the VAMOS detection of the evaporation residues produced in fusion reactions. GEMINI calculations suggest (see §5.2.2) a $B\rho$ distribution of the evaporation residue ranging from ~ 0.3 Tm to ~ 0.85 Tm. Being the momentum acceptance in the focal plane $\frac{\Delta B\rho}{B\rho} = \pm 10\%$ one single optical setting of the spectrometer allows for a partial transmission of the p/q distribution of produced fragments. Thus, a limited A/q range of fragments can pass through the spectrometer. It imposed to scale the set of magnetic fields several times in order to scan all the magnetic rigidities (and therefore the momenta) of the reaction products of interest. Six $B\rho$ windows, slightly overlapping, have been selected from GEMINI simulations and on the event counting rate during the experiment (see Fig.3.4).
Once selected the first $B\rho$ window, the others have been set varying of $\sim 8.7\%$ the previous value. The $B\rho$ values are set by setting the magnetic field of the two quadrupole and of the dipole. The magnetic field values set have been verified by means of a nuclear magnetic resonance measure. For each $B\rho$ value a VAMOS background measurement has been performed.

In addition, to avoid a bias of the different deexcitation channels, it had been necessary to put the spectrometer into, at least, two different angular positions, to

cover the residues angular distribution. Thanks to the possibility to rotate the spectrometer around the target point, three angular positions have been explored for the reactions with stable beams: 0°, 4° and 8°. For the ^{34}Ar+^{58}Ni reaction, only 0° and 2° have been explored, due to the low statistics.

3.4 Online checks

3.4.1 Silicon detector reverse current

Monitoring the leakage current is a fairly common practice which has been performed during the measurement.
When voltage is applied to a junction detector (reverse biased junction), a current of the order of a microampere [138] is normally observed. The origins of this leakage current are related both to the bulk volume and surface of detector. The leakage current fluctuations affect the energy resolution, introducing a source of noise.
Moreover, the bias voltage to the detector is supplied through a series of resistors, therefore the true bias voltage applied to the junction is reduced from that of the voltage source by the product of the leakage current and the series resistance. If the leakage current is large enough, the drop across the resistor can appreciably diminish the voltage applied to the detector, reducing the depletion voltage. Sometimes it is therefore necessary to raise the voltage, to compensate the leak.

Monitoring the leakage current one can also detect the onset of an abnormal detector behaviour. During steady operation, the leakage should normally maintain a steady value, and any abrupt changing or increasing can indicate a change in detector performance, which may degrade the energy resolution.
Finally, the long-term behaviour of the leakage current is often a useful monitor of the degree of the radiation damage suffered by a given detector. The proper operation of any semiconductor detector depends on the near perfection of the crystalline lattice to prevent defects that can trap charge carriers and lead to incomplete charge collection. The form of the most common irradiation-induced defect is produced by the displacement of an atom of the semiconductor material from its normal lattice site. The vacancy left behind, together with the original atom now at an interstitial position, constitutes a trapping site for charge carriers. When enough of these defects have been formed, carriers lifetime is reduced and the energy resolution of detector is degraded due to fluctuations in the amount of charge lost.

The observed leakage current value during the experiment is ∼ $1\mu A$ with an applied voltage of ∼ 70 V, for each detector.

3.4.2   Spectra control

Experiments in nuclear reactions typically acquire large amounts of data. During the experiment one and two dimensional spectra of the raw as well as derived parameters could be displayed in the on-line acquisition system VISUGAN. Since the data collected were available on disk, it was possible to begin the off-line analysis even while the experiment was still in progress, helping to notice problems and improving the experimental conditions.

An on-line spectra analysis has allowed to control the INDRA and VAMOS electronic chains synchronization and the detectors behaviour, as well as to monitor the acquired statistics.

3.4.2.1   Control on VAMOS-INDRA electronic chains synchronization

The synchronization is monitored by analyzing the correlation between an INDRA silicon detector signal processed by the two electronic chains, as described in §3.2.1 (see Fig.3.1)

Referring to Fig.2.13 we can note that the time distance ($t_{SI-INDRA}$) between the INDRA FAST TRIGGER generation and the VAMOS trigger signal ($L2$) is indicative of the electronic chains synchronization. Fig.3.5 shows a $t_{SI-INDRA}$ spectrum, realized in "VAMOS master" trigger configuration. The Start signal is given by the trigger signal (which is fired by VAMOS), while the Stop is given by INDRA fast trigger signal.   The presence of a single peak gives confidence on the correct synchronization between the two electronic chains. The integral of the spectrum is the number of events in which INDRA detects at least one particle in coincidence with a residue detected in VAMOS.

Fig.3.7 shows the same spectrum for a pulser run. Pulser signal are sent to both VAMOS and INDRA detectors. In this case the Stop signal, given by an INDRA pulser trigger signal, is delayed with respect to the FAST TRIGGER signal generated in physics events, obtaining a spectrum concentrated in the highest TDC channels.

3.4.2.2   Controls on statistic

During the experiment controls on the acquired statistic have been performed. In particular the number of residues detected in VAMOS for each run (i.e a given $B\rho$ value and a given Θ_{VAMOS}) has been monitored and recorded on the logbook, as well as the number of coincidences between INDRA and VAMOS. Since the compound system is created in an excited state, it evaporates particles, therefore the ratio between the number of INDRA-VAMOS coincidence and the number of detected
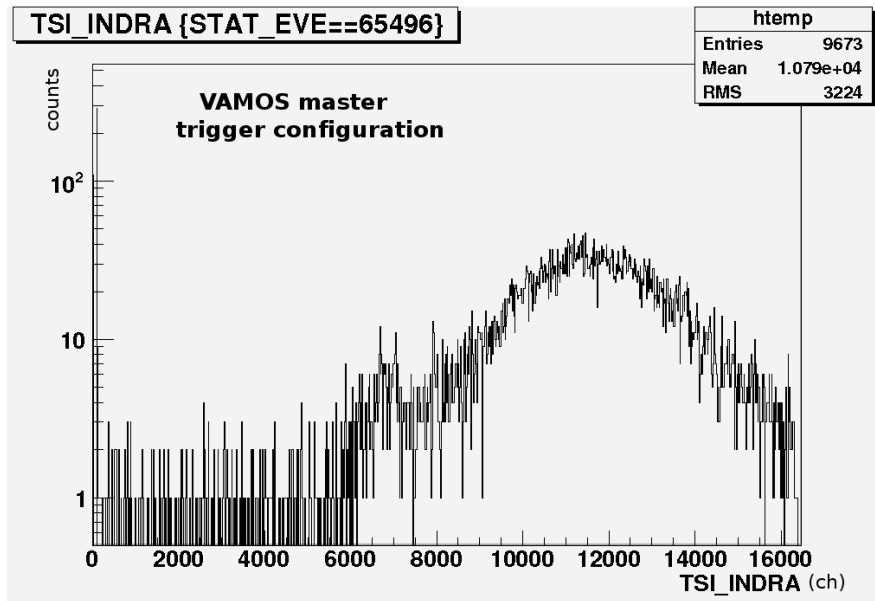
Figure 3.5 – Time distance between the VAMOS trigger signal, obtained by the logic OR of VAMOS silicon detectors signals, and the INDRA FAST TRIGGER signal, obtained by the INDRA signals multiplicity analysis. The number of INDRA-VAMOS trigger signal coincidences is given by the integral of the peak. A peak at ch∼ 6700 is present. The contribution comes from two silicons at the border of the VAMOS silicon wall. Actually we are not able to clearly identify this contribution, but, as can be seen from Fig.3.6, it does not affect the residue region.
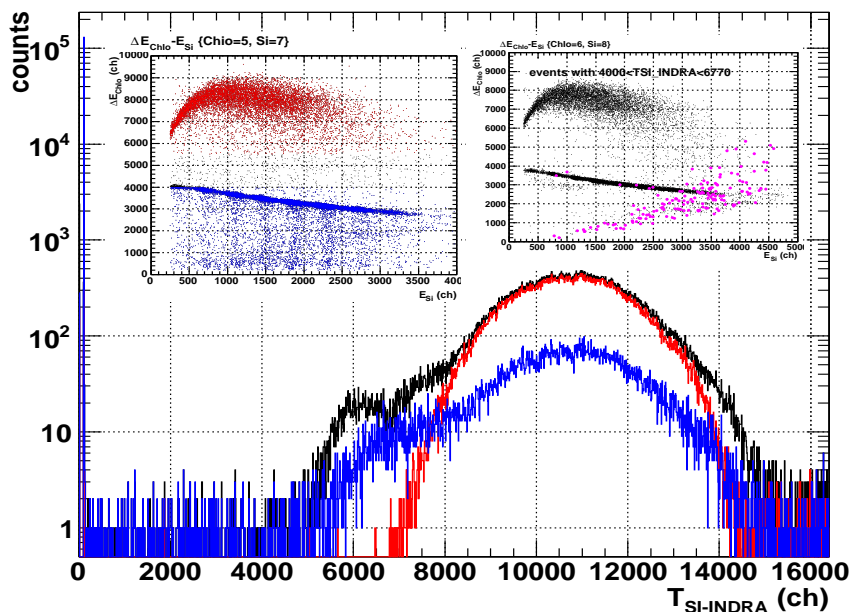
Figure 3.6 – Time distance between the VAMOS trigger signal and the INDRA FAST TRIGGER signal ($t_{S I_I N D R A}$). It is displayed, in black, the total $t_{S I_I N D R A}$ spectrum, in red the residue $t_{S I_I N D R A}$ spectrum and in blue the elastic and light particles $t_{S I_I N D R A}$ spectrum. The three different regions are shown in the left panel. The right panel shows, in red, the events where $t_{S I_I N D R A}$ is ∼ 6700 ch.
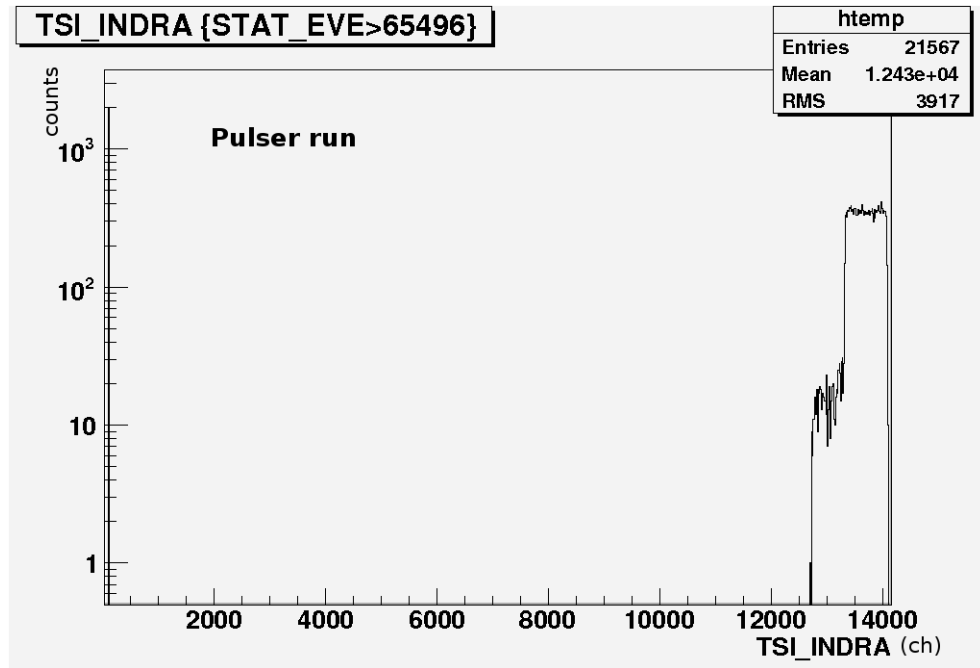
Figure 3.7 – Time distance between the VAMOS and the INDRA trigger signals in case of pulser run.

residues indicates the percentage of events in which at least one of the evaporated particles is detected. This percentage is found to be dependent, as well as on the reaction, on the $B\rho$ and Θ_{VAMOS} values set, as expected.

3.4.2.3 Controls on detectors behaviour

Controls on both VAMOS and INDRA detectors behaviour have been performed. The resolution has been monitored during all the experiment, periodically checking the available spectra ($\Delta E_{ChIo} - E_{Si}$, $\Delta E_{ChIo} - E_{CsI}$ and fast-slow in INDRA and $\Delta E_{HARPEE} - E_{Si}$ in VAMOS) for all detectors.

In Fig.3.8 typical VAMOS $\Delta E_{HARPEE} - E_{Si}$ spectrum is displayed. The Bragg peak is clearly identifiable at high ΔE values. Each pad is related to a segment of the ionization chamber HARPEE, that means to different impact point distance from the reference trajectory. Depending on the $B\rho$ value different segments of HARPEE are the most enlightened.
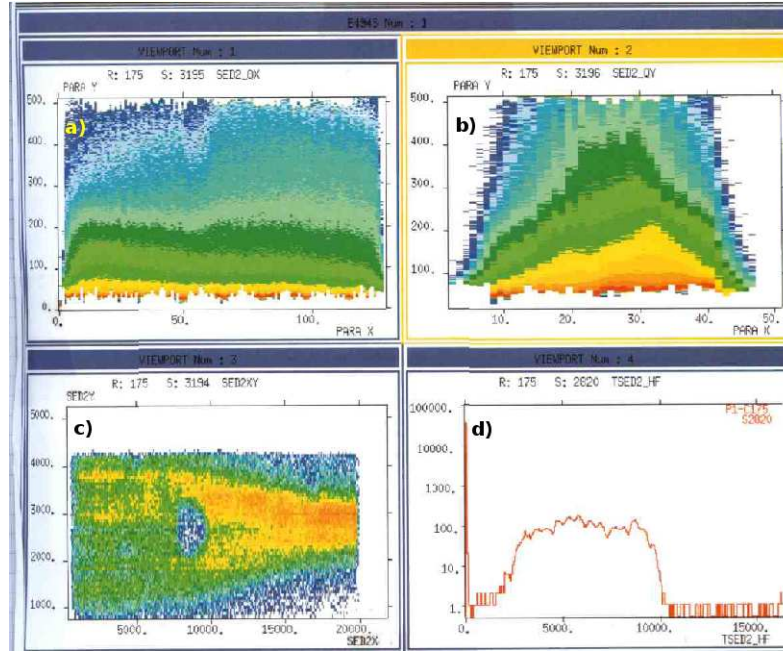A projection on the ΔE axis allow to have a rough estimation of the evaporation residues statistics.

Time signals of both the apparatus have been checked.
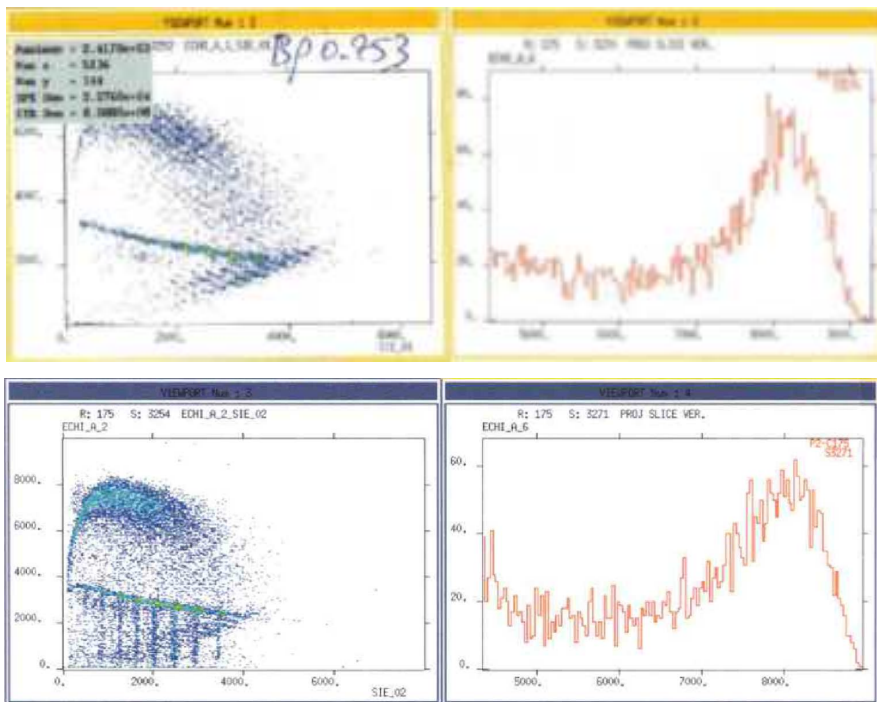
Figure 3.8 – Online spectra obtained for ^{40}Ar+^{64}Ni reaction. The selected $B\rho$ is 0.753 Tm and the VAMOS angular position is Θ_{VAMOS} = 0°. On left side: typical VAMOS $\Delta E_{HARPEE} - E_{Si}$ spectra (in channels) obtained by online analysis. ΔE and E signals are given by a segment of HARPEE and its corresponding silicon detector respectively. On right: ΔE_{HARPEE} projection. The integral of the peak corresponds, in a first approximation, to the number of detected residues.
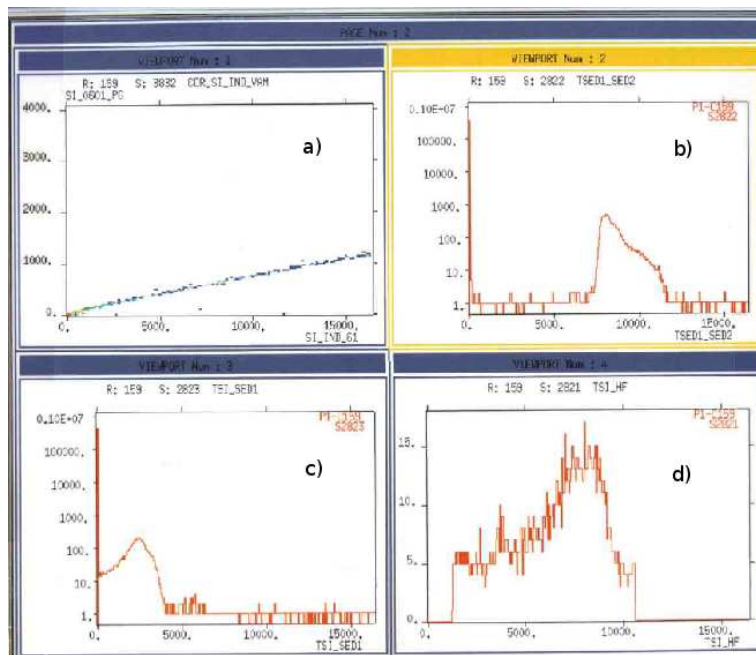
Figure 3.9 – Online controls on VAMOS time signals for the ^{40}Ar+^{64}Ni reaction in Θ_{VAMOS} = 0°, $B\rho$ = 0.693 Tm configuration.

Figure 3.10 – Secondary electron detectors signals for the ^{40}Ar+^{64}Ni reaction in $\Theta_{VAMOS} = 0°$, $B\rho = 0.693$ Tm configuration. a) and b): measured charge on a strip ("PARAY"), expressed in channels, versus the strip number ("PARAX") in the x and y wire plane, respectively. c): measured charge on strip y ("SED2Y") versus strip x ("SED2X"). d): time distance between the second SED signal and the RF signal.

Panel a in Fig.3.9 is an example of the correlation between INDRA and VAMOS electronic chain and it is obtained as previously described. In the remaining panels VAMOS time signals, related to particles time of flight, are shown. In panel b the *Start* and *Stop* signals are given by the first and the second SEDs respectively. In panels c and d the *Start* is given by the VAMOS trigger while the *Stop* by the first SED (opportunely delayed) and the RF signal respectively. In the three last panels a peak related to physical events is present. The monitor of the position of the peaks during the measurement checks the electronic stability.

In Fig.3.10 raw SED's signals are shown. In the upper part the measured charge on a strip versus the strip number in the x and y wire plane are plotted. Since secondary electrons produce a charge distribution on the strip a further processing is necessary to identify the impact position of the incident ion. For this reason each point in the measured charge on strip y versus the measured charge on strip x plot (panel c) does not represent a particle impact point position. The time distance between the second SED signal and the RF signal is shown in panel d).

INDRA $\Delta E_{Si} - E_{CsI}$ spectra (Fig.3.11) are useful to monitor the detectors status and resolution. The spectrum, obtained in INDRA SOLO $M \geq 1$ trigger config-
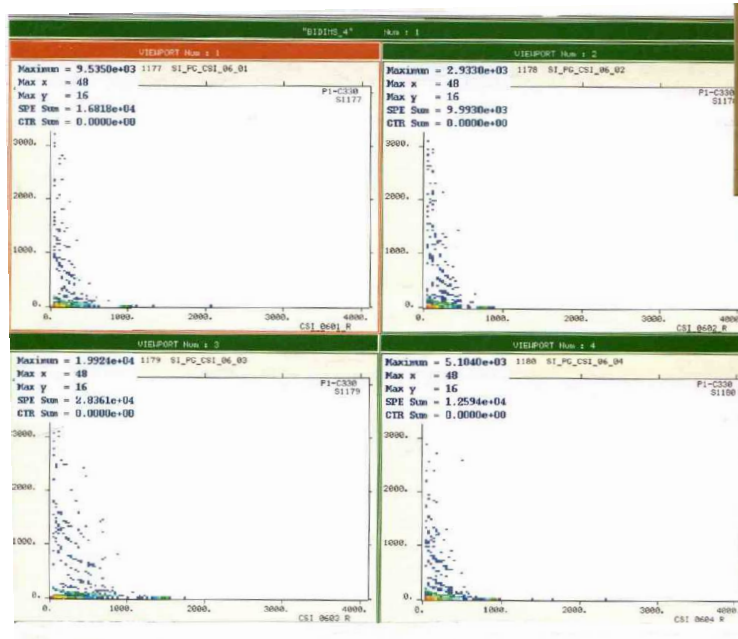
Figure 3.11 – Online INDRA $\Delta E_{Si} - E_{CsI}$ spectra obtained for the ^{34}Ar+^{58}Ni reaction in INDRA SOLO $M \geq 1$ trigger configuration. The detectors are located at $14° \leq \theta \leq 20°$ (ring 6) and cover $\Delta\phi = 15°$ in the $15° \leq \phi \leq 75°$ region.

uration, shows a good Z resolution even if the online presentation is compressed. Energetic fragments with a charge up to $Z \sim 7$ are detected in ^{34}Ar+^{58}Ni reaction.
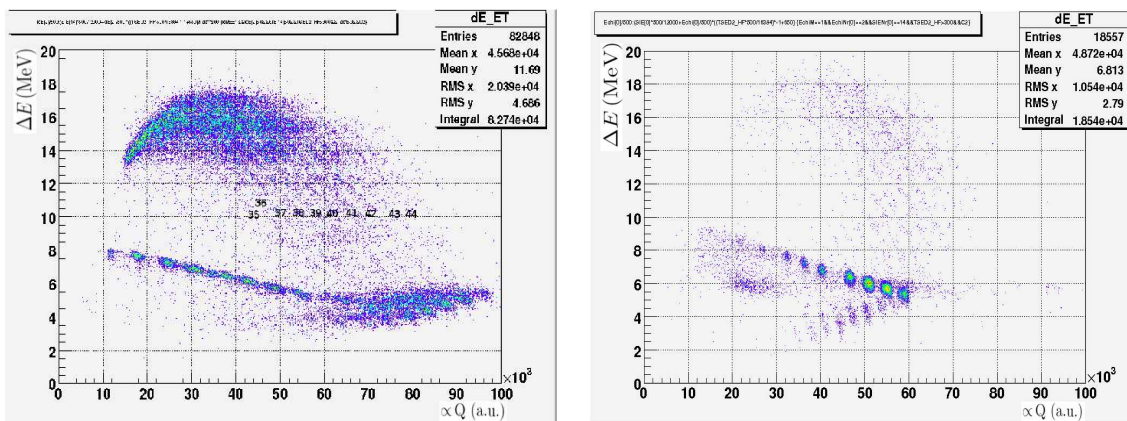

Figure 3.12 – $\Delta E_{HARPEE} vs Q$ spectrum. The ΔE values have been roughly calibrated in MeV. Different residues charge state are well separated and they can be identified in the descending part of the Bragg peak. The Bragg peak presence depends on the HARPEE pressure, that is 25 mbar and 15 mbar in first and second panel respectively. The charge state value has been obtained plotting the particle total energy E and the particle time of flight (t) product (Et), which is proportional to $B\rho dQ$, where d is the flight path. Being $B\rho$ and d almost constant, $Et \propto Q$. The data are relative to ^{36}Ar+^{58}Ni reaction ($\Theta_{VAMOS} = 0°$, $B\rho = 0.693$ Tm)
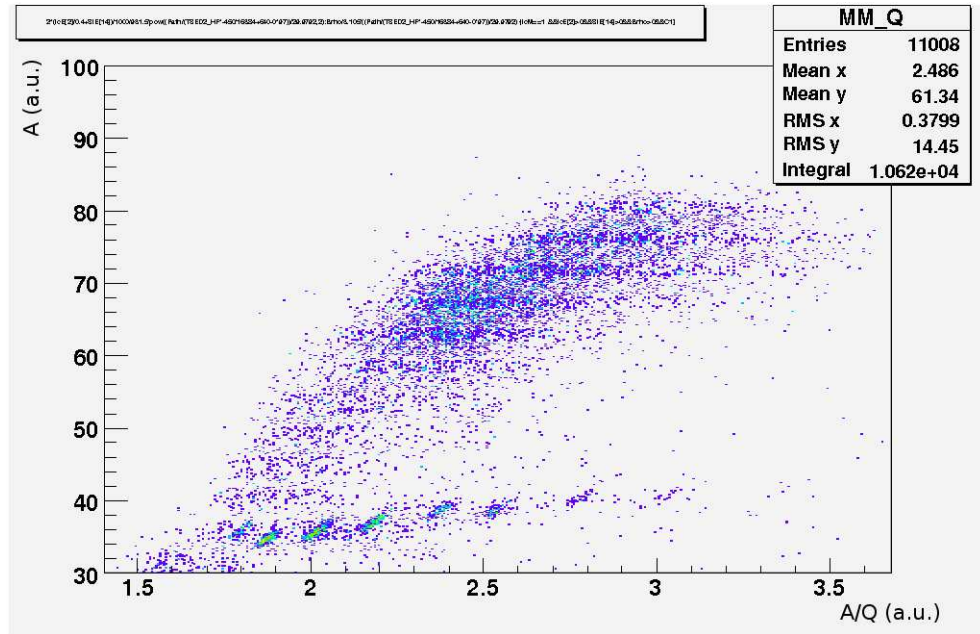
Figure 3.13 – *A* vs. *A/Q* correlation of fusion evaporation residue detected around 0°
($\Delta\theta_{VAMOS} = \pm 4°$).

An off-line analysis, performed during the experiment, has allowed to sum different runs and to perform a rough calibration. A typical ($\Delta E_{HARPEE} - Q$) VAMOS spectrum is displayed in Fig.3.12: the different residues charge states are well separated and a good charge resolution, up to Z close to the residue charge, is evident.

A mass versus mass/charge state (*A vs A/Q*) spectrum has been obtained plotting the ratio between the total energy and the square of the fragment residue velocity versus the ratio between the $B\rho$ value and the fragment velocity, such as in Fig.3.13. Different *A/Q* ratio are separated from each other, allowing, once known the mass number of a particle, to determine its charge state.

Off-line INDRA $\Delta E_{Si} - E_{CsI}$ spectra, shown in Figs.3.14(a) and (b), have been obtained in "VAMOS master" trigger configuration: fragments with Z up to ~ 7 are detected in coincidence with evaporation residues and a good isotopic separation is obtained for Z = 1 and Z = 2. The INDRA CsI(Tl) crystal multiplicity is shown in Fig.3.14(c). The mean detected multiplicity is 6 for ^{40}Ar+^{60}Ni reaction and $\Theta_{VAMOS} = 4°$, but the distribution extends from 1 to ~ 12 particle per event in coincidence with an evaporation residue.

A CsI(Tl) scintillator spectrum is shown in Fig.3.15: a good isotopic resolution for Z = 1 and Z = 2 is obtained, allowing a light charged particles mass identification.
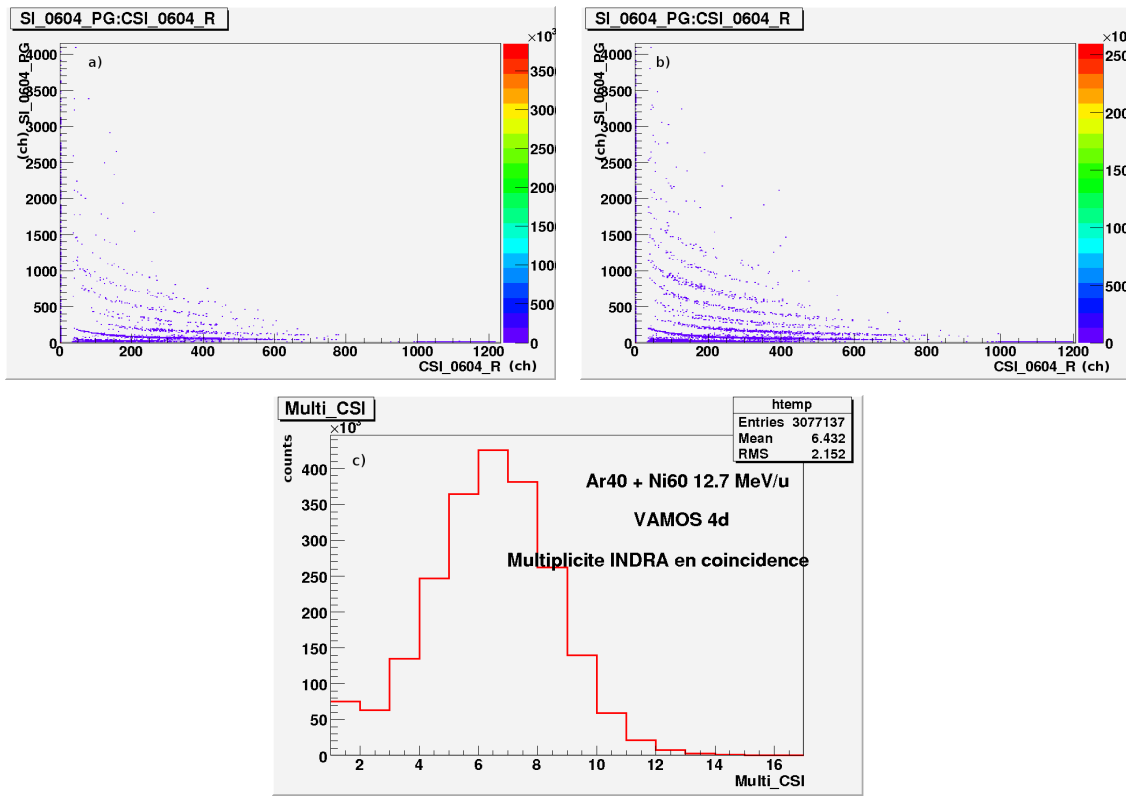
Figure 3.14 – INDRA $\Delta E_{Si} - E_{CsI}$ spectra (in channels) and INDRA CsI(Tl)s multiplicity obtained for the ^{40}Ar+^{64}Ni reaction in VAMOS master trigger configuration (i.e. particles detected in INDRA are in coincidence with at least one fragment detected in VAMOS). The VAMOS angles are Θ_{VAMOS} = 0° and 4° in panels (a) and (b-c), respectively.
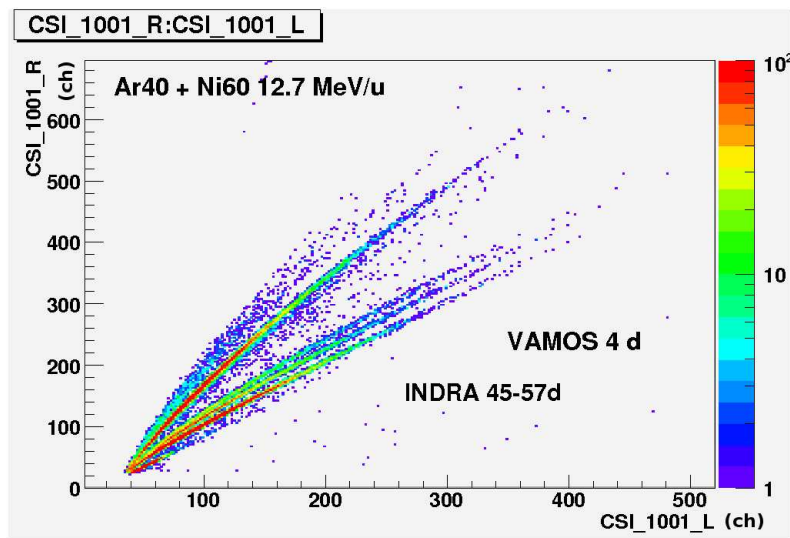

Figure 3.15 – INDRA CsI(Tl) fast-slow correlation obtained in ^{40}Ar+^{60}Ni reaction. The detector lies in the 10th ring, covering 45° ≤ θ ≤ 57°. Θ_{VAMOS} is 4°.

3.4.3   Dead time check

The dead time is the time interval during which the acquisition system acquires the measured parameters. During this time window the system is inhibited and all new events are lost.

The dead time is an important parameter to check during the experiment because it limits the counting rate.

In the "VAMOS master" trigger configuration the dead time is mainly due to the INDRA acquisition, which inhibits any further VAMOS trigger (see Fig.2.29) during its encoding.

Obviously in "INDRA SOLO" trigger configuration the dead time is due to the INDRA encoding and acquisition time.

INDRA electronic system is provided by some internal electronics (pulse generators and a series of scalers) to monitor the dead time.

gene_direct: it is an internal clock with a period of $\sim 1/185\,\mathrm{s}$. The scaler counts the number of pulse delivered during a run: such value gives the run period.

dead time generator: it generates the internal clock output if the INDRA trigger is inhibited (during the encoding). The `Selector` is in "physics mode". The total number of pulses generated during a run is proportional to the dead time of the encoding procedure.

gene_marque: it generates the internal clock output if the `Selector` is in "test mode". The total number of pulses during a run is related to the time interval devoted to stability controls.

The dead time percentage can be obtained by combining these values:

$$t_{dead\_time}(\%) = \frac{dead\ time\ generator}{gene\_direct - gene\_marque} \tag{3.6}$$

The dead time percentage has been monitored during the experiment and kept around 20% (never greater than $\sim 40\%$.) by adjusting the beam intensity.

p			
INDRA	Ring 4 − 5	$30^{(3)}$ mbar	
	Ring 6 − 7	50 mbar	
	Ring 8 − 12	30 mbar	runs up to 292
		$20^{(4)}$ mbar	runs from 298
	Ring 13 − 17	30 mbar	
HARPEE	25 mbar		runs up to 281
	15 mbar		runs from 282
SED1		SED2	
p (mbar)	V (V)	p (mbar)	V (V)
7.0 ÷ 7.1	470 ÷ 510	7.0 ÷ 7.2	470

Table 3.5 – Gas pressure values set in INDRA ionization chambers, HARPEE and SEDs. For the two SEDs also the voltage values have been reported.

3.4.4   Pressure controls

During all the measurements the gas pressure stability in the ionization chambers has been monitored, since a pressure variation requires a new energy calibration of the ionization chambers.

The gas pressure in INDRA ionization chambers has been set in order to obtain a good charge resolution in $\Delta E_{ChIo} - E$ spectra. Increasing the gas pressure, the resolution gets better, but simultaneously the energy threshold for particle punching through the ionization chamber increases. The gas pressure values, listed in Tab.3.5, are a good compromise between these two effects.

HARPEE gas pressure has been set in order to be able to identify the Bragg peak region and to have, in this region, the best Z resolution.

The SEDs operating pressure is ∼ 7 mbar.

3.5   Calibration runs

During the experiment several calibration runs have been performed:

Pedestal runs: The QDC measured values are acquired without any particle firing the detectors. These runs permit to identify the pedestal postion on each QDC and on CsI ADCs and thus to determine the 0 MeV position on the energy scale.

---

[3]The gas pressure has not been set to the nominal value (50 mbar) due to gas regulator problems.
[4]Gas leakage problems have required to decrease the gas pressure.

Figure 3.16 – VAMOS silicon detectors energy spectra in pulser runs. A pulser signal is sent to each silicon detector preamplifier, varying the amplitude pulse signal in order to span all the QDCs range.

α **source and** ^{40}**Ar+Au runs:** They allow to obtain at least two energy calibration points, one from the known α energy and one from the known elastic scattered projectile energy in INDRA detectors.

Ar beams without target runs: The Ar beam is directly sent into the spectrometer, on which the beam $B\rho$ value had been set, to obtain an energy calibration point for HARPEE detector.

Pulser runs: a pulser signal is sent to HARPEE and silicon detector preamplifiers in order to get the mV/ch calibration factor (Fig.3.16). The INDRA detectors are fired by the INDRA pulser, when the trigger is set in "test mode", thus they do not require dedicated pulser runs.

Time calibrator runs: Time calibrator signals, with a known period, are sent to all the TDC used in the electronic chains. It allows to determine the ch/ns calibration factor for each TDC.

HARPEE pulser: Pulser signals, with known and variable amplitude, are sent to each HARPEE preamplifiers, in order to verify the response linearity.
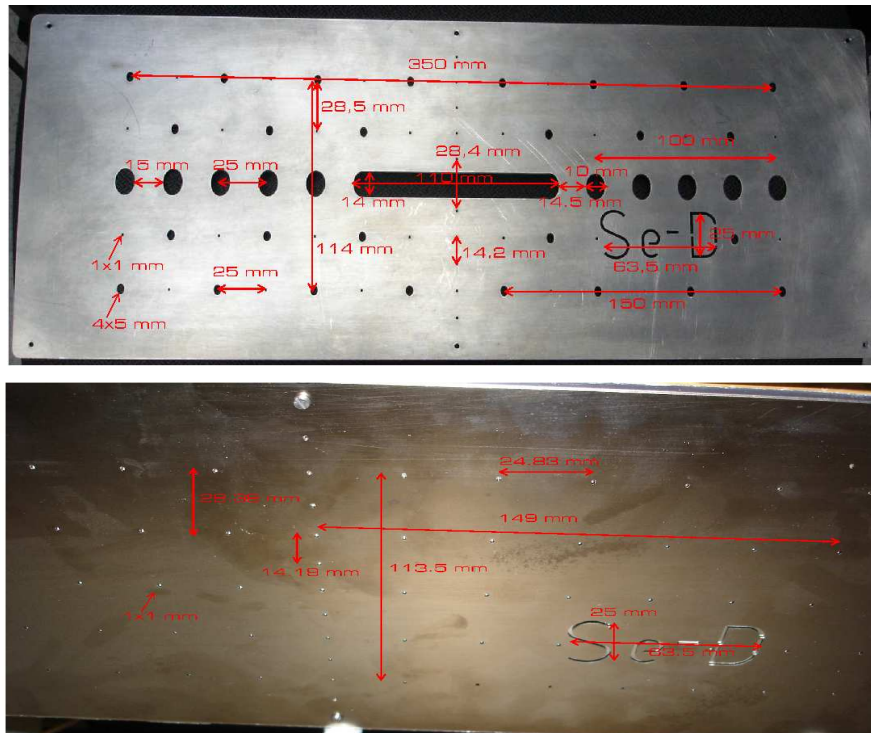
Figure 3.17 – Geometric configuration of two aluminium masks. The calibrated holes allow
to select given trajectories, mapping the SED surface.

## 3.5.1   SEDs position calibration (SED cartographie)

Unlike conventional gas detectors, the ionization in SEDs is not produced by the
incident ion but by secondary electrons. Due to their low mass and energy, they
undergo a very strong straggling in crossing the entrance foil[5]. As a consequence
a charge distribution is obtained on the strips, from which the position has to be
extracted.

Position tests were made at the beginning and at the end of the measurement. Fis-
sion fragments coming from a Cf source had been used, being the collected charge
with α particles to low for an accurate position measurement [139]. Position cal-
ibration was performed using an aluminium mask (Fig.3.17) located just behind
($2 \div 3$ cm) the emissive foil. The calibrated holes were placed to select a given and
known trajectory in order to map all SED's surface. The position of the image of
each hole on the SED was extracted by a charge-weighted center of gravity calcula-
tions [112]. The image of this mask can be seen in Fig.3.18(c).

Localization tests have been made also removing the magnet which ensures the fo-
cusing of the electrons moving towards the low pressure gas chamber. The resolu-

---

[5]For 10 keV electrons going through 0.9 mm Mylar, the angular straggling and the energy loss are
around 15° and 3.1 keV, respectively [139].

tion on impact position gets worse as can be seen comparing Fig.3.18 and Fig.3.19. Each calibration is valid only for a given voltage applied to the carbon foil and a given magnetic field set (V_0, B_0).
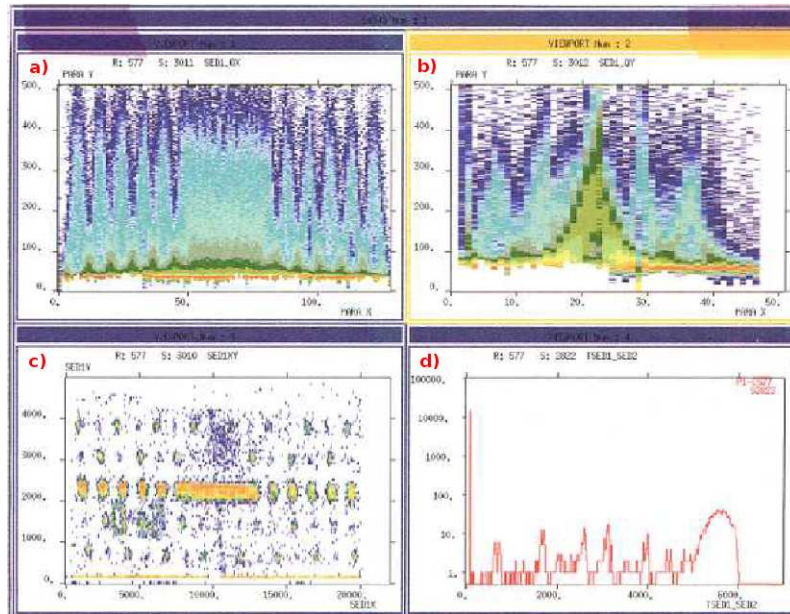
Figure 3.18 – SED position calibration. a,b) measured charge on a strip versus the strip number in x and y wires plane, respectively. c) Image of the mask. d) Measured particle time of flight between the two SEDs.
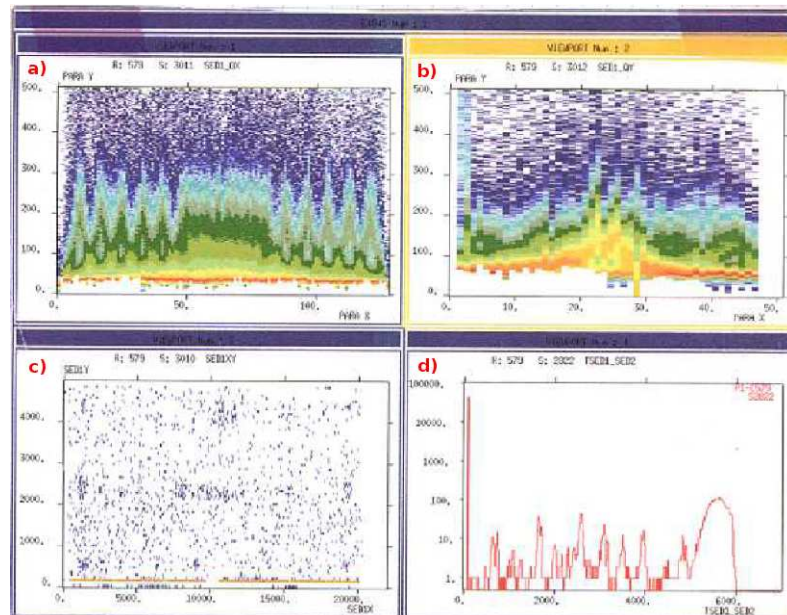
Figure 3.19 – SED position calibration performed without the electron focusing magnetic field. With respect to Fig.3.18 the measured charge distribution is more spread: the obtained mask image has no resolution.

Chapter 4

Preliminary data analysis

4.1 Raw data reconstruction

A *raw* event is a list of acquisition data parameters characterized by the same event number. The events reconstruction consists in the analysis of the acquired parameters in order to reconstruct physical particles, transforming list of hit detectors into list of particles. A *reconstructed event* is characterized by the event number and the particles multiplicity, while each particle is characterized by the identification number of the hit telescope and by the energy and time marker signals of each fired detector.

In previous INDRA campaigns [140–143], the event reconstruction have been performed by `KaliVeda` [144]. `Kaliveda` is an object oriented data analysis framework based on `ROOT`, whose main purpose is to provide simulation and analysis tools for the INDRA charged particle multidetector .

On the occasion of the present experiment, where INDRA is coupled with VAMOS, `KaliVeda` has been implemented in order to reconstruct also the VAMOS data.

While the INDRA analysis tools are well tested, checks on the VAMOS reconstructed data have been performed to verify the events reconstructions accuracy. Some VAMOS spectra have been generated and compared with the ones realized, with raw data, during the measurement (see §3.4.2). Moreover a comparison between the residues statistics deduced from the reconstructed VAMOS spectra and the one estimated during the measurement has been performed. The obtained VAMOS spectra and the residues statistics are in agreement with the ones obtained during the acquisition (see, as example, Figs.4.1 and 4.2), giving confidence in INDRA and VAMOS events reconstruction procedure.

The following data analysis will be focused on INDRA data, while the VAMOS
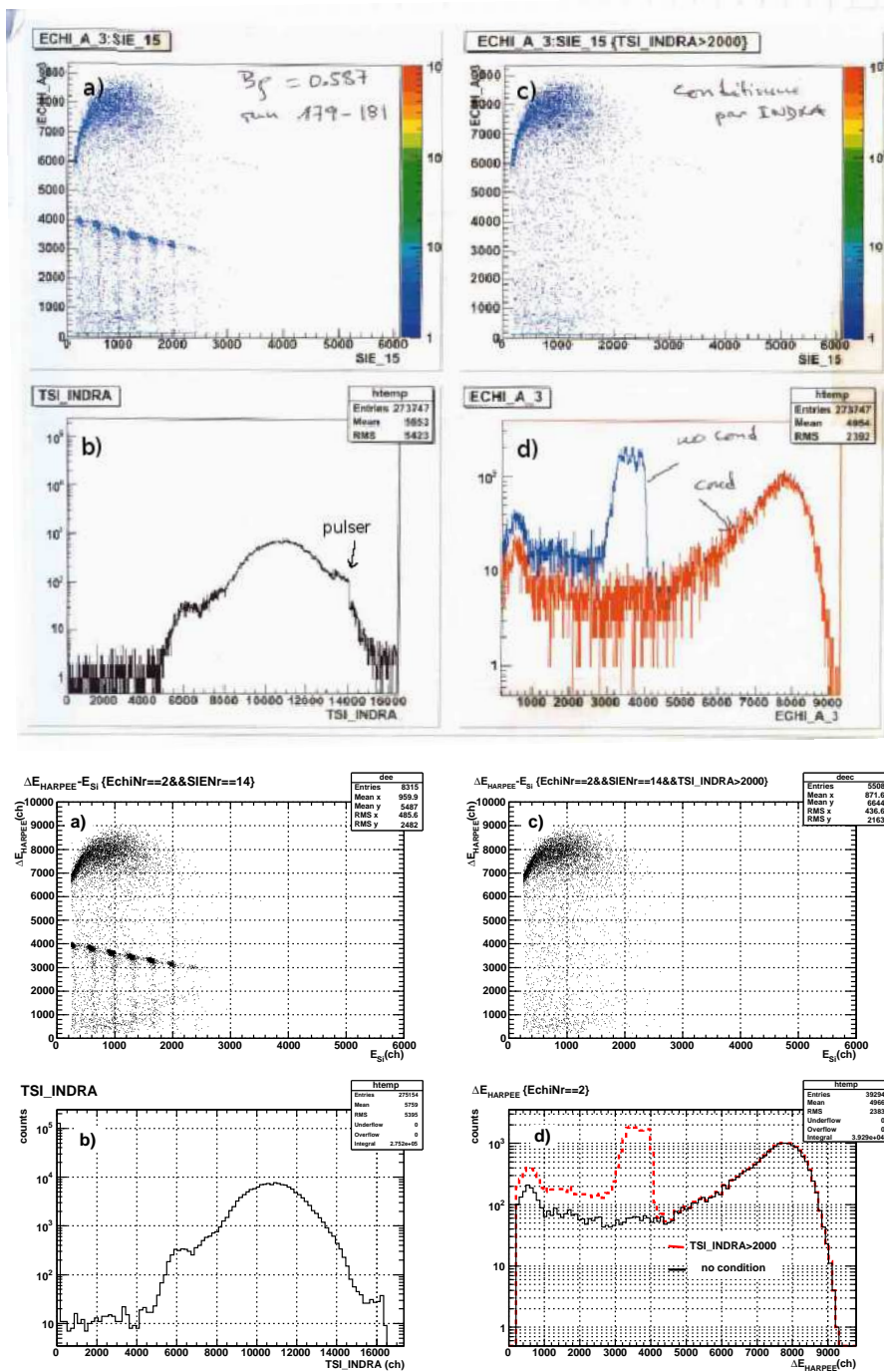
Figure 4.1 – Comparison between online spectra (upper part) and spectra obtained by "reconstructed events" for ^{40}Ar+^{64}Ni reaction ($B\rho = 0.587$ Tm, $\theta_{VAMOS} = 0°$). a) VAMOS $\Delta E_{HARPEE} - E_{Si}$ spectrum; b) Time distance between VAMOS and INDRA trigger signals (TSI_INDRA). In the online spectrum a peak around $ch \sim 14000$ related to pulser events is present. The offline spectrum is, instead, concerned only to physics events. c) $\Delta E_{HARPEE} - E_{Si}$ spectrum with the condition of a short time distance between the two apparatuses trigger signals; d) ΔE_{HARPEE} projection of the $\Delta E_{HARPEE} - E_{Si}$ spectra in a) (red) and c) (black). The constraint on TSI_INDRA allows to reject the elastic contribution.
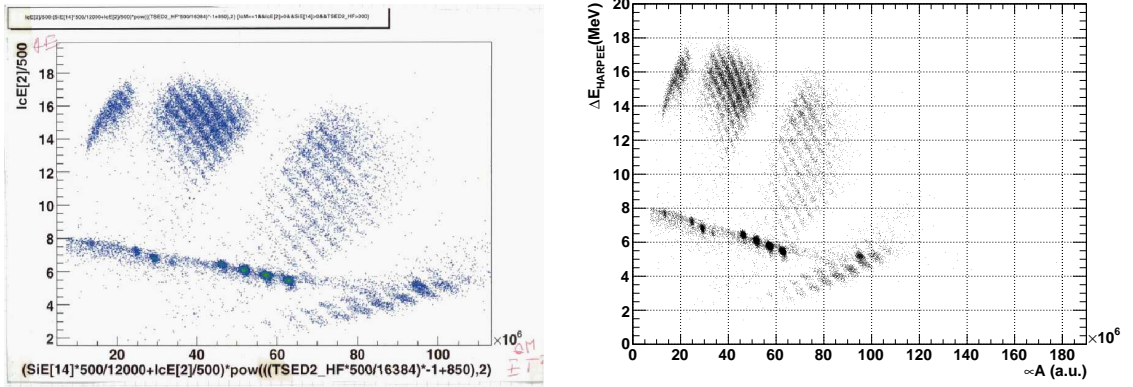
Figure 4.2 – Online and offline ΔE_{HARPEE} vs. A correlation for ^{40}Ar+^{60}Ni reaction ($B\rho$ = 0.693 Tm, θ_{VAMOS} = 0°). The ΔE value has been roughly calibrated in MeV. The A value is obtained by plotting the total energy (E) and the square of time of flight (t^2) product (Et^2): being the flight distance constant for a given HARPEE segment, $Et^2 \propto A$.

data analysis will not be performed in this work.

4.2 INDRA $\Delta E - E$ and "fast-slow" correlations

The study of the N/Z level density parameter dependence requires fragments and light particles mass and charge identifications over a wide energy range. INDRA multidetector, thanks to its structure constituted by telescopes, i.e. different detection layers, allows to perform the identification in mass A and charge Z of the detected particles through $\Delta E - E$ technique, or through the two components of the scintillator light ("fast-slow").

The CsI(Tl) scintillator output has, indeed, two light components (see §2.1.3) which, integrated in two different gates, acquired separately and plotted one versus the other, give rise to a "fast-slow" correlation.

The $\Delta E - E$ method requires that the incident particle punches through at least the first detection layer, while the "fast-slow" method requires the particle to be detected in the CsI(Tl) scintillator. The latter method can be therefore applied only to the most energetic light particles.

The $\Delta E - E$ correlations are built between the ionization chamber and the silicon detectors signals ($\Delta E_{ChIo} - E_{Si}$) and between the silicon detector and the fast [1] component of the CsI signals ($\Delta E_{Si} - E_{fast}$) depending on the polar detector angle.

---

[1] The *fast* component is directly related to the energy deposited in the crystal.

The specific energy loss $(-\frac{dE}{dx})$ for charged particles in a given absorber, with density ρ and charge and mass respectively Z_T and A_T, is described by the *Bethe formula* [138]:

$$-\frac{dE}{dx} = 4\pi N_A r_e^2 \rho m_e c^2 \frac{Z_T}{A_T} \left(\frac{Z}{\beta}\right)^2 \left[ln\left(\frac{2m_e c^2 \beta^2}{I(1-\beta^2)}\right) - \beta^2 \right] \tag{4.1}$$

where $r_e = \frac{e^2}{4\pi\epsilon_0 m_e c^2}$ is the classical electron radii and m_e the electron rest mass. The parameter I represents the average excitation and ionization potential of the absorber. Z and β are the charge state and velocity of the incident ion, respectively.

Eq.4.1 takes into account interactions between the incident ion and the electrons of the absorber, neglecting the interactions with the absorber nuclei, which are significant just at the end of the particle track. It is generally valid for different types of charged particles provided their velocity remains large compared with the velocity of the orbital electrons in the absorbing atoms.

In non-relativistic limit ($\beta \to 0$), eq.4.1 becomes:

$$-\frac{dE}{dx} = C_1 \frac{m_e Z^2}{\beta^2} ln(C_2 \frac{\beta^2}{m_e}) \tag{4.2}$$

and, neglecting the logarithmic β dependence,

$$-\frac{dE}{dx} \approx \frac{Z^2}{\beta^2} \propto \frac{Z^2 A}{E} \tag{4.3}$$

where E is the incident particle kinetic energy and A its mass.

The specific energy loss, for a given incident energy E, presents a relevant dependence from the incident particle charge Z and a lesser one from its mass A. Therefore a $\Delta E - E$ correlation presents the typical Z edges as shown in Fig.4.11(a), and, if the ΔE energy resolution is sufficiently good, also the A dependence can be pointed out.

The response of CsI(Tl) scintillators has a non-linear dependence on the energy of the incident particle, and, for a given energy, the light output depends on the type of the particle [94–97].

The differential light output per unit path length expression is given by [94,95]:

$$\frac{dL}{dx} = S \frac{\frac{dE}{dx}}{(1 + KB\frac{dE}{dx})} \tag{4.4}$$

where S and KB are the scintillation efficiency and the quenching factor, respectively. $\frac{dL}{dx}$ is then related to the specific energy loss and therefore it depends on Z and A of incident particle, allowing a particle charge and mass identification by specific pro-
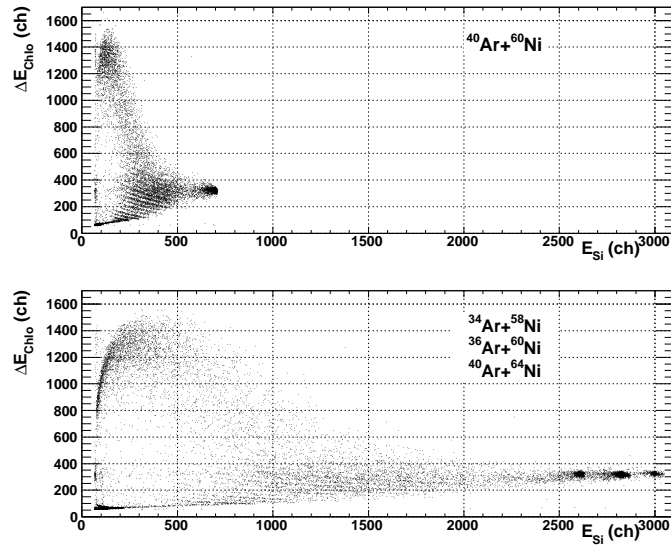
Figure 4.3 – $\Delta E_{ChIo} - E_{Si}$ spectra obtained in INDRA SOLO $M \geq 1$ trigger configuration. For a fixed incident energy the elastic peak positions are related to the silicon depletion voltage: in ^{40}Ar+^{60}Ni reaction the diffused projectile energy (E^{el}_{proj}) is ~ 500 MeV, corresponding to channel ~ 700. In ^{34}Ar+^{58}Ni, ^{36}Ar+^{60}Ni and ^{40}Ar+^{64}Ni reactions $E^{el}_{proj} \sim 450$, ~ 470, ~ 500 MeV, respectively, corresponding to channels between 2500 and 3000. This shift can be attributed to a silicon depletion voltage shift.

cedures.

The $\Delta E - E$ and "fast-slow" spectra analysis allow to check the detector performances and, as a first approximation, the preamplifier (where present) and amplifier gains stability. $\Delta E - E$ correlations have been realized for both "high gain" and "low gain" signals.

4.2.1 Detectors stability and performances

To have good $\Delta E - E$ and "fast-slow" correlations it is necessary to check the detectors status and, qualitatively, their stability during the measurement. Moreover it permits to have a first estimation of Z and A resolutions.

Forward detectors, located at polar angles smaller than the grazing angle of the analyzed reaction (see Tab.5.2), are fired by intense elastically scattered projectile nuclei (Rutherford scattering) and thus are more subject to radiation damage. Radiation damage could modify their response, so that they have been monitored during the measurement. Runs acquired for time to time during the measurement campaign provide a time evolution information on the detectors status.
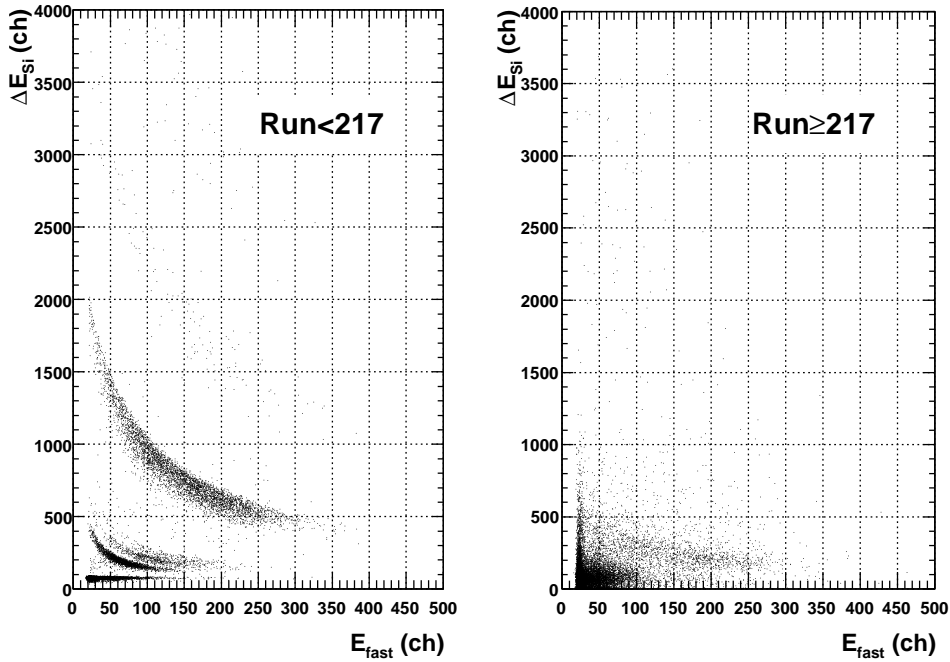
Figure 4.4 – The silicon polarization is responsible of the quick migration of the carriers produced by the passage of a particle in the n-p junction. A decreasing in the applied bias degrades the detector resolution.

First of all a correlation analysis allows to point out problems on silicon depletion voltage, as shown in Figs.4.3 and 4.4. The shift of the elastic peak (whose energy is fixed and known) in the first case and the absence of Z resolution in the second one suggest a shift of the silicons depletion voltage, which have to be corrected during the energy calibration procedure. Fig.4.5 highlights a problem on an electric contact between the silicon wafer and the HV supply.

Some abnormal functioning of the detectors have been pointed out, such as in Fig.4.6, where no low energetic fragments are present in the detector spectra contrary to what is observed in the adjacent detectors, probably due to high silicons thresholds. The loss of such particles must be taken into account in further analysis.

A monitor of the electronic chains stability of silicons and ionization chambers, in particular of preamplifier and amplifier gains, can also be performed by the analysis of $\Delta E_{ChIo} - E_{Si}$ matrices. Comparing, for each detector, the Z edge positions on the $\Delta E - E$ spectrum obtained for different runs a rough idea of the detector and its electronic stability can be obtained. Fig. 4.7 shows a Z lines shift, which could be due to a CsI(Tl) drift[2]. It can be verified and, eventually, taken into account by the analysis of the laser position in the CsI spectra.

---

[2] A similar CsI drift has been observed in INDRA campaign 2003.
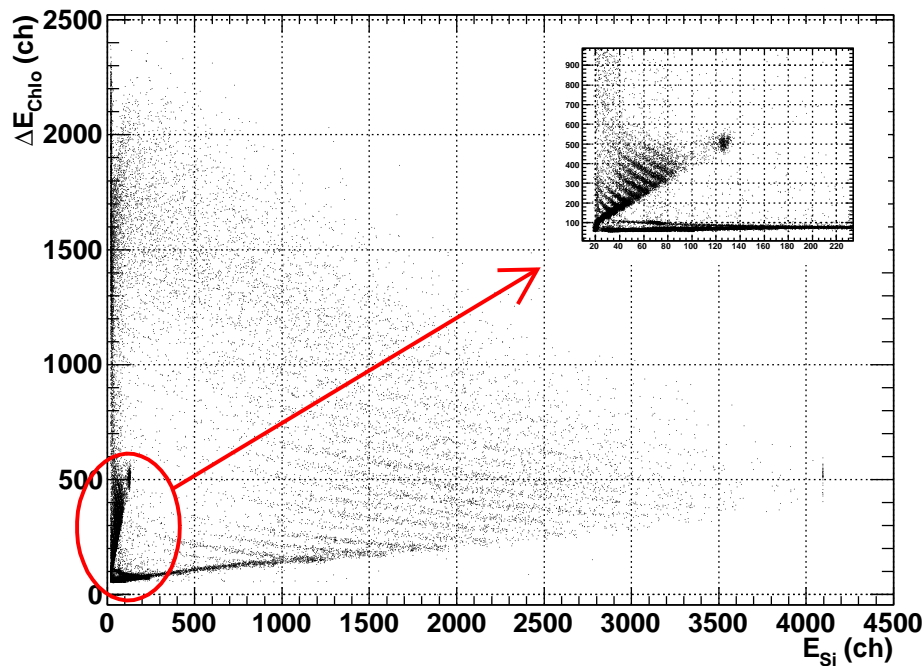
Figure 4.5 – Problems on silicon depletion voltage supply during the measurement cause a
shift in the silicon response.

Eventual abnormal functioning should be corrected by a detailed analysis of pulser
runs.

Moreover a $\Delta E_{ChIo} - E_{Si}$ ($\theta < 45°$) or $\Delta E_{ChIo} - E_{CsI}$ ($\theta > 45°$) spectrum analysis permit
to verify qualitatively the gas pressure chamber stability: Z and A resolutions are,
infact, mainly set by the ionization chamber resolution, which is strictly connected
with the gas pressure[3]. A resolution worsening corresponds to a gas pressure re-
duction, as shown in Fig.4.8, where the ionization chamber gas pressure varies from
30 mbar to 20 mbar.

"Fast-slow" correlations permit to point out possible abnormal functioning on the
CsI(Tl) electronic chain or high threshold (see Fig.4.9) on the CsI(Tl) CFDs, which
cause a loss of very low ionizing particles.

Detectors performances   The $\Delta E - E$ method, requiring the punch-through of the
first detector, introduces a threshold in the identified particles.

For a forward telescope we can specify three thresholds level with respect to the Z

---

[3]As suggested by Bohr [145], the energy straggling caused to an incident particle by the presence
of a material on its flight path is proportional to the square root of the material thickness. Therefore
the relative energy loss fluctuations increase decreasing the material thickness, i.e. the gas pressure
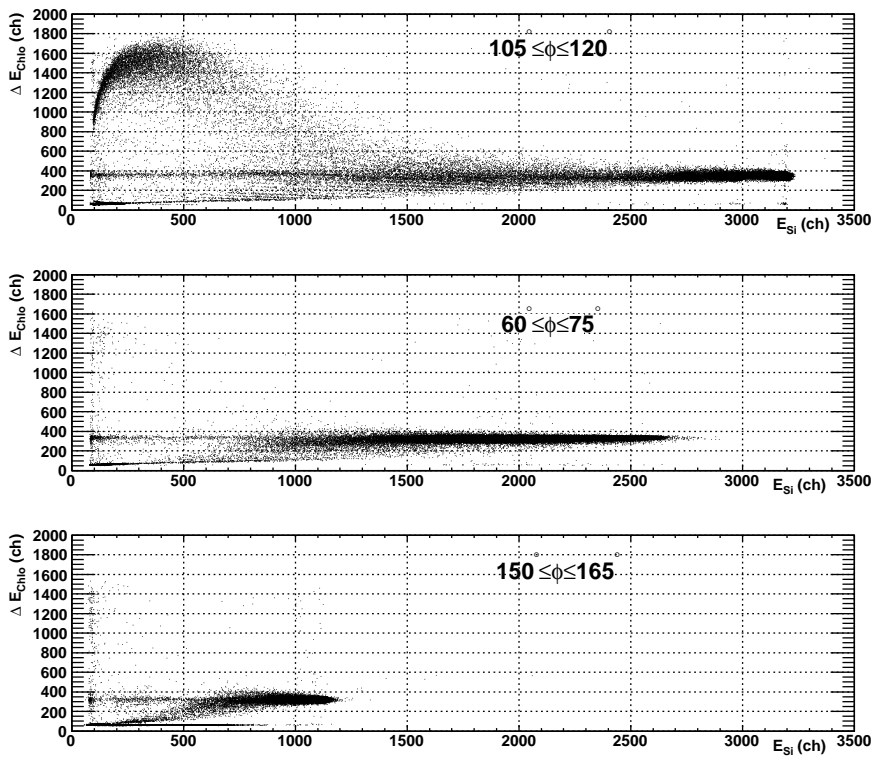in the ionization chamber.

Figure 4.6 – $\Delta E_{ChIo} - E_{Si}$ spectra of three different telescopes in ring 4 ($7° \leq \theta \leq 10°$). The first one has been chosen as reference. The absence of the highest part of the spectra, which has to be taken into account in further analysis, suggests probable high silicon detectors thresholds, which prevent the silicons triggering.
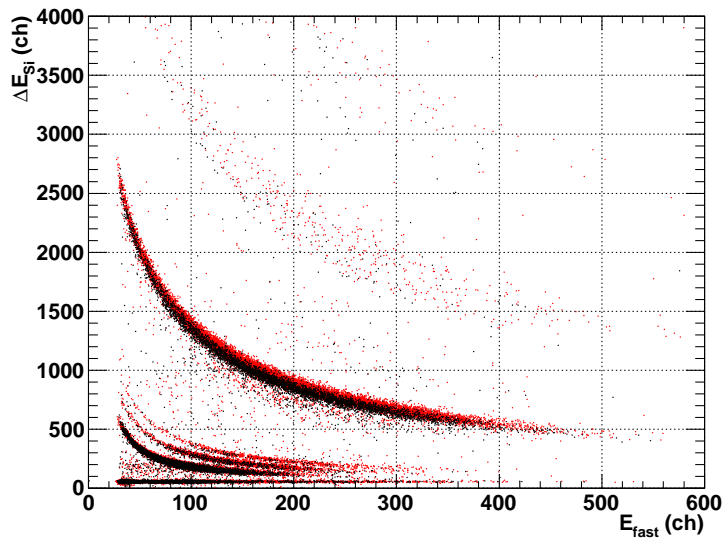

Figure 4.7 – $\Delta E_{Si} - E_{fast}$ spectrum. A CsI drift causes a shift in the Z edges positions. Black and red markers are relative to data acquired in different moments of the measurement campaign.

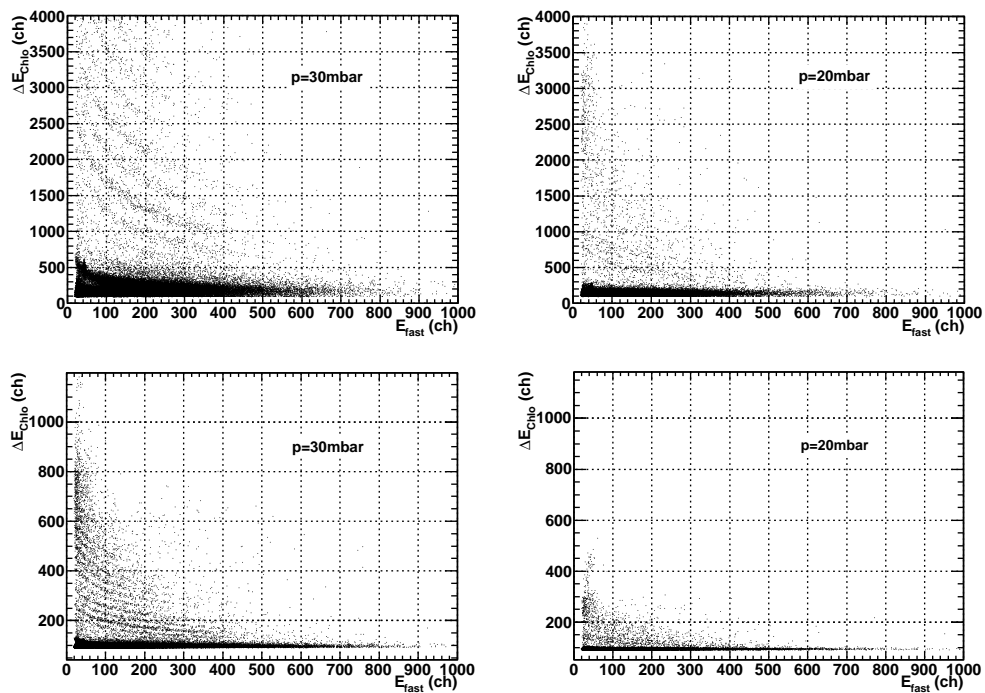**Figure 4.8** – A gas pressure reduction corresponds to a resolution degrading. The pressure varies from 30 (left) to 20 mbar (right). Ionization chamber high gain (upper) and low gain (lower) signals are shown.
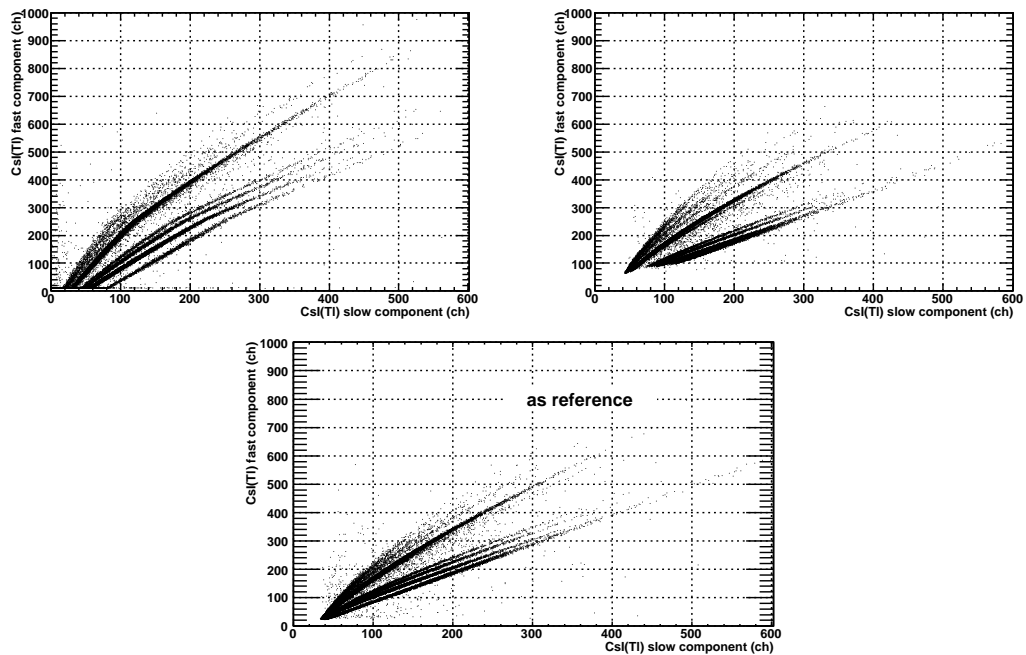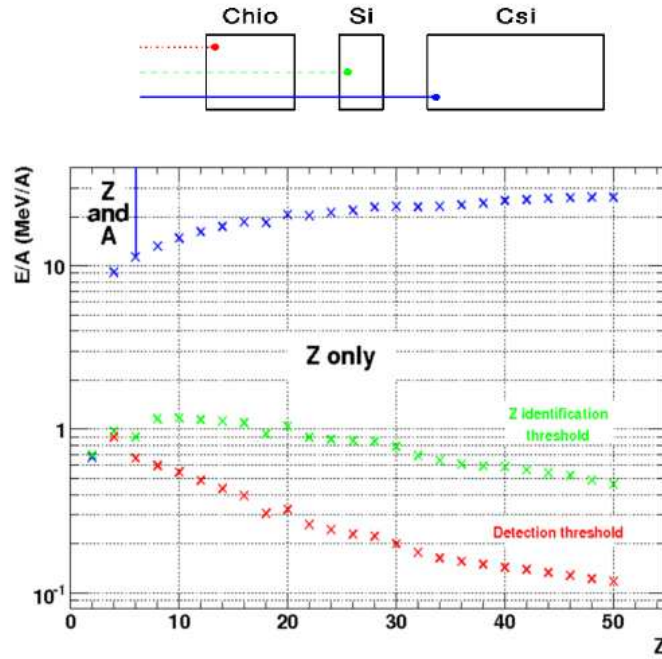

Figure 4.9 – Fast-slow spectra in different modules. Abnormal functioning of CsI(Tl) and incorrect CsI(Tl) energy threshold position cause the loss of the most energetic particles.

Figure 4.10 – INDRA detection thresholds for a forward telescope including the silicon layer [146]. The red lines corresponds to a particle energy loss in the ionization chamber of $\sim 5\,\text{MeV}$, the green line corresponds to the detection of the particle in the silicon detector (1.5MeV released in $30\,\text{mbar}$ C_3F_8 gas). The blue line indicates the energy required to detect the particle by cesium iodide detector.

and E of the incident particle (see Fig.4.10):

- Detection threshold: particles are detected in the ionization chamber, i.e. they have released at least $\sim 5\,\text{MeV}$ in the detector. It corresponds to $\sim 0.8\,\text{AMeV}$ for particles with charge $Z \lesssim 10$ and decreases to $\sim 0.1 \div 0.2\,\text{AMeV}$ for heavier fragments ($Z \sim 30$).

- Z identification threshold: the silicon detector detects the incident particle. The upper limit on the Z identification is due to the ionization chamber energy resolution. It corresponds to $\sim 0.8\,\text{AMeV}$ for all incident particles.

- Isotopic identification threshold: the CsI detector detects the incident particle.

For ionization chamber-CsI telescopes, the thresholds are similar and the isotopic separation threshold corresponds to the CsI identification threshold.

As an example of Z and A resolutions of the INDRA detector some experimental spectra are presented. In order to obtain a good estimation of the Z resolution, the analysis has been performed on events obtained in INDRA SOLO $M \geq 2$ trigger configuration (see §3.2.1). In such a way, since the energy of the elastically recoiled

(a) (b)
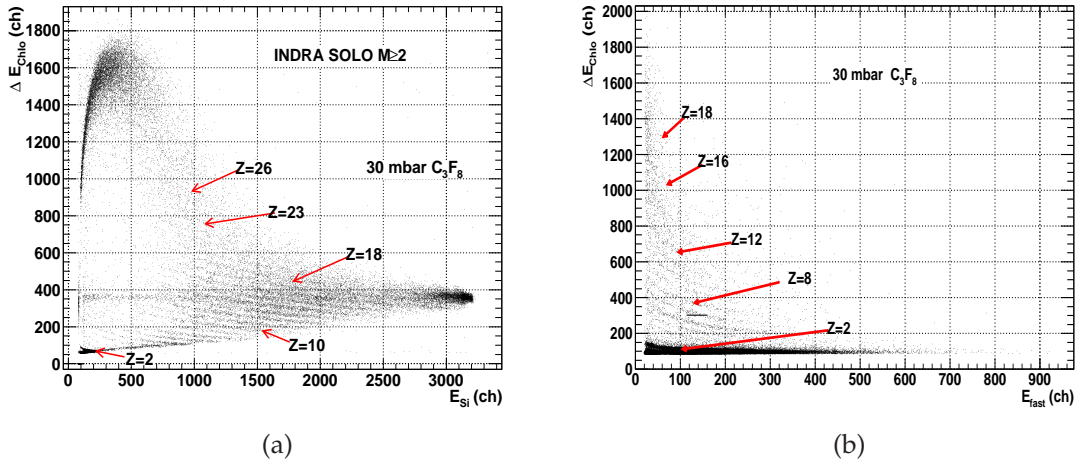
Figure 4.11 – $\Delta E_{ChIo} - E_{Si}$ and $\Delta E_{Chio} - E_{fast}$ spectra obtained in INDRA SOLO $M \geq 2$ trigger configuration. Different Z edges can be identified thanks to the relatively high carbon yields compared with its neighbours and to the absence of the ^{9}Be edge. Detectors are located at $\phi = 210° \div 225°$ and $\theta = 7° \div 10°$ and $\theta = 45° \div 57°$, respectively.

target nuclei is well below[4] 0.8 AMeV (see Tab.5.2), their contribution has been removed, obtaining more "clean" spectra.

An example of the detectors response is reported in Fig.4.11(a), which shows the $\Delta E_{ChIo} - E_{Si}$ matrix obtained for the reaction ^{40}Ar+^{64}Ni. The telescope covers $\theta = 7° \div 10°$ and $\phi = 210° \div 225°$. Identification up to $Z = 26$ is observed. Results at backward angles ($\Delta E_{ChIo} - E_{CsI}$) are shown in Fig.4.11(b), where Z up to 18 are clearly separated form each other. Mass separation can not be observed.

$\Delta E_{Si} - E_{fast}$ matrix ,obtained for a module of ring 4, is shown in Fig.4.12. Nuclei up to $Z = 7$ are detected. A clear separation is observed both in charge, between $Z = 1$ and $Z = 2$, an in mass, up to $Z = 2$.

Fig 4.13(a) shows the fast-slow rappresentation of the two CsI(Tl) components for a forward ring where mass and charge identification up to $Z = 3$ is observed. Similar result for ring 10 are shown in fig 4.13(b).

---

[4]We remark that ionization chamber signals do not contribute to the multiplicity signal generation, which is obtained by the silicon and the CsI(Tl) signals analysis (see §2.2.3). Thus the reference threshold is the energy necessary to punch through the ionization chamber.
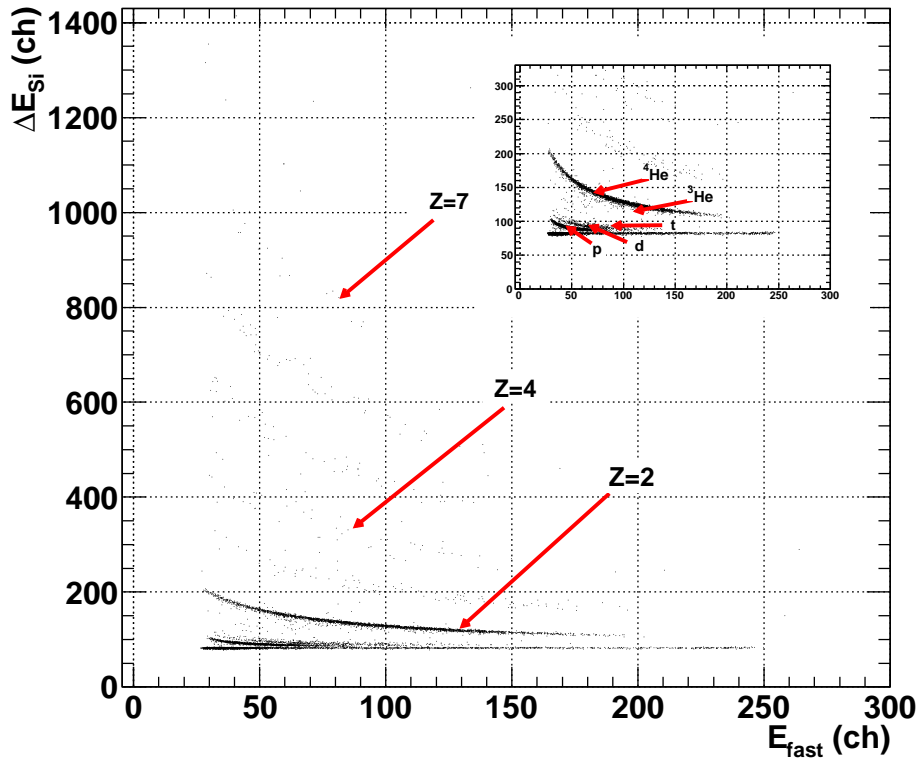
Figure 4.12 – $\Delta E_{Chio} - E_{fast}$ spectrum obtained for ^{40}Ar+^{64}Ni reaction in INDRA SOLO $M \geq 2$ trigger configuration. Fragments with charge up to $Z = 7$ are detected. Light charged particles are well separated in mass (see zoom on right corner). The detector is located at $\phi = 210° \div 225°$ and $\theta = 7° \div 10°$.
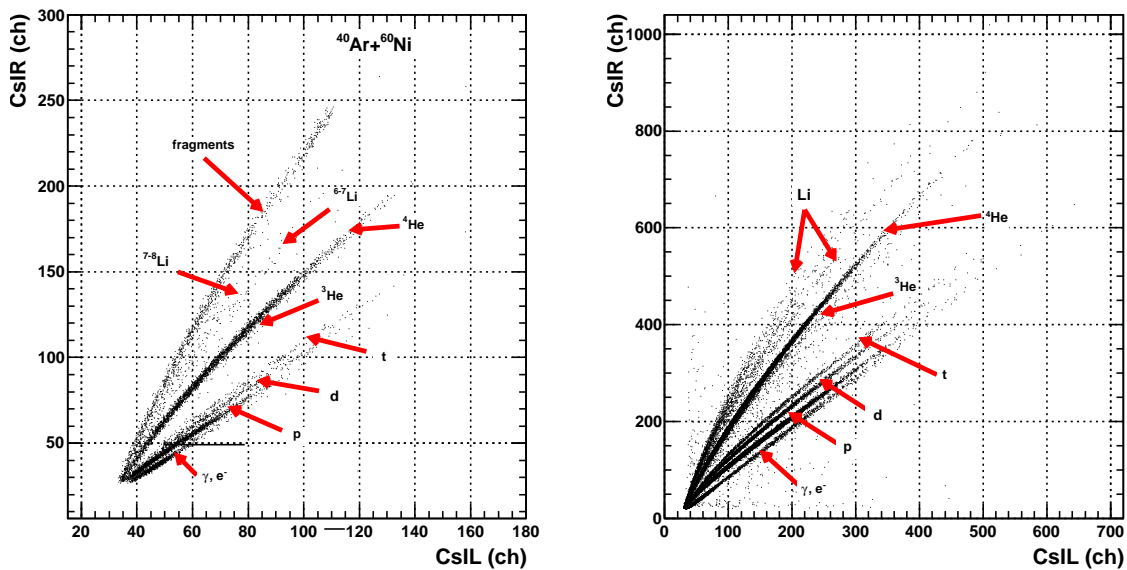
Figure 4.13 – Light charged high energetic particles identified in CsI(Tl) scintillators in forward (left) and backward (right) rings.

Chapter 5

INDRA data analysis

The essential information for the measurement of the differential cross section for the Ar+Ni fusion-evaporation reaction consists in the determination of the amount of the total collected fusion-evaporation events at each polar angular range, i.e. in each ring, where the evaporation residue can be detected.

Fusion evaporation residues must be discriminated from fragments produced in other reaction mechanisms. Being the transition from one reaction mechanism to another a smooth process, it is not easy in all cases to determine whether a given final product can be characterized as an evaporation residue. This is especially true at intermediate and higher bombarding energy when an overlap in energy and mass range exists for different processes, e.g. between deep inelastic collisions and fusion evaporation.

The following analysis thus requires a selection of fragments on the basis of the reaction mechanism in which they have been produced. Being performed up to now neither energy and time of flight calibrations, nor Z and A identifications, the fragment selection that can be performed is inclusive. Later on more exclusive fragment selection could be done, by multidimensional analysis methods and this is a long and time-expensive procedure. The fragment selection performed in this work is therefore preliminary and the elastically scattered nuclei, the fragments resulting from deep inelastic collisions and the fusion-evaporation residues can be selected only in first approximation, on the basis of general considerations.

A first selection of fragments produced in different reaction mechanisms can be based on the analysis of $\Delta E - E$ spectra (Fig.5.1).

For central collisions the reaction mechanism is dominated (at this incident energy) by fusion reactions, which can evolve by evaporation toward fusion-evaporation residues. The evaporation residues are massive and have a small kinetic energy after the evaporation process (see Tab.5.1), thus they lose the main part of their kinetic energy in the ionization chamber and a small residual energy in the silicon detector,
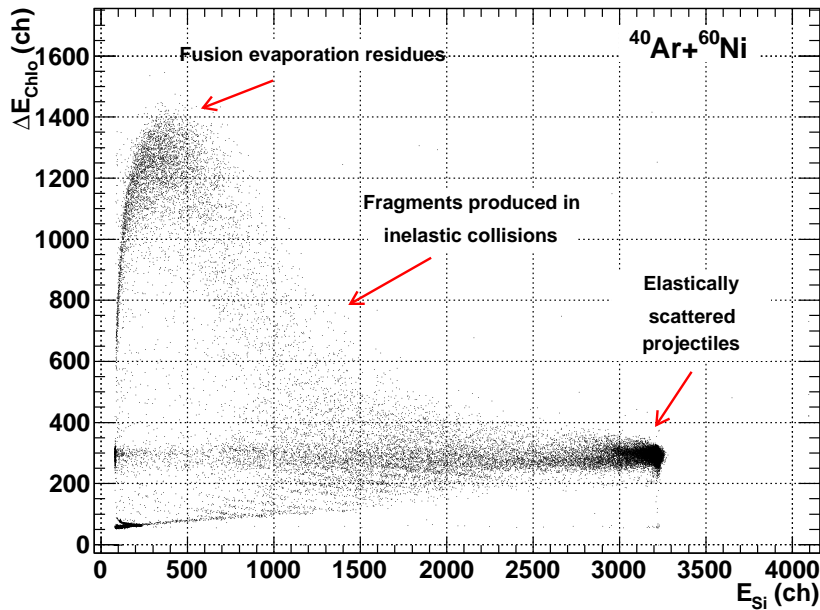
(a) $\Delta E_{ChIo} - E_{Si}$ spectrum (detector located at $7° \leq \theta \leq 10°$ and $75° \leq \phi \leq 90°$).
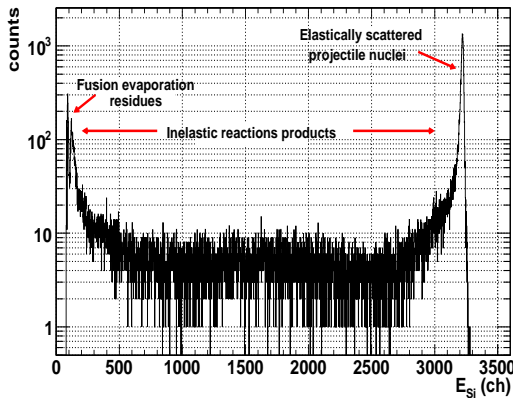
(b) Projection on the E_{Si} axis of $\Delta E_{ChIo} - E_{Si}$ spectrum.
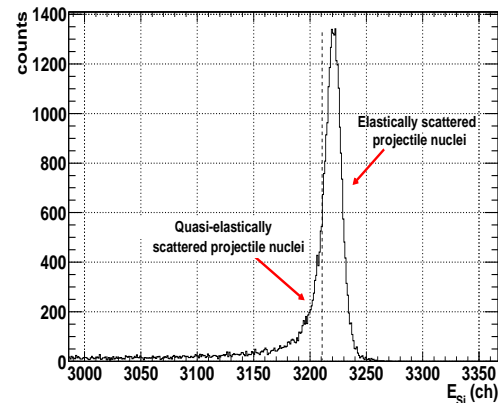
(c) Zoom of the E projection. The asymmetry of the elastic peak is due to quasi-elastic events.

Figure 5.1 – First selection of fragments produced in different reaction mechanisms. Three main region can be identified: the elastically scattered projectile region (or elastic region) corresponds to the highest energy loss in the silicon detector. Fusion-evaporation residue region (or residue region), corresponding to the Bragg peak region, is separated from the elastic region by fragments produced in inelastic reactions (inelastic region) which present intermediate characteristics between the elastically diffused nuclei and the fusion-evaporation residue characteristics. Spectra have been realized with data obtained in INDRA SOLO $M \geq 1$ trigger configuration.

Reaction	$\overline{A_{res}}$	$\overline{E_{res}}$(MeV)
^{34}Ar+^{58}Ni	71	131
^{36}Ar+^{58}Ni	73	142
^{36}Ar+^{60}Ni	74	139
^{40}Ar+^{60}Ni	78	158
^{40}Ar+^{64}Ni	81	162

Table 5.1 – Mean mass ($\overline{A_{res}}$) and kinetic energy ($\overline{E_{res}}$) of fusion-evaporation residues obtained by GEMINI simulation.

placing themselves in the Bragg peak region. We refer to the $\Delta E - E$ region of fusion-evaporation residues as residue region.

Increasing the impact parameter, inelastic reactions cover the region between central ($b \lesssim b_{gr}/2$) and peripheral collisions ($b \approx b_{gr}$). With the increase of b, less and less kinetic energy is dissipated in internal degrees of freedom of the system, up to quasi-elastic collisions. In elastic collisions the initial kinetic energy of the system is shared (according to the reaction kinematics) between the two partners without any loss. Therefore the kinetic energy associated to the elastically scattered projectile nuclei is the highest kinetic energy which can be carried out by a projectile nucleus in a reaction and the highest energy which can be deposited in silicon detectors. It allows to individuate an elastic region.

5.1 Beam alignment

Compound nucleus deexcitation process (particles evaporation and residue recoil) is axial symmetric in LAB reference system, so that computation of fusion-evaporation events can be performed in a restricted $\Delta\phi$ region, not including telescopes not properly working. In this way uncertainties due to detectors not properly working are strongly reduced. This procedure is based on the assumption of a correct beam alignment. It is therefore necessary to verify the accurate beam alignment with respect to the symmetry axis of the apparatus and eventually to take it into account during the following analysis. Elastic fragments, diffused in the first INDRA ring (see Tab.5.2), provide an effective tool to this goal.

In the following we refer to Rutherford scattering as elastic scattering, being the Rutherford scattering predominant with respect to the nuclear one (see §1.2.1) in these reactions for angles smaller than the grazing ones.

As discussed in §1, elastically scattered projectile nuclei[1] are diffused within the

---

[1]Here we refer to the elastically scattered projectile nuclei and not to the target ones because the latter have lower kinetic energy with respect to the former (see Tab.5.2). The elastically diffused target nuclei have not enough energy to punch through the ionization chamber, since their kinetic

Reaction	E_{beam} (AMeV)	θ_{gr}^{lab}	θ_{proj}^{el}	E_{proj}^{el} (MeV)	θ_{targ}^{el}	E_{targ}^{el} (MeV)	Ring
^{34}Ar+^{58}Ni	13.5	10.2°	7.0°	455.00	84.5°	4.00	4
			10.0°	450.88	82.1°	8.12	
			10.0°	450.88	82.1°	8.12	5
			10.2°	450.55	81.9°	8.45	
^{36}Ar+^{58}Ni	13.3	9.7°	7.0°	474.38	84.3°	4.42	4
			9.7°	470.37	82.1°	8.71	
^{36}Ar+^{60}Ni	13.3	9.6°	7.0°	474.53	84.4°	4.27	4
			9.6°	470.81	82.4°	7.99	
^{40}Ar+^{60}Ni	12.7	8.8°	7.0°	502.97	84.2°	5.03	4
			8.8°	500.07	82.7°	7.93	
^{40}Ar+^{64}Ni	12.7	8.7°	7.0°	503.28	84.3°	4.72	4
			8.7°	500.73	82.9°	7.28	

Table 5.2 – Kinematic characteristics of Rutherford scattering reactions. For each reaction the beam energy (E_{beam}) and the corresponding grazing angle (θ_{gr}^{lab} [1]) are listed. The minimum and the maximum projectile diffusion angle (θ_{proj}^{el}) for each ring, the corresponding target diffusion angle (θ_{targ}^{el}) and the kinetic energies of both projectile (E_{proj}^{el}) and target (E_{targ}^{el}) nuclei are reported. The angular aperture ($\Delta\theta = 3°$ in ring 4) of detectors introduces a spread in energy that is, in the worst case, of ~ 4 MeV (^{34}Ar+^{58}Ni reaction).

grazing angle, which corresponds, in most cases, just to ring 4. Rutherford scattering differential cross section (eq.1.15) is isotropic in ϕ and very much dependent on polar angle θ, so that elastic scattering reactions can be exploited to check a misalignment of the beam.

For each reaction, if the beam is accurately aligned with the apparatus symmetry axis, the statistics of the elastically scattered projectiles in each detector of the same ring ($\theta_{ring} \leq \theta_{gr}$) must be constant, within statistical uncertainties.

The elastically diffused projectile nuclei correspond to the highest energy loss in silicon detectors and the elastic cross section is 6 order of magnitude greater than the reaction cross section, so that projectile fragments produced in elastic scattering reactions can be easily identified in the $\Delta E - E$ spectrum (see Fig.5.1). By projecting on the E axis the $\Delta E - E$ spectrum shown in Fig.5.1(a), the residual energy plots shown in Fig.5.1(b,c) were produced. The asymmetry of the elastic peak (see Fig.5.1(c)) can be ascribed to the quasi-elastic contribution: the transition from a reaction mechanism to another is not sharp and implies a mixing between the two kinds of events. The width of the "elastic peak" is mainly due to the angular aperture ($\Delta\theta \simeq 3°$) of

_____

energy is lower than 0.5 AMeV

each silicon detector, being the detector intrinsic resolution negligible ([90]) with respect to the energy spread introduced by the finite angular aperture of the detector (see Tab.5.2).

The statistics of elastically scattered projectiles in each detector i has been evaluated by fitting, with the gaussian function

$$h_i(E) = A_i \cdot e^{\dfrac{(E - \overline{E})^2}{2\sigma_i^2}}, \tag{5.1}$$

the higher energy region of the elastic peak. With the intent of minimizing the quasi-elastic contribution, the total collected elastic events (N_i) are evaluated by the A_i values, resulting from the fit procedure. A_i is related to the area of the gaussian function N_i by

$$A_i = \frac{N_i}{\sigma_i \sqrt{2\pi}} \tag{5.2}$$

where σ_i is the standard deviation of $h_i(E)$.
The uncertainty on N_i can be expressed as:

$$\frac{\Delta N_i}{N_i} = \frac{\Delta A_i}{A_i} + \frac{\Delta \sigma_i}{\sigma_i} \tag{5.3}$$

where ΔA_i and $\Delta \sigma_i$ are given by the fit procedure.

Each fit has been repeated varying the marker position on the elastic peak, to estimate the uncertainty due to the arbitrary position of the markers. The number of elastic events for each detector (N_i) is the weighted mean of the obtained values:

$$\overline{N_i} = \frac{\sum_j \frac{N_j}{\sigma_j^2}}{\sum_j \frac{1}{\sigma_j^2}}. \tag{5.4}$$

To take into account the marker position dependence of N_i, the uncertainty has been chosen larger than the one obtained by eq.5.3.

To verify the beam alignment, the N_i values obtained for each detector of ring 4 have been normalized to an arbitrary value and plotted (see Fig.5.2). All four reactions present similar periodic behaviour instead of the expected flat one, suggesting possible beam mis-alignments.

For further analysis the beam mis-alignment in each reaction must be estimated. The beam mis-alignment can be described by the beam polar coordinates in the apparatus polar reference system, θ_b and ϕ_b. θ_b takes into account the polar angle
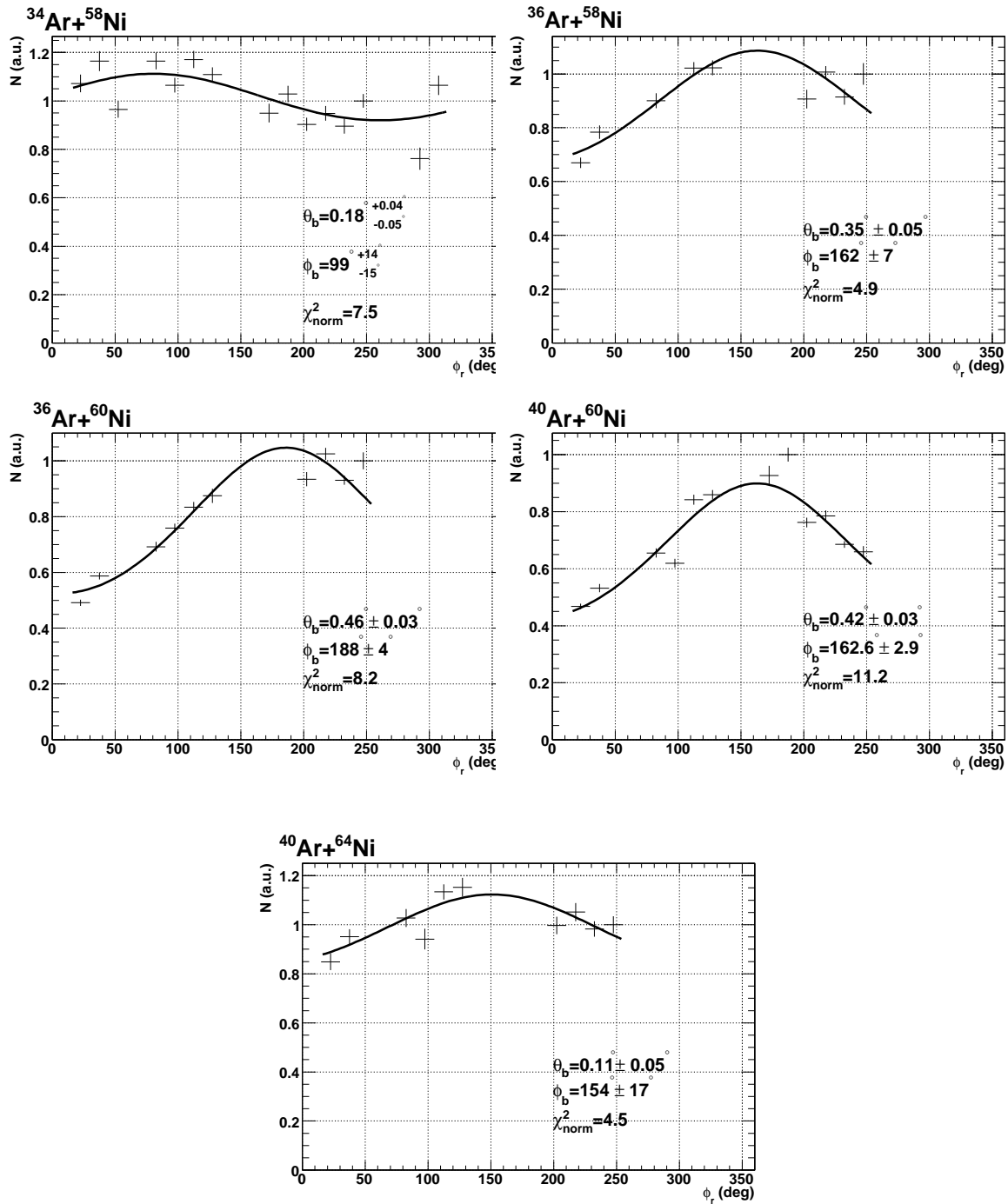
Figure 5.2 – Total collected elastic events N_i in the detector i versus the detector mean azimuthal angle ϕ_{r_i}. In all reactions N shows a periodic behaviour as function of ϕ. The full line is the fitting function $f(\phi_{r_i}, C, \theta_b, \phi_b)$. The θ_b and ϕ_b values obtained in fit procedure are reported in each panel.

between the apparatus axis and the beam direction and ϕ_b takes into account the relative beam position with respect to a chosen detector.

The number of elastic events hitting each detector is related to its effective position with respect to the beam position. In the center of mass (CM) reference system N_i is proportional to the integral of the Rutherford differential cross section

$$N_i \propto f = \int_{\Theta_{V_i}}^{\Theta_{gr}} \frac{1}{\sin^4 \frac{\theta}{2}} d\theta = -2 \cdot C \left[cotg \frac{\Theta_{gr}}{2} - cotg \frac{\Theta_{V_i}}{2} + \frac{1}{3} cotg^3 \frac{\Theta_{gr}}{2} - \frac{1}{3} cotg^3 \frac{\Theta_{V_i}}{2} \right] \quad (5.5)$$

where Θ_{gr} is the grazing angle and Θ_V is the effective minimum polar angle covered by the detector i, in the CM reference system, taking into account the beam misalignment.

Later on quantities expressed in CM reference system will be written in capital letters, while small letters will be used for quantities in laboratory (LAB) reference system.

The effective polar angle Θ_V of each detector can be expressed in LAB reference system by means of kinematic considerations (CM momentum conservation law):[2]

$$\cos \Theta_{V_i} = -\frac{m_p}{m_t} \sin^2 \theta_{V_i} + \cos \theta_{V_i} \sqrt{1 - \left(\frac{m_p}{m_t} \sin \theta_{V_i} \right)^2} . \quad (5.6)$$

Geometrical considerations allow to relate θ_{V_i} to known quantities. Referring to Fig.5.3, known the distance between the target (T) and the center of the ionization chamber entrance window ($\overline{TC}$), the target distance from the *"ring 4 plane"* (π) can be expressed as:

$$\overline{OT} = \overline{TC} \cos \overline{\theta}_{\substack{ChIo \\ Ring4-5}} \quad (5.7)$$

where $\overline{\theta}_{\substack{ChIo \\ Ring4-5}}$ is the mean polar angle where the ionization chamber[3] of ring 4 and 5 is positioned. Being R the lower detector border of a silicon detector (characterized by its azimuthal angle ϕ_{r_i} and by minimum and maximum ring polar angle, θ_r^{MIN} and θ_r^{MAX}), the detector distances from target ($\overline{TR}$) and from the target projection on π (O) are respectively

$$\overline{TR} = \frac{\overline{OT}}{\cos \theta_r^{MIN}} \quad (5.8)$$
$$\overline{OR} = \overline{OT} \tan \theta_r^{MIN} .$$

---

[2]The negative solution has been discarded being θ_{V_i} in the first quadrant.
[3]We remember that each INDRA ionization chamber covers two rings.
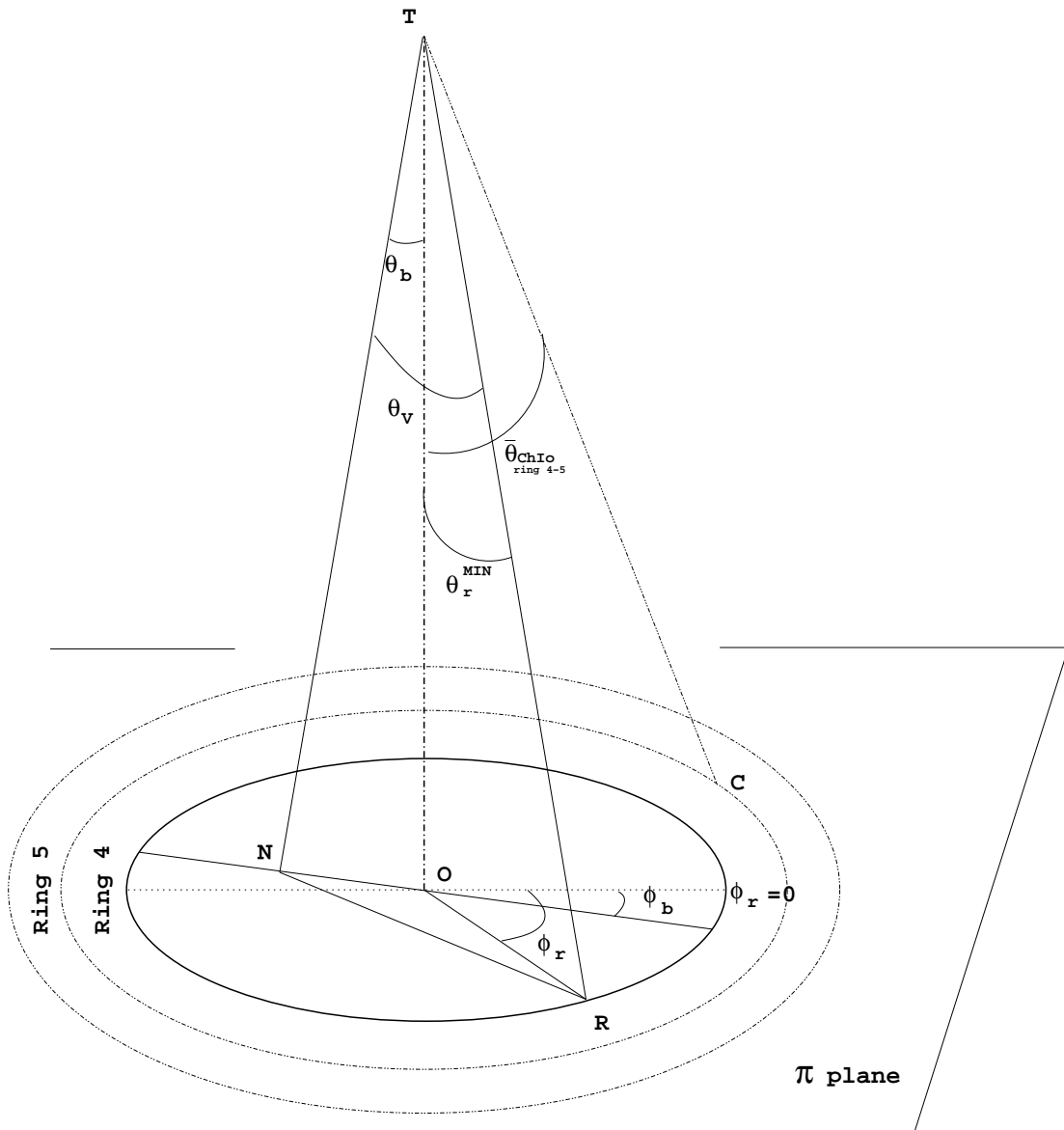
Figure 5.3 – Geometrical outline of the detector position (*R*) with respect to the target (*T*) and to the beam impact position (*N*) on the π plane. The π plane is the ring 4 plane.

(a)

Figure 5.4 – Example of grid in ϕ_b vs θ_b plane to determine the minimum of eq.5.11.
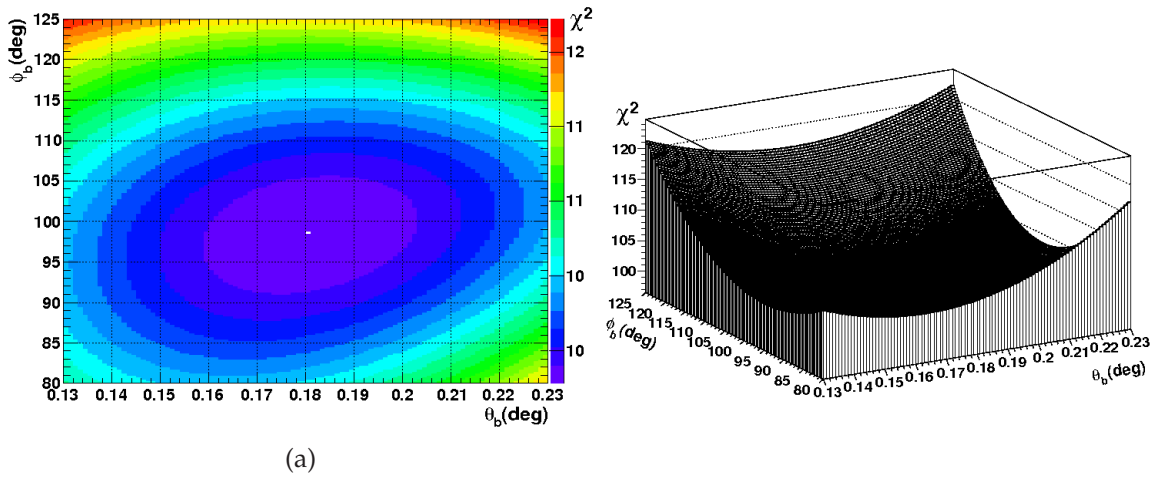
Indicating with N the beam impact point on π plane:

$$\overline{ON} = \overline{OT} \tan \theta_b$$
$$\overline{TN} = \frac{\overline{OT}}{\cos \theta_b} \quad . \tag{5.9}$$

$\cos \theta_{V_i}$ can be expressed as:

$$\cos \theta_{V_i} = \frac{\overline{TN}^2 + \overline{TR}^2 - \overline{NR}^2}{2 \cdot \overline{TR} \cdot \overline{TN}}, \tag{5.10}$$

where $\overline{NR}$ is given by the Carnot theorem

Using eq.5.6 and eq.5.7÷5.10, eq.5.5 ($f(\phi_r, C, \theta_b, \phi_b)$) describes the dependence of the number of elastic events (N_i) as function of the detector azimuthal angle (ϕ_{r_i}), taking into account the beam mis-alignment. $f(\phi_{r_i}, C, \theta_b, \phi_b)$ depends, for each reaction, on each detector azimuthal angle ϕ_{r_i}, on a normalization factor C and on the beam angles θ_b and ϕ_b. As a first approximation the mean value of ϕ of each detector has been used as ϕ_{r_i}. It means that the dependence of θ_V on ϕ in each detector has been neglected.

A fitting procedure, with the function $f(\phi_r, C, \theta_b, \phi_b)$, of the number of elastic events detected in each detector vs. the detector ϕ_r allows to estimate the parameters C, θ_b and ϕ_b (see Fig.5.2). Being $f(\phi_{r_i}, C, \theta_b, \phi_b)$ non-linear in θ_b and ϕ_b, to obtain parameters and parameter errors estimations, the fit has been performed minimizing the χ^2 quantity within a grid of values of unknown quantities, as shown in Fig.5.4. χ^2 is

defined as:

$$\chi^2 = \sum_{i=1}^{\substack{detector \\ number}} \frac{(f(\phi_{r_i}, C, \theta_b, \phi_b)_{th_i} - N_i)^2}{\sigma_i^2} \tag{5.11}$$

where $f(\phi_r, C, \theta_b, \phi_b)_{th_i}$ is the expected number of elastic event statistics in the detector i,

$$\sigma_i^2 = \sigma_{N_i}^2 + (\frac{\partial f}{\partial \phi_r})^2 \Delta \phi_r^2, \tag{5.12}$$

and $\Delta\phi_r$ is the azimuthal angular aperture of the detector ($\Delta\phi_r = 15°$).

The uncertainties on parameters have been calculated according to [147], choosing a confidence level of 90%. The obtained values are listed in Tab.5.3.

5.2   Fusion-evaporation residues

Considerations on fusion-evaporation reaction mechanism allow to perform a more restrictive fusion-evaporation residue selection, taking into account that the transition from one reaction mechanism to the other is smooth and fragments produced in different reactions often present intermediate characteristics, requiring some criteria to identify them. In particular some constrains will be set to separate, in a first approximation, fusion-evaporation events from deep inelastic collisions.

A fusion reaction is characterized by the formation of an hot composite system, or compound nucleus (CN). The excitation energies of CN produced in the analyzed reactions are listed in tab 3.3. The highly excited CN deexcites, besides γ emission, by two competing mechanisms: evaporation and fission. If the deexcitation mode is dominated by fission, at least two heavy fragments with masses close to half of the total system mass, in case of symmetric fission[4], are present in the exit channel of the reaction. Otherwise, if the evaporation is the preferential deexcitation mode, the compound nucleus evaporates light particles, and therefore only one heavy fragment, called residue, with mass close to the total system mass, and a certain number of light particles are present in the exit channels. We refer to the heavy fragment as fusion-evaporation residue (FE residue) or simply residue and to the light particles as evaporated particles. The angular distribution of the evaporated particles is isotropic in the CN reference system, if the CN angular momentum $\vec{J} = 0$, otherwise evaporated particles are emitted preferentially in the reaction plane.
We identify an event as fusion-evaporation event if

---

[4]According to Refs. [148–150] at least for the heaviest system we are close to the critical point at which fission can be asymmetric.

	ROOT FIT	χ^2 MINIMIZATION by grid	
		range of the minimum of χ^2	grid step
		^{40}Ar+^{64}Ni	
c	$(3.41 \pm 0.04)10^{-3}$		
ϕ_b	151 ± 5	154 ± 16	0.25
θ_b	0.154 ± 0.024	0.105 ± 0.047	0.002
χ^2_{norm}	2.7	4.5	
		^{40}Ar+^{60}Ni	
c	$(2.244 \pm 0.021)10^{-3}$		
ϕ_b	162.8 ± 1.4	162.6 ± 2.9	0.25
θ_b	0.417 ± 0.015	0.421 ± 0.030	0.001
χ^2_{norm}	13.1	11.2	
		^{36}Ar+^{60}Ni	
c	$(1.914 \pm 0.015)10^{-3}$		
ϕ_b	186.0 ± 2.0	188 ± 4	0.25
θ_b	0.477 ± 0.017	0.462 ± 0.033	0.001
χ^2_{norm}	8.1	8.2	
		^{36}Ar+^{58}Ni	
c	$(2.241 \pm 0.021)10^{-3}$		
ϕ_b	163.0 ± 3.1	162 ± 7	0.25
θ_b	0.336 ± 0.026	0.354 ± 0.054	0.001
χ^2_{norm}	5.4	4.9	
		^{34}Ar+^{58}Ni	
c	$(2.235 \pm 0.021)10^{-3}$		
ϕ_b	81 ± 9	99^{+14}_{-16}	0.25
θ_b	0.148 ± 0.018	0.18 ± 0.04	0.001
χ^2_{norm}	5.8	7.5	

Table 5.3 – Fit procedure results. For each reaction the fit has been performed both by ROOT and minimizing the χ^2 quantity, defined in eq.5.11, thanks to a grid, whose steps in ϕ_b and θ_b are reported. The reported uncertainties have been determined by ROOT procedure and according to [147], respectively. The obtained values are consistent.

- the heaviest fragment's mass and charge are greater than half of the total system mass and charge

- the second heaviest fragment charge is smaller than $Z = 12$. This constraint allows to separate evaporated particles from fragments produced in DI collisions, as will be shown later.

As previously mentioned, the fusion-evaporation differential cross section $d\sigma_{FE}$ can be estimated by counting the total collected fusion-evaporation events in each ring. Since each event is characterized by the detection of a residue, $d\sigma_{FE}$ can be expressed as

$$\frac{d\sigma_{FE}}{d\theta} \propto \frac{\Delta R}{\Delta \theta} \tag{5.13}$$

where ΔR is the number of total collected residues in each angular range and $\Delta\theta$ is the detector angular coverage. The aim of the following analysis is thus the computation of the detected residues number. The procedure consists in the following steps:

- identification, in $\Delta E - E$ correlation, of a residue region

- estimation of a possible contribution to residues from non fusion-evaporation events.

Residue characteristics   Residues are characterized by high mass and charge and low kinetic energy, so that we expect the residue region is approximately limited to the Bragg peak region in the $\Delta E - E$ spectrum.
Being A_{res} and A_{evap} the evaporation residue and the evaporated particles masses $(A_{res} + A_{evap} = A_{CN})$, the residue kinetic energy $E_{res}(\Theta)$ can be evaluated from the relation:

$$E_{res}(\Theta) = E_{CN}\frac{A_{res}}{A_{CN}}\left[1 + 2\frac{V_{res}}{v_{rec}^{CN}}\cos\Theta + \left(\frac{V_{res}}{v_{rec}^{CN}}\right)^2\right] \tag{5.14}$$
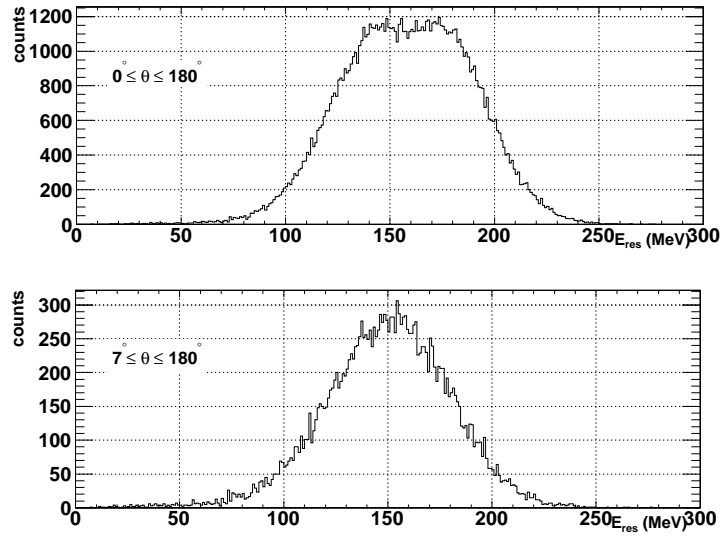
where the residue velocity in CM, V_{res}, is given by:

$$V_{res} = V_{rel}\frac{A_{evap}}{A_{evap} + A_{res}} \tag{5.15}$$

The kinetic energy of a compound nucleus (E_{CN}) can be calculated as:

$$E_{CN} = \frac{1}{2}A_{CN}v_{CM}^2 = \frac{1}{2}A_{CN}v_{rec}^{CN\,2}$$

where the CN recoil velocity (v_{rec}^{CN}) is related to the beam incident energy (E_i), ex-

Figure 5.5 – Kinetic energy distribution of fusion-evaporation residues emitted in all the solid angle (upper panel) and at a polar angle $\theta \geq 7°$ (angular region covered by INDRA apparatus). Spectra, predicted by GEMINI, have been obtained for ^{40}Ar+^{60}Ni reaction.

pressed in MeV, and to the projectile (A_p) and CN (A_{CN}) masses, by

$$v_{rec}^{CN} = 1.39 \sqrt{\frac{E_i A_p}{A_{CN}^2}} \, cm/ns.$$

The kinetic energy distribution for the ^{40}Ar+^{60}Ni reaction is shown in Fig.5.5. It presents a broad peak, related to the kinematic allowed angles. Limiting the diffusion angles to $\theta \geq 7°$ (the angular region covered by INDRA) the distribution is less spread and single peaked. Both kinetic energy distributions have been obtained by GEMINI calculation: the evaporation code, developed by Charity [151–153], based on the Statistical Evaporation Model, which assumes the statistical equilibrium of the hot nucleus. GEMINI code follows the decay channel of a compound nucleus via sequential binary decay.

Residue charge and mass distributions, obtained by GEMINI calculation, are shown in Fig.5.6. GEMINI predictions indicate residue distributions peaked respectively at $A \sim 78$ and $Z \sim 36$, for the ^{40}Ar+^{60}Ni reaction, and spanning respectively from 60 to 86 and from 28 to 40. Similar behaviours have been obtained for the other analyzed reactions.
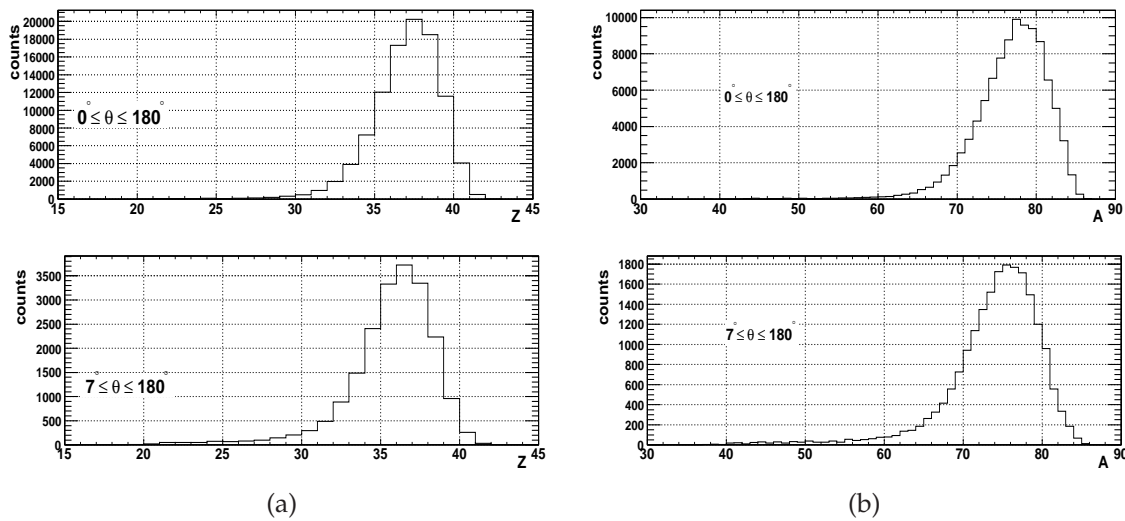
Figure 5.6 – Charge (left side) and mass (right side) distributions predicted by GEMINI simulation, for ^{40}Ar+^{60}Ni reaction. Fusion-evaporation residues are emitted in all the solid angle (upper panels) and in $\theta \geq 7°$ region (lower panels).

5.2.1   Deep inelastic contribution

The transition between the three classes of phenomena (Compound Nucleus, Deep Inelastic Collision and Quasi Elastic processes) occurring in heavy ion reactions at low energy is smooth [154]. Deep inelastic collisions (DIC) appear to occur for incident angular momenta (or *b*) larger than those leading to the compound nucleus (CN) formation but smaller than those corresponding to the soft grazing collisions (quasi-elastic process, QE). Corresponding QE processes and CN formations to very different impact parameters, the reaction products kinetic energies are very different from each other, allowing an easy separation, in $\Delta E - E$ spectra, of fusion from quasi-elastic products. This is not true for DIC and CN processes, where the involved *b* are only slightly different, so that it is not trivial to separate their reaction products in $\Delta E - E$ spectra.

Deep inelastic collision are characterized by following features:

1. they represent a binary process which nearly preserves the identity of the colliding ions: the charge and mass distributions of the two outgoing fragments spread over the whole available *Z* and *A* ranges, but are centered in the vicinity of the charges and masses of the projectile and the target

2. the initial kinetic energy of relative motion is almost entirely converted into intrinsic excitation of the outgoing fragments, i.e. the CM kinetic energy of the outgoing fragments is equal to the Coulomb repulsion of two highly deformed nuclei in a scission configuration, independently of the incident kinetic energy.
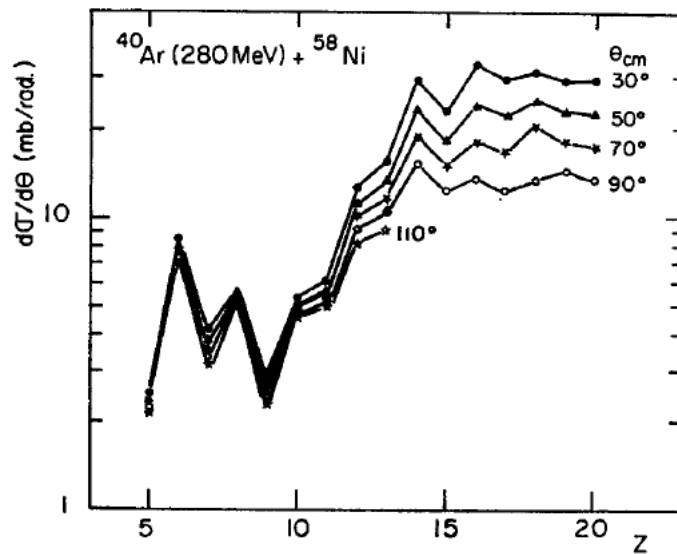
Figure 5.7 – Evolution of the deep inelastic collision differential cross sections as a function of the PL charge number at various CM angles in 280 MeV ^{40}Ar+^{58}Ni reaction. The differential cross section has been obtained in the range $\theta_{lab} = 8° \div 90°$, where the individual fragments have been identified in Z and A. Strong even-odd fluctuations can be seen, especially for the smallest charges, resulting possibly from a sequential decay process [154].

The relative motion is strongly damped.

3. a large variety of emitted products

4. a wide forward peaked angular distribution of the deep inelastic component.

These reactions have been described by several authors in terms of friction process [155–157] or diffusion process [158].

As discussed in §1.2.2, the charge and mass distributions of the primary fragments produced in a deep inelastic collision extend to the whole available Z and A range (see Fig.1.6(b)) and are centered on the initial Z and A value of the incoming reaction partners. This behaviour can be easily understood in terms of friction forces acting during the collision. As the reaction becomes more and more dissipative, i.e. the impact parameter decreases, the interaction time increases and friction forces acting between the two partners can cause nucleons transfer. More dissipative is the collision, broader is the primary fragments mass distribution.

Fig.5.7 shows the evolution of the DIC cross sections as a function of the projectile-like charge number Z at various CM angles in 280 MeV ^{40}Ar+^{58}Ni reaction [154].

Cross sections are increasing with increasing Z, remaining, however more or less constant for $Z \geq 12$.

Decreasing Z, the cross section decreases, suggesting that the most significant contribution to the deep inelastic cross section is given by fragments with Z within ± 6 unit from the initial value.

In Ar+Ni reactions it means that the projectile-like and target-like charge distributions cover respectively:

$$Z_p = 18\,(\pm 6) \Rightarrow 12 \div 24 = Z_{PL} \tag{5.16}$$

$$Z_t = 28\,(\pm 6) \Rightarrow 22 \div 34 = Z_{TL} \tag{5.17}$$

We remark that the target-like and the fusion-evaporation residue charge distributions (the latter one obtained by GEMINI calculation),

$$Z_{res} = 30 \div 40\,, \tag{5.18}$$

overlap, avoiding a residue identification based on the fragment charge.

The angular distribution of PL fragments is peaked in forward direction in CM.

Fully relaxed deep inelastic collisions represent the border of DIC: they correspond to the tail of the charge distribution, $Z < 12$ and $Z > 34$, and show a flat CM angular distribution. $Z > 34$ reaction products clearly overlap the FE residue charge distribution and, their cross section being $\sim 1/4$ of the $Z > 12$ DIC cross section, they must be taken into account in the fusion-evaporation residue computation.

Moreover for the 280 MeV ^{40}Ar+^{58}Ni reaction a DIC cross section of about 700 mb (± 100 mb) has been found [154], which is comparable with the evaporation residue cross section of 900$\pm$120 mb [136]. An estimation of the total cross section of 1850 mb, as suggested in [154], demonstrates clearly the large importance of DIC in such reactions.

A discrimination of fully relaxed DI products from fusion-evaporation residues should require an energy and charge calibration, actually not available. So that their contribution will be taken into account in the computation of the detected residue number uncertainty.

To continue the analysis it is necessary to verify if quasi-target nuclei produced in DIC lie in the residue region, and, eventually, to evaluate their contribution to the statistics in the residue region.

In order to evaluate the presence and eventually the magnitude of this effect, a code (`DIFFIL`) computing the kinematics for elastic diffusion, fission and deep inelastic fully relaxed reactions have been used. A detailed description of the code is reported in app.B.

Fully relaxed deep inelastic collisions are characterized by the complete dissipation of initial CM kinetic energy in internal degrees of freedom of the system: the two primary fragments move away thanks only to their Coulomb repulsion. Elastic collisions, instead, are characterized by the conservation, in relative motion, of the initial kinetic energy of the system. Therefore these two processes set up the lower and upper limits respectively of the kinetic energy of the products.
Contrary to fusion reactions, elastic and deep inelastic collisions are both binary processes, thus the presence of a target or quasi-target fragment (QT) is associated with the presence of a projectile or quasi-projectile nucleus (QP). While quasi-projectile can be discriminated from residues by their charge, the discrimination of QT from residues requires a heavy fragments multiplicity analysis. Binary processes kinematics (relative emission angles of the two partners) is univocally determined by two-body kinematics, so that `DIFFIL` permits, once set a quasi-target angular range (typically the angular aperture of a detector $\Delta\theta$), to estimate the respective quasi-projectile angular range, ranging from elastic collisions to fully relaxed deep inelastic collisions. Deep inelastic fully relaxed events set the QP diffusion angle lower limit for a fixed QT emission angle: QP is diffused at a larger angle in all less dissipative collisions, up to elastic collisions, which set the upper limit.

The angle and the kinetic energy of projectile and target fragments elastically diffused, and the corresponding value in case of deep inelastic fully relaxed collision are then evaluated, requiring as products charge ratio both the initial charge ratio ($Z_{QP} = 18$, $Z_{QT} = 28$, elastic events) and a charge ratio such as the target fragment has a charge equal to 33 (DI fully relaxed events, see eq.5.17). The obtained value are listed in Tab.5.4 for the different reactions.

The analysis of the angular correlations between the "residue" (i.e. a heavy fragment lying in the residue region) and coincident heavy particles ($Z \geq 12$, see eq.5.16) detected within the expected quasi-projectile angular range suggests the kind of the occurred reaction mechanism.
The inelastic collisions being binary processes, the reaction takes place on a plane (known as *reaction plane*), so that the azimuthal angular distance between the two reactions products is $\phi \simeq \pi$.

		^{40}Ar+^{60}Ni			$A_{PL} = 39.1$			
R_{TL}	θ_{TL}	θ_{PL}^{DI}	E_{PL}^{DI} MeV	E_{PL}^{DI} AMeV	$\theta_{(MAX)PL}^{inel}$	$E_{(MAX)PL}^{inel}$ MeV	$E_{(MAX)PL}^{inel}$ AMeV	R_{PL}
	7°	39.2°	14.8	0.4	141.5°	26.7	0.7	
4								9 ÷ 15
	10°	44.4°	23.7	0.6	128.6°	35.0	0.9	
5								10 ÷ 15
	14°	46.0°	40.5	1.0	114.7°	48.9	1.2	
6								9 ÷ 14
	20°	42.5°	77.2	2.0	98.8°	77.4	1.9	
7								8 ÷ 13
	27°	30.0°	152.0	3.9	84.4°	120.8	3.0	
8								8 ÷ 12
	35°	╱	╱	╱	70.9°	180.8	4.5	

		^{40}Ar+^{64}Ni			$A_{PL} = 40.7$			
R_{TL}	θ_{TL}	θ_{PL}^{DI}	E_{PL}^{DI} MeV	E_{PL}^{DI} AMeV	$\theta_{(MAX)PL}^{inel}$	$E_{(MAX)PL}^{inel}$ MeV	$E_{(MAX)PL}^{inel}$ AMeV	R_{PL}
	7°	40.4°	13.7	0.3	145.0°	34.2	1.0	
4								9 ÷ 16
	10°	45.4°	22.2	0.5	132.6°	41.6	1.0	
5								10 ÷ 15
	14°	46.9°	38.3	0.9	118.8°	55.2	1.4	
6								9 ÷ 14
	20°	43.3°	73.1	1.8	102.4°	83.3	2.1	
7								8 ÷ 13
	27°	31.8°	140.7	3.5	87.4°	126.2	3.2	
8								8 ÷ 12
	35°	╱	╱	╱	73.2°	185.3	4.6	

		^{36}Ar+^{58}Ni			$A_{PL} = 36.8$			
R_{TL}	θ_{TL}	θ_{PL}^{DI}	E_{PL}^{DI} MeV	E_{PL}^{DI} AMeV	$\theta_{(MAX)PL}^{inel}$	$E_{(MAX)PL}^{inel}$ MeV	$E_{(MAX)PL}^{inel}$ AMeV	R_{PL}
	7°	43.9°	11.6	0.3	145.3°	32.9	0.9	
4								9 ÷ 16
	10°	48.6°	19.4	0.5	133.0°	39.9	1.0	
5								10 ÷ 15
	14°	49.6°	34.2	0.9	119.2°	52.7	1.3	
6								10 ÷ 14
	20°	45.8°	65.9	1.8	102.7°	79.2	2.0	
7								9 ÷ 13
	27°	35.6°	122.6	3.5	87.7°	119.5	3.0	
8								9 ÷ 12
	35°	╱	╱	╱	73.5°	175.1	4.4	

			^{36}Ar+^{60}Ni		$A_{PL} = 37.6$			
R_{TL}	θ_{TL}	θ_{PL}^{DI}	E_{PL}^{DI} MeV	E_{PL}^{DI} AMeV	$\theta_{(MAX)PL}^{inel}$	$E_{(MAX)PL}^{inel}$ MeV	$E_{(MAX)PL}^{inel}$ AMeV	R_{PL}
	7°	44.6°	11.1	0.3	146.8°	36.6	1.0	
4								9 ÷ 16
	10°	49.2°	18.8	0.5	134.8°	43.5	1.1	
5								10 ÷ 15
	14°	50.2°	33.2	0.9	121.1°	56.2	1.4	
6								10 ÷ 14
	20°	46.3°	64.0	1.7	104.5°	82.4	2.1	
7								9 ÷ 13
	27°	36.2°	118.7	3.2	89.1°	122.4	3.1	
8								9 ÷ 12
	35°	╱	╱	╱	74.6°	177.6	4.4	
			^{34}Ar+^{58}Ni		$A_{PL} = 36$			
R_{TL}	θ_{TL}	θ_{PL}^{DI}	E_{PL}^{DI} MeV	E_{PL}^{DI} AMeV	$\theta_{(MAX)PL}^{inel}$	$E_{(MAX)PL}^{inel}$ MeV	$E_{(MAX)PL}^{inel}$ AMeV	R_{PL}
	7°	47.7°	9.7	0.3	147.8°	37.6	1.0	
4								10 ÷ 16
	10°	51.9°	16.8	0.5	135.9°	44.1	1.1	
5								10 ÷ 15
	14°	52.4°	30.2	0.8	122.3°	56.3	1.4	
6								10 ÷ 14
	20°	48.3°	58.8	1.6	105.6°	81.3	2.0	
7								9 ÷ 13
	27°	38.6°	107.7	3.0	90.1°	119.4	3.0	
8								8 ÷ 12
	35°	╱	╱	╱	75.4°	172.0	4.3	

Table 5.4 – For each ring (R_{TL}) the lower and the upper polar angle are chosen as TL emission angles (θ_{TL}). The corresponding projectile diffusion angles (θ_{PL}^{DI}, $\theta_{(MAX)PL}^{inel}$) and kinetic energies (E_{PL}^{DI}, $E_{(MAX)PL}^{inel}$) for DI fully relaxed process and for processes corresponding to the minimum energy dissipation, respectively, are reported. The last column shows the QP angular range, moving from DI to the lowest dissipative events. The products charge ratio is the initial one ($Z_{PL} = 18$, $Z_{TL} = 28$) and the QP mean mass (A_{PL}) is given by `DIFFIL` code.
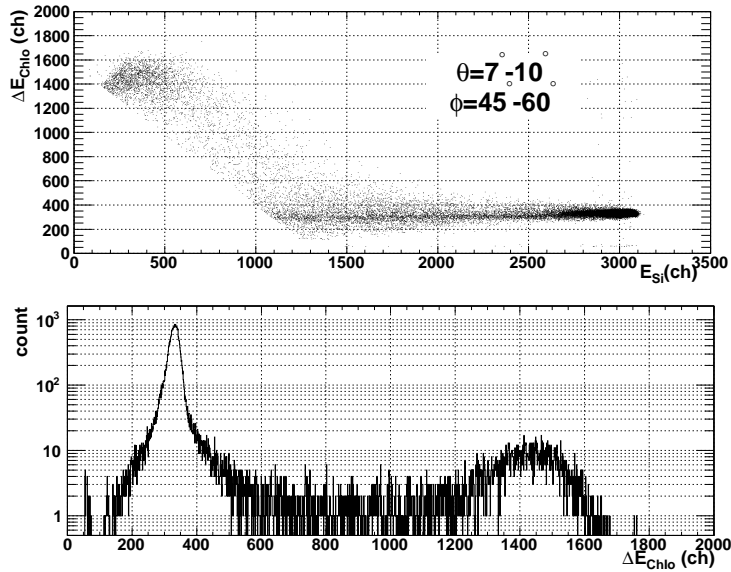
Figure 5.8 – ^{40}Ar+^{60}Ni $\Delta E_{ChIo} - E_{Si}$ spectrum and its ΔE_{ChIo} projection. A part of the spectrum, not related to evaporation residues, has been removed in $\Delta E_{ChIo} - E_{Si}$ spectrum to get a cleaner ΔE_{ChIo} projection.

Therefore the heaviest fragment in each event, lying in the residues region, can be ascribed to quasi-target nuclei if

1. the second heaviest fragment charge is $Z \geq 12$ and it is emitted in the QP polar angular range (see Tab.5.4), fixed by the binary reaction kinematics

2. the second heaviest fragment lies in the same plane of the heaviest fragment

To continue the analysis a border must be set, on $\Delta E - E$ spectra, to separate FE residues from QT fragments.
The borders of the residue region can be chosen taking into account that, if the residue region and the QT region do not overlap, there is a minimum in the cross section as a function of Z when Z increases above $Z \sim 34$ [154] (see Fig.5.7). In Fig.5.8 the obtained $\Delta E_{ChIo} - E_{Si}$ spectrum is shown: the position of the minimum cannot be determined with sufficient precision, so that it is necessary to get a more precise idea of the quasi-target region extension, combining `DIFFIL` code and the `GEMINI` simulation.

5.2.2 GEMINI simulation

`GEMINI` evaporation code can be useful to have an idea of the residue region position in $\Delta E - E$ spectra for different values of the residue emission angle θ. To get
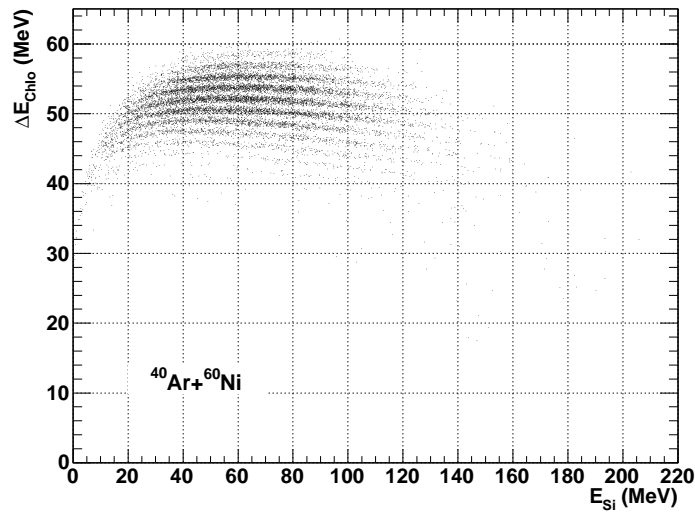
Figure 5.9 – `GEMINI` output filtered by "INDRA experimental filter". Only fusion-evaporation residues have been plotted.

realistic outputs the experimental set-up must be taken into account. The developed "INDRA experimental filter" takes into account:

- the entrance and exit ionization chamber windows ($2.5\mu m$ of mylar each)

- the gas thickness and the gas pressure in the ionization chamber. Special care has been paid to set the correct pressure value in the code, since it determines the energy lost in the ionization chamber

- the silicon thickness ($300\mu m$)

- the ionization chamber and silicon detector energy distribution, which are approximated as a gaussian with a width of 1.5% of the calculated energy loss value.

The energy lost in the target has been neglected[5]. The "experimental filter", evaluating the energy loss in the ionization chamber and the residual energy lost in the silicon detector (by mean of energy loss table [159][6]), permits to reconstruct the expected $\Delta E - E$ spectra, starting from `GEMINI` outputs, and compare them with the experimental ones.

Fig.5.9 shows the residue positions in a simulated $\Delta E - E$ spectrum. As expected, since the residue charge is high ($Z = 33 \div 40$), the residues deposit the larger amount of their kinetic energy in the ionization chamber and only a small residual amount

---

[5]The fused CN lose ~ 0.06 AMeV ($\sim 3\%$ of their initial kinetic energy) in the target assuming the reaction takes place at half of target thickness.

[6]Data are normalized to [160] below 2 AMeV.
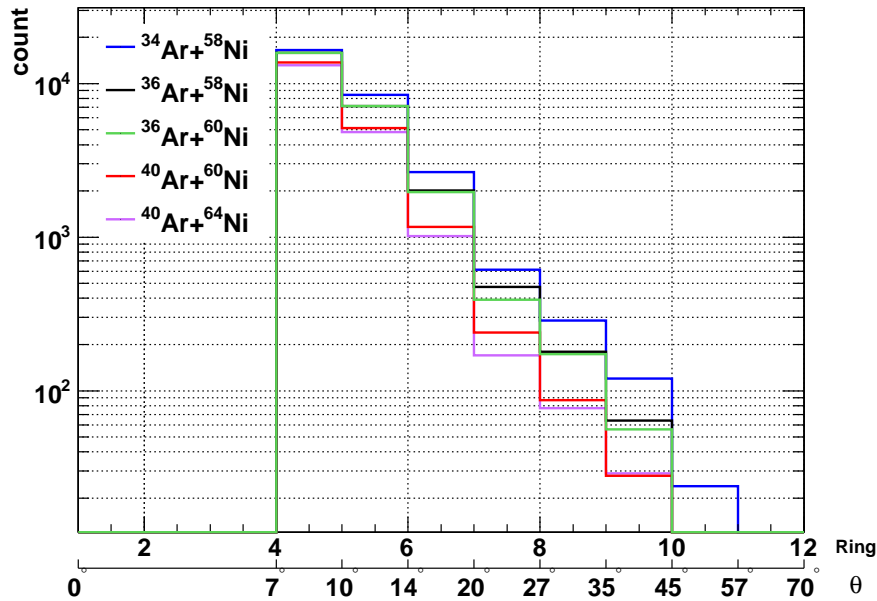
Figure 5.10 – Expected angular distributions for the analyzed reactions obtained with
GEMINI simulation. They suggest the expected decreasing in the fusion-
evaporation residue number as the angle θ increases. When only 4 points are
visible, the 5th is superimposed.

in the silicon detector.

The expected angular distributions of fusion-evaporation events for the five dif-
ferent reactions are shown in Fig.5.10: the statistics decreases by a factor 100 varying
$\overline{\theta_{ring}}$ from 8.5° (ring 4) to 24.5° (ring 7). The same behaviour is present in experimen-
tal data, as shown in Fig.5.11.

During the deexcitation of the compound system, α particles and heavier frag-
ments can be emitted by the hot nucleus, causing the emission of the residue in a
wide angular range, which can extend, as suggested by the GEMINI simulations, up
to $\theta \sim 30°$ (and, with very low probability, up to $\theta \sim 50°$, see Fig.5.10). Increasing
θ, a greater number of residues lie in the region below the Bragg peak, as shown in
Fig.5.12 (see tab 5.5). Moreover increasing θ, the maximum in the Bragg peak popu-
lation moves towards smaller value of residual energy E, suggesting that the residue
kinetic energy decreases increasing the emission angle, as expected from eq.5.14.
These behaviours indicate that a threshold effect could affect the number of detected
residues: indeed, increasing θ, the number of residues which could produce a signal
lower than the silicon CFD threshold increases.
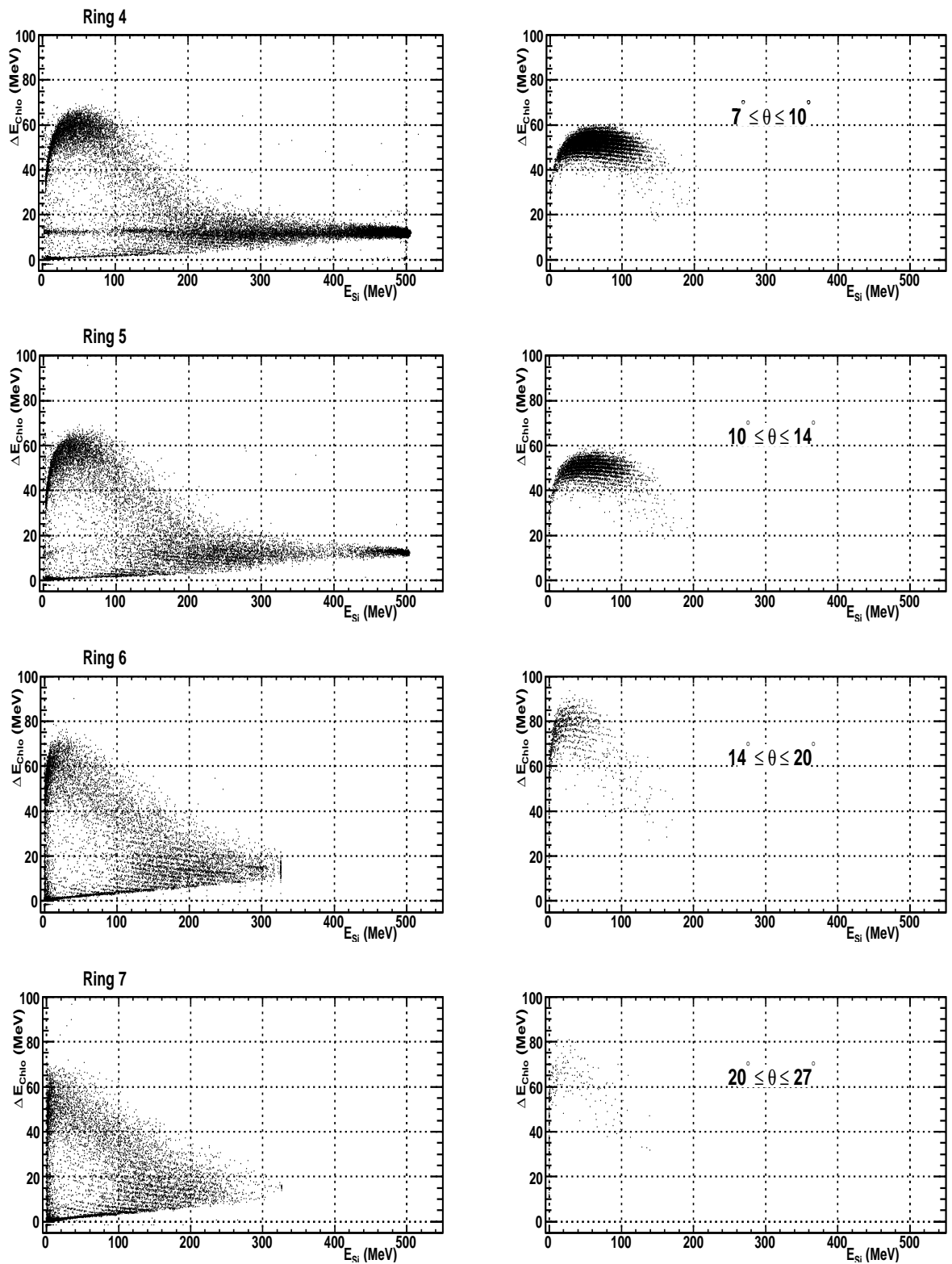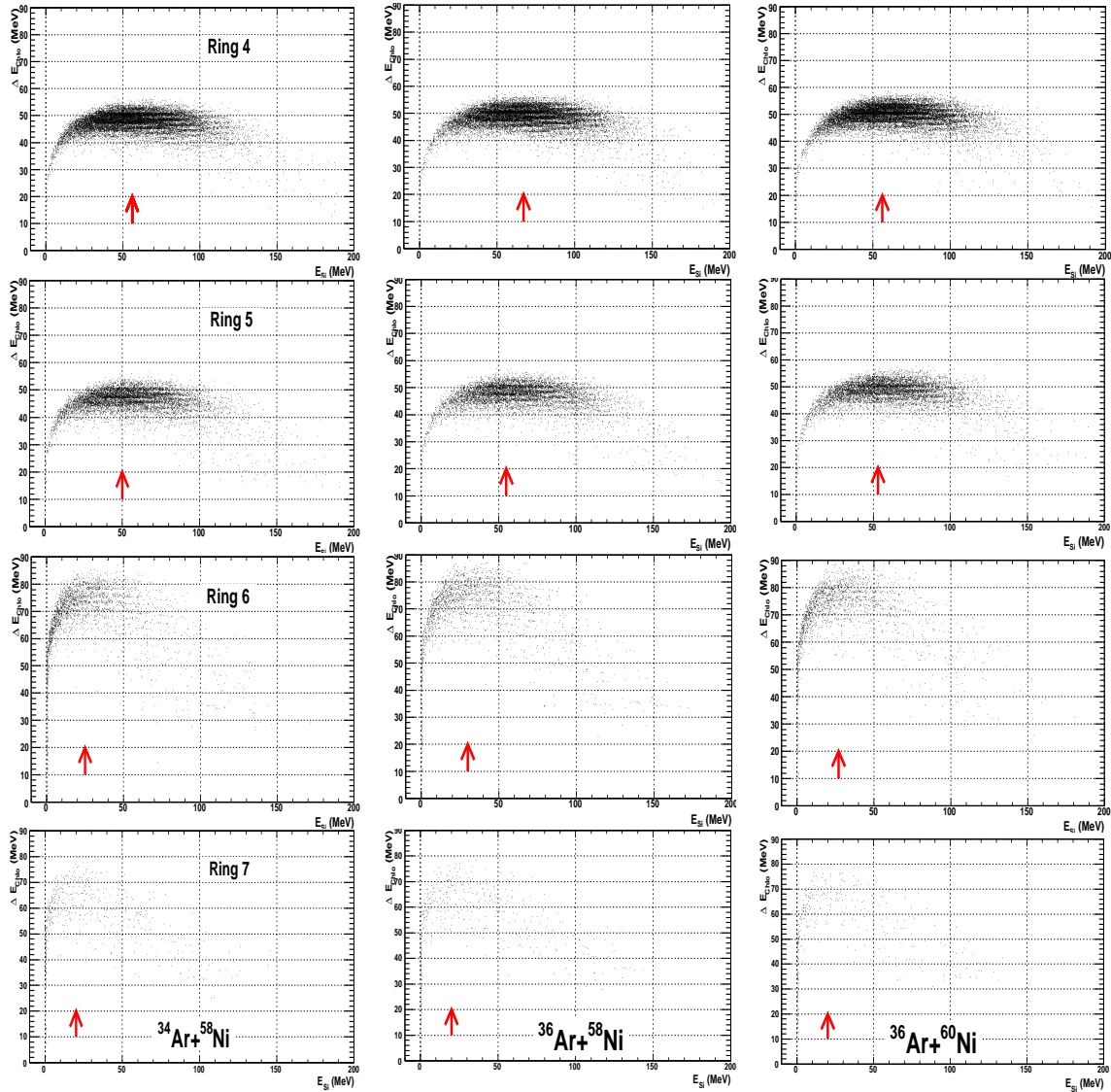A pronounced change is observed (Figs.5.11 and 5.12) between ring 6 and 7: the

Figure 5.11 – Comparison between experimental (left) and simulated (right) $\Delta E - E$ spectra for the ^{40}Ar+^{60}Ni reaction. Simulated data contains only fusion-evaporation residues. A preliminary rough energy calibration (see beyond in the text) has been performed for a better comparison.
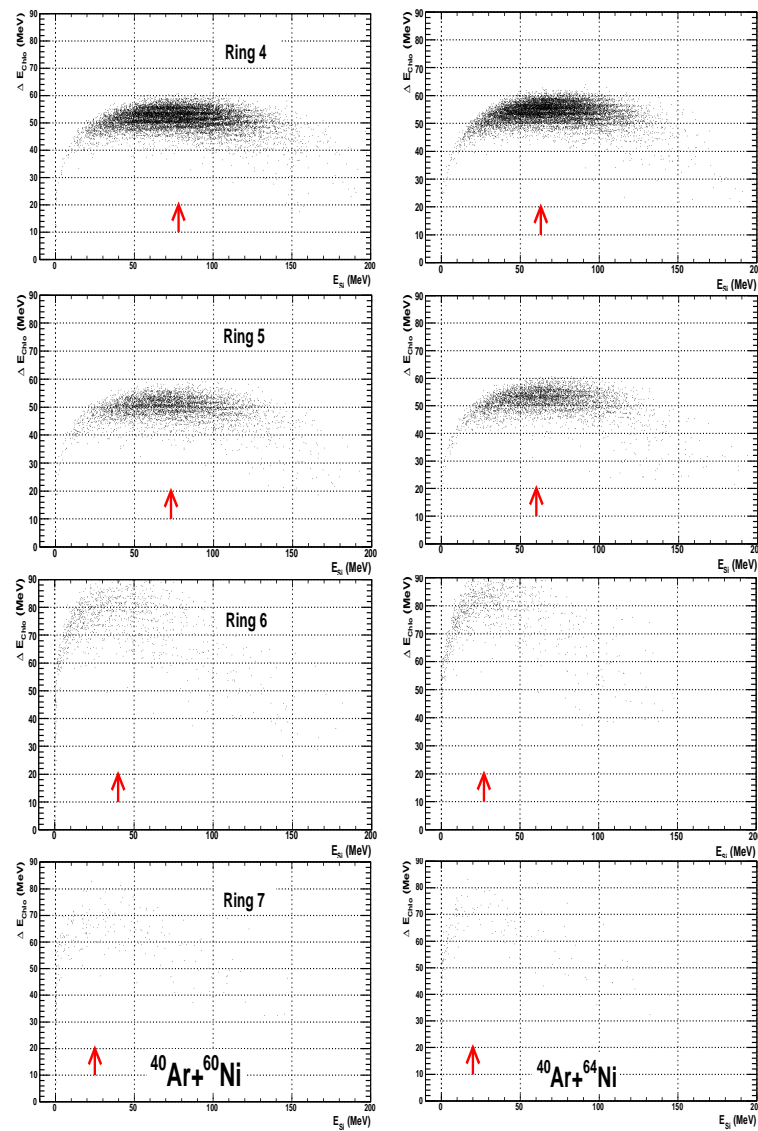
Figure 5.12 – $\Delta E_{ChIo} - E_{Si}$ simulated spectra for rings 4 to 7 for all the analyzed reactions. The arrow indicates the Bragg peak position.

Ring	Percentage of events
4	~ 20%
5	~ 28%
6	~ 43%
7	~ 55%

Table 5.5 – Percentage of residues whose residual energy is smaller than 20 MeV (^{40}Ar+^{60}Ni reaction), according to GEMINI simulation.

statistics clearly decreases, such as the energy deposited in the ionization chamber. It suggests that the contribution of residues could be strongly hidden for rings more backward than ring 7 by the deep inelastic contribution.

In order to compare the experimental data with the simulated ones, a preliminary rough energy calibration has been performed.

Rough energy calibration   The corresponding MeV value (x) of a channel χ, in an energy spectrum, is given by the relation:

$$x(MeV) = a(MeV/ch)(\cdot \chi(ch) - p(ch)) \tag{5.19}$$

where a is the calibration factor and p is the pedestal position, which sets the zero value of the MeV scale.
Two methods have been used to estimate a:

- the analysis of elastically diffused projectiles

- the analysis of α particles emitted by $^{252}_{98}$Cf nuclei[7]

For each $\Delta E - E$ spectrum, two projections on the two axes have been realized. Gaussian fits are performed on the obtained peak, in order to estimate the peaks' positions in ch, both for elastic scattered projectiles (where present) and $^{252}_{98}$Cf's α particles.

Analysis of elastically diffused projectiles   Knowing the beam incident energy and the scattering angle, kinematic relations relate the elastic scattered projectile

---

[7] $^{252}_{98}$Cf fission fragments, produced by a $^{252}_{98}$Cf source used in previous INDRA campaign, can remove $^{252}_{98}$Cf nuclei from the source itself (self–transfer phenomenon [161]). These nuclei implanted in INDRA detectors and, being $t^{252}_{98}Cf_{1/2}$ = 2.6 y, they are still present.

E_α(MeV)	Y_α
6.076	15 %
6.118	82 %

Table 5.6 – Energies (E_α and branching ratio (Y_α) of α particles emitted by $^{252}_{98}$Cf source [162].

kinetic (T_{p_f}) and total energies ($E_{tot_{p_f}}$) at a given angle

$$T_{p_f}(\theta_{proj}) = E_{tot_{p_f}}(\theta_{proj}) - m_p c^2$$

$$E_{tot_{p_f}}(\theta_{proj}) =$$
$$= \frac{2E_{TOT_{sist}}(m_t c^2 E_{TOT_{p_i}} + m_p^2 c^4)}{2(E_{TOT_{sist}}^2 - p_{p_i}^2 c^2 \cos^2\theta_{proj})} +$$
$$+ \frac{p_{p_i} c \cdot \cos\theta_{proj}\sqrt{4(m_t c^2 E_{TOT_{p_i}} + m_p^2 c^4)^2 - 4m_p^2 c^4(E_{TOT_{sist}}^2 - p_{p_i}^2 c^2 \cos^2\theta_{proj})}}{2(E_{TOT_{sist}}^2 - p_{p_i}^2 c^2 \cos^2\theta_{proj})}$$

where

$$\begin{cases} E_{TOT_{sist}} = T_{p_i} + m_p c^2 + m_t c^2 \\ E_{TOT_{p_i}} = T_{p_i} + m_p c^2 \\ p_{p_i} c = \sqrt{E_{TOT_{p_i}}^2 - m_p^2 c^4} \end{cases} \tag{5.20}$$

m_p and m_t are the projectile and target masses (in MeV/c^2) respectively; T_{p_i} and p_{p_i} the incident projectile kinetic energy and momentum, respectively, and θ_{proj} the elastic scattered projectile diffusion angle in laboratory system of reference.
This method is limited to INDRA rings located around the grazing angle for the analyzed reaction.

Analysis of α particles   In rings located at $\theta > \theta_{gr}$ elastically diffused nuclei are no more useful, since their statistics is very low, but these rings can be roughly calibrated in energy taking advantage of α particles emitted by $^{252}_{98}$Cf nuclei. Knowing the emitted α energies (reported in Tab.5.6), it is possible to deduce the calibration factor a.
This method is quite inaccurate because:

1. the α peak is broad (FWHM$_{Si}$ = (0.64 ± 0.08) MeV and FWHM$_{ChIo}$ = (0.28 ± 0.03) MeV)

2. the calibration point obtained with this method is around 6 MeV and it is necessary to extrapolate the linear calibration to energy of the order of 50÷60 MeV in ionization chamber and silicon detectors.

The "INDRA experimental filter" provides the energy loss in the ionization chamber and in silicon detector by elastically diffused projectiles or by α particles, permit-

Ring	a_{ChIo} (MeV/ch)	p_{ChIo} (ch)	a_{Si} (MeV/ch)	p_{Si} (ch)
4	0.04	50	0.16	70
5	0.04	50	0.16	60
6	0.03	50	0.08	15
7	0.03	50	0.07	15

Table 5.7 – Ionization chambers and silicons energy calibration parameters for the "low gain" amplification.

ting to assign a MeV values to the centroid of the calibration energy distribution in ionization chamber and silicon spectrum. The obtained values are listed in Tab.5.7.

Experimental and simulated data comparison   A comparison between the experimental and simulated data is shown in Fig.5.11, where the energy calibration has been applied to the experimental data.

The GEMINI simulation reproduces the global data behaviour (Bragg peak population shift, energy loss decreasing, increasing of counts under the Bragg peak) but does not reproduce at all the Z edges bending[8], being flatter than the experimental one.

The disagreement between the simulated and experimental data in ring 6 can be attributed to the quite inaccurate energy calibration.

In order to verify if the residue region and the QT region overlap in the $\Delta E - E$ spectra, it is necessary to know the region populated by the QT. Using the simulation, for each ring, the energy lost in the ionization chamber and silicon detectors by quasi-target nuclei, emitted at the maximum and minimum angles covered by the detector, have been calculated by DIFFIL code. The calculations have been performed for both Z_{QT} = 28 (the most probable QT Z value in a DIC collision) and Z_{QT} = 33 (the limit QT charge value which affects the residue counts). Once filtered these values by "INDRA experimental filter", it is possible to individuate, on a $\Delta E - E$ simulated matrix, the extension of the quasi-target region. Both kinematic solutions have been plotted. The obtained value are listed in Tab.5.8 (and plotted in Fig.5.14(a)) for the ^{40}Ar+^{60}Ni reaction.

Fig.5.13 shows the position of QT region for the ^{40}Ar+^{60}Ni in $\Delta E - E$ spectrum of ring 4. Both the allowed kinematic solutions have been plotted in the picture for both Z_{QT} = 28 and Z_{QT} = 33. The arrows delimit the QT region for the minimum and maximum angles covered by the ring.

---

[8]This effect is due to the energy loss table used in the "INDRA experimental filter".
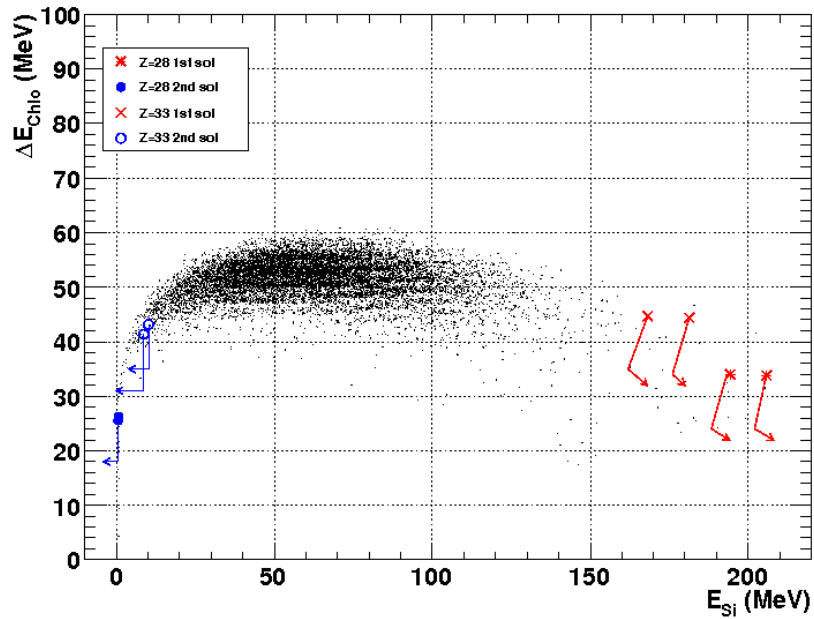
Figure 5.13 – Limits of QT region in a $\Delta E - E$ spectrum for ^{40}Ar+^{60}Ni reaction.

Fig.5.14 shows the positions of quasi targets regions for all the analyzed reactions. Increasing the angle, the deep inelastic contribution increases. QTs populate both the low energy region below the Bragg peak, where the residue number increases increasing the observed angle, and the region related to a high energy loss in silicon detector, up to the elastic region (which is not reported in the picture).

Increasing the observed angle, the overlap between the residue region and the deep inelastic region increases. Therefore, to evaluate the total number of residues in each ring, becomes more and more important to take into account the DIC contribution.

As previously mentioned good criteria to discriminate a residue from a quasi-target nucleus is provided by the analysis of the angular coincidence for each candidate as residue.

The code developed to this aim allows to select a region in a $\Delta E - E$ spectrum (see Fig.5.15(a)) and allows to draw a bidimensional plot, which shows, in ring vs module plane, the number of telescope hit by a heavy fragment ($Z \geq 12$) in coincidence with the one lying in the residue region. If QP energy (see Tab.5.4) is lower than 1 AMeV, the code analyzes the coincidence with particles which stop in the ionization chamber, otherwise with particles with $Z \geq 12$. To this aim it has been necessary to set some Z thresholds on the detected particles.

For each telescope in the forward rings thresholds delimiting the $Z < 4$, $Z < 12$ and $Z < 18$ regions have been drawn for each $\Delta E - E$ correlation, both $\Delta E_{ChIo} - E_{Si}$

(a)

(b)

(c)
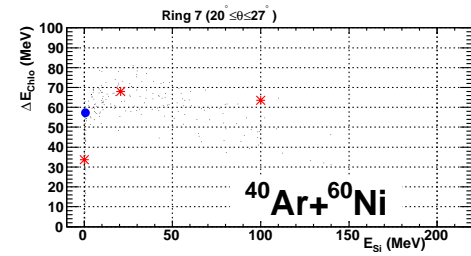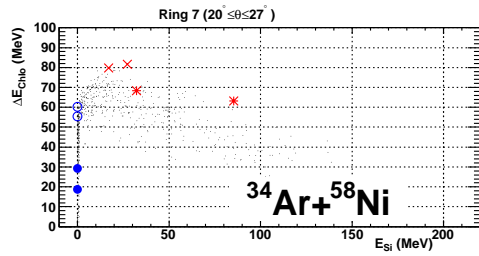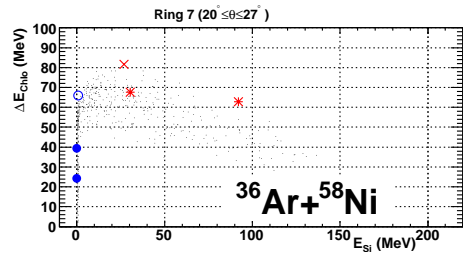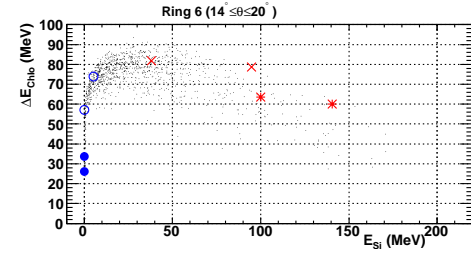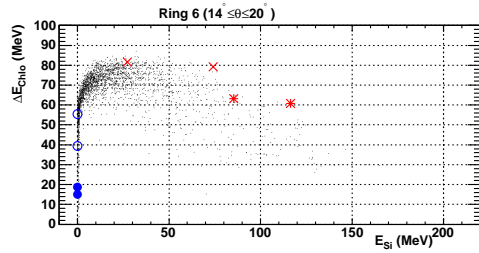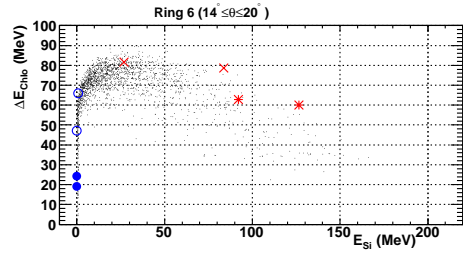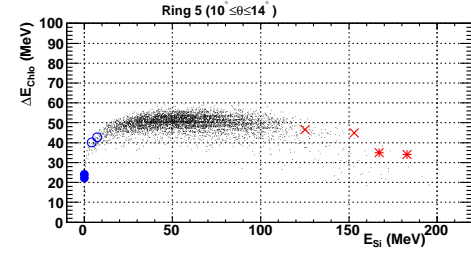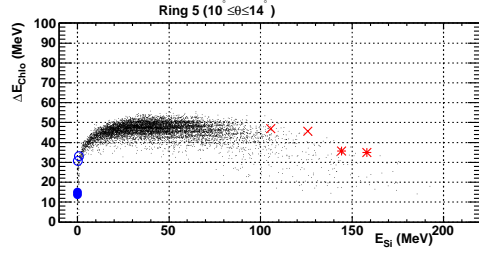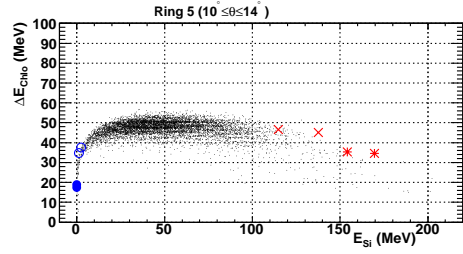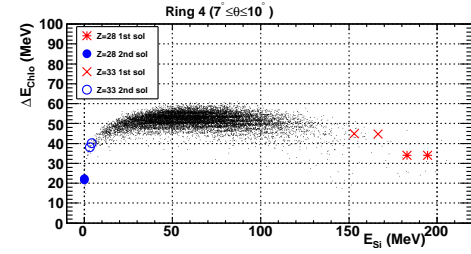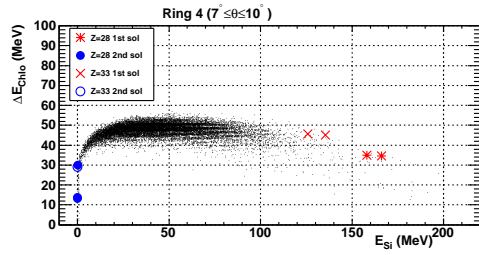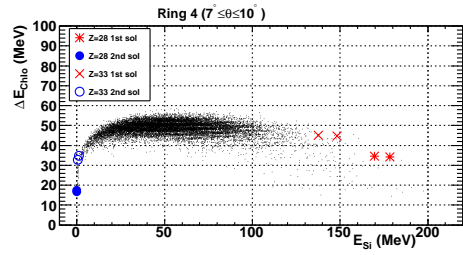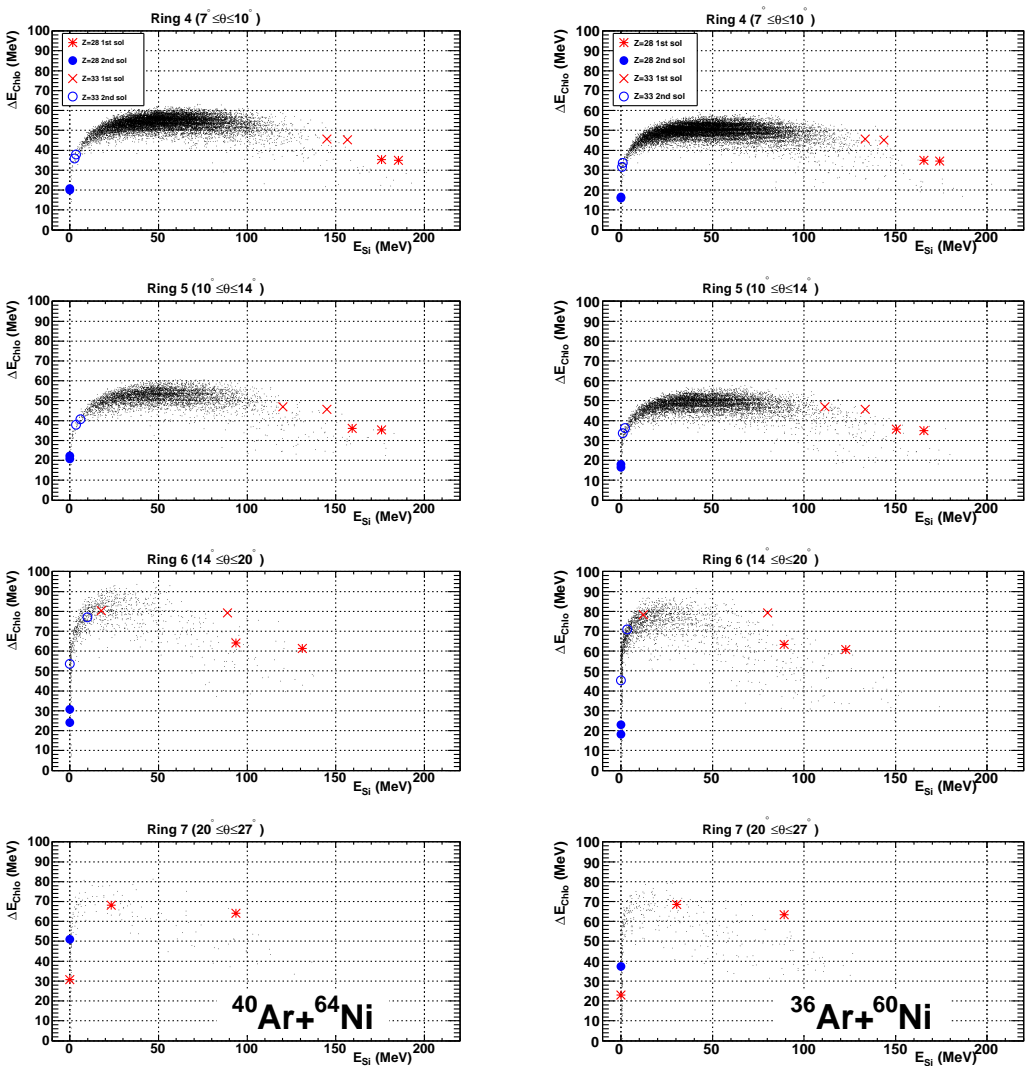
Figure 5.14 – For each ring, the energy lost in the ionization chamber and silicon detectors by quasi-target nuclei, emitted at the maximum and minimum angles covered by the detector, are plotted on simulated $\Delta E_{Chlo} - E_{Si}$ spectra.

Ring	p(mbar)	θ_{QT}	Z_{QT}	E_{QT}(MeV)	$E_{loss_{chio}}$ (MeV)	$E_{loss_{si}}$ (MeV)
		7°	28	256.1	34.0	194.4
				36.9	21.7	╱
		10°	28	247.2	34.3	183.0
4	30			38.2	22.3	╱
		7°	33	248.2	44.7	166.4
				66.6	38.1	3.2
		10°	33	235.8	45.0	153.0
				70.1	40.1	4.2
		10°	28	247.2	34.3	183.0
				38.2	22.3	╱
		14°	28	230.4	35.3	167.1
5	30			41.0	24.1	╱
		10°	33	235.8	45.0	153.0
				70.1	40.1	4.2
		14°	33	211.1	46.5	125.1
				78.3	42.7	7.3
		14°	28	230.4	60.0	140.6
				41.0	26.2	╱
		14°	33	211.1	78.6	94.8
6	50			78.3	57.1	╱
		20°	28	193.7	63.6	100.1
				48.8	33.6	╱
		19°	33	155.7	81.8	35.1
				106.2	73.8	5.2
		20°	28	193.7	63.6	100.1
7				48.8	33.6	╱
		27°	28	118.9	68.0	20.7
				79.5	57.2	0.8

Table 5.8 – For each ring the lower and the upper polar angle are chosen as QT emission angle (θ_{QT}). The corresponding QT kinetic energy E_{QT} is reported, considering both kinematic solutions. The energy loss in the ionization chamber and in silicon detector are evaluated by the experimental filter. Computations have been performed for QT charge Z_{QT} = 28 and Z_{QT} = 33 for the ^{40}Ar+^{60}Ni reaction.

(a) $\theta = 7° \div 10°$, $\phi = 45° \div 50°$

(b)
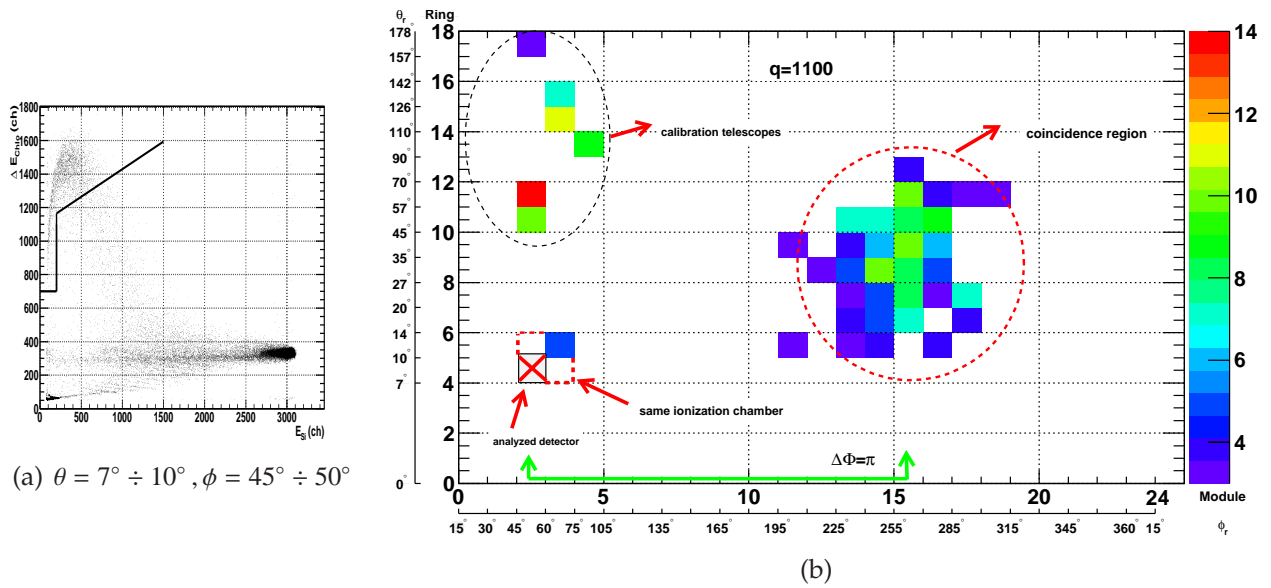
Figure 5.15 – a) Selection of a residue region on a $\Delta E_{ChIo}-E_{Si}$ spectrum in ^{40}Ar+^{60}Ni reaction. The selected residue region includes the Bragg peak. b) Ring vs. module spectrum obtained by the code to estimate the QT events presents in the selected residue region.

and $\Delta E_{Si} - E_{CsI}$ correlations. In particular the following regions have been selected:

$Z > 4$ **region** It delimites the light particles region. In the backward rings (10 ÷ 17) the thresholds have been set on $\Delta E_{ChIo} - E_{CsI(Tl)}$ correlations, while in the forward rings (4 ÷ 9), since light particles have enough energy to punch-through the silicon detector, the thresholds have been set on $\Delta E_{Si} - E_{CsI(Tl)}$ correlations.

$Z > 12$ **region** It delimites the lower limit to the quasi-projectile region. Kinematic considerations suggest that the QP allowed angular range is between $\theta \sim 30°$ and $\theta \sim 148°$ (see Tab.5.4), but the statistics permits to identify $Z = 12$ only for $\theta < 90°$. Therefore thresholds have been set for rings 8 ÷ 12 in $\Delta E_{ChIO} - E_{Si}$ and $\Delta E_{ChIO} - E_{CsI}$ spectra.

$Z > 18$ **region** It indicates the lower part of the fission fragments region: evaporation and fission compete in deexcitation process of hot compound system and, while evaporation is characterized by an heavy residues, with mass close to the one of the compound nucleus, symmetric fission is characterized by the presence of two "big" fragments, with mass close to one-half of the compound system mass.

The code permits, as well as to estimate the QT events present in the selected residues region (N_{DIC}), to extract:

- the total number of events lying in the residue region N_i

- the number of cross talk events, which have to be removed (see §A.1)

- the number of particles which hit the same ionization chamber (see §A.2)

- the number of events with a heavy fragment in coincidence with $Z \geq 18$

Fig.5.15(b) shows the positions of heavy fragments, which stop in the ionization chambers, detected in coincidence (`coincidence region`) with fragments in the residue region selected in Fig.5.15(a). "Particles hit the same ionization chamber" events can be easily identified since they produce an increase of counts in detectors placed behind the same ionization chamber of the analyzed silicon detector. As a first approximation calibration telescope have not been analyzed, so that their contribution has been removed from the computing. Most of the counts are confined in a restricted region around ring 8 module 15 ($\theta = 27° \div 35°$, $\phi = 225° \div 240°$) which presents the maximum count. This telescope is located on the reaction plane ($\Delta\Phi = \pi$), suggesting the presence, in the selected region, of DI fragments.

Expanding the selected residues region, as shown in Fig.5.16, the corresponding coincidence region in ring vs module plane (see Fig.5.17) expands, being centered around the same telescope. The percentage of deep inelastic contribution in each selected residue region is reported in Fig.5.16. This behaviour is consistent with the fact that deep inelastic region lies between the residues and the elastic ones, and, expanding the selected region, a part of deep inelastic region is included.
Figs.5.16 and 5.18 show the increase of deep inelastic contribution to the residues region as the observed polar angle increases. As predicted by the previous analysis, the deep inelastic contribution is more and more significant for less forward rings.
In ring 7 a large percentage of deep inelastic contribution lies in the region below the Bragg peak. In this case it is impossible to separate deep inelastic from fusion-evaporation events, so that the obtained total residues number will set just the upper limit.

The chosen criteria to select the residue region is the requirement of a maximum deep inelastic contribution of 1% in ring 4, i.e. the contribution to the residual count of the deep inelastic products is limited to $\sim$ 1%. In backward rings the tolerated deep inelastic contribution is greater (up to $\sim$ 20% in ring 7 for the $^{40}Ar+^{60}Ni$ reaction), being the two regions more overlapped.
Fully relaxed deep inelastic contribution can be estimated thanks to [154]. Being a light fragment ($Z < 12$) emitted in coincidence with the heavy one ($Z \geq 34$), the
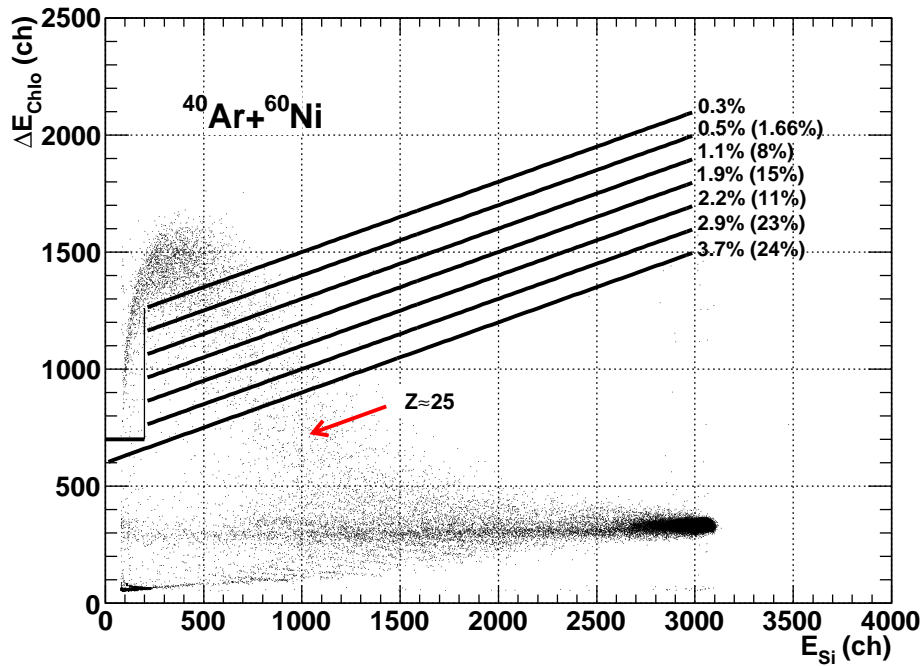
Figure 5.16 – Selection of different residue regions. The percentage indicates the DI contribution integrated in the region over the line. The parenthetical percentage is the DI contribution in the region between two lines.
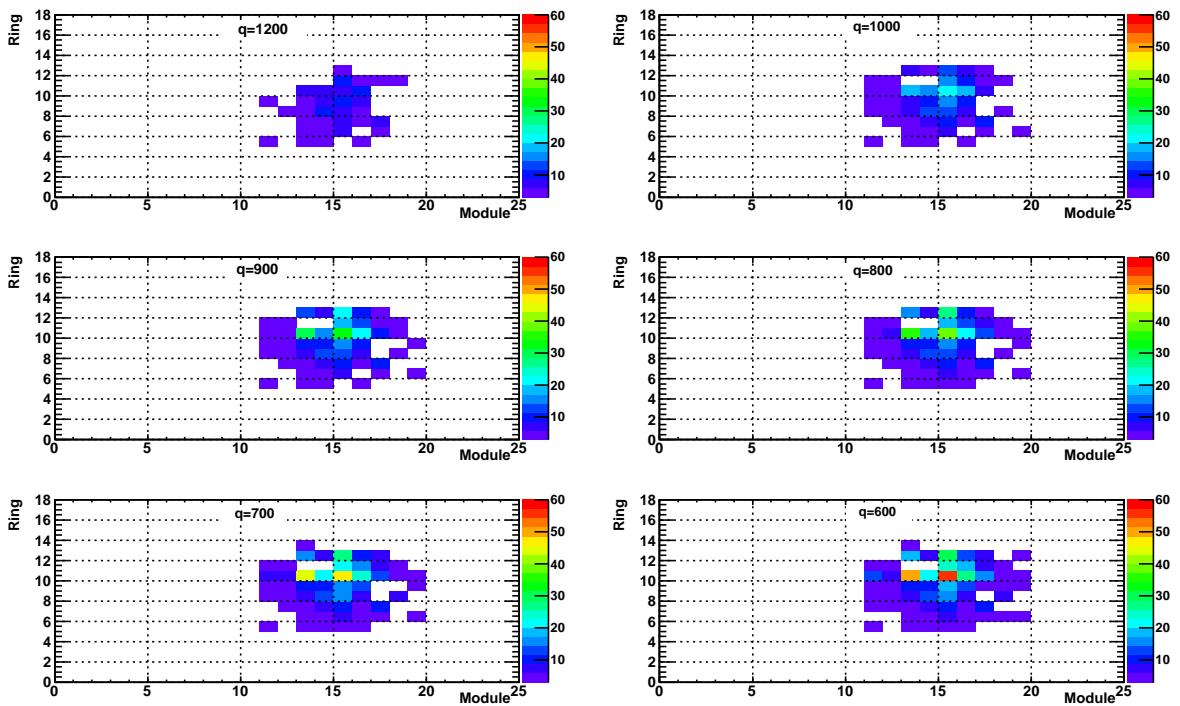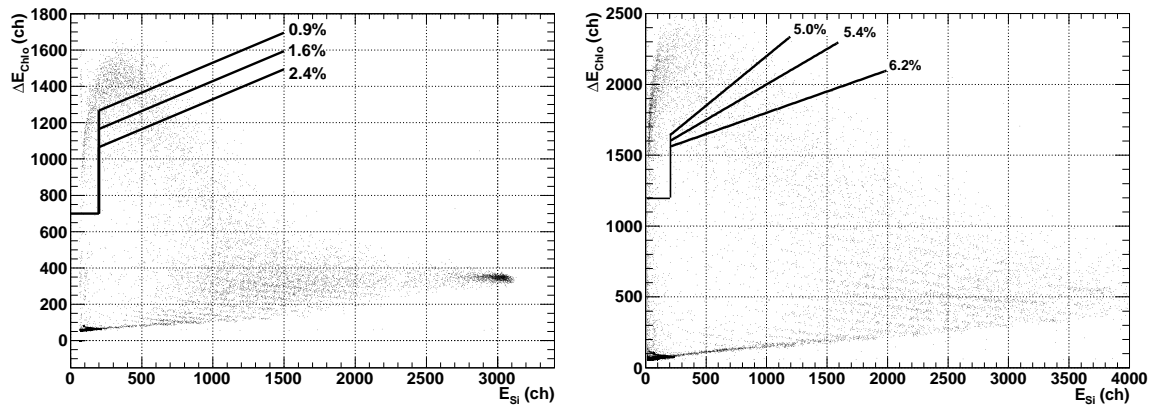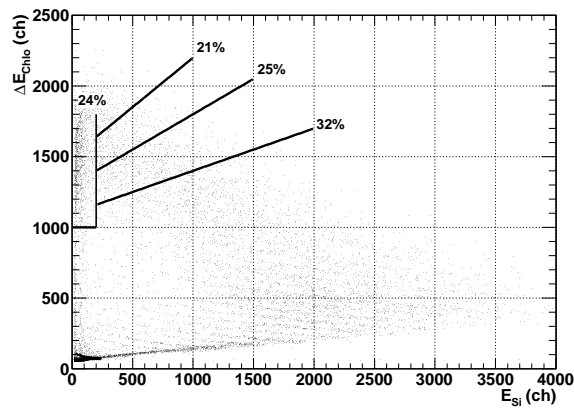

Figure 5.17 – Coincidence regions corresponding to the different residues region selected in Fig.5.16.

(a) Ring 5: $10° \leq \theta \leq 14°$

(b) Ring 6: $14° \leq \theta \leq 20°$

(c) Ring 7: $20° \leq \theta \leq 27°$

Figure 5.18 – Selection of different residue region and DI contribution percentage there in, for increasing polar angle for the ^{40}Ar+^{60}Ni reaction. The residue region shapes have been chosen depending on the polar angles covered by each ring.

Z	σ_Z
5	6.8
6	22.7
7	10.5
8	14.55
9	7.5
10	16.0
11	28.3
12	31.0
$5 \div 12$	137.35
$13 \div 24$	552.8
σ_{tot}	690.15

Table 5.9 – Cross section in mbarn, integrated over θ, for detected nuclei resulting from DIC in reaction ^{40}Ar+^{58}Ni at 7 AMeV incident energy [154].

fully relaxed QT cross section is equal to the $Z < 12$ DI fragments cross section (see Tab.5.9) and represent $\sim$ 25% of the DI $Z > 12$ cross section. This contribution has been taken into account in the estimation of DI contribution.
Once selected the residue region in each detector, following these criteria, the number of fragments lying in this region has been counted.

5.2.3 Cross section determination

Due to the axial symmetry of the fusion evaporation reactions, the number of evaporation residues can be evaluated in a selected $\Delta\phi$ region for each ring, in order not to include in the counts also not properly running detectors (see §4.2.1). Therefore fusion-evaporation events have been counted in a limited region in $\Delta\phi$ for a $7° \leq \theta \leq 27°$ for each reactions. The selected $\Delta\phi$ region is the same for all the analyzed rings and reactions: $\Delta\phi = 45° \div 180°$

For each ring the total number of detected residues ($\overline{R}$) in a detector is the mean value over the measured values (R_i) in the n modules of the $\Delta\phi$ selected region:

$$\overline{R} = \frac{\sum_{i=1}^{n} R_i}{n} \tag{5.21}$$

where n is the number of analyzed telescopes.
The percentage of DI coincidence introduces a systematic error in computing the residues, which has been taken into account.
The uncertainty has been obtained by the quadratic sum of the statistical (σ_{stat}) and

systematic errors (σ_{sist}), being the two contribution independent:

$$\frac{\Delta\overline{R}}{\overline{R}} = \sqrt{\left(\left.\frac{\Delta\overline{R}}{\overline{R}}\right|_{stat}\right)^2 + \left(\left.\frac{\Delta\overline{R}}{\overline{R}}\right|_{sist}\right)^2} \tag{5.22}$$

where the statistical uncertainty $\left.\frac{\Delta\overline{R}}{\overline{R}}\right|_{stat}$ is given by

$$\left.\frac{\Delta\overline{R}}{\overline{R}}\right|_{stat} = \frac{1}{\sqrt{\sum_{i=1}^{n} R_i}} \tag{5.23}$$

The systematic uncertainty, due to the deep inelastic contribution present in the residues region, can be estimated as:

$$\left.\frac{\Delta\overline{R}}{\overline{R}}\right|_{sist} = \frac{\sum_{i=1}^{n} N_{DIC_i}}{\sum_{i=1}^{n} R_i} \tag{5.24}$$

where N_{DIC_i} is the number of heavy fragments, in each analyzed detectors, which, according to our criteria, are QT fragments.

Fusion-evaporation differential cross section is given by:

$$\frac{d\sigma_{FE}}{d\theta} = \frac{\overline{R}}{\Delta\theta}$$

$$\tag{5.25}$$

$$\frac{\Delta(\frac{d\sigma_{FE}}{d\theta})}{\frac{d\sigma_{FE}}{d\theta}} = \frac{\Delta\overline{R}}{\overline{R}}$$

where $\Delta\theta$ is the polar angular aperture of the detector of each ring. The angular uncertainty is given by the detector angular aperture.

The obtained cross section values are expressed in counts/rad and have to be converted in mbarn/rad to compare different behaviours corresponding to different reactions. However we remark that, for all the reactions, the $\frac{d\sigma_{FE}}{d\theta}$ obtained for $20° \leq \theta \leq 27°$ represents the upper limit of the fusion-evaporation cross section, due to the high deep inelastic contribution in this region.

Mbarn/count conversion factor   Evaporation residue cross section has been normalized with respect to the yields of elastic scattered beam particles measured in first INDRA ring.

As previously discussed, the number of elastic events hitting a detector i, N_i, should be costant over all detectors belonging to the same ring if the beam is correctly

aligned. It is therefore necessary to take into account the beam mis-alignment and to correct by a factor $K_i(\phi_{r_i}, \theta_b, \phi_b)$ each N_i in order to obtain a unique $\overline{N_{ring}}_4$ value for all detectors on the ring.

For each detector i

$$N_{\frac{ring}{4}i} = \frac{N_i}{K_i(\phi_{r_i}, \theta_b, \phi_b)}$$

$$\frac{\Delta N_{\frac{ring}{4}i}}{N_{\frac{ring}{4}i}} = \frac{\Delta N_i}{N_i} + \frac{\Delta K_i}{K_i}$$

(5.26)

assuming, as a first approximation, that N_i and K_i are independent.

The correction factor $K_i(\phi_{r_i}, \theta_b, \phi_b)$ for each detector is defined as

$$K_i(\phi_{r_i}, \theta_b, \phi_b) = \frac{f(\phi_{r_i}, C, \theta_b, \phi_b)}{f(\phi_{r_i}, C, \theta_b = 0, \phi_b = 0)}$$

(5.27)

where $f(\phi_{r_i}, C, \theta_b, \phi_b)$ is the expected number of elastic projectile nuclei hitting the detector i (whose mean azimuthal angle is ϕ_{r_i}), taking into account the beam mis-alignment (see eq.5.5). $f(\phi_{r_i}, C, \theta_b = 0, \phi_b = 0)$ would be the expected number of elastic projectile nuclei hitting the detector i if the beam was aligned, i.e.:

$$f(\phi_{r_i}, C, \theta_b = 0, \phi_b = 0) = \int_{\Theta_{R4}^{MIN}}^{\Theta_{gr}} \frac{1}{\sin^4 \frac{\theta}{2}} d\theta$$

(5.28)

where Θ_{R4}^{MIN} is the the minimum polar angle in CM covered by each detector, corresponding to $\theta_{R4}^{MIN} = 7°$ in LAB.

The uncertainty on the correction factor K_i is given

$$\frac{\Delta K_i}{K_i} = \frac{\Delta f(\phi_{r_i}, C, \theta_b, \phi_b)}{f(\phi_{r_i}, C, \theta_b, \phi_b)}$$

(5.29)

where

$$\Delta f(\phi_{r_i}, C, \theta_b, \phi_b) = \left| \frac{\partial f(\phi_{r_i}, C, \theta_b, \phi_b)}{\partial \theta_b} \right| \Delta \theta_b + \left| \frac{\partial f(\phi_{r_i}, C, \theta_b, \phi_b)}{\partial \phi_b} \right| \Delta \phi_b.$$

(5.30)

The partial derivatives can be expressed as:

$$\frac{\partial f(\phi_{r_i}, C, \theta_b, \phi_b)}{\partial \theta_b} = \frac{\partial f(\phi_{r_i}, C, \theta_b, \phi_b)}{\partial \Theta_{V_i}} \frac{\partial \Theta_{V_i}}{\partial \theta_{V_i}} \frac{\partial \theta_{V_i}}{\partial \theta_b}$$

$$\frac{\partial f(\phi_{r_i}, C, \theta_b, \phi_b)}{\partial \phi_b} = \frac{\partial f(\phi_{r_i}, C, \theta_b, \phi_b)}{\partial \Theta_{V_i}} \frac{\partial \Theta_{V_i}}{\partial \theta_{V_i}} \frac{\partial \theta_{V_i}}{\partial \phi_b}$$

(5.31)

From eq.5.5 one gets:

$$\frac{\partial f(\phi_{r_i}, C, \theta_b, \phi_b)}{\partial \Theta_{V_i}} = \frac{-1}{\sin^4\left(\frac{\Theta_{V_i}}{2}\right)} \tag{5.32}$$

and, from eq.5.6,

$$\frac{\partial \Theta_{V_i}}{\partial \theta_{V_i}} = -\sin\theta_{V_i} \cdot \frac{2\frac{m_p}{m_t}\cos\theta_{V_i} + \sqrt{1 - \left(\frac{m_p}{m_t}\sin\theta_{V_i}\right)^2} + \left(\frac{m_p}{m_t}\cos\theta_{V_i}\right)^2\left[1 - \left(\frac{m_p}{m_t}\sin\theta_{V_i}\right)^2\right]^{-\frac{1}{2}}}{\sqrt{1 - \left(-\frac{m_p}{m_t}\sin^2\theta_{V_i} + \cos\theta_{V_i}\sqrt{1 - \left(\frac{m_p}{m_t}\sin\theta_{V_i}\right)^2}\right)^2}} \tag{5.33}$$

Combining eqs. 5.7÷5.9, the derivatives of eq.5.10 are

$$\frac{\partial \theta_{V_i}}{\partial \theta_b} = \frac{\sin\theta_b \frac{\overline{OT}^2 + \overline{TR}^2 - \overline{OR}^2}{2 \cdot \overline{OT} \cdot \overline{TR}} - \cos\theta_b \frac{\overline{OR}}{\overline{TR}}\cos(\phi_{r_i} - \phi_b)}{\sqrt{1 - \left[\cos\theta_b \frac{\overline{OT}^2 + \overline{TR}^2 - \overline{OR}^2}{2 \cdot \overline{OT} \cdot \overline{TR}} + \frac{\overline{OR}}{\overline{TR}}\sin\theta_b \cos(\phi_{r_i} - \phi_b)\right]^2}} \tag{5.34}$$

$$\frac{\partial \theta_{V_i}}{\partial \phi_b} = -1 \cdot \frac{\frac{\overline{OR}}{\overline{TR}}\sin(\phi_{r_i} - \phi_b)\sin\theta_b}{\sqrt{1 - \left[\cos\theta_b \frac{\overline{OT}^2 + \overline{TR}^2 - \overline{OR}^2}{2 \cdot \overline{OT} \cdot \overline{TR}} + \frac{\overline{OR}}{\overline{TR}}\sin\theta_b \cos(\phi_{r_i} - \phi_b)\right]^2}}$$

For each detector N_i has been corrected according to eq.5.26 and the obtained values $N_{ring_{4\,i}} \pm \Delta N_{ring_{4\,i}}$ have been plotted in Fig.5.19.

    Values are normalized to an arbitrary value to highlight the relative differences. As expected, N_{ring_4} in function of ϕ_r is costant. A costant fit has then been performed to extrapolate the best $\overline{N_{ring_4}} \pm \Delta\overline{N_{ring_4}}$ value.

    The *mbarns/counts* conversion factor (μ) is given by

$$\mu = \frac{\sigma_{Ruth}(\theta_{R4}^{MIN} \div \theta_{R4}^{MAX})}{N_{ring_4}} \tag{5.35}$$

where $\sigma_{Ruth}(\theta_{R4}^{MIN} \div \theta_{R4}^{MAX})$ is the integrated Rutherford cross section in the angular range covered by the first INDRA ring (ring 4).

In the evaluation of the integrated Rutherford cross sections, an attempt of taking into account the behaviour of $\sigma_{el}/\sigma_{Ruth}$ around Θ_{gr} has been done. Being Θ_{gr} the angle at which $\sigma_{el}/\sigma_{Ruth} = 1/4$, integrating up to Θ_{gr} with $\sigma_{el} = \sigma_{Ruth}$, an overestimation of the elastic cross sections is obtained. In Ref. [163], the elastic scattering angular distributions for ^{40}Ar+^{109}Ag at energies up to 8.4 AMeV are reported. To our knowledge no data for Ar+Ni reactions at ~ 13 AMeV energy are present in literature.

(a) ^{34}Ar+^{58}Ni

(c) ^{36}Ar+^{58}Ni

(b) ^{36}Ar+^{60}Ni

(d) ^{40}Ar+^{60}Ni

(e) ^{40}Ar+^{64}Ni
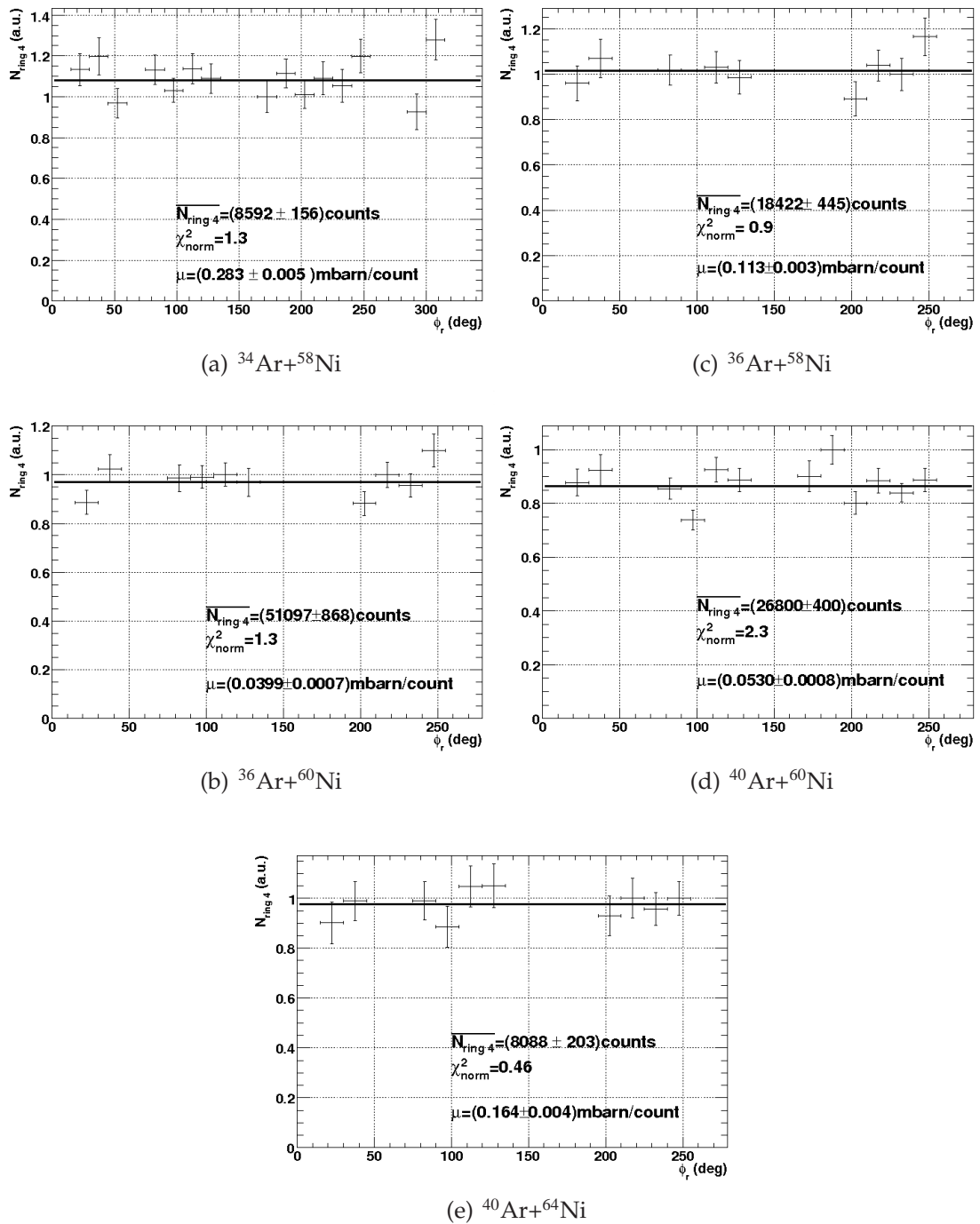
Figure 5.19 – "Corrected" total collected elastic events $N_{ring_4\,i}$ in the detector i (normalized to 1) versus the detector mean azimuthal angle ϕ_{r_i}. The behaviour is flat, as expected. The full line is the costant fit result.

A theoretical calculation of the elastic scattering angular distributions has been performed by E. Khan and H. Sy Than[9] for all the reactions. The calculation is based on

---
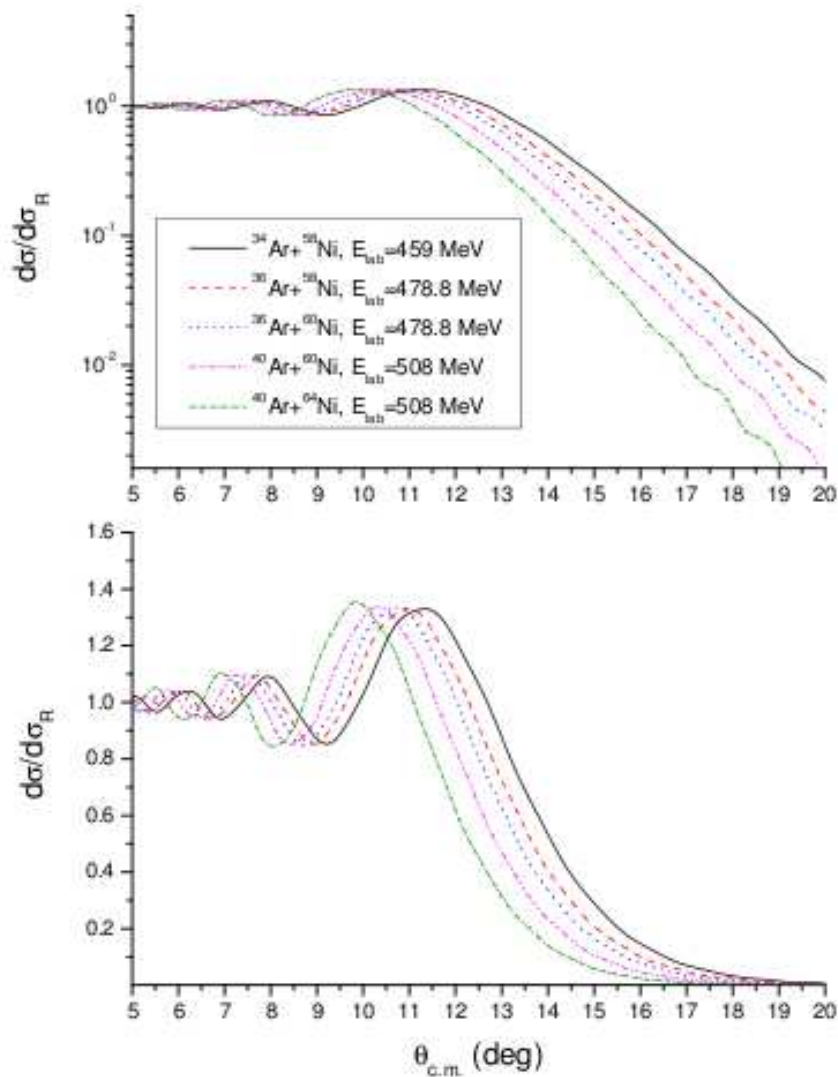
Figure 5.20 – Elastic scattering angular distributions for the five analysed reactions.

a purely microscopic model: proton and neutron densities have been determined by using the HF Gogny interaction, while a double folding potential has been used to deduce the optical potential. The calculation has been performed in the distorted-wave Born approximation (DWBA) and the obtained angular distributions are plotted in Fig.5.20.

Referring to the ^{40}Ar+^{109}Ag at 8.4 AMeV reaction, the elastic scattering angular
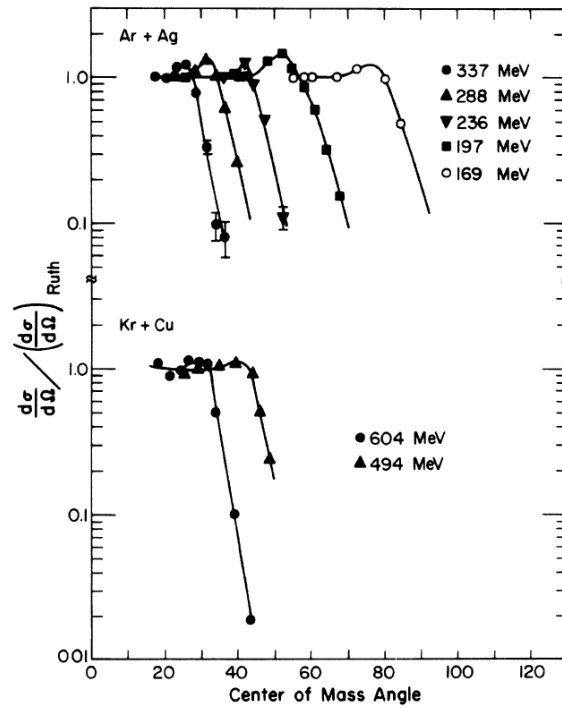
Figure 5.21 – Elastic scattering angular distributions for the Ar+Ag and Kr+Cu reactions. Curves are normalized at 1.0 in the region where count rate to Rutherford cross section ratios were constant. Picture is taken from [163].

distribution shown in Fig.5.21 can be parametrized as:

$$\frac{\frac{d\sigma}{d\Theta}\big|_{el}}{\frac{d\sigma}{d\Theta}\big|_{Ruth}} = 1 \qquad\qquad \Theta \leq \Theta_{gr} - 4°$$

$$\frac{\frac{d\sigma}{d\Theta}\big|_{el}}{\frac{d\sigma}{d\Theta}\big|_{Ruth}} = e^{-k(\Theta - \Theta_{gr} + 4°)} \qquad \Theta \geq \Theta_{gr} - 4°$$

(5.36)

where the coefficient $k = -0.3466$ has been obtained by fitting the angular distribution. The Rutherford cross sections have then been integrated in INDRA ring 4 angular range by weighting $\frac{d\sigma}{d\Omega}$ for the exponential factor in the region $\Theta \geq \Theta_{gr} - 4°$. The presence of an eventual isotopic dependence has been neglected, assuming the same slope of the exponential decrease for all the systems, being the available energies much greater than the Coulomb barrier. Moreover also possible isotopic effects on the grazing angles have been neglected, since no parametrizations have been found in literature.

$\sigma_{Ruth}(\theta_{R4}^{MIN} \div \theta_{R4}^{MAX})$, $\overline{N_{ring_4}} \pm \Delta\overline{N_{ring_4}}$ and μ values are listed in Tab.5.10 for the different reactions.

	θ_{gr}	σ_{Ruth} (barn)	$\overline{N_{ring}}_{4}$ (counts)	μ (mbarn/count)
^{34}Ar+^{58}Ni	10.2078°	1.73	8590 ± 155	0.201 ± 0.004
^{36}Ar+^{58}Ni	9.6622°	1.61	18420 ± 445	0.087 ± 0.002
^{36}Ar+^{60}Ni	9.5808°	1.22	51100 ± 870	0.0239 ± 0.0004
^{40}Ar+^{60}Ni	8.8485°	0.74	26800 ± 400	0.0275 ± 0.0004
^{40}Ar+^{64}Ni	8.7102°	0.67	8090 ± 200	0.083 ± 0.002

Table 5.10 – Rutherford cross sections integrated over ring 4 solid angle(σ_{Ruth}), mean value of number of elastic events hitting each detector of ring 4 ($\overline{N_{ring}}_{4}$) and conversion factor μ for all the reactions.

The relative uncertainty on μ is the relative uncertainty on $\overline{N_{ring}}_{4}$, given by the fit procedure:

$$\frac{\Delta\mu}{\mu} = \frac{\Delta\overline{N_{ring}}_{4}}{\overline{N_{ring}}_{4}}. \tag{5.37}$$

The fusion-evaporation differential cross section is given by:

$$\frac{d\sigma_{FE}}{d\theta} = \frac{\overline{R}}{\Delta\theta}(count/rad) \cdot \mu(mbarn/count)$$

$$\frac{\Delta(\frac{d\sigma_{FE}}{d\theta})}{\frac{d\sigma_{FE}}{d\theta}} = \frac{\Delta(\frac{\overline{R}}{\Delta\theta})}{\frac{\overline{R}}{\Delta\theta}} + \frac{\Delta\mu}{\mu} \tag{5.38}$$

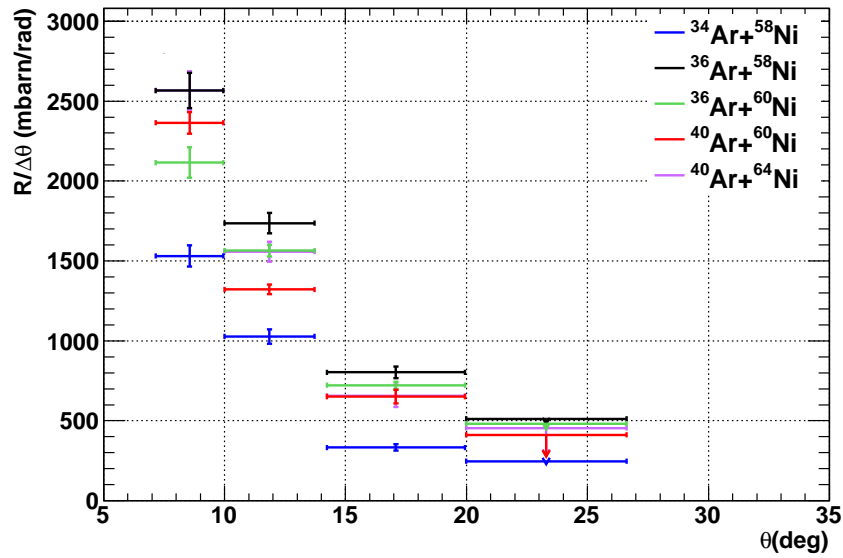The obtained fusion evaporation differential cross sections are plotted in Fig.5.22.

Figure 5.22 – Measured differential fusion-evaporation cross sections. When only 4 points are visible, the 5th is superimposed.
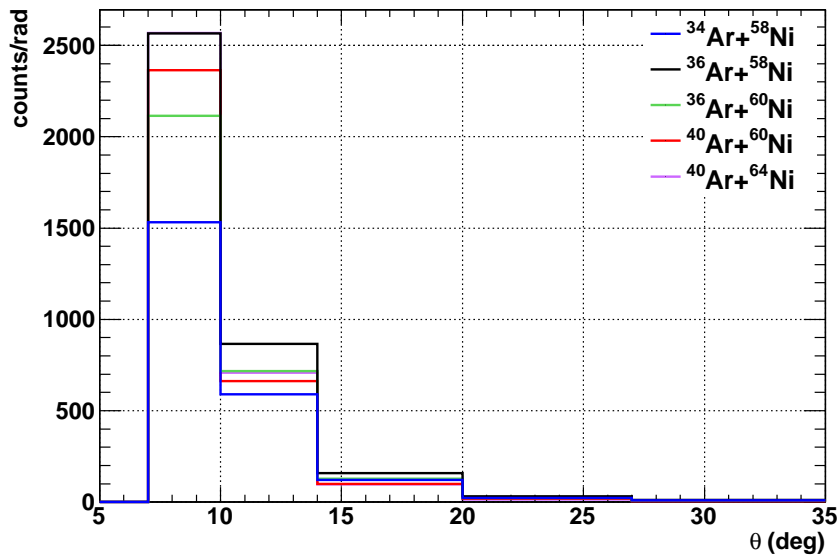

Figure 5.23 – GEMINI differential fusion-evaporation cross sections. When only 4 points are visible, the 5th is superimposed.

5.3 Conclusions

Differential fusion-evaporation cross sections measured for Ar+Ni are listed in Tab.5.11 and shown in Fig.5.22. Results obtained with GEMINI simulation are also displayed in Fig.5.23 for comparison.

Once normalized GEMINI to experimental data, both distributions show the same

Ring	$\frac{\bar{R}}{\Delta\theta}$ (counts/rad)	$\bar{R}$ (counts)	$\bar{R}$ (mbarn)	$\frac{\bar{R}}{\Delta\theta}$ (mbarn/rad)
		^{34}Ar+^{58}Ni		
4	7607 ± 191	370 ± 9	75 ± 4	1532 ± 66
5	5103 ± 131	332 ± 9	67 ± 3	1027 ± 45
6	1654 ± 67	165 ± 7	33 ± 2	333 ± 19
7	1225 ± 67	142 ± 8	28 ± 2	246 ± 18
	$\sigma_{FE}(7° < \theta < 27°) =$		203 ± 10 mbarn	
		^{36}Ar+^{58}Ni		
4	29393 ± 549	1431 ± 27	125 ± 5	2566 ± 110
5	19895 ± 248	1295 ± 16	113 ± 4	1736 ± 63
6	9205 ± 199	916 ± 20	80 ± 4	803 ± 37
7	5857 ± 231	678 ± 27	60 ± 4	511 ± 32
	$\sigma_{FE}(7° < \theta < 27°) =$		377 ± 17 mbarn	
		^{36}Ar+^{60}Ni		
4	88661 ± 2468	4317 ± 120	103 ± 5	2115 ± 95
5	65554 ± 449	4268 ± 29	102 ± 2	1564 ± 37
6	30248 ± 444	3009 ± 44	72 ± 2	722 ± 23
7	20203 ± 1152	2338 ± 133	56 ± 4	482 ± 36
	$\sigma_{FE}(7° < \theta < 27°) =$		332 ± 14 mbarn	
		^{40}Ar+^{60}Ni		
4	85964 ± 1175	4186 ± 57	115 ± 3	2364 ± 67
5	48079 ± 365	3130 ± 23.8	86 ± 2	1322 ± 30
6	23689 ± 1172	2356.7 ± 117	65 ± 4	651 ± 42
7	14976 ± 4704	1733 ± 544	48 ± 16	412 ± 135
	$\sigma_{FE}(7° < \theta < 27°) =$		313 ± 25 mbarn	
		^{40}Ar+^{64}Ni		
4	30820 ± 674	1501 ± 33	125 ± 6	2567 ± 121
5	18706 ± 274	1218 ± 18	101 ± 4	1558 ± 62
6	7876 ± 649	784 ± 65	65 ± 7	656 ± 70
7	5460 ± 1940	632 ± 224	53 ± 20	485 ± 173
	$\sigma_{FE}(7° < \theta < 27°) =$		344 ± 37 mbarn	

Table 5.11 – Fusion-evaporation cross sections ($\bar{R}$) and differential fusion-evaporation cross sections expressed both in *counts* and in *mbarn* are reported for each analysed INDRA ring. The total measured fusion-evaporation cross section for each reaction ($\sigma_{FE}(7° < \theta < 27°)$) is also reported.

trend: a strong decreasing in $d\sigma_{FE}/d\theta$ as the CN mass decreases. These results are, of course, very preliminary since the measured angular distributions are not complete and the peaks of the distributions are missed. As an example the GEMINI ^{40}Ar+^{60}Ni angular distribution has been reported in Fig.5.24 and the measured part has been shaded. A further analysis including the VAMOS data will allow to get informations also on the peak region of the angular distributions.
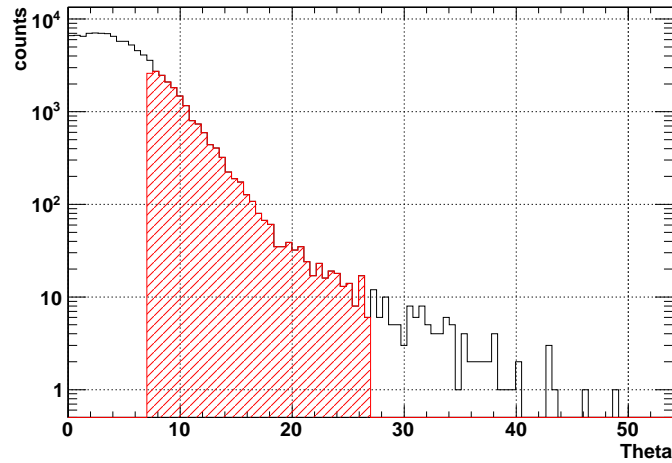
Figure 5.24 – GEMINI ^{40}Ar+^{60}Ni residue angular distribution. The shaded part enlightens the experimentally measured angular distribution

Basing on GEMINI and assuming that experimental and calculated angular distributions have the same shape, it is possible to extrapolate the fusion-evaporation cross sections. In Tab.5.12 the percentage of measured σ_{FE} is reported, showing an increase from the *n*-rich to the *n*-poor systems. It can be qualitatively understood in terms of nucleus recoil. The *n*-rich systems evaporates a great number of neutrons with respect to the *n*-poor one, which mainly evaporates α particles. Being the nucleus recoil due to a *n* emission smaller than the one due to an α particle emission, the angular distribution of a *n*-rich system will be more forward peaked and narrow than the one of a *n*-poor system. This effect is shown in Fig.5.25, where the peak positions are reported for each reaction. Experimental distributions are broader than GEMINI ones, but the ratios of counts in ring 4 and 5 have the same trend, giving confidence in a proper description, by GEMINI, of the occurring physic processes.

The extrapolation of σ_{FE} is, of course, very sensitive to possible uncertainties, being the measured angular distributions less than 25% of the total angular distri-

	$\sigma_{FE}(7° < \theta < 27°)$	% of σ_{FE}^{tot} measured	σ_{FE} extrapolated	σ_{reac}
^{34}Ar+^{58}Ni	203 ± 10	26.037%	780 ± 39	2497
^{36}Ar+^{58}Ni	377 ± 17	23.599%	1598 ± 72	2562
^{36}Ar+^{60}Ni	332 ± 14	23.455%	1417 ± 57	2606
^{40}Ar+^{60}Ni	313 ± 25	18.675%	1680 ± 134	2713
^{40}Ar+^{64}Ni	344 ± 37	17.626%	1953 ± 210	2801

Table 5.12 – Experimentally measured fusion-evaporation cross section $\sigma_{FE}(7° < \theta < 27°)$, percentage of measured angular distribution obtained by a GEMINI comparison (% of σ_{FE}^{tot} measured), extrapolated σ_{FE} and reaction cross section [1] for each reactions. The FE cross sections are expressed in mbarn
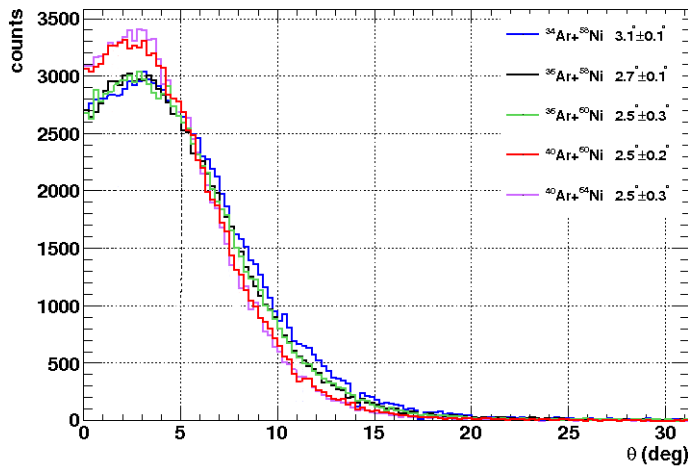
Figure 5.25 – `GEMINI` angular distributions. The peak positions (reported in the legend) and the distribution width decrease as the CN mass increases.

butions. Moreover the experimental and calculated angular distributions shapes are slightly different, however the extrapolations permit to compare the obtained values with the ones reported in literature. Other experimental results found in literature are listed in Tab.5.13 and displayed in Fig.5.26.

System	Ref.	E/A (AMeV)	σ_{FE} (mbarn)	σ_{FF} (mbarn)
^{40}Ar+^{nat}Ni	[136]	4.2	900 ± 80	
		4.9	890 ± 80	
		5.7	930 ± 60	
	[164]	7.2	900 ± 120	
^{32}S+^{59}Co	[137]	4.0	756 ± 76	
		4.5	995 ± 100	
		4.9	916 ± 92	243 ± 25
		5.6	850 ± 85	342 ± 35
		6.2	848 ± 85	387 ± 40
^{40}Ar+^{68}Zn	[36]	14.6	490 ± 50	500 ± 50
		19.6	300 ± 40	200 ± 40
^{35}Cl+^{62}Ni	[165]	4.0	929 ± 46	
		4.1	980 ± 49	
		4.6	998 ± 50	60 ± 20
		4.7	1089 ± 54	90 ± 30
		4.8	1091 ± 55	140 ± 45
	[166]	4.6	998 ± 70	78 ± 15
		4.7	1089 ± 76	114 ± 22
		4.9	1091 ± 76	126 ± 24
		5.7	960 ± 70	340 ± 100
		6.1	956 ± 70	420 ± 85

Table 5.13 – Fusion-evaporation and fusion-fission cross sections published in literature.
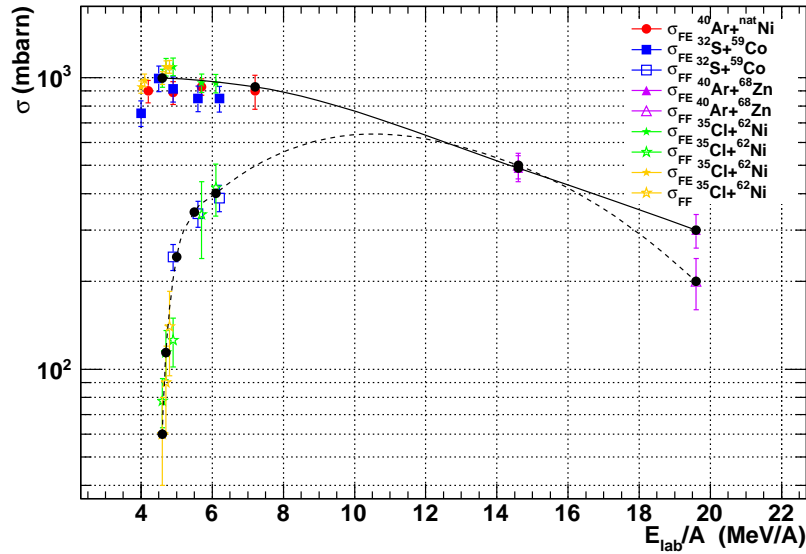
Figure 5.26 – Experimental results found in literature for both fusion-evaporation (full symbols) and fusion-fission (open symbols) cross sections. The lines are only to drive the eyes. References are reported in the text.

Data are for ^{40}Ar+^{nat}Ni [136, 164], ^{32}S+^{59}Co [137], ^{40}Ar+^{68}Zn [36] and ^{35}Cl+^{62}Ni [165, 166]. The total masses of these systems vary from 90 to 108, while the incident energies from 4 AMeV to 20 AMeV. In Fig.5.26, both fusion-evaporation and fusion-fission cross sections are reported; the lines have the aim of driving the eyes. On these basis a fusion-evaporation cross section of about 600 mbarn is expected for ^{40}Ar+^{60}Ni. We would remark that the fusion-fission cross section is comparable with the fusion-evaporation one, but fusion-fission events have been removed during the analysis. The obtained high cross section values are not in agreement with the values present in literature. Possible uncertainties sources have been identified in:

- the extrapolation of σ_{FE} from the GEMINI angular distributions, which are slightly different from the experimental angular distributions

- the choice of the grazing angle, which affects the integrated Rutherford cross section value

- the slope of the exponential decrease of $\sigma_{el}/\sigma_{Ruth}$, which has been chosen constant for all the systems

- the energy resolution. The peak identified as elastic peak could include some inelastic events, due to the energy resolution.

However a strong decrease in the fusion-evaporation cross sections, even larger than the decrease of the reaction cross sections, is observed with the CN mass decrease.
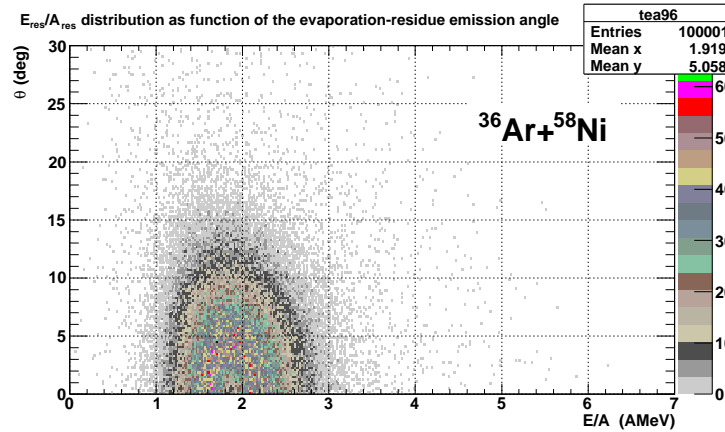
Figure 5.27 – Residue angular distribution as function of the fragment emission energy (in AMeV). The detector threshold can be located, as a first approximation, around 1 AMeV.

Being the decrease of σ_{FE} bigger than the σ_{reac} one, it cannot be explained in terms of a smaller number of partial waves participating to the reaction. Moreover the decrease of σ_{FE} can be due neither to the behaviour of σ_{Ruth}, which has the opposite trend, nor to the percentage of measured $d\sigma/d\theta$, which increases when decreasing the CN mass. The effect can neither be ascribed to a detector threshold effects. The contribution of the detector thresholds to the residue estimation is, theoretically, less than 0.3% for all the analyzed reactions. As example in Fig.5.27 a θ vs. E/A correlation obtained by GEMINI simulation is shown. The percentage of events lying in $E/A < 1$ AMeV region is less than 0.3%.

All these observations are summarized in Fig.5.28, where the behaviours of the Rutherford ($\sigma_{Ruth}(7° \leq \theta \leq \theta_{gr})$), the reaction ($\sigma_{reac}$) and the extrapolated ($\sigma_{extrap}$) and measured ($\sigma_{FE}^{meas}$) cross sections are shown. The slope of the measured σ_{FE} is clearly higher than the σ_{reac} and σ_{Ruth} ones. The strong decreasing of σ_{FE} for the ^{92}Pd, lying close to the p-drip line in the nuclide chart, could also be explained by the opening of new deexcitation channels, such as the multifragmentation one: moving toward the p-drip line a limit may appear in the excitation energy which can be supported by a nucleus, either in the total energy [167] or in the energy per nucleon [168, 169]. The latter can be related to a limiting temperature for nuclei as derived from Hartree-Fock calculations [170]. In this case one deals with a limit imposed by the exit channel looked at, namely fusion evaporation. This idea is supported by the detection of heavy particles, with Z up to 7, in coincidence with a residue in VAMOS.

We now discuss to what extent experimental fusion cross section can be understood qualitatively in terms of simple models.
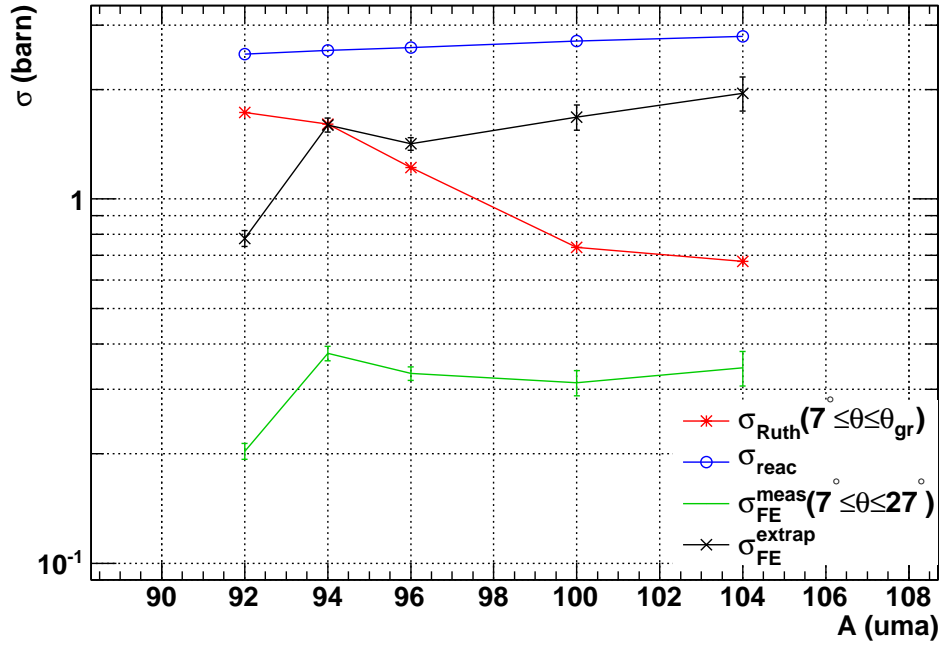
Figure 5.28 – Integrated Rutherford cross section ($\sigma_{Ruth}(7° \leq \theta \leq \theta_{gr})$), reaction cross section (σ_{reac}) and the extrapolated (σ_{extrap}) cross section as function of the CN mass is plotted.

The fusion process is connected to the presence of a pocket in the interaction potential between the two colliding nuclei. The potential shape and therefore the critical angular momentum l_{cr} for fusion, which could limit the fusion processes [31], are determined by the competition between the Coulomb repulsion and the sum of nuclear attraction and the l-dependent centrifugal force. Increasing the system neutron number, the nuclear interaction increases, while the Coulomb repulsion remains unchanged, increasing the well depth. Therefore the fusion reaction is more probable in n-rich systems and the n-rich fusion cross sections are higher than the n-poor ones.

Three different models have been taken into account to evaluate a theoretical l_{cr} and to estimate the corresponding fusion cross section from the equation:

$$\sigma_F = \pi \lambda^2 l(l + 1). \tag{5.39}$$

As already discussed in §1.2 the effective interaction potential between two ions can be written as

$$V_l^{eff}(r) = V_{CB}(r) + V_N(r) + V_l(r) \tag{5.40}$$

$V_{CB}(r)$ and $V_l(r)$ have the expression reported in eq.1.7 and 1.16. The $r_{0\,gr}$ values of

	$r_{0\,gr}$(fm)
^{34}Ar+^{58}Ni	1.430
^{36}Ar+^{58}Ni	1.430
^{36}Ar+^{60}Ni	1.430
^{40}Ar+^{60}Ni	1.428
^{40}Ar+^{64}Ni	1.427

Table 5.14 – $r_{0_{gr}}$ values used in the computation of R_{gr} (eq.1.4). These values, inserted in DIFFIL code (see app.B allow to obtain a θ_{gr} value equal to the one obtained by [1].

eq.1.4 are reported in Tab.5.14. It remains to specify the nucleus-nucleus potential. The energy density formalism provides us a way of calculating the interaction energy between two colliding ions. The model consists in writing the total energy of fermion systems under the form of a functional of the one-body densities. In the case of colliding heavy ions, the interaction energy calculated as a function of the relative distance R between the two centers of mass can be interpreted as the real part of the interaction potential.

In the model proposed by C. Ngô and B. Tamain [171], the calculations are made in the so-called sudden approximation, which means that the densities ρ_1 and ρ_2 describing the two ions, respectively, overlap during the collision without rearrangements. For physical situations implying essentially the surface and the tail of the potential, so that the central part of the potential is irrelevant, such as in the analyzed reactions, comparisons with experimental data [172, 173] have shown this approach to be capable of supplying with valuable information.

Starting from the statement that *the force, $F(s)$, between two gently curved undeformable bodies in close proximity, as a function of the least separation distance, s, is proportional to the interaction potential per unit of area between two flat surfaces made of the same material, multiplied by a proportionality factor* (proximity theorem, [174, 175]), C. Ngô and B. Tamain [171] have pointed out that $V_N(R)$ can be written as:

$$V_N(R) = \frac{A_1^{1/3} A_2^{1/3}}{A_1^{1/3} + A_2^{1/3}} U_N(R) \tag{5.41}$$

where the first term is a geometrical factor, due to the assumption, in the calculations, of spherical nuclei, while the second term has been found to be "universal", once applied the transformation

$$s = R - R_0.$$

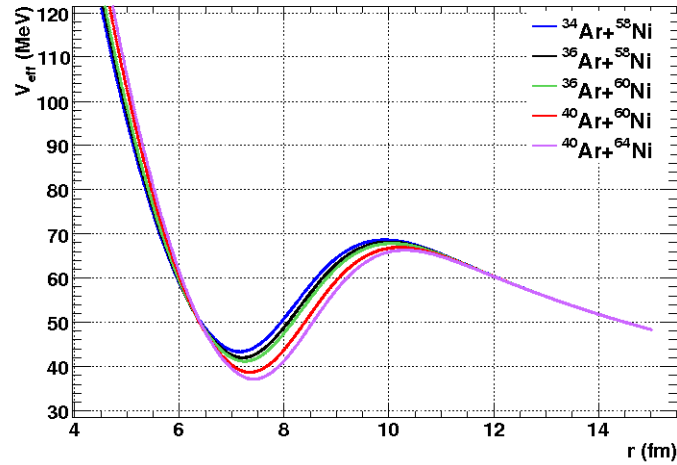R_0 denotes the position of the minimum of the function $U_N(R)$ and can be calculated

Figure 5.29 – Effective potential shape ($l = 0$) obtained within the model [171].

from the relationship

$$R_0 = r_0 \left(A_1^{1/3} + A_2^{1/3} \right). \tag{5.42}$$

The universal function $U_N(R)$ has been parametrized as:

$$U_N(s) = \begin{cases} -V_0 \, e^{-0.27 \, s^2 / fm^2} & s \geq 0 \\ -V_0 + 6.3 \, s^2 \, MeV/fm^2 & s \leq 0 \end{cases} \tag{5.43}$$

where $r_0 = 0.97$ fm and $V_0 = 30$ MeV for the ^{40}Ar+^{63}Cu reaction.

The effective potentials obtained for the different reactions are shown in Fig.5.29. For each reaction the critical angular momentum has been determined by a numerical derivative of the effective potential, and the fusion cross section has been estimated. The obtained values are reported in Tab.5.15.
In the model the shell effects and the neutron excess in the surface (as a function

	l_{gr} ($\hbar$)	l_{cr} ($\hbar$)	V_0 (MeV)	σ_F (barn)	$\sigma_F/\sigma_F(^{100}Pd)$ th	$\sigma_{FE}/\sigma_{FE}(^{100}Pd)$ exp
^{34}Ar+^{58}Ni	153	76	31.4	0.618	0.944	0.46 ± 0.04
^{36}Ar+^{58}Ni	159	78	32.2	0.616	0.940	0.95 ± 0.09
^{36}Ar+^{60}Ni	163	80	32.6	0.632	0.965	0.84 ± 0.07
^{40}Ar+^{60}Ni	173	85	34.1	0.655	1	1
^{40}Ar+^{64}Ni	181	89	35.0	0.683	1.043	1.16 ± 0.16

Table 5.15 – Grazing angular momentum (l_{gr}), obtained according to [1]; critical angular momentum l_{cr}, well depth V_0 with respect to the Coulomb barrier, obtained from C. Ngô model [171] are reported. For each reaction the ratios of the cross section and the ^{100}Pd cross section have been calculated both from theoretical prediction ($\sigma_F/\sigma_F(^{100}Pd)$ th) and experimental data ($\sigma_{FE}/\sigma_{FE}(^{100}Pd)$ exp).
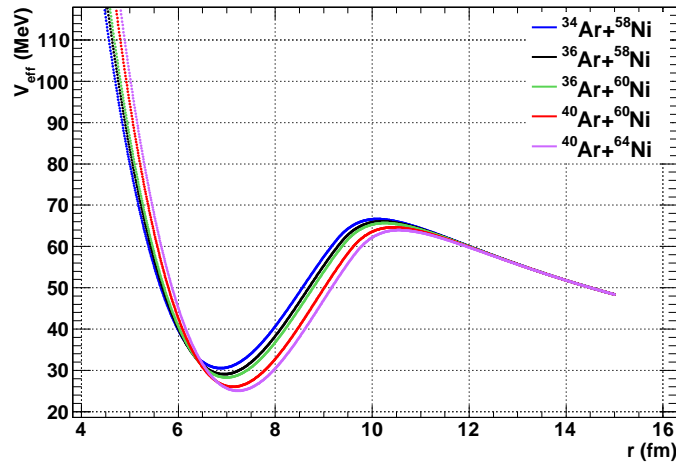
Figure 5.30 – Effective potential shape ($l = 0$) obtained within the J. Blocki model [174].

of N and Z) are present in the calculated densities, but not in the functional used to compute $V_N(R)$, however this Z and N dependence shows a qualitative behaviour in agreement with what we found in our reactions.

A more recent parametrization, based on the proximity theorem and using the nuclear Thomas-Fermi approximation, expresses the proximity potential as

$$V_N(\xi) = 4\pi\gamma\overline{R}b\Phi(\xi) \tag{5.44}$$

where

$$
\begin{aligned}
&\gamma = 0.9517\left(1 - 1.7826I^2\right) Mev/fm^2 \\
&I = \frac{N-Z}{A} \\
&\overline{R} = (1.28A^{1/3} - 0.76 + 0.8A^{-1/3})fm \\
&b = 1fm \\
&\Phi(\xi) = \begin{cases} -\frac{1}{2}(\xi - \xi_0)^2 - k(\xi - \xi_0)^3 & \xi \le \xi_1 \\ -3.437e^{-\frac{\xi}{0.75}} & \xi \ge \xi_1 \end{cases}
\end{aligned}
\tag{5.45}
$$

with

$$
\begin{cases}
\xi_1 = 1.2511 \\
\xi_0 = 2.54 \\
k = 0.0852
\end{cases}
\tag{5.46}
$$

N, Z and A in eq.5.45 refer to the combined system of the two interacting nuclei. As for the previous model the effective potentials are shown in Fig.5.30 and for each reaction the critical angular momentum and the fusion cross section have been estimated and reported in Tab.5.16.

	l_{cr} $(\hbar)$	V_0 (MeV)	σ_F (barn)	$\sigma_F/\sigma_F(^{100}Pd)$ th	$\sigma_{FE}/\sigma_{FE}(^{100}Pd)$ exp
^{34}Ar+^{58}Ni	77	36.1	0.635	0.905	0.46 ± 0.04
^{36}Ar+^{58}Ni	81	37.0	0.664	0.946	0.95 ± 0.09
^{36}Ar+^{60}Ni	82	37.4	0.663	0.946	0.84 ± 0.07
^{40}Ar+^{60}Ni	88	38.6	0.702	1	1
^{40}Ar+^{64}Ni	91	38.8	0.714	1.012	1.16 ± 0.16

Table 5.16 – Critical angular momentum l_{cr} and well depth V_0 with respect to the Coulomb barrier, obtained from J. Blocki model [174] are reported. For each reaction the ratios of the cross section and the ^{100}Pd cross section have been calculated both from theoretical prediction ($\sigma_F/\sigma_F(^{100}Pd)$ th) and experimental data ($\sigma_{FE}/\sigma_{FE}(^{100}Pd)$ exp).

In the last analysed model, taken from [176], the critical angular momentum l_{cr} for fusion is calculated by equating the maximum possible attractive nuclear force due to the proximity potential to the sum of the repulsive Coulomb and l-dependent centrifugal forces. The droplet model is used to determine static nuclear parameters which are not dependent on the bombarding energy, such as the matter half density radius C and the coefficient of surface tension γ entering in the strength factor of the proximity model potential for heavy ions. The maximum critical angular momentum for fusion is given by

$$l_{cr} = \frac{7}{5}\sqrt{\frac{-\mu m_u S^3}{\hbar^2}\left[4\pi\gamma\overline{C}\phi b + \frac{Z_1 Z_2 e^2}{S^2}\right]} \tag{5.47}$$

with

$$
\begin{aligned}
\mu &= \frac{A_p A_t}{A_p + A_t} \\
m_u &= 931.5 \; MeV/c^2 \\
S &= C_p + C_t + 0.3 fm \\
C &\simeq R\left(1 + \frac{1}{R^2}\right) \\
R &= (1.28 A^{1/3} - 0.76 + 0.8 A^{-1/3}) \; fm \\
\overline{C} &= \frac{C_p C_t}{C_p + C_t} \\
\phi &= -0.96 \\
b &= 1 \; fm \\
\gamma &= 0.9517(1 - 1.7826 I^2) \\
I &= \frac{N - Z}{A}
\end{aligned}
\tag{5.48}
$$

The obtained value are listed in Tab.5.17.

For all the models the obtained l_{cr} values are in agreement with what predicted by [177]. The obtained theoretical σ_F are not in agreement with what expected from experimental data in literature, being a factor of ~ 2 smaller. However they show a decreasing trend as the CN masses decrease, in agreement with what we found

	l_{cr} ($\hbar$)	σ_F (barn)	$\sigma_F/\sigma_F(^{100}Pd)$ th	$\sigma_{FE}/\sigma_{FE}(^{100}Pd)$ exp
^{34}Ar+^{58}Ni	68	0.494	0.817	0.46 ± 0.04
^{36}Ar+^{58}Ni	72	0.526	0.869	0.95 ± 0.09
^{36}Ar+^{60}Ni	74	0.543	0.898	0.84 ± 0.07
^{40}Ar+^{60}Ni	82	0.605	1	1
^{40}Ar+^{64}Ni	85	0.630	1.041	1.16 ± 0.16

Table 5.17 – Critical angular momenta l_{cr}, obtained according to [176], are reported. For each reaction the ratios of the cross section and the ^{100}Pd cross section have been calculated both from theoretical prediction ($\sigma_F/\sigma_F(^{100}Pd)$ th) and experimental data ($\sigma_{FE}/\sigma_{FE}(^{100}Pd)$ exp).

experimentally.

The ratios between the fusion cross section and the ^{100}Pd fusion cross section have been estimated both from experimental data and theoretical predictions. It can be pointed out that the decrease of σ_{FE} cannot be explained only as a dependence of σ_F from l_{cr}, being the obtained experimental and theoretical ratios different one from each other.

The decrease of σ_{FE} suggests then a possible dependence of the fusion-evaporation cross section from the isospin of the reactions.

Appendix A

Data sample selection

In order to perform an analysis of the residue statistic, it is necessary to select a "clear data sample", removing, in particular,

- events where the cross talk between two pads of the same silicon wafer occurs

- events where two particles hit the same ionization chamber

A.1   Cross talk events and time marker signals

The analysis of the time marker signals of detectors hit in an event allows, in first approximation, to identify a cross talk event.

We remark that for each detector of an INDRA telescope, a time marker signal is generated when the signal induced by the incident particle hitting a detection layer is greater than the detector CFD threshold. The detector ADC integration gate, instead, is fired by the logic OR between the CFD signals produced by the hit detector and the following detection layer. Therefore an incident particle can cause an energy signal and not a time signal, but not vice-versa.

The time marker of each signal is related to:

- the particle time of flight. As previously discussed, the *Start* to the Time Marker is given by the detector CFD logic signal, while the *Stop*, a common stop, is given by the trigger signal. The time marker value is thus related to the particle energy and mass.

- the rise time of the signal of the fast amplifier, which increases the time difference between light charged particles or high energy fragments and low energy residues.
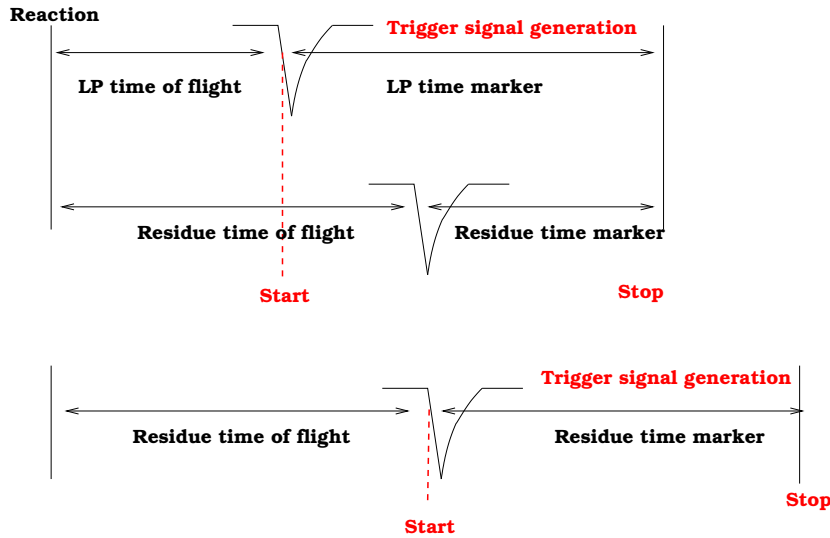
Figure A.1 – Sketch of time marker signal production for a light particle (LP, upper panel) and for a $M = 1$ residue event (lower panel)

- the selected trigger multiplicity. In particular if the selected multiplicity is $M \geq 1$, when the event multiplicity is $M = 1$, the time marker position is related only to the delay introduced by cables, and it is independent from the particle energy and mass.

A sketch is presented in Fig.A.1.

A silicon time marker spectrum generally extends from *channel*~ 90 to *channel*~ 115: the lower part is associated with the "residue", whose time marker peak is centred around *channel*~ 100, while the upper part with light particles, whose peak is centred about *channel*~ 110 (see Fig.A.2). A small peak, around *channel*~ 110, is present in the residue time marker spectrum: such events are $M \geq 1$ events.

A.1.1   Cross talk events

As discussed in §2.1, each ionization chamber in forward rings is followed by a silicon wafer, divided in 4 pads. This configuration reduces the dead region between two contiguous detectors, but may introduce cross talk effects. We refer to cross talk effects as the production of a signal in a not-fired pad. When an incident particle deposits energy in one pad, a part of the ionization charge can drift towards a contiguous pad, producing a signal also in the latter. Due to the charge sharing, the energy signals associated to a couple of detectors where cross talk occurred is not simply usable: in order to get the correct energy information, each event where cross talk had occurred should be identified and reconstructed.

The cross talk origin is related to the n^+ wafer region, which is common to all the
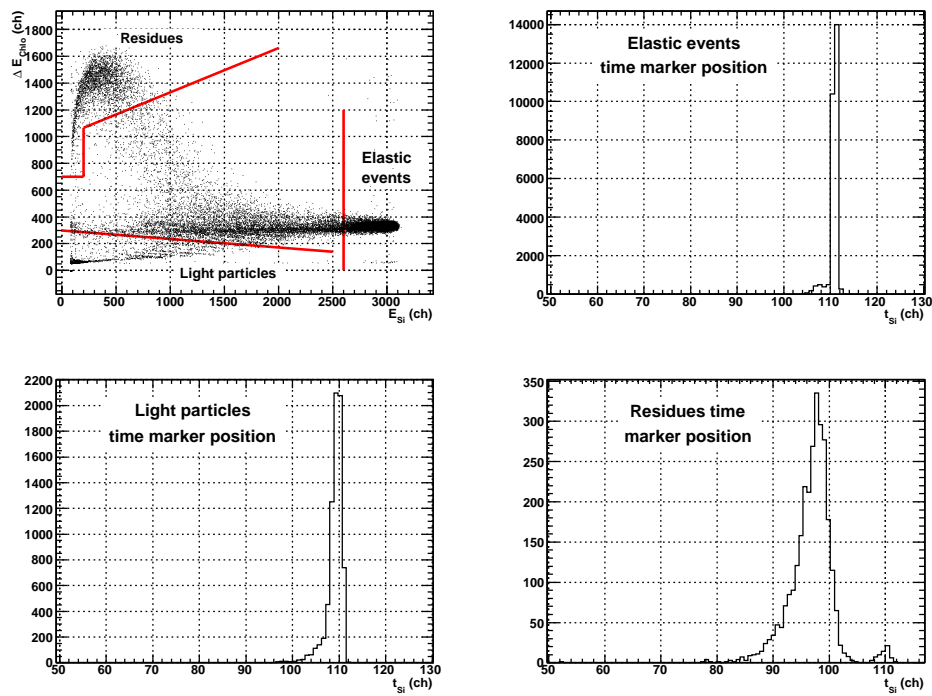
Figure A.2 – $\Delta E - E$ spectrum for a detector located under the grazing angle: the residue, light particle and elastic events regions are identified. For each region the corresponding time marker positions are displayed in the other three pads.

four pads and which should be grounded. It has been pointed out in Ref. [178] that an impedance of $\sim 1\Omega$ can be associated to this region and that it is the reason of induced signals.

A cross talk event can be identified by the time marker associated to silicon detectors. In case of a cross talk event the signal induced in neighbour silicon pads has an inverse sign with respect to the main one: i.e. it is a positive signal. Moreover
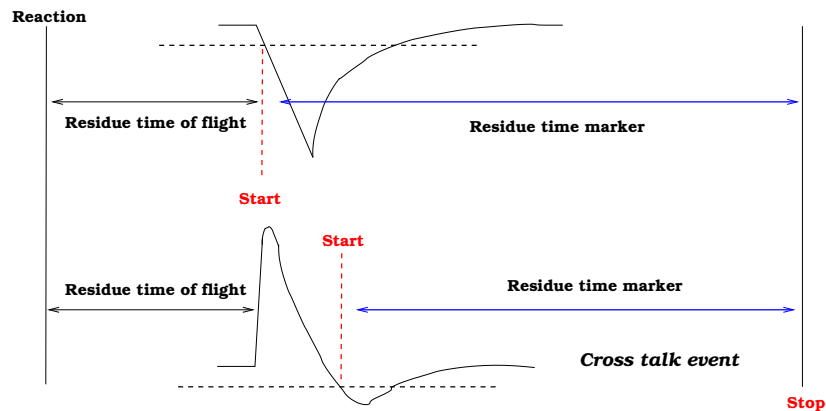
Figure A.3 – Sketch of time marker signal production for events without (upper panel) and with (lower panel) cross talk effect.
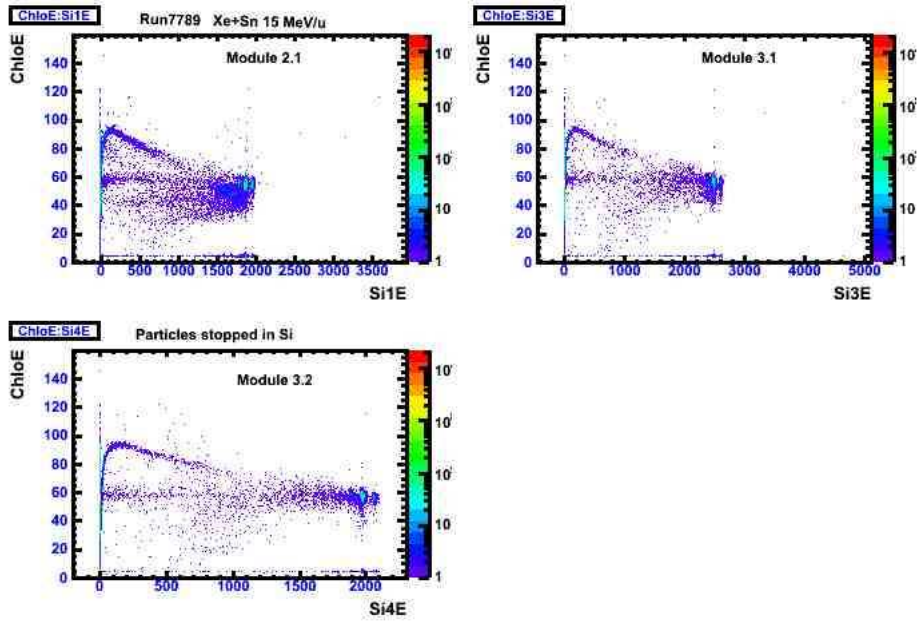
Figure A.4 – $\Delta E - E$ spectra obtained in a previous INDRA campaign for the reaction Xe+Sn at 15 Ame incident energy.

the signal rise time is short while the signal decrease time is comparable to the main signal rise time. The CFD, which works in leading edge mode, fires on the descending part of the signal introducing a delay in the logic signal production. The time marker position of a cross talk event will therefore lie at smaller value with respect to the main one position (see Fig.A.3). As an example a $\Delta E - E$ and time marker spectra of a previous INDRA campaign, where cross talk occurred, are shown in Fig.A.4 and Fig.A.5. In the present campaign no cross talk effects have been observed.

A.2 Removal of events where two particles hit the same ionization chamber

As it has been previously pointed out, INDRA forward telescopes are constituted by three detection layers, the first of which has a granularity lower than the silicon and cesium iodide detectors: each ionization chamber indeed is followed by 4 telescopes made by a silicon and a CsI(Tl) scintillator detectors. This configuration introduces some uncertainties in event reconstruction and in particular in particles identification without any energy calibrations. When two particles hit the same ionization chamber, the induced signal is the result of the sum of the ionization of both particles. If at least one of them punches through the second layer, the deposited energy associated to each particle can be reconstructed on the basis of the
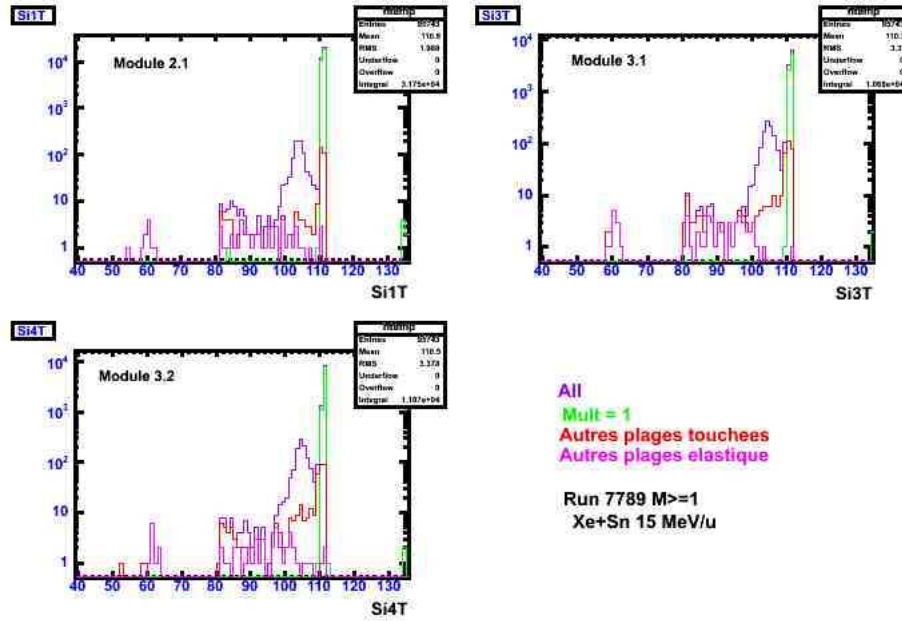
Figure A.5 – Time marker spectra obtained in a previous INDRA campaign for the reaction Xe+Sn at 15 Ame incident energy. $M = 1$ events, elastic events and cross talk events time markers are shown in different colours: cross talk events time marker is located at lower values (channels $80 \div 90$).

residual energy deposited in the second and third detection layers by the punching through particle: the $\Delta E - E$ method provides the particle charge Z, allowing to reconstruct the incident energy, and thus the energy lost in the ionization chamber. From the energy deposited by the first particle, the energy of the second particle can be estimated. This method, however, requires the energy calibrations of all detectors (energy loss must be calculated), which, in this moment, are not yet available. Therefore, in a first approximation, all the events where two particles hit the same ionization chamber have been removed from the data sample. During all the analysis care has been payed in checking the percentage of these removed events lying always below 1.0%.

Appendix B

`Diffil` code

The `Diffil` code, written by B. Tamain (IPN-Orsay) in 1975, computes the kinematics for elastic diffusion, fusion-fission and deep inelastic fully relaxed reactions, being all the three processes binary processes. The code input parameters are the mass and charge of the projectile and target nuclei (A_p, Z_p and A_t, Z_t respectively) and the beam incident energy (E_i). The charge ratio of the products is required for fusion-fission and DI reactions. The code is valid only if the target mass is equal or bigger than the projectile one.

The code output is a list of kinematic parameters, such as emission angles, velocities and kinetic energies. Once chosen the outgoing fragment of interest, its characteristics and its partner characteristics are calculated for all available emission angle θ. The emission angle step can be set by user.

Later on we refer to quantities calculated in CM with capital letters, and small letters will be reserved to quantities in LAB reference system.

B.1   Rutherford elastic diffusion

The electrostatic potential between the two colliding nuclei is assumed to be, in this simple model, the Coulomb potential

$$V(r) = \frac{1}{4\pi\varepsilon_0} \frac{Z_p Z_t e^2}{r} \tag{B.1}$$

where e is the electron charge.

The angular momentum and the energy conservation laws allow to determine the

projectile trajectory in CM, $\Theta(r)$. From the motion equations one gets:

$$\sin\frac{\Theta}{2} = \frac{\frac{a_0}{b}}{\sqrt{1 + \left(\frac{a_0}{b}\right)^2}}, \tag{B.2}$$

where b is the reaction impact parameter and a_0 is the distance of minimum approach:

$$a_0 = \frac{Z_p Z_t e^2}{2E^{(CM)}}. \tag{B.3}$$

$E^{(CM)}$ is the available energy in CM:

$$E^{(CM)} = E_i \frac{A_t}{A_p + A_t}. \tag{B.4}$$

At the distance R_{gr} at which the nuclear interactions become significant, a_0 can be expressed as

$$a_0 = \frac{V_{CB}\big|_{R_{gr}} R_{gr}}{2E^{(CM)}}, \tag{B.5}$$

being the Coulomb barrier

$$V_{CB}(r) = \frac{1}{4\pi\varepsilon_0}\frac{Z_p Z_t e^2}{r}. \tag{B.6}$$

R_{gr} is calculated according to relation

$$R_{gr} = 1.35\left(A_p^{1/3} + A_t^{1/3}\right)\text{fm} \tag{B.7}$$

Remembering eq.1.18, the projectile grazing angle is given by

$$\sin\frac{\Theta_{gr}}{2} = \frac{1}{2\frac{E^{(CM)}}{V_{CB}} + 1} \tag{B.8}$$

B.1.1 Projectile diffusion

Elastic diffusion is characterized by a final projectile velocity (in CM) equal to the initial one and by an initial target velocity (in CM) equal to the CM velocity. Geometrical considerations allow to relate the projectile emission angle in LAB to the projectile emission angle in CM:

$$\tan\theta_p = \frac{V_p \sin\Theta_p}{v_{CM} + V_p \cos\Theta_p} \tag{B.9}$$
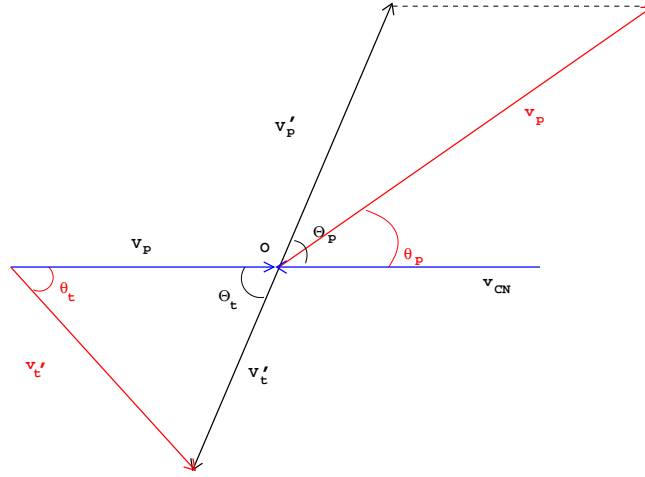
Figure B.1 – Sketch of an elastic collision. Blue arrows are the partners velocities in CM before the collision. Black lines refer to velocities and emission angles in CM after the collision. Red arrows are projectile and target velocity after collision.

where $\overrightarrow{V_p}$ and $\overrightarrow{v_{CM}}$ are the projectile velocity in CM and the center of mass velocity, respectively. Imposing the momentum conservation law in CM ($\overrightarrow{P^{(CM)}} = 0$), the center of mass velocity is related to the projectile and target masses ratio

$$|\overrightarrow{v_{CM}}| = \frac{A_p}{A_t}|\overrightarrow{V_p}| \tag{B.10}$$

Substituting eq.B.10 in eq.B.9 and inverting this relation, one gets the projectile emission angle in CM:

$$\Theta_p = \arcsin\left(\frac{A_p}{A_t}\sin\theta_p\right) + \theta_p. \tag{B.11}$$

The projectile kinetic energy in LAB can be determined by the projectile emission velocity $\overrightarrow{v_p'}$ (see Fig.B.1)

$$v_p'^2 = \left(V_p\sin\Theta_p\right)^2 + \left(v_{CM} + V_p\cos\Theta_p\right)^2 \tag{B.12}$$

Being

$$v_{CM} = \frac{A_p}{A_p + A_t}v_p$$
$$V_p = v_p - v_{CM}, \tag{B.13}$$

one gets

$$E_p^{lab} = \frac{1}{2}A_p v_p'^2 = (1 + k^2 + 2k\cos\Theta)\left(\frac{A_t}{A_p + A_t}\right)^2 E_i \tag{B.14}$$

where k is the projectile and target mass ratio $k = \frac{A_p}{A_t}$.

B.1.2   Target diffusion

The target emission angles, as function of the projectile emission angle Θ_p, can be deduced by geometrical considerations:

$$\Theta_t = \pi - \Theta_p$$
$$\theta_t = \frac{\pi - \Theta_p}{2} \tag{B.15}$$

Noting that the target emission velocity is

$$v_t = 2v_0 \cos \theta_t \tag{B.16}$$

the target kinetic energy in LAB is

$$E_t = 2(1 + \cos \Theta_t) \left(\frac{A_t}{A_p + A_t} \right)^2 \frac{A_p}{A_t} E_i \tag{B.17}$$

Similar considerations allow to estimate projectile emission angle, velocity and kinetic energy as function of target emission angle, Θ_t.

B.2   Fusion-fission and deep inelastic kinematics

Central collisions occurring at low and intermediate energy can lead to fusion (complete or incomplete) or to dissipative binary processes.

B.2.1   Complete fusion

When complete fusion occurs, the composite system mass and charge are

$$\begin{cases} A_{CN} = A_p + A_t \\ Z_{CN} = Z_p + Z_t \end{cases} \tag{B.18}$$

and its excitation energy, neglecting the Q-value of the reaction, is equal to the available energy in CM:

$$E_{CN}^\star = E_i \frac{A_t}{A_p + A_t} \text{MeV} \tag{B.19}$$

Within a liquid drop model, the composite system surface energy is parametrized according to Ref. [179], as

$$E_{sup} = 17.9439 \left[1 - 1.7826 \left(\frac{N_{CN} - Z_{CN}}{A_{CN}} \right)^2 A^{2/3} \right] \text{MeV} \tag{B.20}$$

and the Coulomb energy

$$E_{coul} = 0.7053 \frac{Z_{CN}^2}{A_{CN}^{1/3}} \text{ MeV} \tag{B.21}$$

Being the composite system and the CM reference systems coincident, the composite system recoil velocity

$$v_{rec}^{CN} = 1.39 \sqrt{\frac{E_i A_p}{A_{CN}^2}} \text{ cm/ns} \tag{B.22}$$

is obtained combining:

$$\begin{cases} E_{CN} = \frac{1}{2} A_{CN} v_{CN}^2 & composite\ system\ kinetic\ energy \\ v_{CM} = v_{CN} = \dfrac{A_p}{A_p + A_t} v_p & CM\ velocity \end{cases}$$

B.2.2 Fission and deep inelastic fully relaxed kinematic

Fission kinematics calculations are obtained by a simple model based on Coulomb repulsion between prolate spheroids, which predicts that the most probable total kinetic energy released in fission, $\langle E_K \rangle$, depends linearly on the Coulomb parameter, $\frac{Z^2}{A^{\frac{1}{3}}}$, of the fissioning nuclei [180][1]:

$$E_k^{fiss} = 0.1071 \text{ MeV} \frac{Z_{CN}^2}{A_{CN}^{1/3}} + 22.2 \text{ MeV} \tag{B.23}$$

Fixed the charge ratio of the two fragments resulting from the composite system fission or produced in the deep inelastic collision, and indicating with `heavy` and `light` quantities related to the heaviest and the lightest fragments emitted, their mass can be expressed as

$$A_{light} = \frac{A_{CN}}{1 + \frac{Z_{heavy}}{Z_{light}}}$$

$$\tag{B.24}$$

$$A_{heavy} = A_{light} \frac{Z_{heavy}}{Z_{light}}$$

taking into account that $A_{heavy} + A_{light} = A_{CN}$ and assuming that

$$\frac{A_{light}}{A_{heavy}} = \frac{Z_{light}}{Z_{heavy}}$$

, given as input parameter. The considered input charge ratios are $\frac{Z_{light}}{Z_{heavy}} = 1$, for symmetric fission, and values from the initial charge ratio ($\frac{Z_{light}}{Z_{heavy}} = \frac{18}{28}$) to $\frac{Z_{light}}{Z_{heavy}} = \frac{13}{33}$

---

[1]A better parametrization is now available in [181], which shifts E_k^{fiss} of ~ 10 MeV.
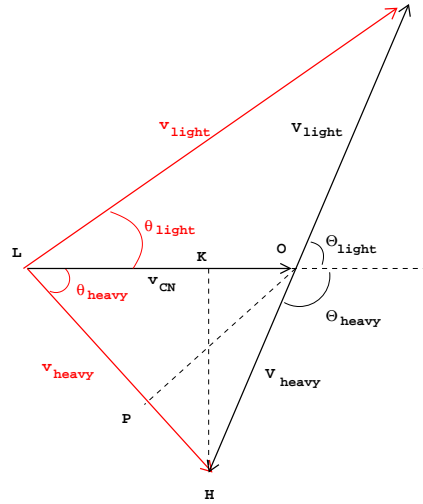
Figure B.2 – Sketch of fission process. Full black lines are the CM velocity and light and heavy fragments velocities in CM after the CN fission, respectively. Red lines individuate the light and heavy fragments velocities in LAB.

(see Fig.5.7), for deep inelastic collisions.

The kinetic energies of the two fragments in CM can be linked to the mean energy released in the fission process, imposing the momentum conservation law

$$E_{heavy}^{(CM)} = \frac{4E_k^{fiss}\frac{Z_{heavy}}{Z_{light}}}{\left(1 + \frac{Z_{heavy}}{Z_{light}}\right)^3}$$

$$E_{light}^{(CM)} = E_{heavy}^{(CM)}\frac{Z_{heavy}}{Z_{light}}$$

(B.25)

Their velocities in CM are trivially given by

$$V_{light} = 1.39\sqrt{\frac{E_{light}^{(CM)}}{A_{light}}} \text{ cm/ns}$$

$$V_{heavy} = 1.39\sqrt{\frac{E_{heavy}^{(CM)}}{A_{heavy}}} \text{ cm/ns} = V_{light}\frac{Z_{heavy}}{Z_{light}}$$

(B.26)

To determine the two fragments emission velocity in LAB (v_{light}, v_{heavy}), let us refer to Fig.B.2 and assume θ_{light} and θ_{heavy} to be the fragments emission angles in LAB.

$$\overline{LH} = \overline{LP} + \overline{PH}$$
$$\overline{PH}^2 = (V_{heavy})^2 - (v_{rec}^{CN}\sin\theta_{heavy})^2$$
$$\overline{LP} = v_{rec}^{CN}\cos\theta_{heavy}$$

(B.27)

then v_{heavy} is given by

$$v_{heavy} = v_{rec}^{CN} \cos \theta_{heavy} + \sqrt{(v_{rec}^{CN} \cos \theta_{heavy})^2 - v_{rec}^{CN\,2} + V_{heavy}^2} \qquad (B.28)$$

Similarly v_{light} is

$$v_{light} = v_{rec}^{CN} \cos \theta_{light} + \sqrt{(v_{rec}^{CN} \cos \theta_{light})^2 - v_{rec}^{CN\,2} + V_{light}^2} \qquad (B.29)$$

Kinetic energies of the two partners in LAB are given by

$$E_{heavy}^{LAB} = \tfrac{1}{2} A_{heavy} v_{heavy}^2$$

$$E_{light}^{LAB} = \tfrac{1}{2} A_{light} v_{light}^2 \qquad (B.30)$$

Applying the Carnot theorem to $L\overset{\triangle}{O}H$ one gets the heavy fragment emission angle in CM (Θ_{heavy}) and, similarly, the light fragment one

$$\cos \Theta_{heavy} = \frac{v_{heavy}^2 - v_{rec}^{CN\,2} - V_{heavy}^2}{2\, v_{rec}^{CN} V_{heavy}}$$

$$\cos \Theta_{light} = \frac{v_{light}^2 - v_{rec}^{CN\,2} - V_{light}^2}{2\, v_{rec}^{CN} V_{light}} \qquad (B.31)$$

Once selected the fragment of interest (i.e. the heavy or the light one) `DIFFIL` code allows to determine the kinematics of the partner one. Known Θ_{heavy}, geometrical considerations (see Fig.B.2) allow to determine the emission angle of the partner fragment of the heavy fragment

$$\tan \theta_{light} = \frac{V_{light} \sin(\pi - \Theta_{heavy})}{V_{light} \cos(\pi - \Theta_{heavy}) + v_{rec}^{CN}} \qquad (B.32)$$

Similarly the emission angle of the fragment partner of the light one is given by

$$\tan \theta_{heavy} = \frac{V_{heavy} \sin(\pi - \Theta_{light})}{V_{heavy} \cos(\pi - \Theta_{light}) + v_{rec}^{CN}}. \qquad (B.33)$$

Bibliography

[1] W. Nöremberg and H. A. Weidenmüller. *Lecture Notes in Physics*. Springer-Verlag, 1980.

[2] B. Povh *et al. Particelle e nuclei*. Bollati Boringhieri, 1998.

[3] J. Wilczyński. *Nucl. Phys. A*, 216:386, 1973.

[4] R. J. Charity *et al. Z.Phys. A*, 341:53, 1991.

[5] A. Mangiarotti. *Characterization of the statistical and mid-velocity emission in peripheral heavy ion collisions at Fermi energies*. PhD thesis, Università di Firenze, 2003.

[6] D. Durand and B. Tamain. *Notes from course held at the International Nuclear Physics School Joliot-Curie* (France).

[7] R. Bass. *Nuclear Reactions with Heavy Ions*. Springer-Verlag, 1980.

[8] N. Ullah. *Phys. Rev. Lett.*, 20(26):1510, 1968.

[9] D. Durand, E. Suraud and B. Tamain. *Nuclear Dynamics in the nucleonic regime*. Institute of physics publishing Bristol and Philadelphia, 2001.

[10] P. E. Hodgson. *Nuclear Heavy Ion Reactions*. Clarendon press - Oxford, 1978.

[11] R. M. De Vries. *Nucl. Phys. A*, 243:528, 1975.

[12] G. Casini *et al.* Testing signal shapes of silicon and scintillation detectors with digital sampling electronics. *Experiment proposal at LNL.*

[13] J. Randrup. *Nucl. Phys. A*, 307:319, 1978.

[14] J. Randrup. *Nucl. Phys. A*, 327:490, 1979.

[15] J. Randrup. *Nucl. Phys. A*, 383:468, 1982.

[16] U. Brosa *et al. Z. Phys. A*, 307:167, 1982.

[17] S. K. Samaddar *et al. Phys. Rev. C*, 31:1053, 1985.

[18] S. Chattopadhyay *et al. Phys. Rev. C*, 41:390, 1990.

[19] N. Bohr. *Nature*, 137:344, 1936.

[20] D. A. Bromley. *Treatise on Heavy-Ion Science*. Plenum Press, New York, 1984.

[21] H. Morgenstern *et al. Phys. Rev. Lett.*, 52:1104, 1984.

[22] R. H. Siemssen. *Nucl. Phys. A*, 400:245, 1983.

[23] INDRA Collaboration. *Eur. Phys. Jour. A*, 27:349, 2006.

[24] B. Borderie *et al. Z. Phys. A*, 316:243, 1984.

[25] B. Borderie *et al. Z. Phys. A*, 318:315, 1984.

[26] F. Rami *et al. Nucl. Phys. A*, 444:325, 1985.

[27] G. Auger *et al. Phys. Lett. B*, 169:167, 1986.

[28] A. A. Sonzogni *et al. Phys. Rev. C*, 53:243, 1996.

[29] J. R. Grover. *Phys. Rev.*, 157:832, 1967.

[30] R. Bass. *MU 73*, 1:614, 1973.

[31] R. Bass. *Nucl. Phys. A*, 231:45, 1974.

[32] R. Bass. *NA 74*, 1:117, 1974.

[33] D. H. E. Gross *et al. Phys. Lett. B*, 48:302, 1974.

[34] J. Galin *et al. Phys. Rev. C*, 10:638, 1974.

[35] U. Jahnke *et al. Phys. Rev. Lett.*, 48:1, 1982.

[36] A. Fahli *et al. Phys. Rev. C*, 34:161, 1986.

[37] R. Bass. *Nucl. Phys. A*, 231:45, 1974.

[38] M. Lefort *et al. Ann. Phys.*, 3:5, 1978.

[39] T. Matsuse *et al. Phys. Rev. C*, 26:2338, 1982.

[40] J. R. Birkelund *et al. Phys. Rep.*, 56:107, 1979.

[41] T. Suomijarvi *et al. Nuovo Cimento A*, 82:51, 1984.

[42] P. Langevin. *C.R.Acad.Sci.*, 146:530, 1908.

[43] C. W. Gardiner. *Handbook of Stochastic Methods*. Springer, Berlin, 1990.

[44] H. Risken. *The Fokker-Planck Equation*. Springer, Berlin, 1984.

[45] K. Tanaka *et al. Nucl. Phys. A*, 583:581c, 1995.

[46] H. A. Bethe. *Revs. Mod. Phys.*, 2:71, 1937.

[47] V. F. Weisskopf *et al. Phys. Rev.*, 57:472 and 935, 1940.

[48] L. Wolfenstein *et al. Phys. Rev.*, 82:690, 1951.

[49] W. Hauser *et al. Phys. Rev.*, 87:366, 1952.

[50] I. Kanestrøm. *Nucl. Phys. A*, 109:625, 1968.

[51] J. Besprovany and S. Levit. *Phys. Lett.*, B217:1, 1989.

[52] S. Levit *et al. Nucl. Phys. A*, 437:426, 1985.

[53] P. Bonche *et al. Nucl. Phys. A*, 427:278, 1984.

[54] H. Q. Song *et al. Phys. Rev. C*, 44:2505, 1991.

[55] H. Q. Song *et al. Phys. Rev. C*, 47:2001, 1993.

[56] H. Q. Song *et al. Phys. Rev. C*, 49:2924, 1994.

[57] Y. Zhang *et al. Phys. Rev. C*, 54:1137, 1996.

[58] M. Baldo *et al. Phys. rev. C*, 59:682, 1999.

[59] J. N. De *et al. Phys. rev. C*, 55:R1641, 1997.

[60] P. Wang *et al. Nucl. Phys. A*, 748:226, 2005.

[61] W. Trautmann *et al. arXiv:nucl-ex*, 0610032v1, 2006.

[62] P. Donati *et al. Phys. Rev. Lett.*, 72:2835, 1994.

[63] T. Rauscher *et al. Phys. Rev. C*, 56:1613, 1997.

[64] J. R. Huizenga *et al. Ann. Rev. Nucl. Sci.*, 22:427, 1972.

[65] R. G. Stokstad. *Treatise on Heavy-Ion Science*. D.A. Bromley (Plenum, New York, 1895), 1985.

[66] H. A. Bethe. *Phys. Rev.*, 50:332, 1936.

[67] A. V. Ignatyuk *et al. Sov. J. Nucl. Phys*, 21:255, 1975.

[68] S. K. Kataria *et al. Phys. Rev. C*, 18:549, 1978.

[69] K. H. Schmidt *et al. Z. Phys. A*, 308:215, 1982.

[70] J. R. Huizenga *et al. Nucl. Phys.*, 29:462.

[71] J. Toke *et al. Nucl. Phys. A*, 372:141, 1981.

[72] G. Nebbia *et al. Phys. Lett. B*, 176:20, 1986.

[73] R. J. Charity. *Phys. Rev. C*, 58:1073, 1998.

[74] R. J. Charity. *Isospin Physics in Heavy-ion Collisions at Intermediate Energies*. edited by B. A. Li and W. U. Shröder, NOVA, New York, 2001.

[75] R. J. Charity *et al. Phys. Rev. C*, 67:044611, 2003.

[76] S. I. Al-Quraishi *et al. Phys. Rev. C*, 63:065803, 2001.

[77] K. A. Hanold *et al. Phys. rev. C*, 52:1462, 1995.

[78] W. E. Ormand *et al. Phys. Rev. C*, 40:1510, 1989.

[79] M. Lunardon *et al. Eur. Phys. Jour. A*, 13:419, 2002.

[80] J. M. Alexander *et al.* In *Symposium on Nuclear Dynamics and Nuclear Disassembly*. American Chemical Society, Word Scientific, April 10-14, 1989.

[81] H. A. Weidenmuller. *Phys. Lett.*, 10:331, 1964.

[82] S. M. Grimes *et al. Phys. Rev. C*, 42:2744, 1990.

[83] S. M. Grimes. *Z. Phys. A*, 343:125, 1992.

[84] C. A. Engelbrech *et al. Ann. Phys.*, 207:1, 1991.

[85] M. G. Mustafa *et al. Phys. Rev. C*, 45:1078, 1992.

[86] N. Le Neindre *et al.* Level density parameter determination for different Pd isotope. *Experiment proposal at GANIL.*

[87] M. R. Bhat. Data extracted from the ENDF database, 1992. In *Evaluated Nuclear Structure Data File (ENSDF), Nuclear Data for Science and Technology*, Springer-Verlag, Berlin.

[88] N. Gelli *et al.* Search for isospin effects on the level density on nuclei involved in the decay of ^{139}Eu. In *Recent achivements and perspectives in nuclear physics*, 2004.

[89] S. Shlomo *et al. Phys. Rev. C*, 44:44, 1991.

[90] J. Pouthas *et al. Nucl. Instr. and Meth. in Phys. Res. A*, 357:418, 1995.

[91] E. Norbeck *et al. Nucl. Instr. and Meth. A*, 314:620, 1992.

[92] Amoroni *et al. Nucl. Instr. Meth. A*, 556:516, 2006.

[93] D. Guinet *et al. Preprint Lycen*, 8903, 1989.

[94] M. Parlog *et al. Nucl. Instr. and Meth. in Phys. Res. A*, 482:693, 2002.

[95] M. Parlog *et al. Nucl. Instr. and Meth. in Phys. Res. A*, 482:674, 2002.

[96] R. T. De Souza *et al. Nucl. Instr. and Meth. A*, 295:109, 1990.

[97] U. Abbondanno *et al. Nucl. Instr. Meth. A*, 488:604, 2002.

[98] VXIbus system specification, authorized by the VXIbus Consortium Inc., revision 1.3, July 1989.

[99] J. Pouthas *et al. Nucl. Instr. and Meth. in Phys. Res. A*, page 222, 1996.

[100] http://www.ganil.fr/vamos/.

[101] H. Savajols and VAMOS Collaboration. *Nucl. Phys. A*, 654:1027c, 1999.

[102] P. Sugathan *et al. EMIS Conference and Nucl. Instr. Meth.* (to be published).

[103] H. Savajols. *Nucl. Phys. A*, 746:260, 2004.

[104] P. Sugathan. Vamos... experience from our recent experiment. *Slide presentation at INDRA meeting*.

[105] A. Chatterjee *et al.* GLAMPS Analysis Package for GANIL Data and Application to VAMOS-EXOGAM experiments. Technical report.

[106] Chi-yeh Hsi-men *et al. Aberration Theory in Electron and Ion Optics*. Academic Press, 1986.

[107] H. Savajols and VAMOS Collaboration. *Nucl. Instr. and Meth. in Phys. Res. B*, 204:146, 2003.

[108] H. J. Whitlow *et al. Charge exchange and electron stripping*. ed. R. Hellborg, 2005.

[109] H. D. Betz. *Rev. Mod. Phys.*, 44:465, 1972.

[110] M. Suter. *Nucl. Instr. and Meth. in Phys. Res. B*, 52:211, 1990.

[111] V. S. Nikolaev *et al. Phys. Lett.*, 28A(4):277, 1968.

[112] A. Drouart *et al. Nucl. Instr. and Meth. in Phys. Res. A*, 579:1090, 2007.

[113] K. E. Pferdekampfer *et al. Z. Phys. A*, 280:155, 1977.

[114] O. H. Odland *et al. Nucl. Instr. and Meth. in Phys. Res. A*, 378:149, 1996.

[115] A. Breskin. *Nucl. Instr. and Meth.*, 196:11, 1982.

[116] S. Ottini-Hustache *et al. Nucl. Instr. and Meth. A*, 431:476, 1999.

[117] M. D.Agostino *et al. Phys. Lett. B*, 473:219, 2000.

[118] P. M. Milazzo *et al. Nucl. Phys. A*, 703:466, 2002.

[119] R. Alba *et al. Nucl. Phys. A*, 749:98c, 2005.

[120] M. D.Agostino *et al. Phys. Lett. B*, 368:259, 1996.

[121] M. D.Agostino *et al. Phys. Lett. B*, 371:175, 1996.

[122] M. Bruno *et al.* Therodynamical aspects in heavy ion reactions. January 2005.

[123] N. Le Neindre *et al. Nucl. Phys. A*, 795:47, 2007.

[124] B. Borderie *et al. Nucl. Phys. A*, 734:495, 2004.

[125] N. Bellaize *et al. Nucl. Phys. A*, 709:367, 2002.

[126] M. Germain *et al. Phys. Lett. B*, 488:211, 2000.

[127] F. Bocage *et al. Nucl. Phys. A*, 676:391, 2000.

[128] M. F. Rivet *et al. Phys. Lett. B*, 388:219, 1996.

[129] B. Borderie *et al. Phys. Lett.*, B388:224, 1996.

[130] http://www.ganil.fr/user/accelerator/index.html.

[131] `http://www.ganil.fr/spiral/cime.html`.

[132] `http://www.ganil.fr/operation/available_beams.html`.

[133] G.A. Lalazissis *et al. Nucl. Phys. A*, 679:481, 2001.

[134] H. Lehr *et al. Nucl. Phys. A*, 415:149, 1984.

[135] H. Morgenstern *et al. Phys. Lett. B*, 113:463, 1982.

[136] H. Gauvin *et al. Phys. Lett. B*, 58(2):163, 1975.

[137] J. P. Coffin *et al. Phys. Rev. C*, 30:539, 1984.

[138] G. F. Knoll. *Radiation detection and measurement*. Wiley, 1989.

[139] A. Drouart *et al. Nucl. Instr. and Meth. in Phys. Res. A*, 477:401, 2002.

[140] F. Grenier *et al. Nucl. Phys. A*, 2008.

[141] L. Manduci *et al. Nucl. Phys. A*, 2008.

[142] S. Piantelli *et al. Nucl. Phys. A*, 2008.

[143] A. Le Fèvre *et al. Phys. Lett. B*, 2008.

[144] J. Frankland *et al.* `http://indra.in2p3.fr/KaliVedaDoc/about.html`.

[145] W. K. Chu *et al. Phys. Rev. A*, 13(6):2057, 1976.

[146] L. Tassangot. Utilisation d'INDRA avec des faisceaux radioactifs. *INDRA documentations*, 1998.

[147] D. Cline *et al. Nucl. Instr. and Meth.*, 82:291, 1970.

[148] U. L. Businaro *et al. Nuovo Cimento*, 1:629, 1955.

[149] U. L. Businaro *et al. Nuovo Cimento*, 1:1277, 1955.

[150] U. L. Businaro *et al. Nuovo Cimento*, 5:315, 1957.

[151] R. J. Charity *et al. Nucl. Phys. A*, 476:516, 1988.

[152] R. J. Charity *et al. Nucl. Phys. A*, 483:371, 1988.

[153] R. J. Charity *et al. Nucl. Phys. A*, 511:59, 1990.

[154] B. Gatty *et al. Nucl. Phys. A*, 253:511, 1975.

[155] H. H. Deubler *et al. Phys. Lett. B*, 56:241, 1975.

[156] J. P. Bondorf *et al. Phys. Rep. C*, 15:83, 1974.

[157] D. H. E. Gross. *Nucl. Phys. A*, 240:472, 1975.

[158] J. S. Sventek *et al. Phys. Rev. Lett.*, 40:697, 1978.

[159] F. Hubert *et al. Atomic Data Nucl. Data tables*. Vol. 46. Elsevier, 1990.

[160] L. C. Northcliffe and R. F. Schilling. Nuclear Data Table A7. 233, 1970.

[161] B. V. Ershler and F.S. Lapteva. *Atomnaya Energiya*, 1:63, 1956. Engl. Trans. in *Journal of Nuclear Energy*, 4:471, 1957.

[162] Particle Data Group. Particle physics booklet, 2004.

[163] H. C. Britt *et al. Phys. Rev. C*, 13:1483, 1976.

[164] H. H. Gutbrod. *IAEA*, 2:309, 1973.

[165] W. Scobel *et al. Phys. Rev. C*, 14:1808, 1976.

[166] B. Sikora *et al. Phys. Rev. C*, 25:1446, 1982.

[167] B. Borderie *et al. Z. Phys. A*, 321:703, 1985.

[168] W. Bohne *et al. Phys. Rev. C*, 41:R5, 1990.

[169] L. Lassen *et al. Phys. Rev. C*, 55:1900, 1997.

[170] P. Bonche *et al. Nucl. Phys. A*, 436:265, 1985.

[171] C. Ngô and B. Tamain. *Nucl. Phys. A*, 252:237, 1975.

[172] C. Ngô *et al. Nucl. Phys. A*, 240:353, 1975.

[173] W. Scheid *et al. Z. Phys.*, 226:364, 1969.

[174] J. Blocki *et al. Ann. Phys.*, 105:427, 1977.

[175] J. Randrup *et al. Lawrence Berkeley Laboratory Report No. 3603*, 1974.

[176] W. W. Wilcke *et al. Atomic Data and Nuclear Data Tables - Reaction parameters for heavy-ion collisions*. Academy press, 1980.

[177] P. Plasil. Heavy-ion-induced fission. In Robinson, editor, *Proceedings of the International conference on reactions between complex nuclei*, volume 2, page 107. Nashville, Tennesse, 1974.

[178] N. Copinet. *Multidétecteur 4π INDRA. Simulation de la géométrie et étude des détecteurs au silicium.* PhD thesis, Université Paris Sud XI and IPN-Orsay, 1990.

[179] W. D. Myers and W. J. Swiatecki. *Arkiv Fysik*, 36:343, 1967.

[180] V. E. Viola. *Nucl. Data Sheets A*, 1:391, 1965.

[181] V. E. Viola. *Phys. Rev. C*, 31:391, 1985.

Acknowledgements

This work has been made possible by the almost daily help of Dr. Marie-France Rivet, Dr. Bernard Borderie and Dr. Nicolas Le Neindre, who guided me in the context of nuclear research and in particular of low and intermediate energy nuclear reactions during the course of these two years. They taught me the importance of working with dedication and patience, trying always to overcome the difficulties, not always related to analysis issues, and to adapt myself to new situations. This experience will be useful also for my everyday life. In this period I took advantage of their experience in nuclear physics, detectors and electronics to acquire knowledge that I didn't had before. The periods spent at IPN ripened myself and taught me to be more independent both in working and in daily life. I'm indebt to the friendly environment established with Marie-France, Bernard and Nicolas during that periods; I hope it could continue also in future. My frequent visit to Paris have also allowed me to discover and live this wonderful city and its surroundings.
Marie-France's careful reading and corrections of the present thesis has also allowed to improve the readability and fluency of this manuscript. The residual errors and typos are only due to myself.

Many thanks also to my tutor, Prof. Mauro Bruno, and to Dr. Michela D'Agostino, who believed in my work and gave me the possibility of participating to the experiment, subject of this thesis, and to spent part of my Ph.D. at IPN-Orsay. They gave me many useful suggestions during these three years, inciting me to improve myself and to focus the work to the right direction. Mauro's comments and advices on this manuscript have allowed the drawing up of this thesis.

I'm grateful to Prof. Andrea Stefanini for the friendliness he has always shown both in work and in daily life. He always helped and gave me many analysis suggestions during these years, continuously encouraging me. The time he spent replying